Baryon spectroscopy from lattice QCD

Ben Genery Lasscock

Centre for the Subatomic Structure of Matter
School of Chemistry and Physics
University of Adelaide
September 2006

Abstract

The formulation of QCD on a discrete space-time lattice allows us to study the non-perturbative aspects of QCD with numerical simulations. This thesis investigates the spectrum of baryon resonances in quenched lattice QCD.

Our investigation begins with high precision studies of the spectrum of nucleon and Δ resonances on a large $20^3 \times 40$ lattice. We use the Luscher-Weisz plaquette plus rectangle gauge action and the FLIC fermion action for near continuum results at finite lattice spacing. We extend this work to include a search for evidence of the N(1440) "Roper Resonance" in quenched lattice QCD, which should appear as the first even parity excited state of the nucleon. A correlation-matrix analysis with a basis of three nucleon interpolators is considered.

With a strong foundation in the study of nucleon resonances on the lattice, we extend our work to search for evidence of the existence of the $S = +1$, Θ^+ pentaquark having minimal quark content ($uudd\bar{s}$). Observations of the Θ^+ pentaquark were reported in several photo-production experiments, which caused tremendous interest from theorists in the field of high energy physics. Later, several non-observations of the Θ^+, particularly in high statistics experiments conducted by the CLAS collaboration have cast doubt on its existence. Currently there is no known law of nature that excludes the possible existence of a pentaquark state. It is therefore important to determine if the theory of QCD does allow the existence of the Θ^+. As a "first principles" approach to QCD, the lattice provides an unique opportunity to do this.

Key to this work is the formulation of a robust signature of a resonance on the lattice that can discriminate a Θ^+ pentaquark from other possible two-particle states. In our study we consider what we refer to as the standard lattice resonance signature, which is evidence of an attractive interaction between the constituents. We see that this resonance signature is universally observed in lattice studies of the nucleon resonances.

We explore the widest possible space of quantum numbers, with both spin-1/2 and spin-3/2, using an extensive set of local pentaquark interpolating fields. A highlight of this work is our exploratory study of the Θ^+ with spin-3/2, which was the first of its kind. We find evidence of the standard lattice resonance signature in the $I(J^P) = 0(3/2^+)$ channel.

Statement of Originality

This work contains no material which has been accepted for the award of any other degree or diploma in any university or other tertiary institution and, to the best of my knowledge and belief, contains no material previously published or written by another person, except where due reference has been made in the text.

I give consent to this copy of my thesis, when deposited in the University library, to be available for loan and photocopying.

Ben G. Lasscock

Acknowledgements

My graduate studies would not have been possible without the guidence and great patience of my supervisors Derek Leinweber and Tony Williams.

I must acknowledge my debt to Derek for so many things. For his great leadership. For his confidence in me and the work I did. For his calm and methodical approach to all things. And for showing me how to be a scientist.

During my graduate studies I have had the great honour and benefit of working with my other collaborators John Hedditch, Waseem Kamleh, Wally Melnitchouk, Tony Thomas, Ross Young and James Zanotti on a range of projects including our pentaquark searches.

I would thank James Zanotti for being a mentor for me in the first years of my graduates studies. I would like to acknowledge Wally Melnitchouk for his guidance on how to prepare a paper for publication. I have also benefitted from much guidance and many discussions of physics with Ross Young.

In particular I would like to acknowledge John Hedditch for our years of working together on the lattice and for help in teaching me how to use unix, from the very basics to the most advanced applications. Working with John as the co-author of our two and three-point analysis software package and our parallel hadrons software was a blast.

I would like to thank Sharon and Sara in the office for all that they do.

I must also acknowlegde all of the students, postdocs and fellows at the CSSM, Alex, Ayse, Ian, James, John, Maria, Mariusz, Marco G., Marco B., Ross, and Waseem for great discussions and friendship over the years.

Of course I have to thank Ramona Adorjan, Grant Ward and all of the SAPAC staff and David Singleton and all of the staff at APAC for the great computing facilites I have had access to.

I would also like to thank my Mum and Dad and all of my family and my dogs for everything.

Contents

List of Figures

List of Tables

Introduction

In this thesis we complete a thorough study of the spectrum of spin-1/2 and spin-3/2 states of the nucleon and Δ. With this study as a solid foundation we expand the universe of particles we can simulate on the lattice with a calculation of the spectrum of both spin-1/2 and spin-3/2 five-quark states.

With the identification by the LEPS Spring-8 collaboration [1] of a strangeness +1 baryon, labeled the Θ^+ pentaquark, with minimal quark content $uudd\bar{s}$, there has been extensive theoretical and experimental interest in the possible existence of pentaquark states. Lattice QCD provided an important theoretical framework for investigating pentaquark states from a first principles approach. At the time that the putative evidence of the Θ^+ was discovered, the field had extensive experience in calculating the mass spectrum of hadron states contained within the quark model. But the search for the pentaquark on the lattice marked the beginning of a concerted effort to search for states beyond the standard quark model. It became clear early on that in the study of spin-1/2 pentaquark states on the lattice, a robust lattice resonance signature was required to discriminate a possible pentaquark state from possible multi-hadron states. As one of the earlier studies into pentaquarks on the lattice, we proposed a lattice resonance signature inspired by our experience in the study of excited baryons on the lattice, which we discuss in Chapter 3.

Those experimental studies that did identify the Θ^+ were only able to measure its mass and strangeness. The spin, isospin and parity of the Θ^+ remains unknown. Consequently we implemented an exhaustive search for the Θ^+ over the largest range of quantum numbers possible, including, at the time of writing, the first of only two studies of possible spin-3/2 states.

In Chapter 2 we present our study of the excited states of the nucleon and Δ baryons at light quark masses in quenched QCD (QQCD). In Chapters 3 and 4 we present our search for the Θ^+ pentaquark in QQCD. Our findings are summarised at the end of each chapter and in Chapter 5.

1.1 Quantum Chromodynamics

Quantum Chromodynamics (QCD) is a gauge theory that describes the strong interaction, which is largely responsible for the masses of particles in the hadron spectrum. Inspired by the success of the quark model in explaining the spectrum of mesons and baryons in terms of composites of valence quarks, in the quantum field theory each quark field ψ carries colour charge, (red, green, blue) and a flavour (up, down, strange, charm, top, bottom). The QCD (CP conserving) Lagrangian density that defines the theory is,

$$\mathcal{L} = \bar{\psi}(i\gamma^\mu D_\mu - m)\psi - \frac{1}{4}F_{\mu\nu}F_{\mu\nu}. \tag{1.1}$$

With $D_\mu = \partial_\mu - igA_\mu$, γ^μ is a gamma matrix (in the Bjorken and Drell representation, see Appendix A), g is the coupling of the fermions to the gauge field, and $F_{\mu\nu}$ is the field strength tensor. We demand that the Lagrangian is invariant under a local gauge

transformation by an arbitrary element of SU(3), $\psi(x) \rightarrow \exp(-i\alpha^a(x)\frac{\lambda^a}{2})\psi(x)$, where $\alpha^a(x)$ is some arbitrary function of spatial coordinates x and the Gell-mann matrices λ are the generators of the group SU(3). Demanding invariance under the local gauge transformation on the fields also requires that,

$$D_\mu\psi \rightarrow \exp(-i\alpha^a(x)\frac{\lambda^a}{2})D_\mu\psi, \tag{1.2}$$

$$A^a_\mu \rightarrow A^a_\mu - \frac{1}{g}\partial_\mu\alpha^a(x) + f^{abc}A^b_\mu\alpha^c(x)\ , \tag{1.3}$$

where f^{abc} are the structure constants of SU(3). The field strength tensor is,

$$F^a_{\mu\nu} = \partial_\mu A^a_\nu - \partial_\nu A^a_\mu + g f^{abc}A^b_\mu A^c_\nu\ . \tag{1.4}$$

Because the gauge fields in QCD are non-Abelian, the term F^2 in the Lagrangian gives rise to terms like A^3 and A^4 which describes a three and four gluon vertex, giving QCD a rich vacuum structure. Furthermore since there are eight generators of the group SU(3) the gauge fields (gluons) come in eight varieties.

Observables in quantum field theory are obtained from vacuum expectation values. The vacuum expectation value of a time ordered operator $<\Omega|T\hat{O}|\Omega>$ is evaluated with a path integral over every possible field configuration of $\psi, \bar{\psi}$ and every possible gauge orbit weighted in importance by the exponential of the QCD action $i\int d^4x\mathcal{L}_{QCD}$,

$$<\Omega|\hat{O}|\Omega> = \frac{1}{Z_0}\int \mathcal{D}\psi(x)\mathcal{D}\bar{\psi}(x)\mathcal{D}A_\mu(x)\ \hat{O}e^{i\int d^4x\mathcal{L}_{QCD}}. \tag{1.5}$$

The integral is normalized by a factor Z_0,

$$Z_0 = \int \mathcal{D}\psi(x)\mathcal{D}\bar{\psi}(x)\mathcal{D}A_\mu(x)e^{i\int d^4x\mathcal{L}_{QCD}}\ . \tag{1.6}$$

As a specific example let the operator be the time ordered product of fermion field creation and annihilation operators. Then the amplitude,

$$<\Omega|T\psi(x_1)\psi(x_2)...\bar{\psi}(x'_1)\bar{\psi}(x'_2)...|\Omega> = \frac{1}{Z_0}\int \mathcal{D}A_\mu(x)\mathcal{D}\bar{\psi}(x)\mathcal{D}\psi(x)\psi(x_1)\psi(x_2)...\bar{\psi}(x'_1)\bar{\psi}(x'_2)...e^{i\int d^4x\mathcal{L}_{\rm QCD}}\ . \tag{1.7}$$

The Grassman integration over the fermion fields demands a sum of all possible contractions of the fields $\psi(x_i)$ and $\bar{\psi}(x'_j)$. Each contraction of the fermions fields leaves a quark propagator $M^{-1}(x_i, x'_j)$, where M is the fermionic matrix $M = (i\gamma^\mu D_\mu - m_q)$. Thus the above expression simplifies to

$$<\Omega|T\psi(x_1)\psi(x_2)...\bar{\psi}(x'_1)\bar{\psi}(x'_2)...|\Omega> = \frac{1}{Z_0}\int \mathcal{D}A_\mu(x)\det(M(A_\mu))e^{i\int d^4x - \frac{1}{4}F_{\mu\nu}F_{\mu\nu}} \times\Big\{M^{-1}(x_1,x'_1)M^{-1}(x_2,x'_2)... - M^{-1}(x_2,x'_1)M^{-1}(x_1,x'_2)... + ...\Big\}\ . \tag{1.8}$$

1.2 Lattice QCD

The formulation of the electro-weak theory as a quantum field theory describing the interactions of fermions with photons and Z^0 and $W^{\pm}$ bosons, is well understood using a perturbative expansion for a small coupling. This approach is successful because the coupling of the fermion fields to the gauge bosons is small in electroweak theory. Similarly because QCD is asymptotically free at a large energy scale the coupling g becomes small and processes like deep inelastic scattering is successfully described by perturbative QCD. For an energy scale less than $\simeq$ 1GeV, the coupling becomes large and so a non-perturbative approach is required to compute such things as the hadron mass spectrum and other properties of hadrons such as the electro-magnetic form factors directly from QCD.

Here we discuss the basic formulation of lattice QCD, which is a non-perturbative approach to solving QCD with numerical simulations. Following Wilson [2], the central approximation of lattice QCD is the replacement of space-time with a discrete lattice in Euclidean space. Derivatives are therefore replaced by differences and integrals by sums. Note that discrete space-time introduces a natural momentum cut-off, so a regularisation scheme is built in. The quark fields $\psi(x)$ reside on the lattice sites and the gluon fields are encoded in SU(3) colour matrices U_μ, $\mu = 1, 2, 3, 4$ called links that can be thought of as residing between lattice sites. We refer to a set of link operators for every lattice site as a gauge field configuration.

The gauge fields are encoded in the link operator, which is a parallel transport operator on a straight line contour connecting neighboring lattice sites. The link operator, along the contour parametrized by t, has the property that under a local gauge transformation $\mathcal{U}(x)$,

$$U(t, t_0) \rightarrow \mathcal{U}(t)U(t, t_0)\mathcal{U}^\dagger(t_0). \tag{1.9}$$

The path ordered product of parallel transport operators along a contour is equivalent to an overall parallel transport operator,

$$U(t, t_0) = U(t, u)U(u, t_0). \tag{1.10}$$

Under an arbitrary local gauge transformation the product of link operators transform like

$$\begin{aligned} U(t, u)U(u, t_0) &\rightarrow \mathcal{U}(t)U(t, u)\mathcal{U}^\dagger(u)\mathcal{U}(u)U(u, t_0)\,\mathcal{U}^\dagger(t_0) \\ &= \mathcal{U}(t)U(t, u)U(u, t_0)\mathcal{U}^\dagger(t_0) \\ &= \mathcal{U}(t)U(t, t_0)\mathcal{U}^\dagger(t_0)\ . \end{aligned} \tag{1.11}$$

On the lattice the link operator is a path ordered exponential of the integral of the gauge field along a straight line contour between neighboring lattice sites parametrised by λ,

$$U_\mu(x) = \mathcal{P}e^{-ig\int_0^a d\lambda A_\mu(x+\lambda\hat{\mu})} \simeq e^{-iga A_\mu(x+\frac{a}{2})}\ . \tag{1.12}$$

Here the μ index on the link labels the direction of the straight line contour from lattice site at x to the lattice site at $x+\hat{\mu}$. The product of link operators around a unit square on the lattice is called a plaquette,

$$U_P = U_\mu(x)U_\nu(x + a\hat{\mu})U_\mu^\dagger(x + a\hat{\nu})U_\nu^\dagger(x). \tag{1.13}$$

Because the plaquette is a closed contour it has the transformation property,

$$U_P \rightarrow \mathcal{U}(x) U_P \mathcal{U}^\dagger(x)$$

The plaquette described explicitly in terms of link operators is,

$$U_P = e^{(-igaA_\mu(x))} e^{(-igaA_\nu(x+a\hat{\mu})} \; e^{(igaA_\mu(x+\hat{\nu})} e^{(igaA_\nu(x))}. \tag{1.14}$$

Using the Baker-Campbell-Hausdorf formula to second order in a,

$$e^A e^B = e^{(A+B+[A,B]+...)}, \tag{1.15}$$

$$U_P = e^{-iga^2(\partial_\mu A_\nu - \partial_\nu A_\mu - g[A_\mu, A_\nu] + O(a^2))}, \tag{1.16}$$

$$U_P = e^{-iga^2(F_{\mu\nu} + O(a^2))}. \tag{1.17}$$

Therefore as the gauge fields can be thought of as being encoded in the link operators, the field strength tensor is encoded in the plaquette. By expanding this exponential,

$$U_P = 1 - iga^2 F_{\mu\nu} + \frac{1}{2} g^2 a^4 F_{\mu\nu} F_{\mu\nu} + O(a^6), \tag{1.18}$$

$$1 - \frac{1}{3} \mathcal{R}eTr[U_P] = a^4 \frac{g^2}{3} Tr[\frac{1}{2} F_{\mu\nu} F_{\mu\nu} + O(a^2)] \; . \tag{1.19}$$

Note that there is no implied sum over indices μ and ν. The trace is over colour indices which are suppressed. The gluon action on the lattice is defined with the condition *a priori* that it reconstruct the correct form in the limit $a \rightarrow 0$,

$$S_G = \beta \sum_x \sum_P (1 - \frac{1}{3} \mathcal{R}eTr[U_P]), \tag{1.20}$$

$\sum_P$ is a sum over every Plaquette.

$$= \beta \sum_x \sum_P (1 - \frac{1}{3} \mathcal{R}eTr[U_P]),$$

$$= \beta \sum_x \sum_{\mu,\nu} \frac{a^4 g_0^2}{6} \frac{1}{2} Tr[F_{\mu\nu} F_{\mu\nu} + O(a^2)] \; . \tag{1.21}$$

In the last line we realize that F^2 is purely real. In the limit that the lattice is removed $a \rightarrow 0$,

$$\sum_x \rightarrow \frac{1}{a^4} \int d^4x,$$

$$O(a^2) \rightarrow 0,$$

$$S_G \rightarrow \beta \frac{g_0^2}{6} \int d^4x \frac{1}{2} Tr[F_{\mu\nu} F_{\mu\nu}] \; . \tag{1.22}$$

Thus to satisfy the condition *a priori* that the lattice action is equivalent to the continuum action in the continuum limit,

$$\beta = \frac{6}{g_0^2} \; . \tag{1.23}$$

As in the continuum limit we demand that the lattice gauge action is invariant under an arbitrary local gauge transformation, using Eq. (1.9),

$$\begin{aligned} U_P &\rightarrow \mathcal{U}(x)U_P\mathcal{U}^\dagger(x) \ , \\ Tr[U_P] &\rightarrow Tr[\mathcal{U}(x)U_P\mathcal{U}^\dagger(x)] \ , \\ &= Tr[\mathcal{U}^\dagger(x)\mathcal{U}(x)U_P] \ , \\ &= Tr[U_P] \ . \end{aligned} \tag{1.24}$$

Similarly we can write down the Wilson fermion action for the lattice,

$$S_{\rm W}^{\rm FL} = \sum_x (am + 4r)\bar{\psi}(x)\psi(x) - \frac{1}{2}\sum_{x,\mu}\Big\{ \bar{\psi}(x)(r - \gamma_\mu)U_\mu(x)\psi(x + \hat{\mu}) \tag{1.25}$$

$$+ \bar{\psi}(x)(r + \gamma_\mu)U_\mu^\dagger(x - \hat{\mu})\psi(x - \hat{\mu})\Big\} \ , \tag{1.26}$$

which is just a discrete version of the continuum fermion action plus the irrelevant terms multiplied by the Wilson parameter r. These terms are included in the lattice action to remove the fermion doublers that appear in the discrete space-time. Naturally we are free to introduce additional terms in our lattice action provided there exists the correct continuum limit. The Wilson parameter is arbitrary, so we choose $r = 1$. Using Eq. (1.9) we see that this action is also invariant under a local gauge transformation.

Core to this study is the computation of the baryon two-point correlation function, which can be expressed in terms of a time ordered product of quark fields. We complete the integration over the quark fields, which are grassman variables, using the Wick reduction discussed in Eq. (1.5). This leaves us with an integration over the gauge fields of the product of quark propagators. In lattice QCD the integration over gauge fields is approximated by a discrete sum over a finite ensemble of gauge field configurations. An uncorrelated ensemble of gauge field configurations is generated using Monte Carlo techniques, with samples weighted in importance by a factor $\det(M[U])e^{-S_G[U]}$, where $S_G[U]$ is the lattice gauge action in Euclidean space. In quenched QCD (QQCD) the determinant of the fermionic matrix is set to 1 to reduce the computational cost of the simulation. Quantifying the impact of quenching on the determination of a particular observable is non-trivial. However we expect that we can still obtain an understanding of QCD in the quenched approximation, particularly at larger quark masses. An excellent description of a Monte Carlo algorithm can be found in [3]. For this study our gauge field configurations are generated using the Cabibbo-Marinari pseudoheat-bath algorithm [4].

A complete description of how we evaluate the baryon two-point function can be found in Chapter 2 and similarly a description of how to evaluate the pentaquark can be found in Chapter 3. A complete description of how we extract the hadron spectrum from the two-point correlation functions can be found in Chapter 2.

Finally, our numerical simulations generate dimensionless quantities. Dimensionful quantities can be extracted with knowledge of the physical scale of the lattice a. This is not a direct input to the simulation. A dimensionless quantity $\hat{M}$ generated in our simulations, corresponding to a physical observable with dimensions of $(mass)^d$ is given a physical value M, by the physical scale of the lattice a,

$$\hat{M} = a^d M \ . \tag{1.27}$$

So every observable which is simulated on the lattice must be combined with the lattice spacing a to give a dimensionful result.

1.2.1 Scale Determination

As discussed in the previous section, observable quantities calculated in our numerical simulations are dimensionless, but we can extract dimensionful quantities with knowledge of the lattice spacing. Making an accurate determination of the lattice spacing is a vital step in any lattice simulation. In principle we can compare the lattice calculation of a given observable to its known empirical value to deduce the lattice spacing. However this approach incorporates quenching artifacts (in quenched simulations), scaling violations, finite volume effects and possible ambiguity in the chiral extrapolation, into the determination of the scale. A better approach is to compare the static quark potential calculated on the lattice, see [5], with phenomenological models of the heavy meson systems. At short range the tree-level interaction between a $q\bar{q}$ pair gives a coulombic potential. At long range QCD has a linear confining potential [2], although the inclusion of quark loops makes this slightly ambiguous in full QCD. However the flux tube picture is well established in quenched lattice QCD for static meson and baryon systems [6, 7]. Combining these qualitative features of the quark potential in a phenomenological model gives a heavy quark potential,

$$V(r) = V_o + \sigma r - \frac{e}{r} \, . \tag{1.28}$$

With the requirement that we restrict ourselves to heavy quark systems (charmonium or heavier), the parameters of this equation can be determined by fitting the energy levels of a non-relativistic Schroedinger equation solved with this potential to the experimentally determined energy levels of heavy mesons [8].

On the lattice we derive the quark potential for static quarks from the product of link operators around some closed contour, commonly called the Wilson loop. For a full description of how we extract the static quark potential from the Wilson loops see [5].

The Lattice Ansatz

In the Fermi-Breit scheme the static quark potential at short range is,

$$V(r) = -\frac{2\alpha_s}{3r} \, . \tag{1.29}$$

This expression is derived using the continuum tree-level gluon propagator. An ansatz for a better model of the potential computed on the lattice uses the lattice tree-level gluon propagator [9–11],

$$V(r) = V_0 + \sigma r - e\left[\frac{1}{\mathbf{r}}\right] + l(\left[\frac{1}{\mathbf{r}}\right] - \frac{1}{r}) \, . \tag{1.30}$$

Where the lattice coulomb potential is derived from the tree-level lattice gluon propagator, which is the Fourier transform of the momentum space gluon propagator of the static quarks in the Breit frame,

$$\left[\frac{1}{\mathbf{r}}\right] = \int \frac{d\mathbf{k}}{(2\pi)^3} \cos(\mathbf{k}\cdot\mathbf{r}) D_{00}(0,\mathbf{k}) \, . \tag{1.31}$$

The lattice gluon propagator in Landau gauge is given by [12],

$$D^{ab}_{\mu\nu}(k) = \frac{\delta_{\mu\nu}\delta^{ab}}{\tilde{k}^2}. \tag{1.32}$$

In this thesis we use the $O(a^2)$-Symanzik improved lattice action [13]. The momentum variable for the improved action [12] is,

$$\tilde{k}_\mu = \frac{2}{a}\sqrt{\sin^2(\frac{k_\mu}{2}) + \frac{1}{3}\sin^4(\frac{k_\mu}{2})}\ . \tag{1.33}$$

This model has lattice artifacts built in and hence is a better model of the potential calculated in a lattice simulation. The term $l([\frac{1}{\mathbf{r}}] - \frac{1}{r})$ is designed to correct for lattice artifacts beyond tree-level. The purpose of this is to improve agreement between the short range behaviour of the potential and the simulation results. In the limit that the lattice spacing is removed $[\frac{1}{\mathbf{r}}] = \frac{1}{r}$, hence this model reproduces Eqn (1.28) in the continuum limit.

By fitting the static quark potential data generated from the Wilson loops to the above ansatz, the parameters V_0, e, σ and l are determined. The Sommer scales r_0 and r_1 [14] are alternative quantities that can be extracted from the static quark potential. These scales are defined by the condition,

$$r_c^2 \frac{\partial V(r)}{\partial r}|_{r_c} = c. \tag{1.34}$$

The scales r_0 and r_1 are defined at $c = 1.65$ and $c = 1.00$ respectively. The phenomenological values of r_0 and r_1 that we use are [14],

$$r_0 = 0.49 \text{ fm}\ , \tag{1.35}$$
$$r_1 = 0.35 \text{ fm}\ . \tag{1.36}$$

In the continuum limit Eq. (1.30) provides,

$$r_c^2 \frac{\partial V(r)}{\partial r}|_{r_c} = r_c^2\sigma + e, \tag{1.37}$$
$$= c, \tag{1.38}$$

Which implies,

$$r_c = \sqrt{\frac{c-e}{\sigma}}. \tag{1.39}$$

If we label the scale set by r_0 and r_1 as a_0 and a_1 respectively then by using the values obtained by fitting the potential ansatz Eq. (1.30) to the lattice potential data,

$$a_0 = \frac{0.49}{\sqrt{\frac{c-e}{\sigma}}} \text{ fm}\ , \tag{1.40}$$

$$a_1 = \frac{0.35}{\sqrt{\frac{c-e}{\sigma}}} \text{ fm}\ . \tag{1.41}$$

The Sommer scales a_0 and a_1 are defined at an intermediate quark separation, between the Coulombic and linear behaviours of the static quark potential. Using these quantities to set the scale has an advantage over setting the scale with the string tension because they are well defined irrespective of the quenched approximation. We choose to set the scale with r_0 for easy comparison with most contemporary lattice calculations.

1.3 Lattice simulations parameters

In Sec. 1.2 we described the Wilson quark and gauge actions as a part of a basic outline of lattice QCD. By construction these actions have the correct continuum limit. But at finite lattice spacing they contain lattice artifacts of $O(a)$ and $O(a^2)$ respectively.

The cost of our lattice simulation is strongly dependent on the size of the lattice spacing and number of lattice sites, and we require a large physical volume to study the hadron spectrum. Further we are free to use different gauge and fermion actions provided that there exists the correct continuum limit. So in this section we provide a brief description of the improved lattice gauge and fermion actions that we use to obtain continuum like results at finite lattice spacing. Note that a more detailed account of the actions has been given by Zanotti *et al.* [15].

Gauge action

We use the $O(a^2)$ improved Luscher-Weisz mean-field improved plaquette plus rectangle gauge action [13]. Which is given by

$$S_{\rm G} = \frac{5\beta}{3}\sum_{\rm sq}\frac{1}{3}\mathcal{R}e\,{\rm tr}[1 - U_{\rm sq}(x)] - \frac{\beta}{12u_0^2}\sum_{\rm rect}\frac{1}{3}\mathcal{R}e\,{\rm tr}[2 - U_{\rm rect}(x)]\,, \qquad (1.42)$$

where the operators $U_{\rm sq}(x)$ and $U_{\rm rect}(x)$ are defined as

$$\begin{aligned} U_{\rm sq}(x) &= U_\mu(x)\,U_\nu(x+\hat{\mu})\,U_\mu^\dagger(x+\hat{\nu})\,U_\nu^\dagger(x)\,, \\ U_{\rm rect}(x) &= U_\mu(x)\,U_\nu(x+\hat{\mu})\,U_\nu(x+\hat{\nu}+\hat{\mu})\,U_\mu^\dagger(x+2\hat{\nu})\,U_\nu^\dagger(x+\hat{\nu})\,U_\nu^\dagger(x) \\ &+ U_\mu(x)\,U_\mu(x+\hat{\mu})\,U_\nu(x+2\hat{\mu})\,U_\mu^\dagger(x+\hat{\mu}+\hat{\nu})\,U_\mu^\dagger(x+\hat{\nu})\,U_\nu^\dagger(x). \end{aligned} \qquad (1.43)$$

The link product $U_{\rm rect}(x)$ denotes the rectangular 1×2 and 2×1 plaquettes, and for the tadpole improvement factor we use the plaquette measure,

$$u_0 = \left\langle \frac{1}{3}\mathcal{R}e\,{\rm tr}\langle U_{\rm sq}\rangle \right\rangle^{1/4}. \qquad (1.44)$$

The gauge configurations are generated using the Cabibbo-Marinari pseudoheat-bath algorithm with three diagonal SU(2) subgroups looped over twice. The simulations are performed using a parallel algorithm with appropriate link partitioning, as described in Ref. [16].

The calculations are performed on a large $20^3\times 40$ lattice at $\beta = 4.53$. As discussed above, the scale is set via the Sommer scale r_0 obtained from the static quark potential [11]. Recall that we use the phenomenological value of $r_0 = 0.49$ fm, the lattice spacing is $a = 0.128(2)$ fm.

Fat-link irrelevant fermion action

For the quark fields, we use the Fat-Link Irrelevant Clover (FLIC) fermion action [15], which provides a new form of nonperturbative $\mathcal{O}(a)$ improvement [17]. This action has previously been used to study hadronic masses [15], as well as the excited baryon spectrum [18]. Here fat links are generated by smearing links with their nearest transverse neighbours in a gauge covariant manner (APE smearing). This has the

effect of reducing the problem of exceptional configurations common to Wilson-style actions [19], and minimising the effect of renormalisation on the action improvement terms. Since only the irrelevant, higher-dimensional terms in the action are smeared, while the relevant, dimension-four operators are left untouched, the short-distance behaviour of the quark and gluon interactions is retained. The use of fat links [20] in the irrelevant operators also removes the need to fine tune the clover coefficient in removing all $\mathcal{O}(a)$ artifacts.

The smearing procedure involves replacing a link, $U_\mu(x)$, with a sum of the link and α times its staples [21, 22],

$$U_\mu(x) \to U'_\mu(x) = (1-\alpha)\, U_\mu(x) + \frac{\alpha}{6} \sum_{\substack{\nu=1 \\ \nu\neq\mu}}^{4} \Big[U_\nu(x)\, U_\mu(x+\nu a)\, U_\nu^\dagger(x+\mu a) + U_\nu^\dagger(x-\nu a)\, U_\mu(x-\nu a)\, U_\nu(x-\nu a+\mu a) \Big] ,$$

followed by projection back to SU(3). The unitary matrix U_μ^{FL} which maximises

$$\mathcal{R}e\,\mathrm{tr}\left[U_\mu^{\mathrm{FL}}\, U_\mu'^\dagger \right]$$

is selected by iterating over the three diagonal SU(2) subgroups of SU(3). The entire procedure of smearing followed immediately by projection is repeated n times. The fat links used in this work are created with $\alpha = 0.7$ and $n = 6$, as discussed in Ref. [15]. The mean-field improved FLIC action is given by [15]

$$S_{\mathrm{SW}}^{\mathrm{FL}} = S_{\mathrm{W}}^{\mathrm{FL}} - \frac{i C_{\mathrm{SW}}\, \kappa r}{2(u_0^{\mathrm{FL}})^4}\, \bar\psi(x)\, \sigma_{\mu\nu}\, F_{\mu\nu} \psi(x) , \tag{1.45}$$

where $F_{\mu\nu}$ is constructed using fat links, and the plaquette measure u_0^{FL} is calculated via Eq. (1.44) using the fat links. The factor C_{SW} is the (Sheikholeslami-Wohlert) clover coefficient [23], defined to be 1 at tree-level. The quark hopping parameter is $\kappa = 1/(2m + 8r)$, and we use the conventional choice of the Wilson parameter, $r = 1$. In Eq. (1.45) the mean-field improved Fat-Link Irrelevant Wilson action is given by

$$S_{\mathrm{W}}^{\mathrm{FL}} = \sum_x \bar\psi(x)\psi(x) + \kappa \sum_{x,\mu} \bar\psi(x) \Big[\gamma_\mu \Big(\frac{U_\mu(x)}{u_0} \psi(x+\hat\mu) - \frac{U_\mu^\dagger(x-\hat\mu)}{u_0} \psi(x-\hat\mu) \Big) - r \Big(\frac{U_\mu^{\mathrm{FL}}(x)}{u_0^{\mathrm{FL}}} \psi(x+\hat\mu) + \frac{U_\mu^{\mathrm{FL}\dagger}(x-\hat\mu)}{u_0^{\mathrm{FL}}} \psi(x-\hat\mu) \Big) \Big] . \tag{1.46}$$

As shown by Zanotti *et al.* [15], the mean-field improvement parameter for the fat links is very close to 1, so that the mean-field improved coefficient for C_{SW} is adequate. A further advantage is that one can now use highly improved definitions of $F_{\mu\nu}$ (involving terms up to u_0^{12}), which give impressive near-integer results for the topological charge [24, 25]. In particular, we employ an $\mathcal{O}(a^4)$ improved definition of $F_{\mu\nu}$, as used by Bilson-Thompson *et al.* [24, 25].

A fixed boundary condition in the time direction is implemented by setting $U_t(\vec{x}, N_t) = 0\ \forall\ \vec{x}$ in the hopping terms of the fermion action, and periodic boundary conditions are imposed in the spatial directions. Gauge-invariant Gaussian smearing [26] in the spatial dimensions is applied at the source to increase the overlap of the interpolating

operators with the ground states. The source-smearing technique [26] starts with a point source, $\psi_0(\vec{x}_0, t_0)$, at space-time location $(\vec{x}_0, t_0) = (1, 1, 1, 8)$, and proceeds via the iterative scheme,

$$\psi_i(x,t) = \sum_{x'} F(x,x')\,\psi_{i-1}(x',t)\,, \tag{1.47}$$

where

$$F(x,x') \;=\; \frac{1}{(1+\alpha)}\Big(\delta_{x,x'} + \frac{\alpha}{6}\sum_{\mu=1}^{3}\left[U_\mu(x)\,\delta_{x',x+\widehat{\mu}} \;+\; U_\mu^\dagger(x-\widehat{\mu})\,\delta_{x',x-\widehat{\mu}}\right]\Big)\,. \tag{1.48}$$

Repeating the procedure N times gives the following fermion field

$$\psi_N(x,t) = \sum_{x'} F^N(x,x')\,\psi_0(x',t)\,. \tag{1.49}$$

The parameters N and α govern the size and shape of the smearing function and in our simulations we use $N = 35$ and $\alpha = 6$. This level of smearing enhances the overlap of our interpolating fields with the ground state, while still allowing the study of the low lying excited states.

Excited Baryons in Lattice QCD

2.1 Introduction

Extracting the hadron spectrum in lattice QCD allows us to gain insight into the underlying dynamics which govern the theory of QCD. In [18] and [27] we establish the formalism for extracting both spin-1/2 and spin-3/2 exited states of the nucleon and Δ. Here we work with a larger lattice volume (2.5 fm here compared to 1.95 fm in [18, 27]), reducing finite volume effects and enhancing our statistics. We probe closer to the chiral limit with lighter quark masses, here we have a pion mass as light as 300 MeV compared to 560 Mev in [18,27], and we enhance our spin-3/2 nucleon and Δ interpolating fields by including a sum over all possible Lorentz indices. Moreover this calculation serves as an important proof of method for extracting the spectrum of spin-1/2 and spin-3/2 states on the lattice and provides the basis of our analysis of the spectrum extracted with our pentaquark interpolators [28] and [29].

The quenched approximation and unphysically large quark masses used in our simulation makes direct comparison with the known hadron spectrum difficult. However in this calculation we are interested in reproducing the correct ordering of states in the spectrum of the nucleon and Δ. We will look for hyperfine and spin-orbit interactions on the lattice by calculating the mass of the odd-parity spin-1/2 $N(1535)$ and spin-3/2 $N(1520)$ states and the odd-parity spin-1/2 $\Delta(1620)$ and the $\Delta(1700)$.

Finally we wish to explain the conspicuous absence of the first even-parity excited state of the nucleon, the Roper resonance, in earlier quenched lattice QCD simulations [18, 30].

Using a variety methods, existing lattice studies that have identified both the first and second even-parity excited states of the nucleon include, [31] using Bayesian analysis, [32] using the maximal entropy method, and [33] using and correlation matrix analysis with three different source and sink smearing prescriptions to create an extended basis of nucleon interpolators.

In this study we apply the standard correlation matrix analysis techniques over our basis of three nucleon interpolators in an attempt to extract the first and second even-parity excited state of the nucleon. Our previous study [18] showed that the χ_1 and χ_2 interpolators did not have significant overlap. Following the approach used in [30] we extend this analysis by including the χ_3 interpolator that was used in [27] to extract spin-3/2 nucleon excited states.

2.2 Lattice Techniques

As discussed in the introduction, Chapter 1, this analysis is based on an ensemble of 400, gauge-field configurations on a $20^3 \times 40$ lattice, using the mean-field $\mathcal{O}(a^2)$-improved Luscher-Weisz plaquette plus rectangle gauge action [13]. The lattice spacing is 0.128 fm, set with $r_0 = 0.49$ fm. For the fermion propagators, we use the FLIC fermion action [15], an $\mathcal{O}(a)$-improved fermion action with excellent scaling properties providing near continuum results at finite lattice spacing [34].

A fixed boundary condition in the time direction is implemented by setting $U_t(\vec{x}, N_t) = 0 \; \forall \; \vec{x}$ in the hopping terms of the fermion action. Periodic boundary conditions are imposed in the spatial directions. To explore the effects of the fixed boundary condition we have examined the effective mass of the pion correlation function and the associated $\chi^2_{\rm dof}$ obtained in various fits. The pion is selected as it has the longest correlation length and will be a worst case scenario for the boundary effects. We find that the fixed boundary effects are only significant after time slice 30, which is the limit of our analysis of the correlation functions presented below.

Gauge-invariant Gaussian smearing [26] in the spatial dimensions is applied at the fermion source at $t = 8$ to increase the overlap of the interpolating operators with the ground states. Eight quark masses are used in the calculations, with $\kappa = \{0.12780, 0.12830, 0.12885, 0.12940, 0.12990, 0.13025, 0.1306, 0.1308\}$ providing $am_\pi = \{0.540, 0.500, 0.453, 0.400, 0.345, 0.300, 0.242, 0.197\}$. The strange quark mass is taken to be the third largest ($\kappa = 0.12885$) quark mass. This κ provides a pseudo-scalar mass of 697 MeV which compares well with the experimental value of $\sqrt{2M_{\rm K}^2 - M_\pi^2} = 693$ MeV motivated by leading order chiral perturbation theory. The error analysis is performed by a second-order, single-elimination jackknife, with the χ^2 per degree of freedom obtained via covariance matrix fits. Further details of the fermion action and simulation parameters are provided in Refs. [15, 34] and [28, 29] respectively.

2.2.1 Interpolating Fields

In this study we use the nucleon and Δ interpolating fields established in [18, 27]. We also consider a correlation matrix analysis with the nucleon interpolators. The nucleon interpolating fields are,

$$\begin{aligned} \chi_1(x) &= \epsilon^{abc}(u^{Ta}(x)C\gamma_5 d^b(x))u^c(x) \\ \chi_2(x) &= \epsilon^{abc}(u^{Ta}(x)C d^b(x))\gamma_5 u^c(x) \\ \chi_3^\mu(x) &= \epsilon^{abc}(u^{Ta}(x)C\gamma_5\gamma^\mu d^b(x))\gamma_5 u^c(x) \; . \end{aligned} \tag{2.1}$$

The Δ interpolating field is,

$$\chi^\mu_{\Delta^{++}}(x) = \epsilon^{abc}(u^{Ta}(x)C\gamma^\mu u^b(x))u^c(x) \tag{2.2}$$

A review of how the nucleon and Δ interpolators transform under proper Lorentz transformation is shown in Appendix B. Note that use the Bjorken and Drell representation of the γ-matrices, see Appendix A, in all of our phenomenology.

2.2.2 Excited baryons on the lattice

We begin our discussion with a detailed review of how to extract the masses of even and odd-parity states with the spin-1/2 χ_1 and χ_2 interpolators. On the baryon level, the two-point correlation function in momentum space is

$$\mathcal{G}(t, \vec{p}) = \sum_{\vec{x}} e^{-i\vec{p}\cdot\vec{x}} \langle 0 \,|T\, \chi(x)\, \bar{\chi}(0) \,|\, 0 \rangle \; . \tag{2.3}$$

Where the interpolator $\chi(\bar{\chi})$ annihilates(creates) baryon states to(from) the vacuum.

First, in our lattice simulations we satisfy the time ordering operator in Eq. (2.3) because we only consider the amplitude for the hadron to propagate forward in time. A fixed boundary condition at time slice 40 in the time direction prevents contamination from the backwards propagating signal.

Next we continue our derivation by inserting a complete set of intermediate momentum, energy and spin states $|B, \vec{p}', s\rangle$,

$$1 = \sum_{B,\vec{p}\,',s} |B,\vec{p}\,',s\rangle\langle B,\vec{p}\,',s| \ . \tag{2.4}$$

$$\mathcal{G}(t,\vec{p}) = \sum_{s,\vec{p}\,',B} \sum_{\vec{x}} e^{-i\vec{p}\cdot\vec{x}} \ \langle 0|\ \chi(x)\ |B,\vec{p}\,',s\rangle\langle B,\vec{p}\,',s|\ \bar{\chi}(0)\ |0\rangle \ , \tag{2.5}$$

where the state B has mass M_B and energy $E_B = \sqrt{M_B^2 + \vec{p}^2}$. This sum over all possible states B with a given set of quantum numbers includes a large tower of resonances and those multi-hadron states created by our interpolators in QQCD. Taking advantage of the relation $\chi(x) = e^{iP\cdot x}\chi(0)e^{-iP\cdot x}$ (with four-momentum P),

$$\begin{aligned}
\mathcal{G}(t,\vec{p}) &= \sum_{s,\vec{p}\,',B} \sum_{\vec{x}} e^{-i\vec{p}\cdot\vec{x}} \ \langle 0|\ e^{iP\cdot x}\chi(0)e^{-iP\cdot x}\ |B,\vec{p}\,',s\rangle\langle B,\vec{p}\,',s|\ \bar{\chi}(0)\ |0\rangle \\
&= \sum_{s,\vec{p}\,',B} e^{-iE_B t} \sum_{\vec{x}} e^{-i\vec{x}\cdot(\vec{p}-\vec{p}\,')} \ \langle 0|\ \chi(0)\ |B,\vec{p}\,',s\rangle\langle B,\vec{p}\,',s|\ \bar{\chi}(0)\ |0\rangle \\
&= \sum_{s,\vec{p}\,',B} e^{-iE_B t}\delta_{\vec{p}\vec{p}\,'} \ \langle 0|\ \chi(0)\ |B,\vec{p}\,',s\rangle\langle B,\vec{p}\,',s|\ \bar{\chi}(0)\ |0\rangle \\
&= \sum_{B} e^{-E_B t} \sum_{s} \langle 0|\ \chi(0)\ |B,\vec{p},s\rangle\langle B,\vec{p},s|\ \bar{\chi}(0)\ |0\rangle \ ,
\end{aligned} \tag{2.6}$$

where on the last line of the above equation we replace it with Euclidean time t.

Next we simplify this expression by evaluating the matrix elements. Here we consider the even parity contributions to the correlation functions, labeled with a +-sign.

The overlap of χ and $\bar{\chi}$ with the even-parity baryons, for example the nucleon, can be expressed as,

$$\begin{aligned}
\langle 0|\ \chi(0)\ |N_{1/2^+}(\vec{p},s)\rangle &= \lambda_{N_{1/2^+}} \sqrt{\frac{M_{N_{1/2^+}}}{E_{N_{1/2^+}}}} u(p_{N_{1/2^+}},s) \\
\langle N_{1/2^+}(\vec{p},s)|\ \bar{\chi}(0)\ |0\rangle &= \bar{\lambda}_{N_{1/2^+}} \sqrt{\frac{M_{N_{1/2^+}}}{E_{N_{1/2^+}}}} \bar{u}(p_{N_{1/2^+}},s) \ ,
\end{aligned} \tag{2.7}$$

where $u(p,s)$ is a Dirac spinor and $\lambda(\bar{\lambda})$ are couplings of the interpolators at the sink (source). We note that $p_{N_{1/2^+}}$ is on shell with $p_0 = \sqrt{\vec{p}^2 + M_{N_{1/2^+}}^2}$. We use the standard convention that under parity quark fields transform like $q(p,s) \rightarrow +\gamma_0 q(\widetilde{p},s)$, with $\widetilde{p} = (p_0, -\vec{p})$ so our interpolators in Sec. 2.2.1 each transform as scalars. The normalisation $\sqrt{\frac{M_{N_{1/2^+}}}{E_{N_{1/2^+}}}}$ is chosen such that $\bar{u}(p,s)u(p,s) = 1$. Note that because we smear the fermion source to optimise overlap of our interpolators with the ground state, $\bar{\lambda}$ is not the adjoint of λ.

We identify the contribution to the correlation function from the even-parity states by substituting the identify,

$$\sum_s u(p,s)\bar{u}(p,s) = \frac{(\gamma\cdot p + M)}{2M} \ , \tag{2.8}$$

into our master formula Eq. (2.6),

$$\mathcal{G}(t,\vec{p}) \ = \ \sum_{B^+} \lambda_{B^+}\bar{\lambda}_{B^+} e^{-E_{B^+}t} \frac{(\gamma\cdot p + M_{B^+})}{2E_{B^+}} + \ldots \ . \tag{2.9}$$

We see that at $\vec{p} = \vec{0}$, the even-parity part of the signal propagates in the (1,1) and (2,2) spinor components of the correlation function.

We have constructed the χ_1 and χ_2 interpolators, Eq. (2.1), such that they transform like scalars under parity. However the interpolators are composite of quark fields. Because quarks propagate from the source to sink through all possible paths, there will exist contributions to the two-point function from configurations of quarks with some relative angular momentum. Some of these wavefunctions will be spatially anti-symmetric under parity transformations. Thus our interpolators will also couple to odd-parity states. On the hadronic level the matrix element,

$$\langle 0|\ \chi(0)\ |N_{1/2^-}(\vec{p},s)\rangle \ = \ \lambda_{N_{1/2^-}} \sqrt{\frac{M_{N_{1/2^-}}}{E_{N_{1/2^-}}}} \gamma_5 u(p_{N_{1/2^-}},s) \ , \tag{2.10}$$

has the opposite parity transformation properties of Eq (2.7). Similarly for the adjoint of χ,

$$\langle N_{1/2^-}(\vec{p},s)|\ \bar{\chi}(0)\ |0\rangle \ = \ -\bar{\lambda}_{N_{1/2^-}} \sqrt{\frac{M_{N_{1/2^-}}}{E_{N_{1/2^-}}}} \bar{u}(p_{N_{1/2^-}},s)\gamma_5 \ . \tag{2.11}$$

Using the identity Eq. (2.8),

$$\sum_s \gamma_5 u(p,s)\bar{u}(p,s)\gamma_5 \ = \ \frac{(-\gamma\cdot p + M)}{2M} \ . \tag{2.12}$$

Finally we add the contributions of the odd-parity terms to the correlation function,

$$\begin{aligned} \mathcal{G}(t,\vec{p}) \ = \ & \sum_{B^+} \lambda_{B^+}\bar{\lambda}_{B^+} e^{-E_{B^+}t} \frac{(\gamma\cdot p_{B^+} + M_{B^+})}{2E_{B^+}} + \\ & \sum_{B^-} \lambda_{B^-}\bar{\lambda}_{B^-} e^{-E_{B^-}t} \frac{(\gamma\cdot p_{B^-} - M_{B^-})}{2E_{B^-}} \ . \end{aligned} \tag{2.13}$$

We see that at $\vec{p} = \vec{0}$, the odd-parity states propagate in the (3,3) and (4,4) spinor components of the correlation function. Because we use a fixed boundary condition in the time direction we can isolate contributions to the correlation functions from either odd or even-parity states, at $\vec{p} = \vec{0}$, by taking the trace of the correlation function with the operator,

$$\Gamma_\pm \ = \ \frac{1}{2}(1 \pm \gamma_0) \ . \tag{2.14}$$

Following from our discussion above, it can easily be shown that states with definite parity can then be obtained from the spinor trace of the parity projected correlation functions,

$$\begin{aligned} G_{\pm}(t,\vec{0}) &= \mathrm{tr}_{\mathrm{sp}}\left[\Gamma_{\pm}\,\mathcal{G}(t,\vec{0})\right] \\ &= \sum_{B^{\pm}} \lambda_{B^{\pm}}\bar{\lambda}_{B^{\pm}}\exp\left(-E_{B^{\pm}}t\right) \\ &\overset{t\to\infty}{=} \lambda_{0^{\pm}}\bar{\lambda}_{0^{\pm}}\exp\left(-M_{0^{\pm}}t\right)\,, \end{aligned} \tag{2.15}$$

where $0^{\pm}$ labels the lowest energy state of the projected quantum numbers. Since the contributions to the two-point function are exponentially suppressed at a rate proportional to the energy of the state, at zero momentum the mass of the lightest state, $M_{0^{\pm}}$, is obtained by fitting a constant in time to the effective mass,

$$\begin{aligned} M^{\mathrm{eff}}_{N^{\pm}}(t) &= \ln\left(\frac{G_{\pm}(t,\vec{0})}{G_{\pm}(t+1,\vec{0})}\right) \\ &\overset{t\to\infty}{=} M_{0^{\pm}}\,. \end{aligned} \tag{2.16}$$

We extract the mass of the lowest energy state from a linear least squares fit of a constant in time to the effective mass data. We use a single elimination Jackknife to calculate the variance used in the least squares fit and to calculate the confidence in the lattice data. For a review of the Jackknife estimate of the error see Sec. 4.2.1. As the effective mass data is correlated in time, a covariance matrix is used to evaluate the χ^2 of the fit, which we use as a measure of the goodness of fit. In extracting the mass we demand that the χ^2 per degree of freedom (χ^2_{dof}) is < 1.5, and ~ 1 if possible. For a complete review of the covariance matrix and our fit procedure see Appendix C.

Now we show how spin-1/2 and spin-3/2 states with even and odd parity are extracted from the correlation functions with the interpolators χ^{μ}_{3} and $\chi^{\mu}_{\Delta^{++}}$, which both transform like pseudo-vectors. The two-point correlation function is,

$$\mathcal{G}^{\mu\nu}(t,\vec{p}) = \sum_{\vec{x}} \exp(-i\vec{p}\cdot\vec{x})\,\langle 0\,|T\,\chi^{\mu}(x)\,\bar{\chi}^{\nu}(0)\,|\,0\rangle\,. \tag{2.17}$$

Following our previous derivation, the analogue of Eq. (2.6) is,

$$\mathcal{G}^{\mu\nu}(t,\vec{p}) = \sum_{B} e^{-E_B t}\sum_{s}\langle 0|\,\chi^{\mu}(0)\,|B,\vec{p},s\rangle\langle B,\vec{p},s|\,\bar{\chi}^{\nu}(0)\,|0\rangle\,. \tag{2.18}$$

The χ^{μ}_{3} and $\chi^{\mu}_{\Delta^{++}}$ interpolating fields overlap with both spin-1/2 and spin-3/2 states. We proceed by evaluating the spin-1/2 components. To create the analogue of the matrix elements Eqs. (2.7) and (2.10) here we have to ensure that we have the correct transformation properties described in Eq. (B.6). Following [27] we make the coefficient of the spinor a linear combination of four-vectors. The four-momentum, which is equivalent to a derivative in coordinate space is one possible coefficient. In general we can also use one of the sixteen matrices $\{1, \gamma^{\mu}, i\gamma_5, \gamma^{\mu}\gamma_5, \sigma^{\mu\nu}|_{\mu>\nu}\}$, provided the expression still transforms as a pseudo-vector under parity. Thus the only other possibility

is γ^μ. So our analogue of Eqs. (2.7) and (2.10) is,

$$\langle 0|\chi^\mu(0)|N_{1/2^+}(\vec{p},s)\rangle = (\alpha_{N_{1/2^+}} p^\mu_{N_{1/2^+}} + \beta_{N_{1/2^+}}\gamma^\mu)\sqrt{\frac{M_{N_{1/2^+}}}{E_{N_{1/2^+}}}}\,\gamma_5 u(p_{N_{1/2^+}},s), \quad (2.19)$$

$$\langle 0|\chi^\mu(0)|N_{1/2^-}(\vec{p},s)\rangle = (\alpha_{N_{1/2^-}} p^\mu_{N_{1/2^-}} + \beta_{N_{1/2^-}}\gamma^\mu)\sqrt{\frac{M_{N_{1/2^-}}}{E_{N_{1/2^-}}}}\,u(p_{N_{1/2^-}},s), \quad (2.20)$$

$$\langle N_{1/2^+}(\vec{p},s)|\bar{\chi}^\mu(0)|0\rangle = -\sqrt{\frac{M_{N_{1/2^+}}}{E_{N_{1/2^+}}}}\,\bar{u}(p_{N_{1/2^+}},s)\gamma_5(\bar{\alpha}_{N_{1/2^+}} p^\mu_{N_{1/2^+}} + \bar{\beta}_{N_{1/2^+}}\gamma^\mu), \quad (2.21)$$

$$\langle N_{1/2^-}(\vec{p},s)|\bar{\chi}^\mu(0)|0\rangle = \sqrt{\frac{M_{N_{1/2^-}}}{E_{N_{1/2^-}}}}\,\bar{u}(p_{N_{1/2^-}},s)(\bar{\alpha}_{N_{1/2^-}} p^\mu_{N_{1/2^-}} + \bar{\beta}_{N_{1/2^-}}\gamma^\mu), \quad (2.22)$$

where the factors α_B, β_B denote the coupling strengths of the interpolating field χ_μ to the baryon B, and similarly for the adjoint. Here the γ_5 sits next to the spinor in the even-parity term because at the quark level χ_3^μ and $\chi^\mu_{\Delta^{++}}$ transform as pseudo-vectors under parity and so this must also be true at the baryon level. Combining these expressions with their respective adjoints,

$$\sum_s \langle 0|\chi^\mu(0)|N_{1/2^+}(\vec{p},s)\rangle\langle N_{1/2^+}(\vec{p},s)|\bar{\chi}^\nu(0)|0\rangle = -\frac{M_{N_{1/2^+}}}{E_{N_{1/2^+}}}(\alpha_{N_{1/2^+}} p^\mu_{N_{1/2^+}} + \beta_{N_{1/2^+}}\gamma^\mu)\times \gamma_5\frac{\gamma\cdot p_{N_{1/2^+}} + M_{N_{1/2^+}}}{2M_{N_{1/2^+}}}\gamma_5(\bar{\alpha}_{N_{1/2^+}} p^\nu_{N_{1/2^+}} + \bar{\beta}_{N_{1/2^+}}\gamma^\nu)\,,$$

$$\sum_s \langle 0|\chi^\mu(0)|N_{1/2^-}(\vec{p},s)\rangle\langle N_{1/2^-}(\vec{p},s)|\bar{\chi}^\nu(0)|0\rangle = \frac{M_{1/2^-}}{E_{1/2^-}}(\alpha_{1/2^-} p^\mu_{N_{1/2^-}} + \beta_{N_{1/2^-}}\gamma^\mu)\times \frac{\gamma\cdot p_{N_{1/2^-}} + M_{N_{1/2^-}}}{2M_{N_{1/2^-}}}(\bar{\alpha}_{N_{1/2^-}} p^\nu_{N_{1/2^-}} + \bar{\beta}_{N_{1/2^-}}\gamma^\nu)\,.$$

Next we evaluate the spin-3/2 terms. Up to this point in this chapter we have been dealing with spin-1/2 particles which we describe using spinors. Following [27], spin-3/2 particles are represented with the Rarita-Schwinger spin vectors $u_\mu(p,s)$. The matrix elements analogous to Eqs. (2.7) and (2.10) are,

$$\langle 0|\chi_\mu(0)|N_{3/2^+}(\vec{p},s)\rangle = \lambda_{N_{3/2^+}}\sqrt{\frac{M_{N_{3/2^+}}}{E_{N_{3/2^+}}}}\,u_\mu(p_{N_{3/2^+}},s)\,, \quad (2.23)$$

$$\langle 0|\chi_\mu(0)|N_{3/2^-}(\vec{p},s)\rangle = \lambda_{N_{3/2^-}}\sqrt{\frac{M_{N_{3/2^-}}}{E_{N_{3/2^-}}}}\,\gamma_5 u_\mu(p_{N_{3/2^-}},s)\,, \quad (2.24)$$

$$\langle N_{3/2^+}(\vec{p},s)|\bar{\chi}_\mu(0)|0\rangle = \bar{\lambda}_{N_{3/2^+}}\sqrt{\frac{M_{N_{3/2^+}}}{E_{N_{3/2^+}}}}\,\bar{u}_\mu(p_{N_{3/2^+}},s)\,, \quad (2.25)$$

$$\langle N_{3/2^-}(\vec{p},s)|\bar{\chi}_\mu(0)|0\rangle = -\bar{\lambda}_{N_{3/2^-}}\sqrt{\frac{M_{N_{3/2^-}}}{E_{N_{3/2^-}}}}\bar{u}_\mu(p_{N_{3/2^-}},s)\gamma_5\,. \quad (2.26)$$

The analogue of Eq. (2.8) is,

$$\sum_s u^\mu(p,s)\bar{u}^\nu(p,s) = \frac{(\gamma\cdot p + m)}{2m}\left\{g_{\mu\nu} - \frac{1}{3}\gamma^\mu\gamma^\nu - \frac{2p_\mu p_\nu}{3m^2} + \frac{p_\mu\gamma_\nu - p_\nu\gamma_\mu}{3m}\right\} \quad (2.27)$$

Using Eq. (2.27) we can show that states of definite parity are extracted from the correlation function Eq. (2.18) using the parity projection operator Eq. (2.14) and states of definite spin are extracted using the spin projection operators [27],

$$\begin{aligned} P^{\frac{3}{2}}_{\mu\nu}(p) &= g_{\mu\nu} - \frac{1}{3}\gamma_\mu\gamma_\nu - \frac{1}{3p^2}(\gamma\cdot p\gamma_\mu p_\nu + p_\mu\gamma_\nu\gamma\cdot p) \ , \\ P^{\frac{1}{2}}_{\mu\nu}(p) &= g_{\mu\nu} - P^{\frac{3}{2}}_{\mu\nu}(p) \ , \end{aligned} \tag{2.28}$$

for spin-$\frac{3}{2}$ and $\frac{1}{2}$, respectively. At zero momentum, where we evaluate the hadron masses, the above spin projection operator is zero for $\mu = 4, \nu = 1-3$ and $\mu = 1-3, \nu = 4$. Hence we can reduce the computational cost of our calculation by ignoring these terms of our correlation function.

Finally in this section we evaluate the two-point function at the hadronic level for the $\langle\Omega|T\chi_3^\mu\bar{\chi}_i|\Omega\rangle$ and $\langle\Omega|T\chi_i\bar{\chi}_3^\mu|\Omega\rangle$ $(i = 1, 2)$. It is important to note that these correlation functions are not Lorentz scalars and so are dependent on the representation of the γ matrices. In this study we use the Bjorken and Drell representation of the γ matrices in our phenomenology. The correlation functions are,

$$\begin{aligned} \mathcal{G}^\mu_{3i}(t,\vec{p}) &= \sum_{\vec{x}} \exp(-i\vec{p}\cdot\vec{x}) \, \langle 0 \, | T \ \chi_3^\mu(x) \ \bar{\chi}_i(0) \ | 0 \rangle \\ \mathcal{G}^\mu_{i3}(t,\vec{p}) &= \sum_{\vec{x}} \exp(-i\vec{p}\cdot\vec{x}) \, \langle 0 \, | T \ \chi_i(x) \ \bar{\chi}_3^\mu(0) \ | 0 \rangle \ . \end{aligned} \tag{2.29}$$

Following the standard analysis we proceed by inserting a complete set of states and evaluating the resulting matrix elements. We evaluate the set of matrix elements for the former correlation function first.

Borrowing from Eqs. (2.19) and (2.7), the even-parity term in the master formula becomes,

$$\begin{aligned} &\sum_s \langle 0|\chi_3^\mu(0)|N_{1/2^+}(\vec{p},s)\rangle\langle N_{1/2^+}(\vec{p},s)|\bar{\chi}_i(0)|\Omega\rangle = \sum_s \frac{M_{N_{1/2^+}}}{E_{N_{1/2^+}}} \\ &\bar{\lambda}_{N_{1/2^+}} \ (\alpha_{N_{1/2^+}} p^\mu_{N_{1/2^+}} + \beta_{N_{1/2^+}}\gamma^\mu) \ \gamma_5 u(p_{N_{1/2^+}},s)\bar{u}(p_{N_{1/2^+}},s) \ . \end{aligned} \tag{2.30}$$

Using the identity Eq. (2.8), this becomes,

$$\begin{aligned} &\sum_s \langle 0|\chi_3^\mu(0)|N_{1/2^+}(\vec{p},s)\rangle\langle N_{1/2^+}(\vec{p},s)|\bar{\chi}_i(0)|\Omega\rangle = \\ &\qquad \bar{\lambda}_{N_{1/2^+}} \ (\alpha_{N_{1/2^+}} p^\mu_{N_{1/2^+}} + \beta_{N_{1/2^+}}\gamma^\mu) \ \gamma_5 \frac{(\gamma\cdot p_{N_{1/2^+}} + M_{N_{1/2^+}})}{2E_{N_{1/2^+}}} \ . \end{aligned} \tag{2.31}$$

Note that by evaluating this expression at $\vec{p} = \vec{0}$ we find that, for $\mu = 1$ the positive parity states propagate in the real part of the (1,2) and (2,1) elements of the correlation function. For $\mu = 2$ the positive parity states propagate in the imaginary part of the (1,2) and (2,1) elements of the correlation function with a relative minus sign. For $\mu = 3$ the positive parity states propagate in the real part of the (1,1) and (2,2) elements of the correlation function with a relative minus sign and for $\mu = 4$ the positive parity states propagate in the real part of the (1,3) and (2,4) elements of the correlation function. Similarly the odd-parity term in the master formula is,

$$\sum_s \langle 0|\chi_3^\mu(0)|N_{1/2^-}(\vec{p},s)\rangle\langle N_{1/2^-}(\vec{p},s)|\bar{\chi}_i(0)|\Omega\rangle =$$

$$\bar{\lambda}_{N_{1/2^-}} \; (\alpha_{N_{1/2^-}} p^{\mu}_{N_{1/2^-}} + \beta_{N_{1/2^-}} \gamma^{\mu}) \gamma_5 \frac{(\gamma \cdot p_{N_{1/2^-}} - M_{N_{1/2^-}})}{2E_{N_{1/2^-}}} \; . \qquad (2.32)$$

Once again using the appropriate terms in Eqs. (2.19) and (2.7), the even-parity contribution to the master formula of the $\langle \Omega | T \chi_i \bar{\chi}_3 | \Omega \rangle$ correlation functions is,

$$\sum_s \langle 0 | \; \chi_i(0) \; | N_{1/2^+}(\vec{p}, s) \rangle \langle N_{1/2^+}(\vec{p}, s) | \bar{\chi}^{\mu}_3(0) | 0 \rangle =$$
$$-\lambda_{N_{1/2^+}} \; \frac{(\gamma \cdot p_{N_{1/2^+}} + M_{N_{1/2^+}})}{2E_{N_{1/2^+}}} \; \gamma_5 (\bar{\alpha}_{N_{1/2^+}} p^{\mu}_{N_{1/2^+}} + \bar{\beta}_{N_{1/2^+}} \gamma^{\mu}) \; . \qquad (2.33)$$

Similarly the odd-parity term is,

$$\sum_s \langle 0 | \; \chi_i(0) \; | N_{1/2^-}(\vec{p}, s) \rangle \langle N_{1/2^-}(\vec{p}, s) | \bar{\chi}^{\mu}_3(0) | 0 \rangle =$$
$$-\lambda_{N_{1/2^-}} \; \gamma_5 \frac{(\gamma \cdot p_{N_{1/2^-}} + M_{N_{1/2^-}})}{2E_{N_{1/2^-}}} \; (\bar{\alpha}_{N_{1/2^-}} p^{\mu}_{N_{1/2^-}} + \bar{\beta}_{N_{1/2^-}} \gamma^{\mu}) \; . \qquad (2.34)$$

We use these functions to combine the appropriate elements of the correlation function with a particular parity.

2.2.3 Mass splittings technique

As the standard analysis in this chapter, at quark masses below the SU(3) flavour limit we fit the splitting between the effective masses at each quark mass and the next largest quark mass. The mass splitting is then subtracted from the hadron mass determined at the larger quark mass to extract the hadron mass at the smaller quark mass. As discussed in [35], the advantage of this technique is the potential canceling of correlated fluctuations and the possibility of a cancellation of excited state contamination. Keeping the same selection of fit regime between the standard analysis and the quark mass splittings analysis, the worst case scenario is that we do more computation in the latter analysis than necessary. However where there is some canceling of excited state contamination we have the opportunity to extract the ground state mass from our data at smaller Euclidean times. This means that we have the potential for making a more precise determination of the hadron spectrum than would otherwise be possible with standard analysis techniques.

2.2.4 Correlation matrix analysis

In the previous section we described how the mass of the ground state is extracted from the two-point correlation function by fitting a constant to the effective mass. Excited state masses can be extracted either by fitting the correlation function with several exponentials (which is, in general, quite difficult to do reliably), or by using more than one interpolating field [36]. In the latter approach, which was implemented in the N^* spectrum analysis in Ref. [18] and which we adopt in this work, a set of linearly independent operators will, in general, overlap with more than one state. We use a correlation matrix analysis to convert a set of N linearly independent operators into a set of N orthogonal operators.

In principle, to access the entire spectrum of states one would require an extremely large tower of operators. In practice we use a 2×2 or 3×3 correlation matrix which should enables us to access two or three states in each channel. If the analysis is performed at large enough Euclidean times, the contributions from the higher energy excited states will be exponentially suppressed.

Generalising the two-point correlation function in Eqs. (2.3) or (2.17) to the case of two different interpolating fields χ_i and $\bar{\chi}_j$ at the sink and source, respectively, the momentum-space two-point correlation function matrix G_{ij} (at $\vec{p} = \vec{0}$) can be written as

$$G_{ij}(t) \;=\; \sum_{\alpha=0}^{N-1} \lambda_i^\alpha \bar{\lambda}_j^\alpha e^{-m_\alpha t} \;, \tag{2.35}$$

where α denotes each of the N states in the tower of excited states, λ_i^α and $\bar{\lambda}_j^\alpha$ are the couplings of the interpolator χ_i and $\bar{\chi}_j$ at the source and sink respectively. Here we have suppressed the parity labels. If the operators χ_i, χ_j are orthogonal, the matrix G_{ij} will be diagonal, with the only t dependence coming from the exponential factor. In general the operators will not be orthogonal, and a new set of operators must be created from a linear combination of the old operators using the eigenvalue equation. In the event that the number of states matches the number of interpolators, an orthogonal set of interpolators can be constructed by diagonalising the correlation matrix subject to the condition

$$G_{ij}(t + \Delta t)\, u_j^\alpha = \lambda^\alpha\, G_{ik}(t)\, u_k^\alpha \;, \tag{2.36}$$

or,

$$\left(G^{-1}(t)\, G(t + \Delta t)\right)_{ij}\, u_j^\alpha = \lambda^\alpha\, u_i^\alpha \;, \tag{2.37}$$

where u_j^α are real eigenvectors, and the corresponding eigenvalue is $\lambda^\alpha = e^{-m_\alpha\, \Delta t}$. As discussed in Appendix D, by averaging over the $\{U\}$ and $\{U^*\}$ gauge fields with equal weight, the spin and parity projected correlation function G_{ij} is purely real.

A real symmetric matrix is diagonalised by its eigenvectors. However, since our smearing prescriptions are different at the source and the sink, the correlation matrix is real but non-symmetric. Consequently, one has to solve the additional left-eigenvalue equation

$$v_i^\alpha\, G_{ij}(t + \Delta t) \;=\; \lambda^\alpha\, v_k^\alpha\, G_{kj}(t) \;, \tag{2.38}$$

for eigenvectors v_i^α, or equivalently

$$v_i^\alpha\, \left(G(t + \Delta t)\, G^{-1}(t)\right)_{ij} \;=\; \lambda^\alpha\, v_j^\alpha \;. \tag{2.39}$$

The eigenvectors u^α and v^α diagonalise the correlation matrix at times t and $t + \Delta t$,

$$v_i^\alpha\, G_{ij}(t + \Delta t)\, u_j^\beta \;=\; \lambda^\alpha\, v_i^\alpha\, G_{ij}(t)\, u_j^\beta = \lambda^\beta\, v_i^\alpha\, G_{ij}(t)\, u_j^\beta \;. \tag{2.40}$$

Clearly if $\lambda^\alpha \neq \lambda^\beta$ for $\alpha \neq \beta$ then this expression must be equal to zero. Therefore,

$$v_i^\alpha\, G_{ij}(t + \Delta t)\, u_j^\beta \;\propto\; \delta^{\alpha\beta} \;. \tag{2.41}$$

The projected correlation matrix $v_i^\alpha G_{ij}(t) u_j^\alpha$ thus describes the single state α.

In the present analysis, for each state considered, our aim will be to optimise the correlation matrix analysis at every quark mass. We use the covariance matrix to find where the χ^2/dof for a least squares fit to the effective masses is < 1.5 for all quark masses. Stepping back one time slice, we then apply the correlation matrix analysis. If the correlation matrix analysis is successful, *i.e.*, the correlation matrix is invertible and the eigenvalues are real and positive, we proceed to the next step. If the correlation matrix analysis fails, we take another step back in time, and continue stepping back until the analysis is successful for a given quark mass.

The mass of the state derived from the projected correlation matrix is then compared with the mass obtained using the standard analysis techniques. Any mixing of the ground state with excited states will result in masses from the unprojected operators which lie between the true ground and excited state masses. Therefore, in the case of the ground state mass where the effective mass approaches a plateau from above, if the new mass is smaller then we use the result derived from the correlation matrix; otherwise, we keep the standard analysis result. For an excited state on the other hand, the result from the correlation matrix analysis is used if the new mass is larger than what we might already obtain from the standard analysis.

2.3 Results

We start our discussion with the analysis of the low lying spin-1/2 and spin-3/2 spectrum of the nucleon with our nucleon interpolating fields. As discussed in Sec. 2.2.2, the χ_3 interpolator couples to both spin-1/2 and spin-3/2 states, with either even or odd parity. States of definite spin and parity are extracted from the two-point correlation function using the projection spin and parity projection operators Eq. (2.28) and Eq. (2.14) respectively.

Then we will extend our analysis by applying correlation matrix techniques in an effort to extract the additional spin-1/2 excited states of the nucleon. In particular we are looking for the first even-parity excited state of the nucleon, the Roper resonance. Then we will continue our analysis with the spectrum of states extracted with $\chi_{\Delta^{++}}$ Eq. (2.1). As discussed in Sec. 2.2.2, the $\chi_{\Delta^{++}}$ interpolator couples to both spin-1/2 and spin-3/2 states, with either even or odd parity. States of definite spin and parity are extracted from the two-point correlation function using the projection spin and parity projection operators Eq. (2.28) and Eq. (2.14) respectively.

2.3.1 Isospin-1/2 states

We begin our discussion with the spectrum extracted with the χ_1 and χ_2 interpolators, and then continue with our analysis of the spectrum extracted with the χ_3 interpolator.

In Fig. 2.1 we show the effective mass of the even-parity state extracted with the χ_1 interpolator. At the three largest quark masses we fit the effective mass data between the dotted and dashed lines, at the five smallest quark masses shown we fit the effective mass splitting between the dotted and dashed lines. The smallest $\chi^2_{\rm dof}$ of each fit to the data is 0.45 at the fourth largest quark mass and the largest $\chi^2_{\rm dof}$ is 1.10 at the second smallest quark mass. The mass of this state extracted at each quark mass is shown in Fig. 2.2 (crosses).

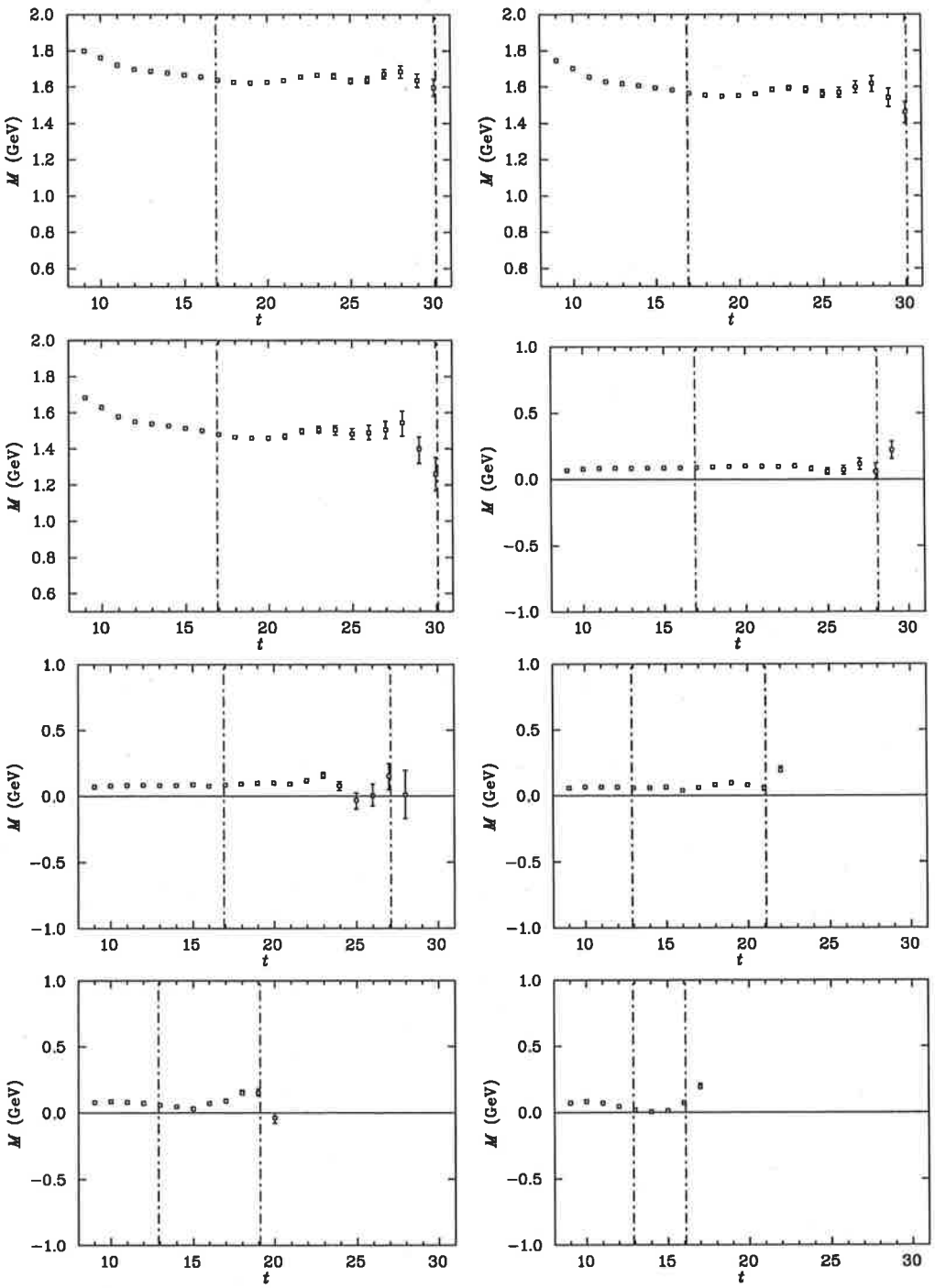

Fig. 2.1: The effective mass of the $1/2^+$ state extracted with the χ_1 interpolator, the data correspond to $m_\pi \simeq 830\,\text{MeV}$ (top left), 770 MeV (top right), 700 MeV (second row left), 616 MeV (second row right), 530 MeV (third row left), 460 MeV (third row right), 370 MeV (bottom row left), and 300 MeV (bottom row right). The data are illustrated only to the point at which the error bars diverge. At the five smallest quark masses we plot the effective mass splittings.

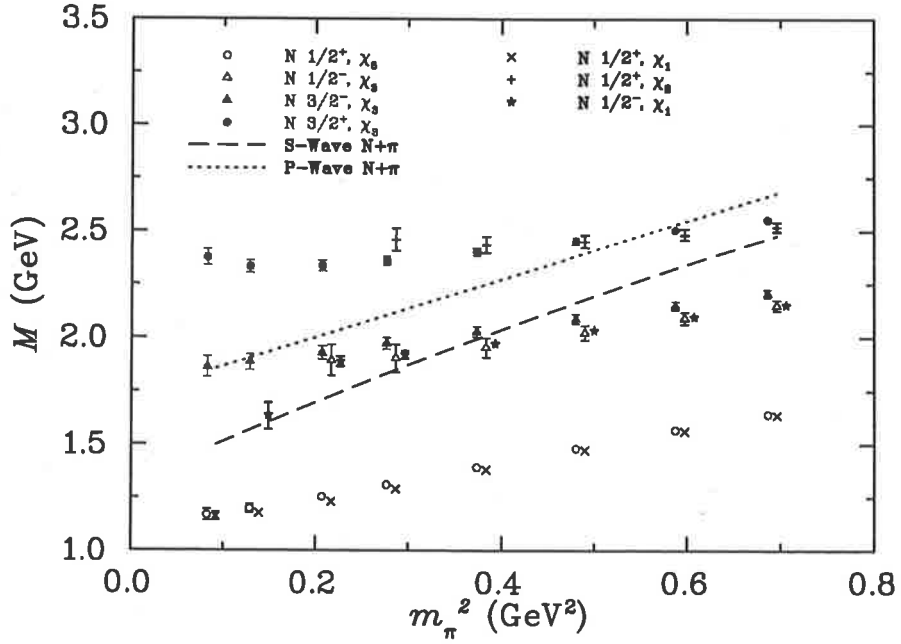

Fig. 2.2: The nucleon mass spectrum from QQCD. The data correspond to $m_\pi \simeq 830$, 770, 700, 616, 530, 460, 370 and 300 MeV.

Next we show in Fig. 2.3 the effective mass of the even-parity state extracted with the χ_2 interpolator. As with the findings of [18], the χ_2 interpolator couples to a more massive state than χ_1. As in that study we find that the signal becomes dominated by noise at relatively small Euclidean times. In each case we fit the data shown. Where $t \geq 11$, the $\chi^2_{\rm dof}$ for the fit to the data at the three largest quark masses is ~ 0.6, and ~ 1.0 at the two smallest quark masses. In this study we limit our analysis to the five largest quark masses after which we judge that the component of noise becomes too large. The mass extracted is shown in Fig. 2.2 (plus signs). In Fig. 2.2 we also plot the energy of the non-interacting $N + \pi$ in relative P-wave, which is the lowest energy even-parity multi-hadron state. We note that the energy of multi-hadron states on the lattice will be different than this non-interacting energy because of finite volume effects, namely repulsive or attrative interactions. We see that the mass of the state extracted with the χ_2 interpolator becomes larger than the non-interacting multi-hadron state at the two smallest quark masses shown. By design, the standard analysis extracts the lowest energy state that the interpolator couples to. In [18] it was shown that the χ_1 and χ_2 interpolators have very little overlap, so we know that the χ_2 interpolator does not couple to the ground state with any strength, but we expect that χ_2 should have some overlap with the multi-hadron state. In Fig. 2.3 find no evidence of a trend towards a lower energy state at the two smallest quark masses, which would appear as a trend towards a larger mass splitting. A higher statistics calculation may reveal signal at larger Euclidean times where such a state may become manifest.

In Fig. 2.4 we show the effective mass of the odd-parity state extracted with the χ_1 interpolator. We fit the range of data shown between the vertical lines and find a $\chi^2_{\rm dof}$ between 0.5 and 1.0 at each quark mass except the second smallest quark mass where the $\chi^2_{\rm dof}$ is 1.36 which is near the limit of our selection criteria of the goodness of fit. A fit to the data one time slice earlier and one time slice later each returns a mass that is

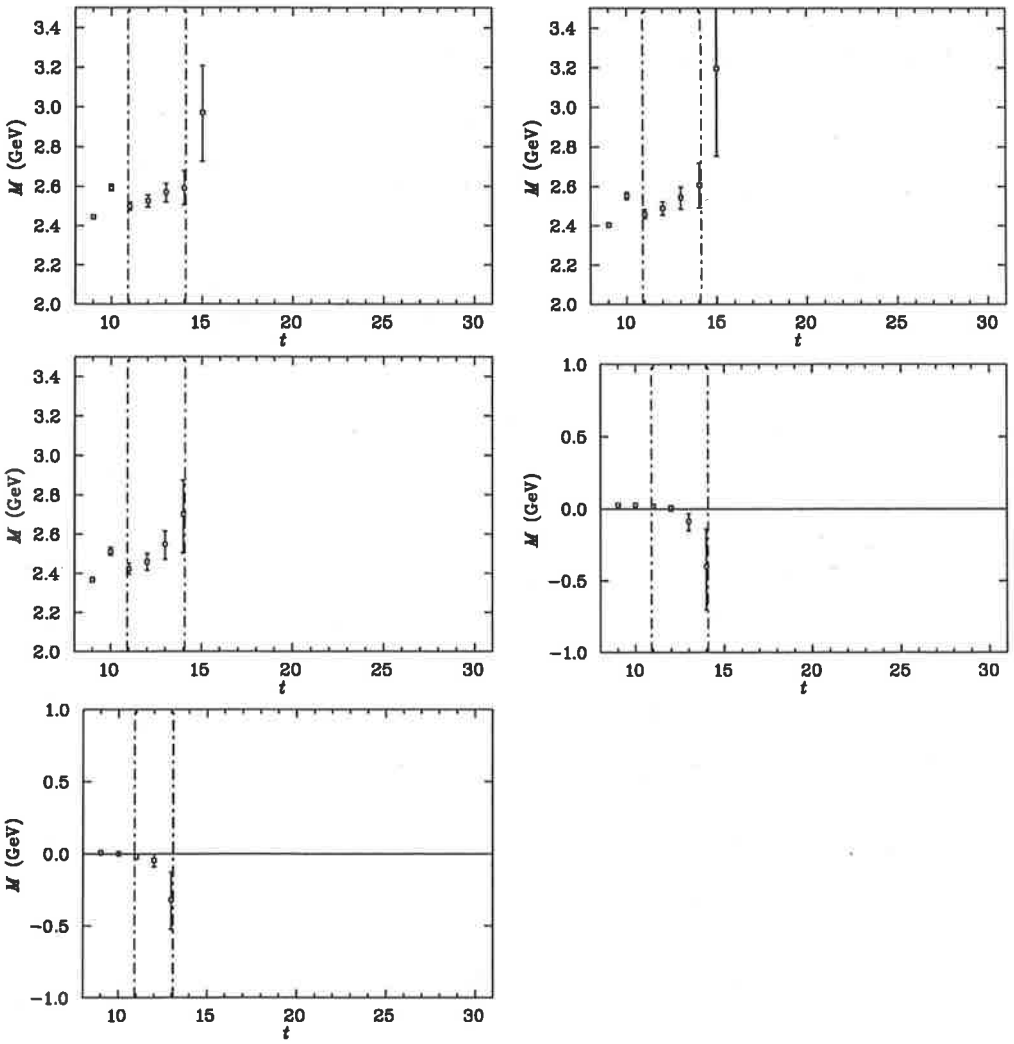

Fig. 2.3: As in Fig. 2.1, but for the mass of the $1/2^+$ state extracted with the χ_2 interpolator.

consistent with this fit. Therefore the selection of data to fit is reasonable. Interestingly, at the smallest quark mass shown, we find that the mass splitting becomes large after time slice 12. If we fit the data $11-12$ the $\chi^2_{\rm dof}$ is 0.55, if we include the data at time slice 13 in the fit the $\chi^2_{\rm dof}$ becomes 3.5. This indicates that the data at the larger Euclidean times correspond to a lower energy state of the correlator. Following [28] and [29] the appropriate procedure is to fix the upper bound of the fit at the limit of the signal, which we judge is time slice 18 here, and then vary the lower bound of the fit until we find an acceptable $\chi^2_{\rm dof}$. In this case a fit to the data $13-18$ returns a $\chi^2_{\rm dof}$ of 0.91 which is ideal, a more detailed discussion of this procedure can be found in Chapter 4. The mass extracted is shown in Fig. 2.2 (stars). Interestingly we find that the mass extracted at the smallest quark mass shown is consistent with the lowest energy odd-parity multi-hadron state in this channel, the S-wave $N+\pi$, which is also degenerate in energy with the S-Wave $N+\eta'$ in QQCD[1]. An analogas calculation of the odd-parity state with the χ_2 interpolator returns equivalent masses so we omit discussion of it in this study.

A correlation matrix analysis in this channel, as in [18], does not extract an excited state in this channel. We attribute this to the large amount of smearing of the fermion source done in this calculation, 35 sweeps compared to just 20 sweeps in [18]. In each case the smearing fraction α was 6. It is possible that we have removed too much of the excited state contributions to the correlation function in this channel. A more thorough analysis of the dependence of the excited state signal on the source smearing prescription is left as future work. The masses of the odd and even-parity states extracted with the χ_1 interpolator are shown in Table 2.1.

We continue our analysis with the excited states of the nucleon extracted with the χ_3 interpolator. In Fig. 2.5 we show the effective mass of the even-parity, spin-1/2 state extracted with the χ_3 interpolator at a range of quark masses. Recall that at the five smallest quark masses we show the effective mass splittings between the effective mass at each quark mass and at the next largest quark mass. Again in each case the dot and dashed vertical lines indicate the range of data that we fit to extract the ground state mass. At the five largest quark masses shown the $\chi^2_{\rm dof}$ for each fit is approximately one, except at the fourth largest quark mass where it is 0.56. At the sixth largest quark mass we have to accept a $\chi^2_{\rm dof}=1.5$ for a fit to the data shown, which is at the limit of our selection criteria, because we do not find a better fit regime. At the two smallest quark masses shown in Fig. 2.5 we fit the data at one time slice earlier and find a $\chi^2_{\rm dof}<1.0$. The extracted masses are summarised in Fig. 2.2 (open circles). Our simulation parameters and high statistics give use clean access to this state even at our lightest quark mass. We find excellent agreement with the mass of the spin-1/2 even-parity state extracted with the χ_1 interpolator, as one would expect based on the Fierz transformation of χ_3. This observation highlights the inconsistency of the findings of Zhou et al. [37], who argue that the full version of the χ_3 interpolators proposed by Chung et al. [38] is required to extract the spin-1/2 state with accuracy.

In Fig. 2.6 we show the effective mass and effective mass splittings of the spin-1/2 odd-parity state extracted with the χ_3 interpolator. At the three largest quark masses we see some systematic drift in the effective mass data towards time slice 14. Therefore we fit the data shown where $t\geq 14$ at the five largest quark masses. In each case we find an acceptable $\chi^2_{\rm dof}$ ranging between 0.57 and 0.79. At the two smallest quark masses

[1]We note that the S-wave $N+\pi$ and S-Wave $N+\eta'$ are degenerate in energy and therefore a small negative metric η' contribution does not spoil the effective mass analysis.

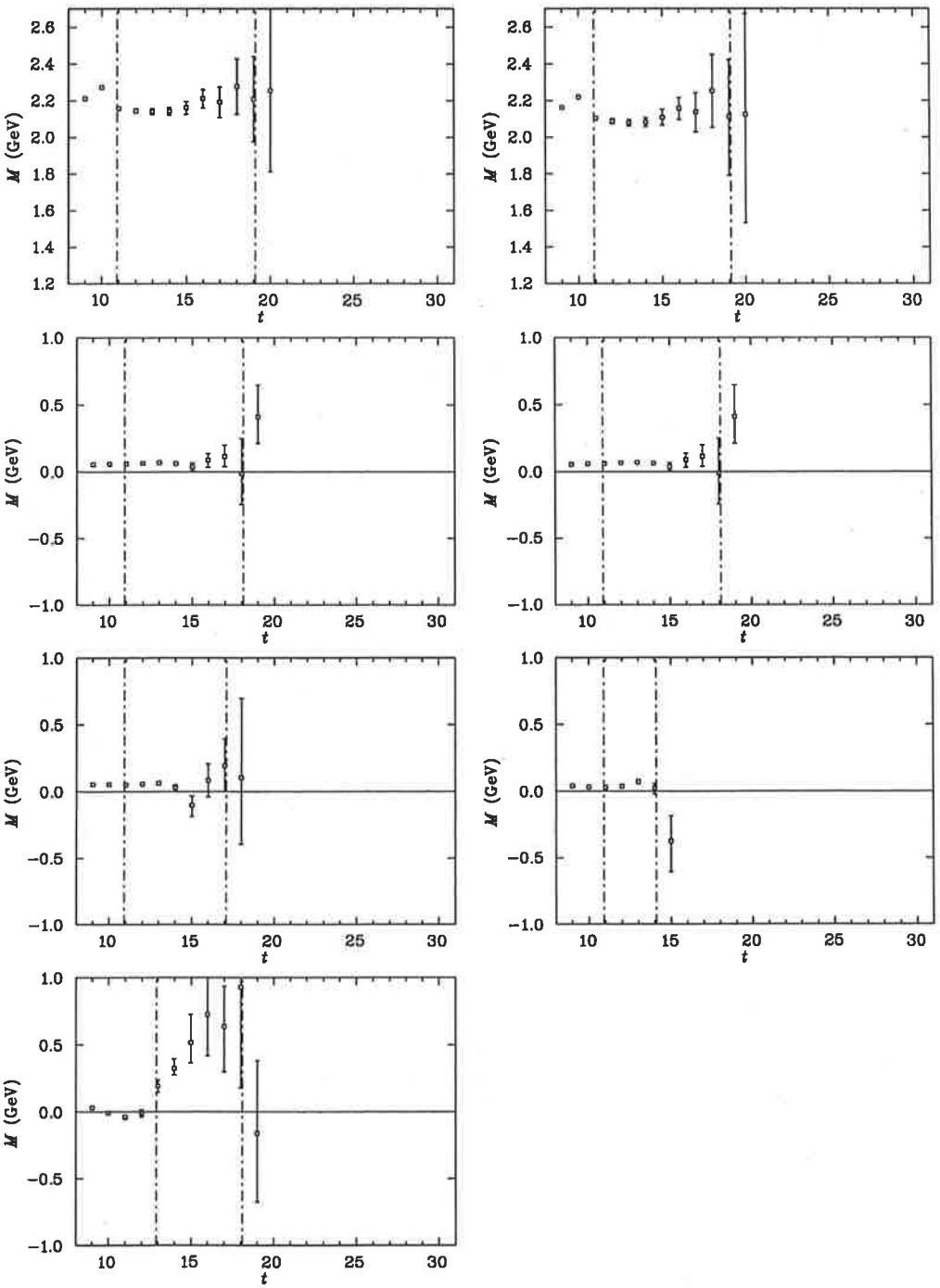

Fig. 2.4: As in Fig. 2.1, but for the mass of the $1/2^-$ state.

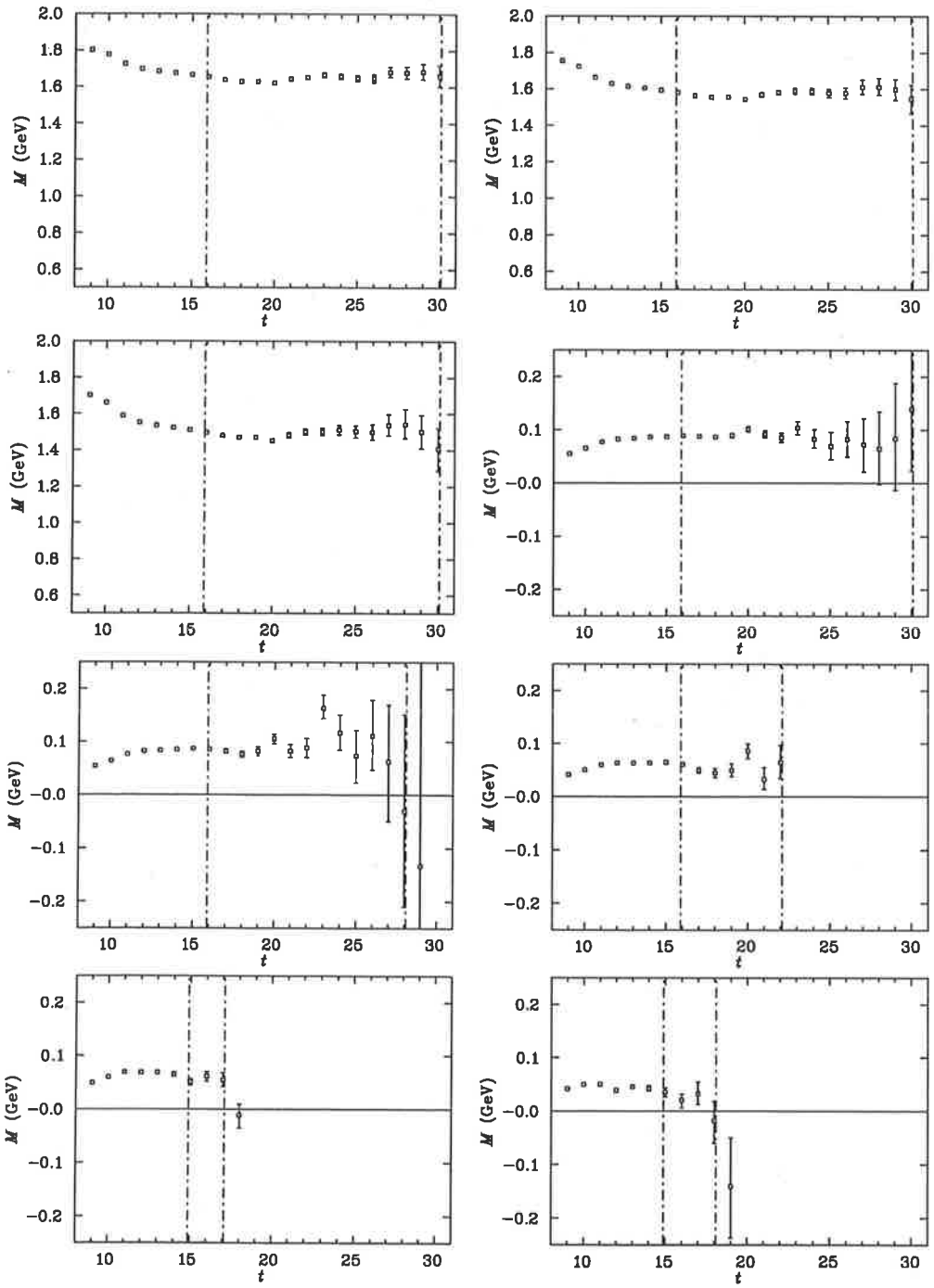

Fig. 2.5: The effective mass of the $1/2^+$ state extracted with the χ_3 interpolator.

we find a $\chi^2_{\rm dof}$ of 0.80 and 0.13 where we fit the data $t \geq 12$. Interestingly we find that at the fifth largest quark mass the non-interacting $N + \pi$ decay channel is very similar to the ground state mass that we extract with our interpolators. Clearly extracting the mass of the odd-parity nucleon at the light quark masses will prove problematic where it is not the lowest energy state that our interpolators couple. Our analysis is limited to the six largest quark masses. The extracted masses are summarised in Fig. 2.2 (open triangles). Again we find precise agreement in the mass of the odd-parity state extracted with χ_1 and χ_3.

In Fig. 2.7 show the effective mass and effective mass splittings of the odd-parity spin-3/2 state extracted with our χ_3 interpolator. In this channel the lowest energy two-particle state is the $N + \pi$ in relative D-wave or the $\Delta + \pi$ in S-wave. So unlike the odd-parity spin-1/2 channel, finite volume effects mean that this state is bound on our lattice at all quark masses used in this study. At the three largest quark masses shown there is putative evidence of a second plateau at the larger quark masses. As we discovered in our study of the spin-3/2 pentaquark states [29], we must be careful to ensure that we do not cut data corresponding to a lower energy state at larger Euclidean times. This remains to be true even if the data appears to have a large component of noise. Therefore we fix the upper bound of fit regime at time slice 23, after which we are confident that the signal is hidden by the noise. At the three largest quark masses we find a $\chi^2_{\rm dof} = 1.02$, 1.14 and 1.24 for a fit to the data with a lower bound fixed at time slice 14. In each case a lower bound of 14 returns the smallest $\chi^2_{\rm dof}$ out of all of the possible alternatives. At the next two smallest quark masses we find that we can fit the effective mass splitting one time slice earlier at time slice 13 with a $\chi^2_{\rm dof} = 1.0$. At the sixth largest quark mass we find the smallest $\chi^2_{\rm dof} = 1.41$ for a fit to the data shown where $t \geq 13$. Although this is near the limit of our selection criteria for a good fit, the mass extracted is consistent with the mass a similar fit to the data with a lower bound of 12 and 14. So we are confident that we have extracted the ground state mass. At the two smallest quark masses we find $\chi^2_{\rm dof} = 0.52$ and 0.97 respectively, for a fit to the data shown where $t \geq 13$. The extracted masses are summarised in Fig. 2.2 (closed triangles). In this channel there is no contamination from a nearby decay channel, as was the case in the odd-parity spin-1/2 channel and we find clean access to this state at our lightest quark masses. The physical mass of the spin-1/2 and spin-3/2, odd-parity states is 1535 MeV and 1520 respectively. As in nature, the mass of the two states is very similar in quenched lattice QCD, but the ordering is reversed. It remains to be determined if this is a finite volume effect, a quenching artifact or if the correct ordering is restored as we approach the chiral limit. We note that [27] comments that the ordering we observe is predicted by quark models of the hyperfine interactions that splits the spin-1/2 and spin-3/2 states.

Finally, in Fig. 2.8 we show the effective mass and effective mass splittings of the even-parity spin-3/2 states extracted with the χ_3 interpolator. In each case we fit the effective mass and effective mass splitting data shown where $t \geq 11$. At the four largest quark masses we find a $\chi^2_{\rm dof}$ for the fit ranging from 0.63 to 0.74. At the fifth smallest quark mass the $\chi^2_{\rm dof}$ of the fit is 0.39 and at the three smaller quark masses the $\chi^2_{\rm dof} \simeq 0.1$. As a general rule a small χ^2 is unlikely to represent a good fit, but in our experience a large component of noise can suppress the estimate of the χ^2 calculated with the covariance matrix. At the smallest quark mass the signal has become hidden by the noise after only a few time slices. We find only putative evidence of a plateau at time slice 11 and 12 which we fit to extract our best estimate of the mass. The

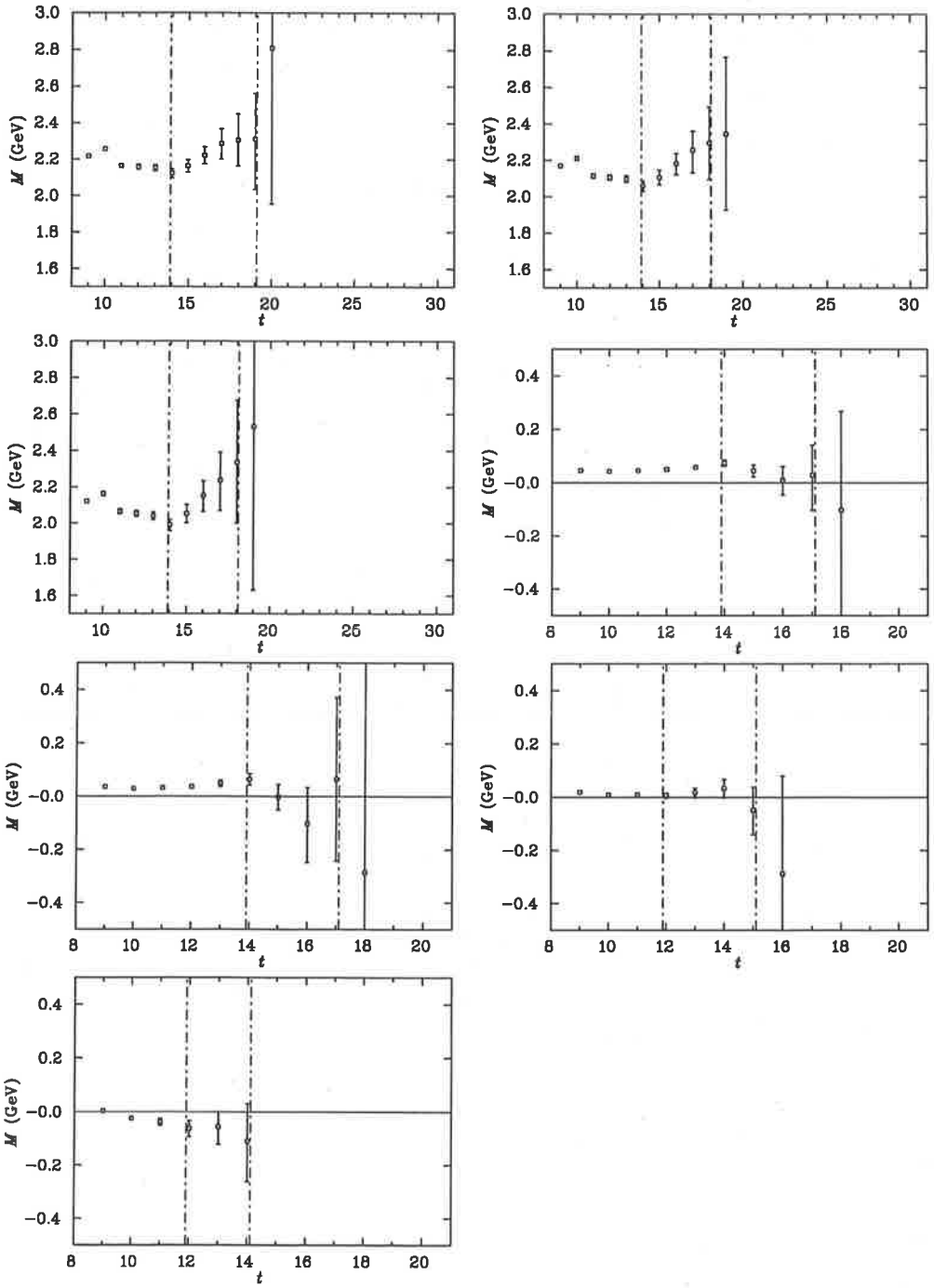

Fig. 2.6: As in Fig. 2.5, but for the mass of the $1/2^-$ state.

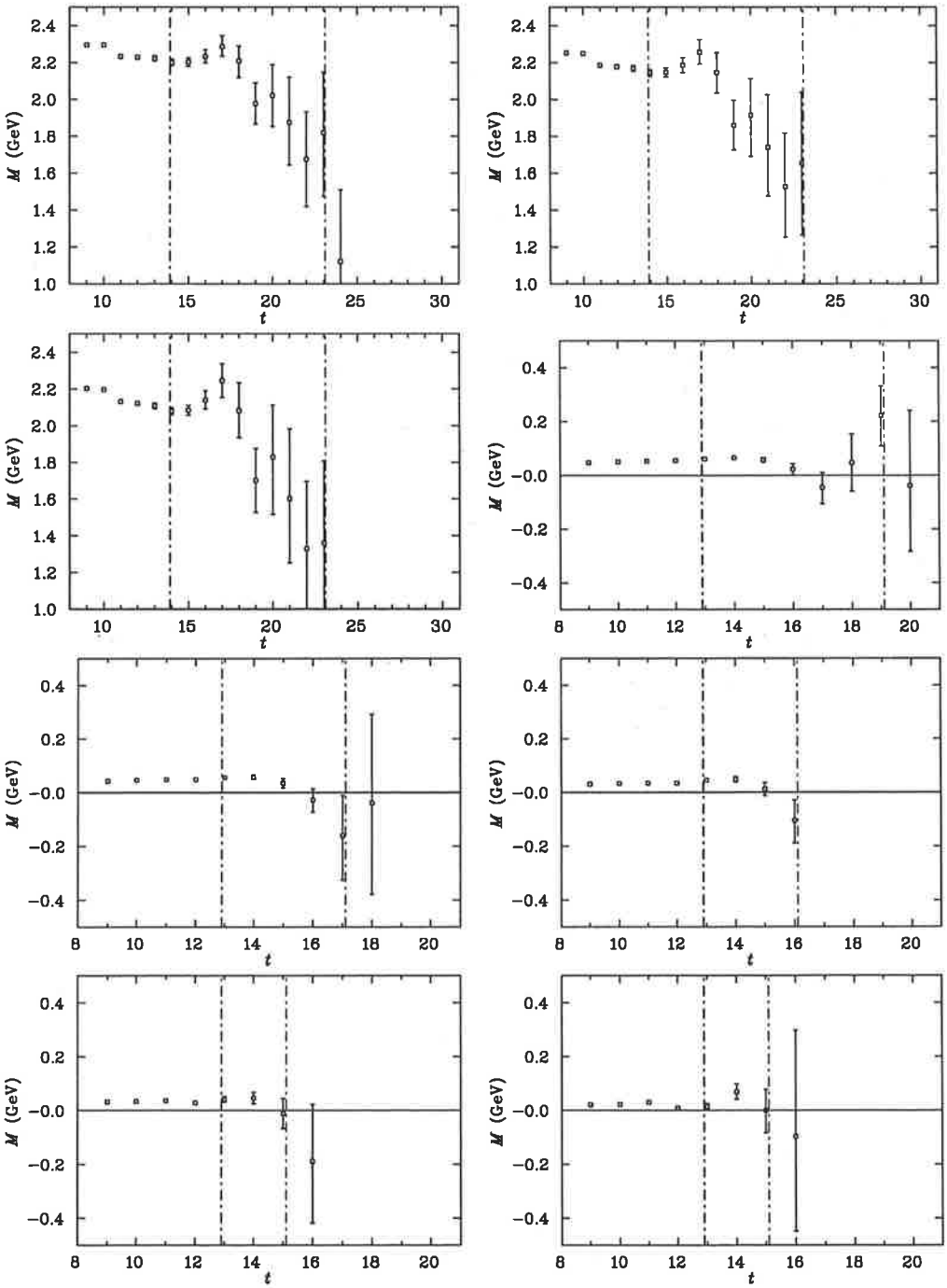

Fig. 2.7: As in Fig. 2.5, but for the mass of the $3/2^-$ state.

extracted masses are shown in Fig. 2.2 (closed circles). We find that we have good access to this state up to the smallest quark mass. At the smallest quark mass we would prefer if possible to fit more than two data point to extract the mass. So a higher statistics calculation is required to extract the mass of this state with more confidence at our smallest quark mass. In this channel the lowest energy two-particle state is the $N + \pi$ (or $N + \eta'$) in P-wave. Here we find that our interpolators do not appear to be accessing the lower energy P-wave $N + \pi$ two-particle state at the smaller quark masses where the 1-particle state is no longer bound. Similarly in our studies of the even-parity pentaquark states [28,29] we found that the mass of the state extracted with our interpolators was generally more consistent with the S-wave $N^* + K$ rather than the lower energy P-wave $N + K$.

Interestingly we see that the mass of the even-parity spin-3/2 state extracted with χ_3 is consistent with the mass of the even-parity spin-1/2 state extracted with the χ_2 interpolator. According to the Particle Data Group [39], the lowest energy even-parity spin-3/2 excited state of the nucleon has a mass of 1720 MeV and the second even-parity spin-1/2 excited state of the nucleon has a mass of 1710 MeV. This analysis suggests that at large quark masses the χ_2 interpolator provides access to the second excited state of nucleon rather than the elusive roper resonance in quenched lattice QCD.

A summary of the masses extracted with the χ_3 interpolator can be found in Table 2.2.

Table 2.1: The masses of the nucleon and the odd-parity excited state of the nucleon extracted with χ_1, and the masses of the three states extracted with the 3×3 correlation matrix analysis with χ_1, χ_2 and χ_3.

aM_π	$aM_N^{1/2^+}$	$aM_N^{1/2^-}$	aM_N^1	aM_N^2	aM_N^3
0.540(1)	1.060(3)	1.395(6)	1.064(4)	1.644(27)	1.633(18)
0.500(1)	1.012(3)	1.359(7)	1.015(4)	1.617(30)	1.609(21)
0.453(1)	0.955(4)	1.319(8)	0.960(5)	1.591(35)	1.587(26)
0.400(1)	0.895(5)	1.278(10)	0.902(6)	...	1.577(34)
0.345(2)	0.836(8)	1.244(13)	0.847(8)	...	1.595(56)
0.300(2)	0.797(9)	1.224(16)	0.809(12)	...	...
0.242(2)	0.762(10)	1.060(43)	...	...	...
0.197(2)	0.752(12)	...	...	...	...

Table 2.2: The masses of the spin-1/2 and spin-3/2 states of the nucleon extracted with the χ_3 interpolator.

aM_π	$aM_N^{1/2^+}$	$aM_N^{1/2^-}$	$aM_N^{3/2^+}$	$aM_N^{3/2^-}$
0.540(1)	1.063(3)	1.394(16)	1.655(10)	1.430(12)
0.500(1)	1.015(4)	1.355(18)	1.624(10)	1.393(13)
0.453(1)	0.960(4)	1.311(23)	1.590(11)	1.353(15)
0.400(1)	0.902(5)	1.267(32)	1.558(12)	1.314(16)
0.345(2)	0.848(7)	1.234(44)	1.531(13)	1.278(18)
0.300(2)	0.812(9)	1.226(47)	1.515(16)	1.250(21)
0.242(2)	0.776(13)	...	1.512(19)	1.223(24)
0.197(2)	0.757(18)	...	1.540(25)	1.208(33)

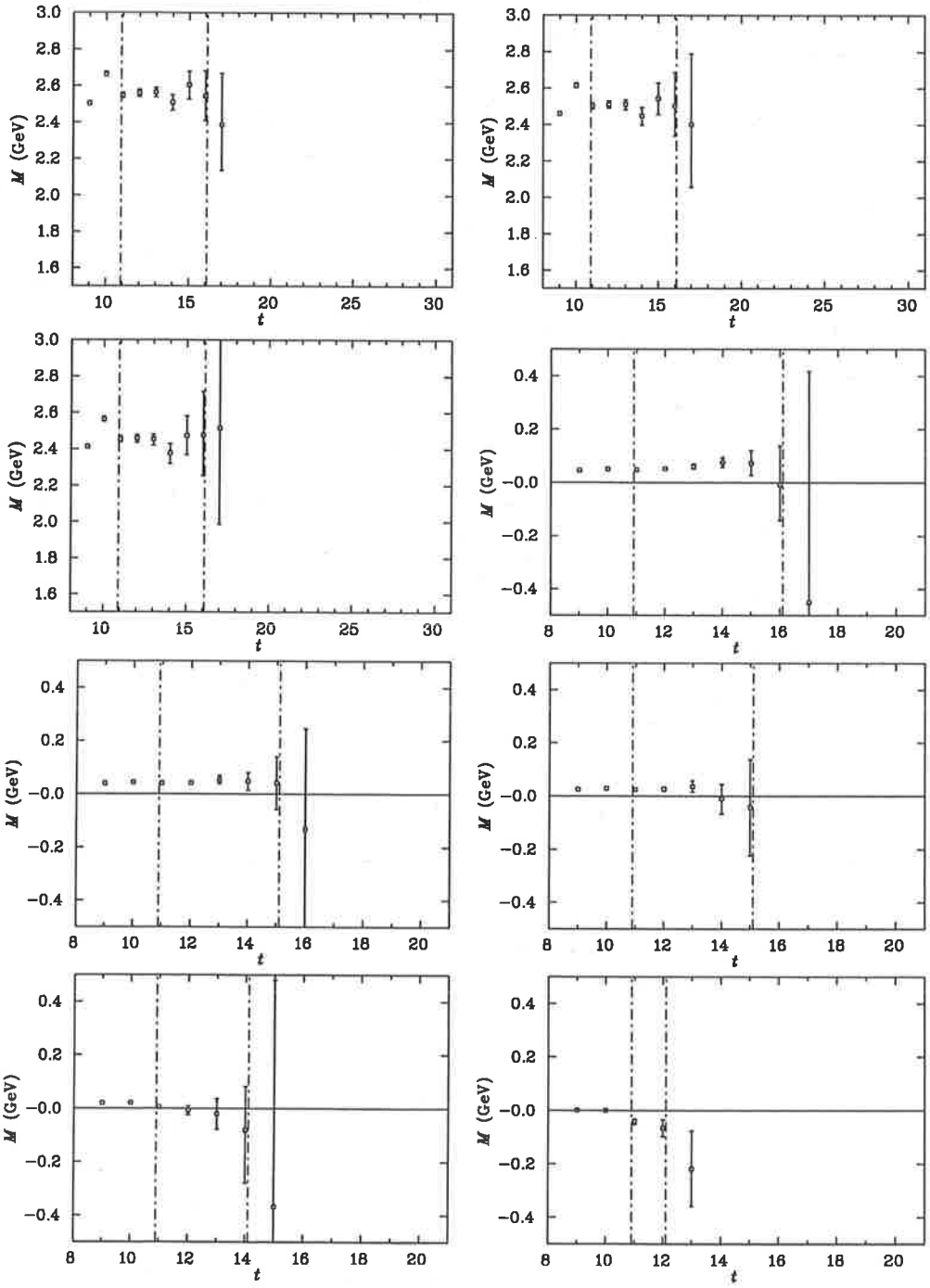

Fig. 2.8: As in Fig. 2.5, but for the $3/2^+$ state.

2.3.2 Roper search

As we discussed in Sec. 2.2.4, we need a complete basis of interpolators to extract the complete tower of excited states in a particular channel. Theoretically the set of basis interpolators would be very large. In practice, by taking advantage of exponential suppression of the higher energy contributions to the correlation function and techniques such as smearing the fermion source of the quark propagator, we can assume that there is only a significant contribution to the correlation function from the lowest energy states.

In our previous study [18] of the nucleon excited states, we used a 2×2 correlation matrix analysis with the χ_1 and χ_2 interpolators. We found that although the two interpolators were largely orthogonal, which is what we wanted, the χ_2 couples to a much higher energy state than we would expect to identify as the Roper. Indeed in the previous section we find that a comparison with the mass of the spin-3/2 even-parity state extracted with the χ_3 interpolator suggests that the state extracted with the χ_2 interpolator is the second even-parity excited state of the nucleon.

In Fig. 2.9 we show the effective mass of the lowest energy state projected from the 2×2 correlation matrix analysis with the χ_1 and χ_3 interpolators as in Eq. (2.41). Where we fit the data shown for $t \geq 17$, we find a $\chi^2_{\text{dof}} \simeq 1.0$ at all quark masses. The effective mass of the excited state extracted with this correlation matrix analysis is shown in Fig. 2.10. Where we fit the data shown for $t \geq 11$, we find a χ^2_{dof} between 0.95 at the largest quark mass and 0.28 at the smallest quark mass shown. A summary of the masses extracted from this data is shown in Fig. 2.11, along with the masses extracted with the χ_1 and χ_2 interpolators individually. We find that the lowest energy state extracted with the correlation matrix analysis is in excellent agreement with the mass of the state extracted with the χ_1 interpolator, and that the mass of the excited state from the χ_1, χ_3 analysis is in excellent agreement with the mass extracted with the χ_2 interpolator. Since we know that the χ_1 interpolator is largely orthogonal to the χ_2 interpolator, this calculation shows that the χ_3 interpolator has a significant overlap with the state accessed by the χ_2 interpolator. If the χ_3 interpolator does couple to a lower energy excited state, i.e. not the ground state of the nucleon, then the coupling of χ_3 to this state must be small compared to its coupling to the second even-parity excited state because we do not find evidence of a lower energy state with this calculation.

In Fig. 2.12 we show the effective mass of the lowest energy state extracted with a 2×2 correlation matrix analysis using the χ_2 and χ_3 interpolators. We find a χ^2_{dof} between 1.53 at the largest quark mass and 0.41 at the smallest quark mass. Although the χ^2_{dof} of the largest quark mass is at the upper limit of our selection criteria, the mass extracted with this fit is in excellent agreement with the masses extracted with both the χ_1 and χ_3 interpolators individually. So we accept this fit in this analysis. In Fig. 2.13 we show the effective mass of the excited state extracted with this correlation matrix analysis. Where we fit the data shown at $t \geq 11$, we find a χ^2_{dof} between 0.61 at the largest quark mass and 0.80 at the smallest quark mass. A summary of the masses extracted with this analysis is shown in Fig. 2.14, along with the masses extracted with the χ_1 and χ_2 interpolators individually. Once again the masses extracted with the correlation matrix analysis are in excellent agreement with the masses extracted with the χ_1 and χ_2 interpolators individually. This indicates that the χ_3 interpolator couples strongly to the ground state extracted with the χ_1 interpolator.

Therefore using the 2×2 correlation matrix analysis we find that the χ_3 interpolator

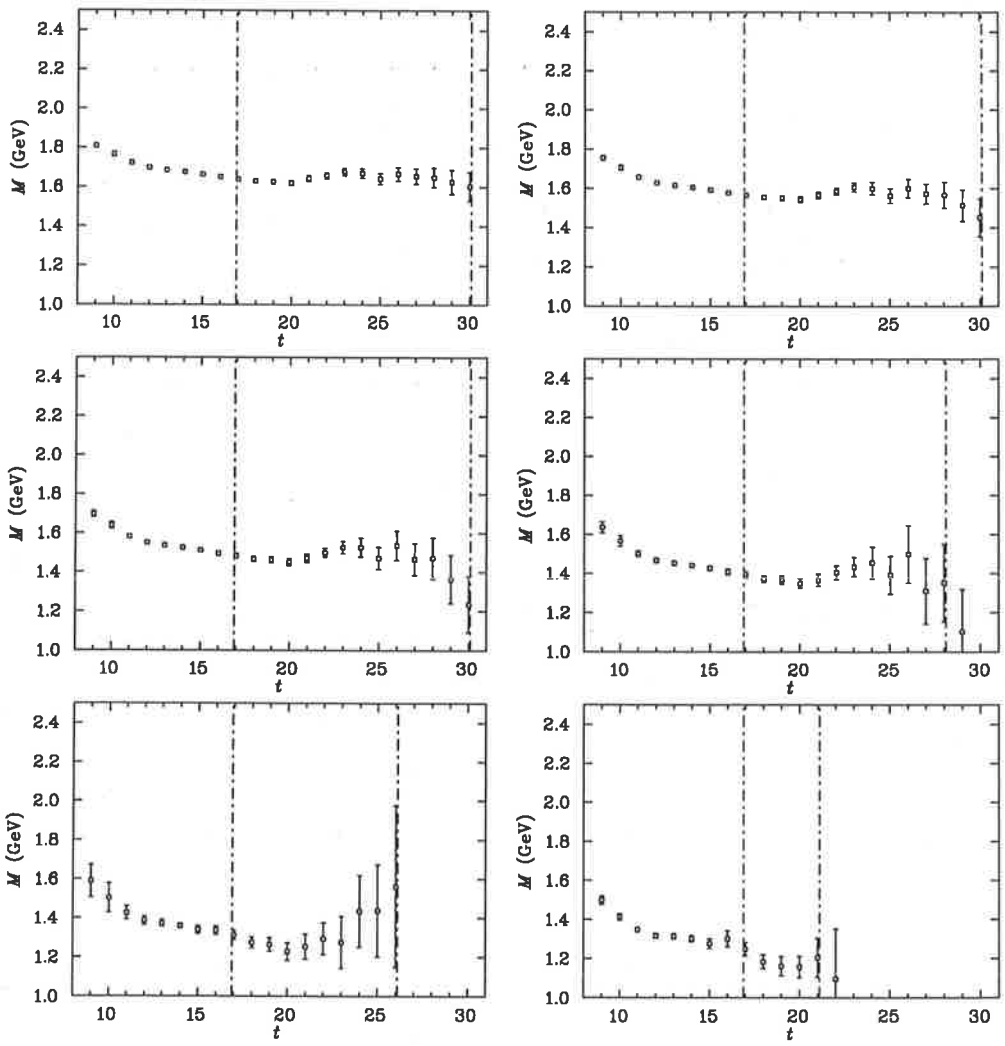

Fig. 2.9: The effective mass of the lowest energy $1/2^+$ state extracted with the 2×2 correlation matrix (χ_1, χ_3). The data correspond to $m_\pi \simeq 830$ MeV (top left), 770 MeV (top right), 700 MeV (middle left), 616 MeV (middle right), 530 MeV (bottom left) and 460 MeV (bottom right).

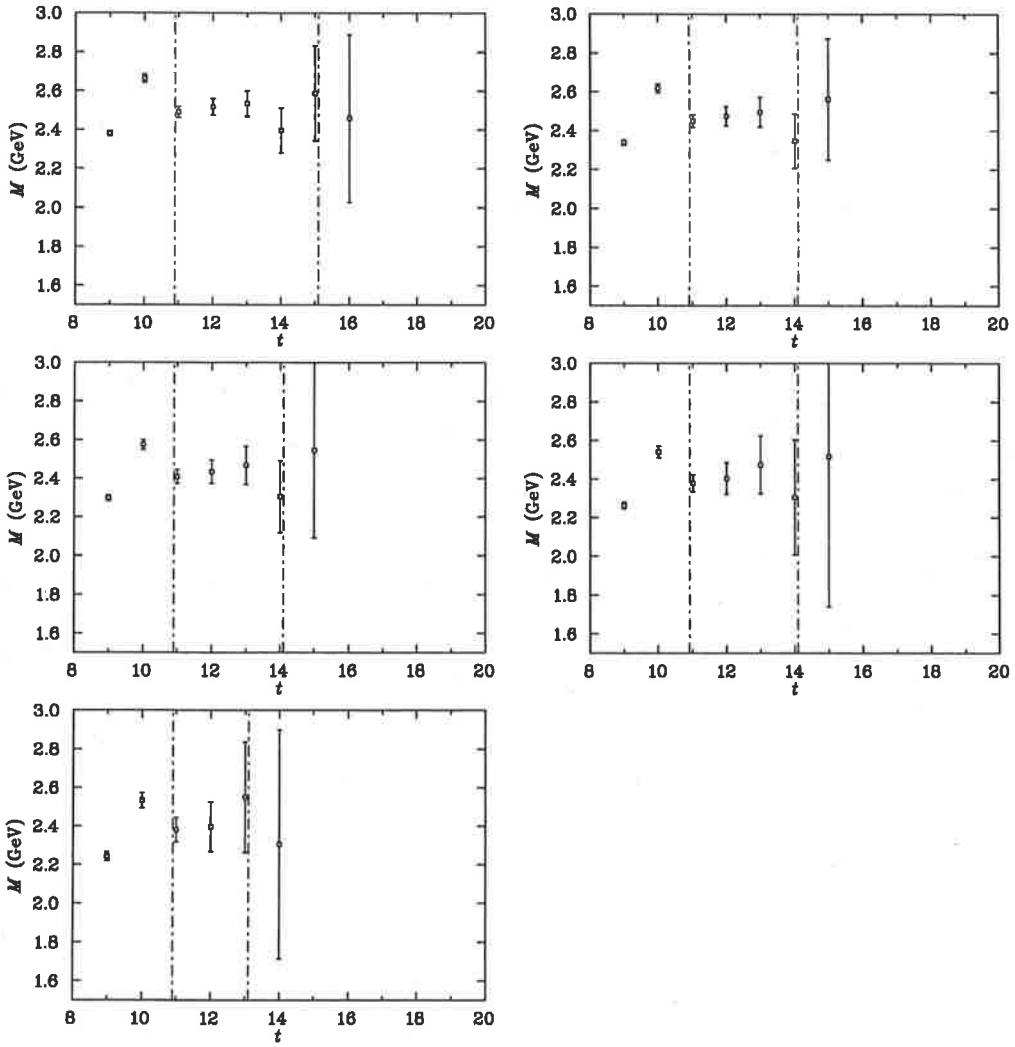

Fig. 2.10: As in Fig. 2.9, but for the excited state extracted with the 2×2 correlation matrix.

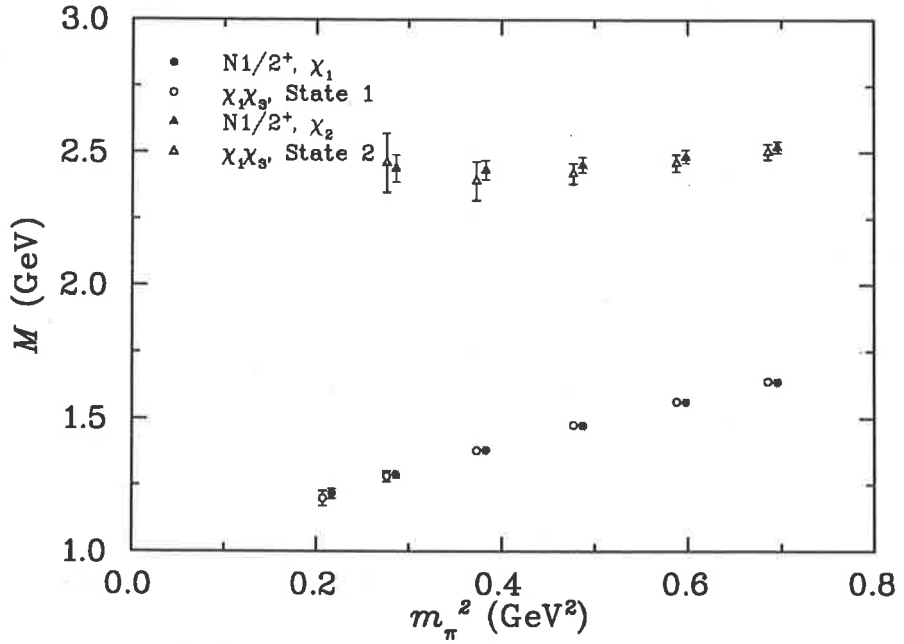

Fig. 2.11: The masses extracted with a 2×2 correlation matrix with the χ_1 and χ_3 interpolators. For comparison the masses extracted with the χ_1 and χ_2 interpolators are shown. The data correspond to $m_\pi \simeq 830\,\text{MeV}$, 770 MeV, 700 MeV, 616 MeV, 530 MeV and 460 MeV.

has strong overlap with both the χ_1 and χ_2 interpolators, and that the coupling to the even-parity Roper state must be relatively small, if it is non-zero.

The results of the 2×2 correlation matrix analysis suggests that χ_3 has significant overlap with $\chi_{1,2}$. Using the Fierz identity,

$$\delta_{\alpha\alpha'}\delta_{\beta\beta'} = \frac{1}{4}\sum_J (\Gamma_J)_{\alpha\beta'}(\Gamma_J^{-1})_{\beta\alpha'} \ .$$

Where Γ is one of the matrices $\{1, \gamma_5, \gamma_\mu, \gamma_\mu\gamma_5, \sigma_{\mu\nu}|_{\mu>\nu}\}$,

$$\begin{aligned}\chi_3^\mu \ = \ & -\frac{1}{4}\gamma^\mu\gamma_5\chi_{\text{Ioffe}} - \frac{1}{8}\gamma^\mu\gamma_5\chi_{\text{A}} \ + \\ & \frac{1}{2}\epsilon^{abc}(u^{aT}C\gamma^\mu u^b)d^c \ - \frac{i}{2}\epsilon^{abc}(u^{aT}C\sigma^{\mu\alpha}u^c)\gamma_\alpha d^c\end{aligned}$$

The interpolating fields χ_{Ioffe} and χ_{A} are,

$$\begin{aligned}\chi_{\text{Ioffe}} \ &= \ \epsilon^{abc}(u^{aT}C\gamma^\alpha u^b)\gamma_5\gamma_\alpha d^c \\ \chi_{\text{A}} \ &= \ \epsilon^{abc}(u^{aT}C\sigma^{\alpha\beta}u^b)\gamma_5\sigma_{\alpha\beta}d^c \ .\end{aligned}$$

Each of these interpolators have been identified as linear combinations of χ_1 and χ_2 [40]. So we find that the Fierz transformation explains our finding that χ_3 is has a strong overlap with both χ_1 and χ_2.

We proceed with a 3×3 correlation matrix analysis with χ_1, χ_2 and χ_3. Eigenvectors for the projection of the correlation matrix are obtained from an analysis at $t = 10$, one step back from the onset of the plateau for $\chi_2\bar{\chi}_2$ In Fig. 2.15 we show the effective

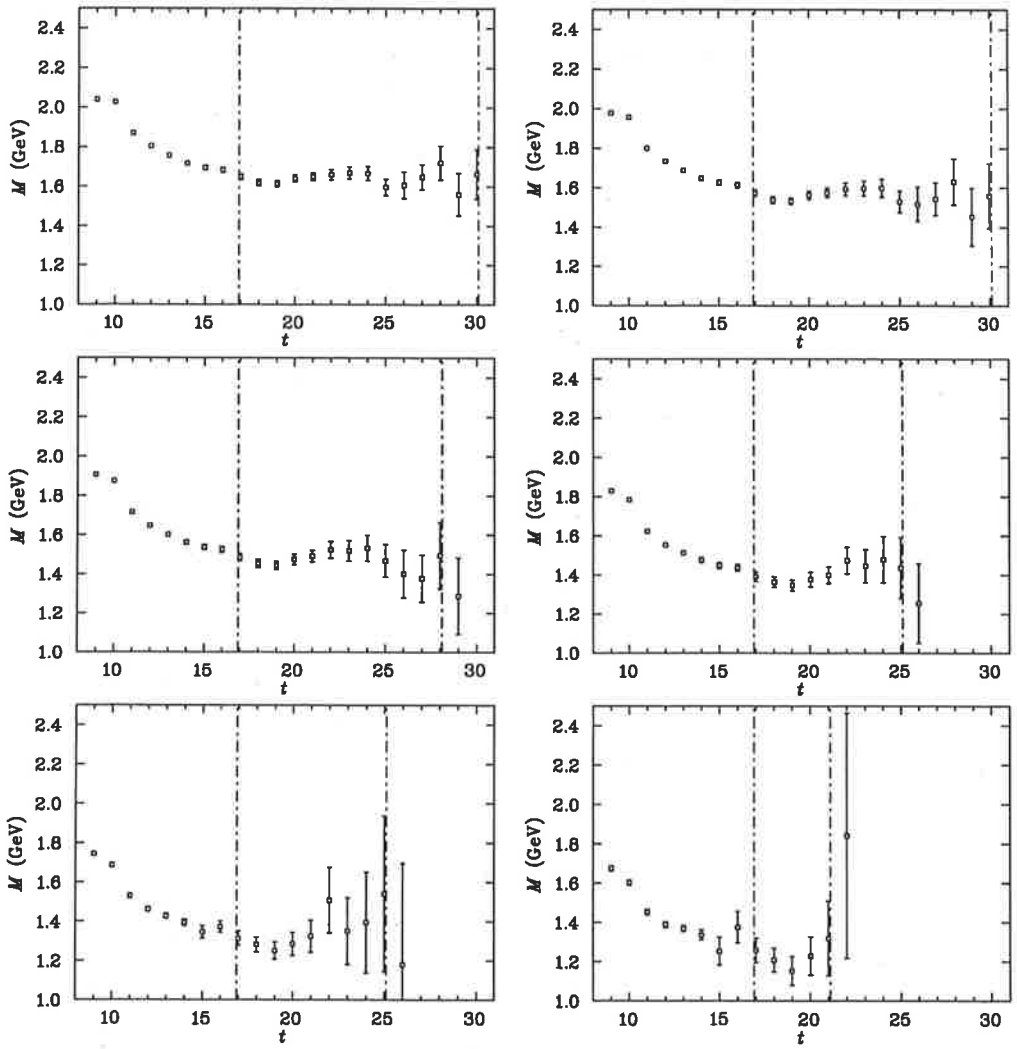

Fig. 2.12: As in Fig. 2.9, but for the ground state extracted with the 2×2 correlation matrix (χ_2, χ_3).

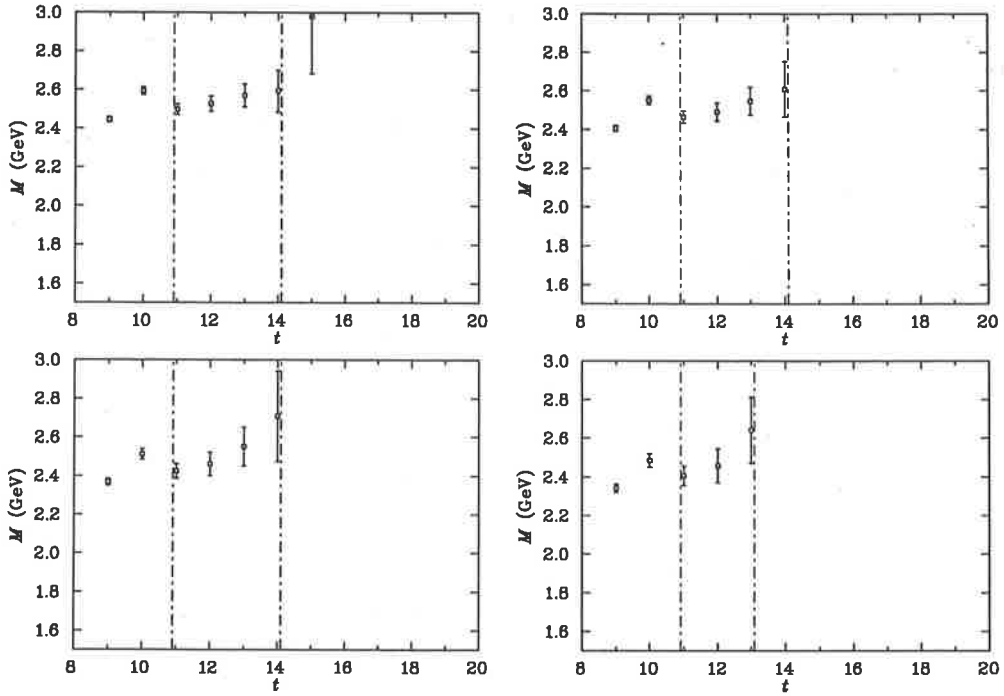

Fig. 2.13: As in Fig. 2.12, but for the excited state extracted with the 2×2 correlation matrix.

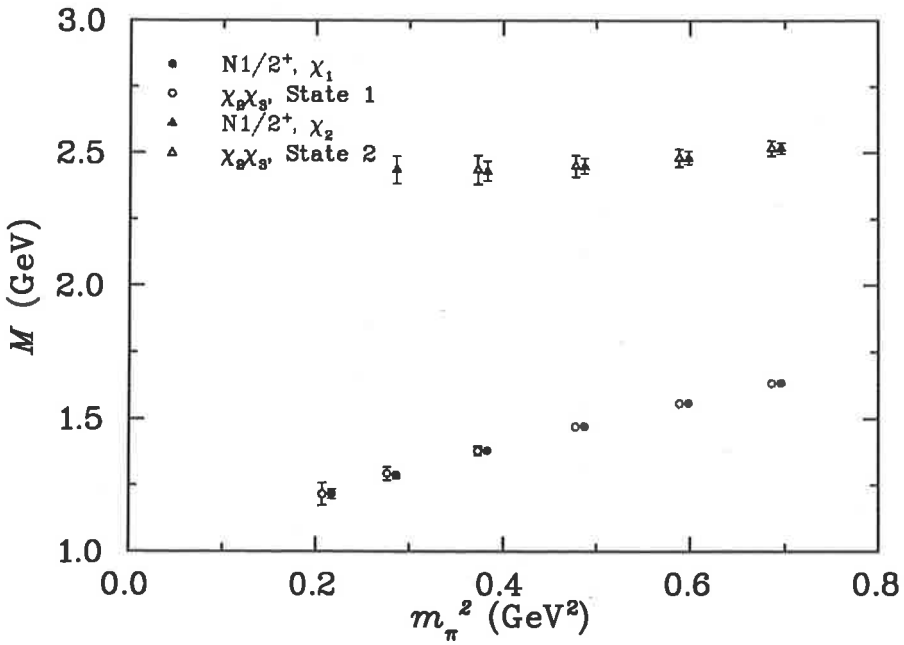

Fig. 2.14: As in Fig. 2.11 but for the 2×2 correlation matrix with the χ_2 and χ_3 interpolators.

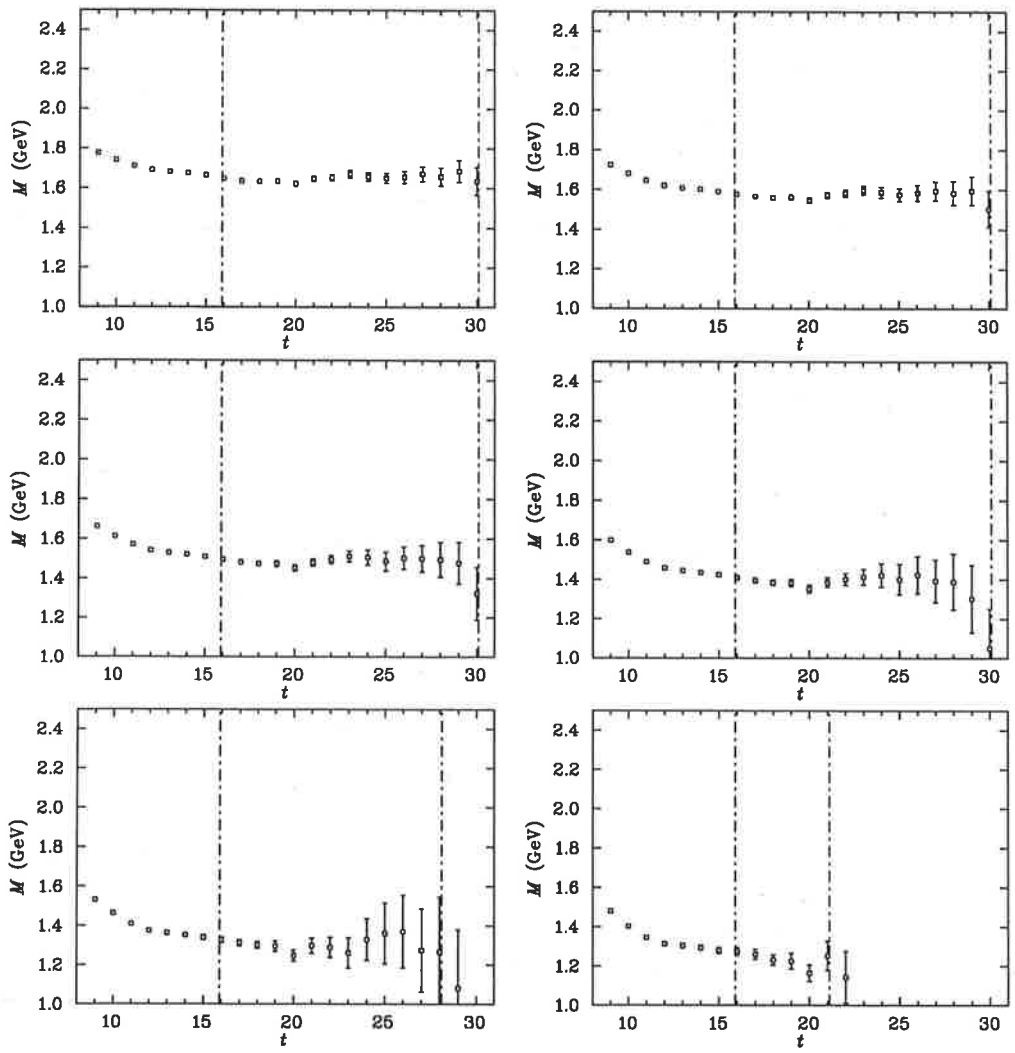

Fig. 2.15: The effective mass of the lowest energy $1/2^+$ state extracted with the 3×3 correlation matrix (χ_1, χ_2, χ_3). The data correspond to $m_\pi \simeq 830\,\text{MeV}$ (top left), 770 MeV (top right), 700 MeV (middle left), 616 MeV (middle right), 530 MeV (bottom left) and 460 MeV (bottom right).

mass of the lowest energy state extracted with our correlation matrix. Where we fit the data shown for $t \geq 16$ we find a $\chi^2_{\text{dof}} \simeq 1$ at the five largest quark masses and a $\chi^2_{\text{dof}} = 1.57$ at the smallest quark mass. The masses extracted are shown in Fig. 2.16 along with the mass extracted with the χ_1, χ_2 and χ_3 interpolators individually. We find that the three determinations of the ground state mass are in excellent agreement.

In Figs. 2.17 and 2.18 we show the effective masses of the two other states extracted with the correlation matrix. Here we are limited to an analysis at the three largest quark masses because of the large component of noise in these effective masses. In each case we find a $\chi^2_{\text{dof}} \simeq 1$ where we fit the data shown for $t \geq 11$. The masses extracted with this analysis are shown in Fig. 2.16. In each case the mass extracted is consistent with the mass extracted with the χ_2 interpolator. So we find that the couplings of the interpolators to a Roper like even-parity excited state of the nucleon must be small if non-zero because we find no evidence of such a state in this study in quenched lattice QCD. As always, greater statistics may yet reveal evidence of the Roper if the coupling

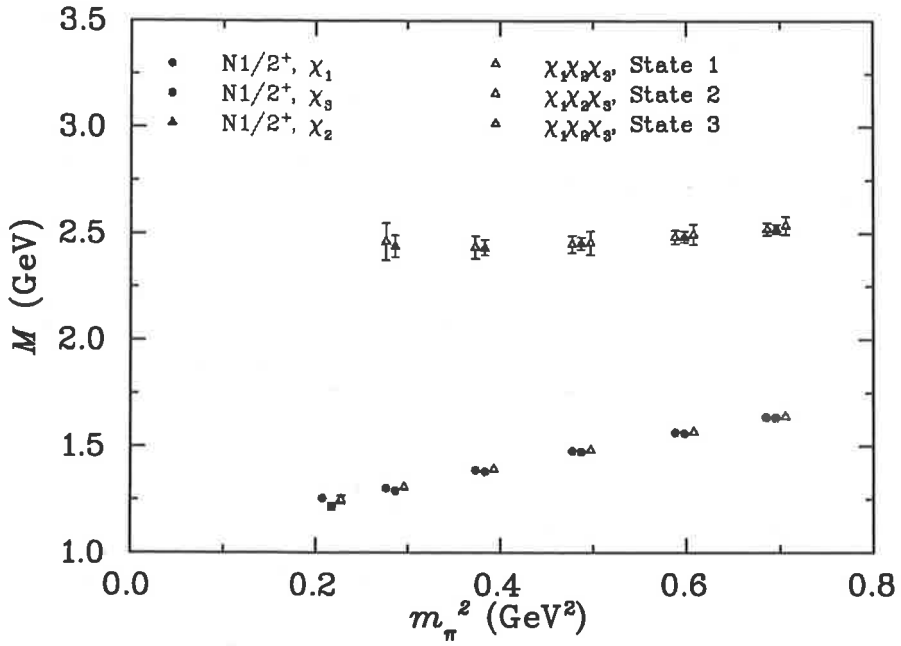

Fig. 2.16: As in Fig. 2.11 but for the 3×3 correlation matrix with the χ_1, χ_2 and χ_3 interpolators.

is indeed small. A review of the impact of the fermion source smearing is warranted as future work. We expect that a future study of the source smearing prescription should also include the approach of [33] who used a variety of source and sink smearing prescriptions to expand their operator basis.

The masses of the three states extracted with the 3×3 correlation matrix are shown in Table. 2.1.

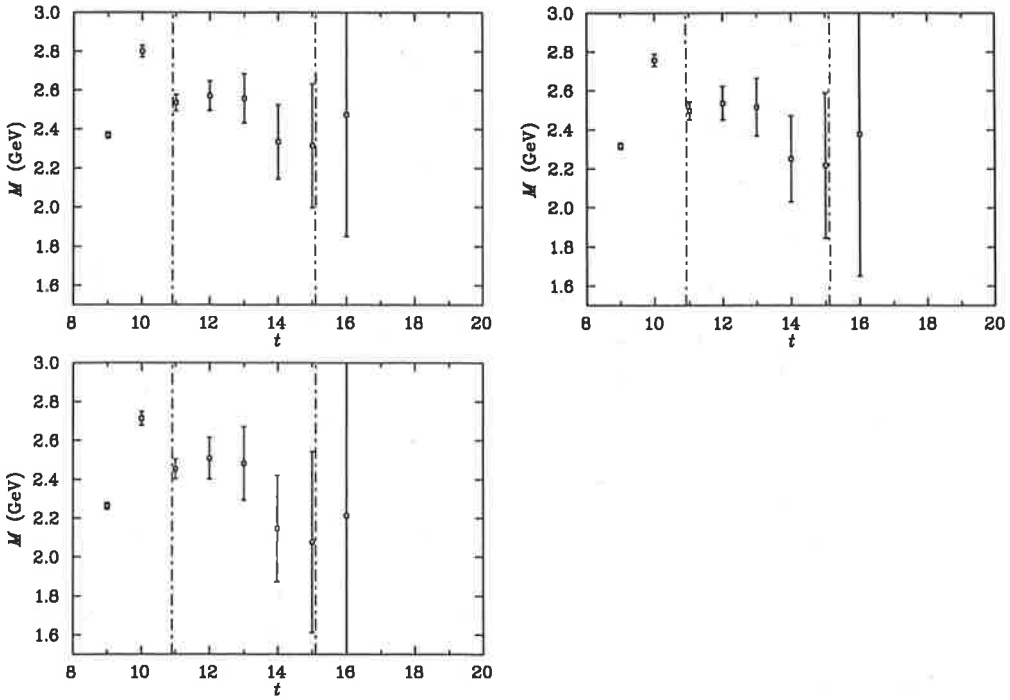

Fig. 2.17: As in Fig. 2.15, but for an excited state extracted with the 3×3 correlation matrix.

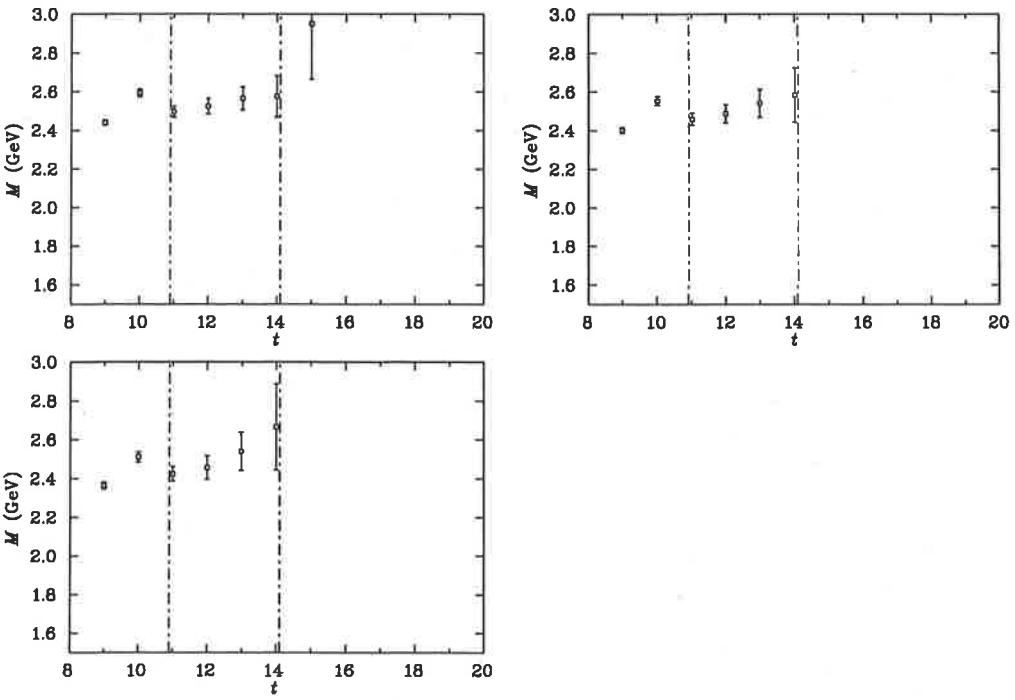

Fig. 2.18: As in Fig. 2.15, but for an excited state extracted with the 3×3 correlation matrix.

2.3.3 Isospin-3/2 states

We continue our discussion with an analysis of the Δ baryon and its excited states in quenched lattice QCD. As with the nucleon, exact isospin symmetry in our simulations means that the $\Delta^-, \Delta^0, \Delta^+$ and Δ^{++} are degenerate in mass. So we extract the mass of the Δ baryon and its excited states using the Δ^{++} interpolator Eq. (2.2).

In Fig. 2.19 we show the effective mass and effective mass splittings of the spin-3/2, even-parity state extracted with our Δ^{++} interpolator. At the three largest quark masses we find a $\chi^2_{\rm dof}$ between 0.61 and 0.76 for a fit to the data shown where $t \geq 15$. At the next two smaller quark masses we find a $\chi^2_{\rm dof} \simeq 1$ where we fit the effective mass splittings at two time slices earlier, where $t \geq 13$. In each case we extract a mass that is consistent with a similar analysis where $t \geq 14$ or $t \geq 15$. So we take advantage of the opportunity to analyse our data at the earlier times. At the three smallest quark masses we find that the signal is becoming hidden by the noise at smaller Euclidean times, but we are fortunatly able to extract the mass splittings from the data where $t \geq 11$. The $\chi^2_{\rm dof}$ in each case is 1.28, 1.07 and 0.56. The extracted masses are shown in Fig. 2.20 (closed circles). Here we find that we are able to make a precise determination of the spin-3/2, even-parity Δ with this simulation. In this channel the lowest energy two-particle state is the $N + \pi$ in relative P-wave, so the Δ is bound in this channel at all quark masses considered in our simulation.

Next we analyse the odd-parity spin-3/2 state. In Fig. 2.21 we show the effective mass and effective mass splittings of this state extracted with our Δ^{++} interpolator. At the three largest quark masses there appears to be a systematic drift in the effective mass data towards time slice 15. However we find a $\chi^2_{\rm dof}$ between 0.36 and 0.56 for a fit to the data shown where $t \geq 13$, which suggests that is just a statistical fluctuation. The effective mass splittings at the next three largest quark masses show no evidence of such a systematic drift. We find a $\chi^2_{\rm dof} < 1$, for a fit to the data where $t \geq 13$. At the two smallest quark masses the signal is degraded at smaller Euclidean time, but we find a $\chi^2_{\rm dof} = 0.56$ and 0.64 where we fit the data where $t \geq 10$. In each case the mass splittings is consistent with a fit to the data where $t \geq 11$ and $t \geq 12$. The masses extracted are shown in Fig. 2.20 (closed triangles). In this channel the lowest energy multi-hadron state is the $\Delta^{++} + \pi$ in S-wave. Thus the lowest energy odd-parity state in this channel is bound in this study.

In Fig. 2.22 we show the mass of the spin-1/2 odd-parity state extracted with our Δ^{++} interpolator. At each quark mass we find a $\chi^2_{\rm dof} < 1$ for a fit to the data where $t \geq 11$. In some cases the $\chi^2_{\rm dof} \sim 0.1$, where we attribute the small χ^2 to the large component of noise in the data. With the statistics of our calculation, the analysis is limited to the seven largest quark masses. The lowest energy two-hadron state in this channel is the S-wave $N + \pi$, but we find no evidence that our interpolators couple to this state. The masses extracted are shown in Fig. 2.20 (open triangles). The masses of the odd-parity spin-1/2 and spin-3/2 states are consistent to within the error bars, which is qualitatively the similar to the physical spectrum where the spin-1/2 state has a mass of 1620 MeV and the spin-3/2 state has a mass of 1700 MeV. In nature the mass of the spin-3/2 odd-parity Δ is very similar to the physical mass of the even-parity spin-3/2 nucleon which is 1720 MeV. However in our lattice simulation the spin-3/2 odd-parity Δ has a much smaller mass at each quark mass. Indeed the mass of the odd-parity spin-3/2, the odd-parity spin-1/2 and the even-parity spin-1/2 Δ baryons display only a small quark mass dependence. In Chapter 3 we argue that binding at quark masses near the physical regime is a lattice resonance signature. Here we

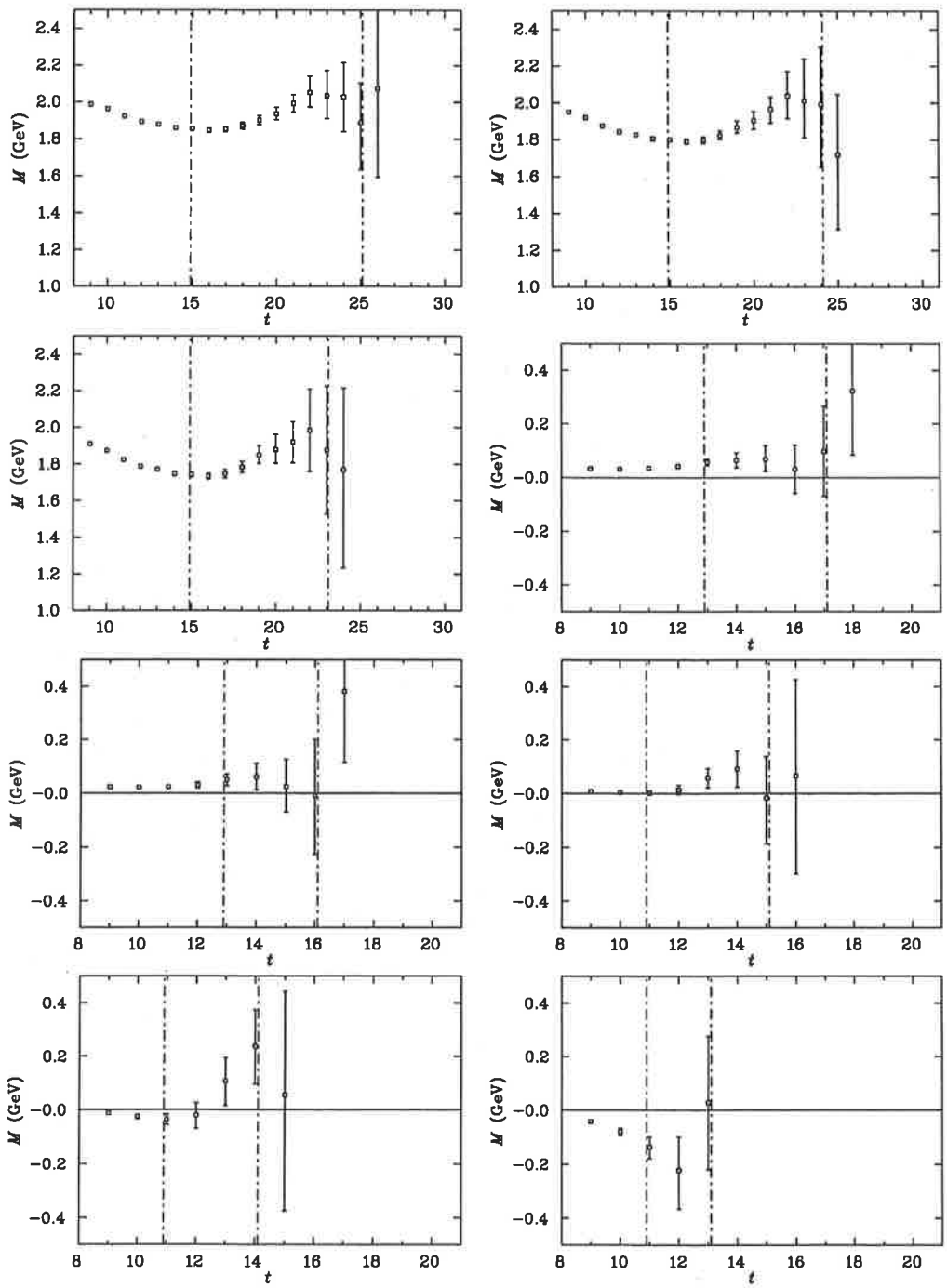

Fig. 2.19: The effective mass of the $3/2^+$ state extracted with the $\chi_{\Delta^{++}}$ interpolator.

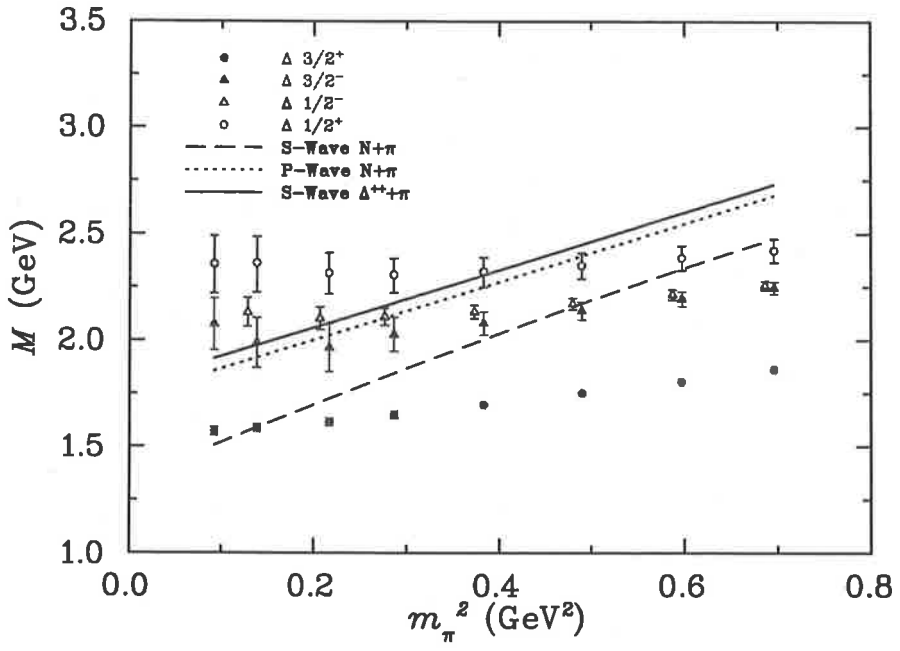

Fig. 2.20: The data correspond to $m_\pi \simeq 830$, 770, 700, 616, 530, and 460 MeV.

find evidence that these Δ resonances are more bound than the comparable nucleon resonances at the quark masses used in our calculation.

Finally, in Fig. 2.23 we show the effective mass of the even-parity, spin-1/2 state. There is a drift in the effective mass data towards time slice 14, but there is a large component of noise, and we are able to fit the data where $t \geq 11$. The extracted masses are shown in Fig. 2.20 (open circles). The physical mass of the lowest energy even-parity, spin-1/2 state is 1750 MeV, which is similar to the physical mass of the odd-parity states in this channel. Here we find that the mass of this state is consistently larger than the mass of the odd-parity states. Which is qualitatively consistent with the physical mass spectrum. However the large component of noise in our correlation functions maybe suppressing the χ^2 and so there maybe some excited state contamination. The masses of the states extracted with the Δ^{++} interpolator are shown in Table. 2.3.

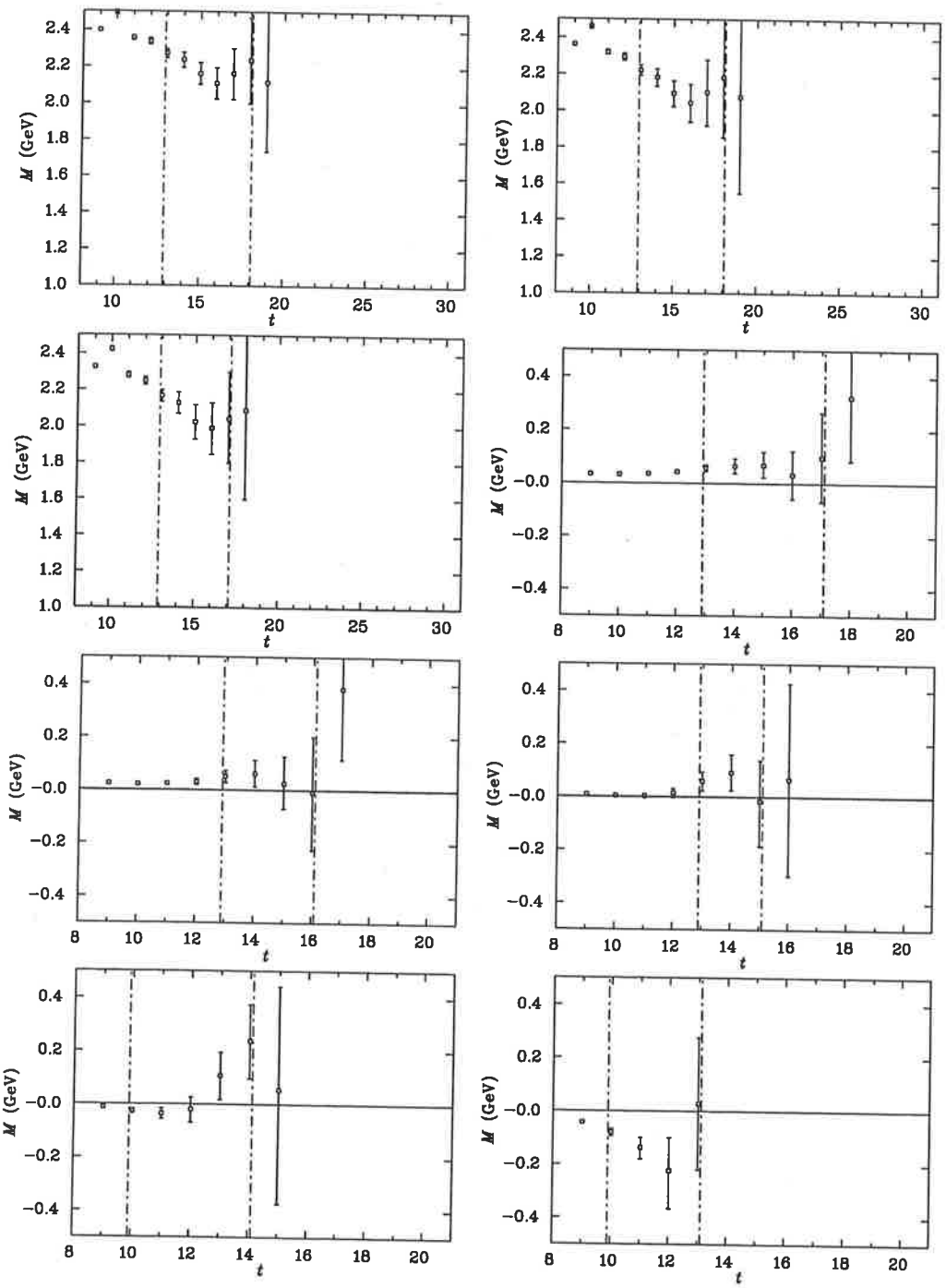

Fig. 2.21: As in Fig. 2.19, but for the $3/2^-$ state.

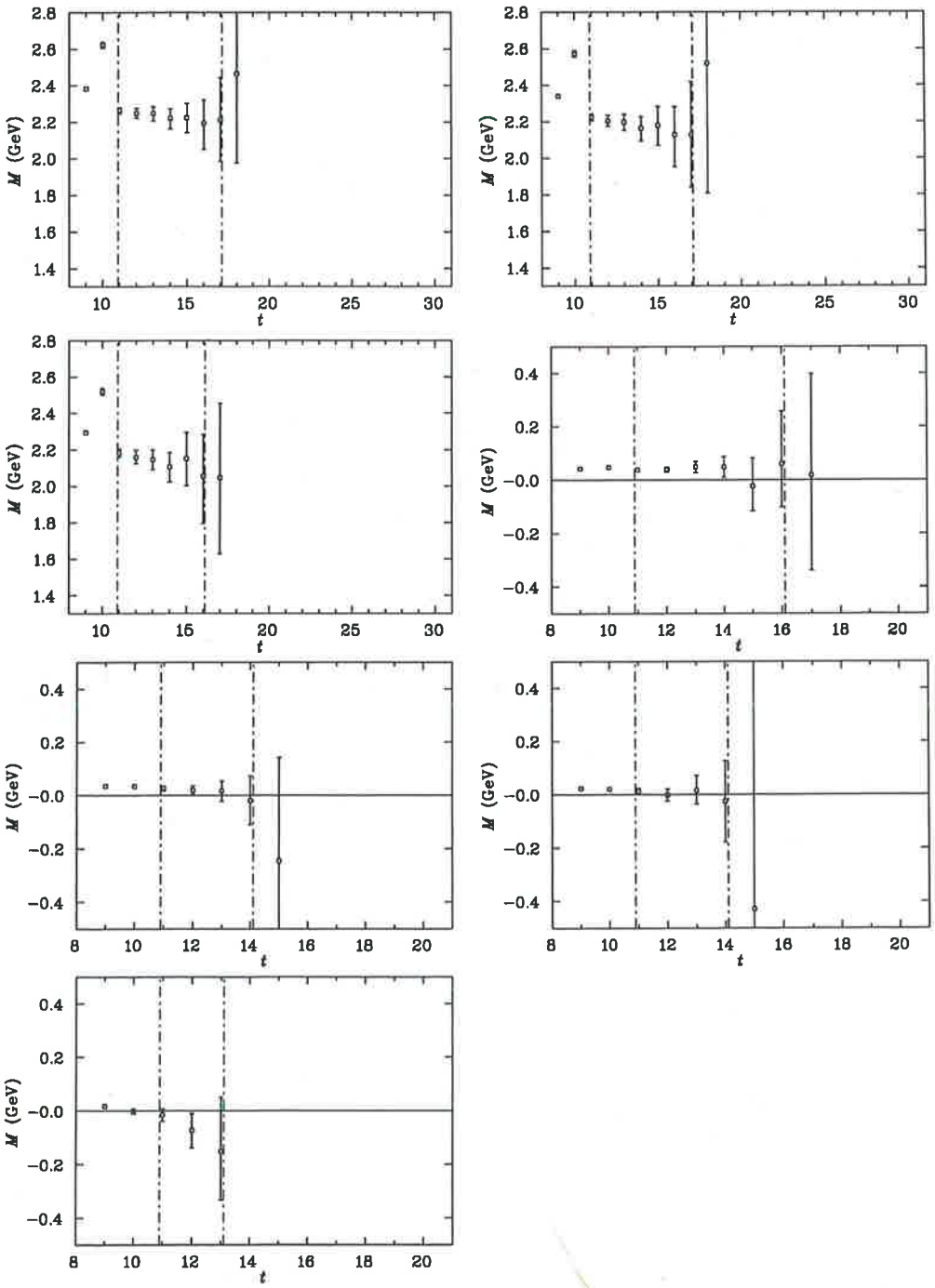

Fig. 2.22: As in Fig. 2.19, but for the $1/2^-$ state.

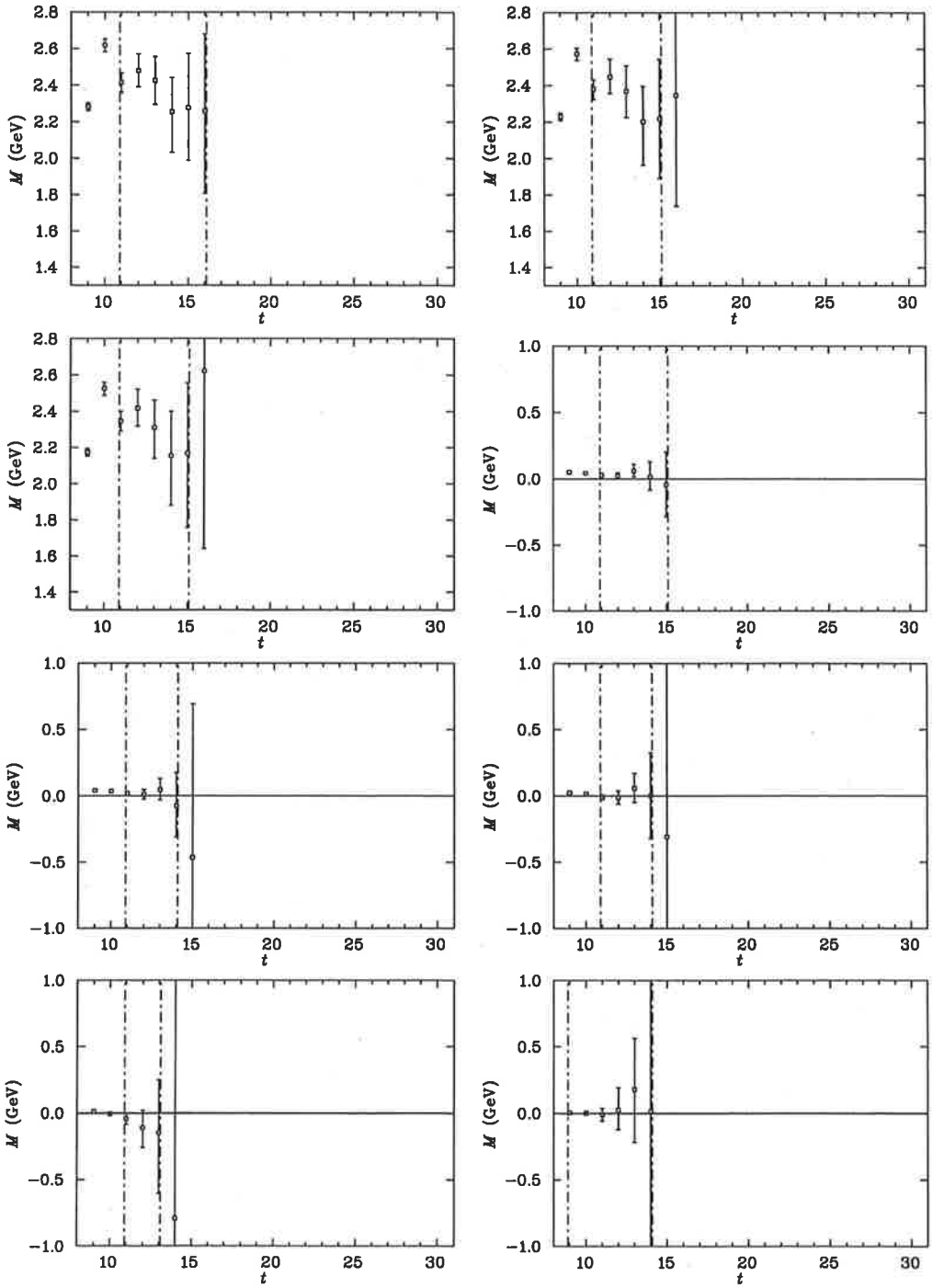

Fig. 2.23: As in Fig. 2.19, but for the $1/2^+$ state.

Table 2.3: The masses of the Δ^{++} and the spin-1/2 and spin-3/2 excited states of the Δ extracted with the $\chi_{\Delta^{++}}$ interpolator.

aM_π	$aM_\Delta^{1/2^+}$	$aM_\Delta^{1/2^-}$	$aM_\Delta^{3/2^+}$	$aM_\Delta^{3/2^-}$
0.540(1)	1.569(36)	1.462(13)	1.206(6)	1.455(19)
0.500(1)	1.547(38)	1.434(15)	1.172(6)	1.422(23)
0.453(1)	1.525(41)	1.406(17)	1.134(7)	1.386(27)
0.400(1)	1.506(47)	1.382(20)	1.098(9)	1.347(36)
0.345(2)	1.495(54)	1.369(25)	1.067(11)	1.314(51)
0.300(2)	1.500(63)	1.363(33)	1.046(11)	1.274(74)
0.242(2)	1.532(89)	1.381(42)	1.027(12)	1.290(77)
0.197(2)	1.529(89)	...	1.016(12)	1.346(78)

2.4 Summary

In this study we have calculated the spectrum of spin-1/2 and spin-3/2 nucleon and Δ resonances in quenched lattice QCD on a large $20^3 \times 40$ lattice. We show that methods for extracting the hadron spectrum developed in [18, 27] are effective in extracting the low lying spectrum at light quark masses.

We observe that the level ordering of the masses of the odd-parity spin-1/2 and spin-3/2 states are similar which is consistent with the empirical spectrum, but that in the case of the odd-parity nucleons the ordering is reversed. In [27] we comment that this ordering of odd-parity excited states is predicted by quark models. It remains as future work to rule out finite volume effects as the cause of this discrepancy. Also, full QCD simulations are vital for removing the artifacts associated with the quenched approximation.

We have demonstrated that the ground and second even-parity excited state of the nucleon can be extracted from a 2×2 correlation matrix with either the χ_1 and χ_3 or χ_2 and χ_3 interpolators. With the use of the Fierz identity we show that the χ_3 interpolator does indeed have a large overlap with the χ_1 and χ_2 interpolators. Continuing with a 3×3 correlation matrix analysis we find no evidence that our interpolators overlap with the first experimentally observed even-parity excited state of the nucleon, the Roper resonance. However we also find that the large amount of smearing of the fermion source has removed overlap of our interpolators with the odd-parity excited states of the nucleon which were successfully extracted in [18] with the χ_1 and χ_2 interpolators. It is possible that we may have more success at extracting excited states with these interpolators with a different smearing prescription. Therefore a study to determine the optimal amount of source smearing for the calculation of the spectrum of these excited states remains as future work.

We find that the χ_1 and χ_2 interpolators couple to a lower energy multi-hadron state in the odd-parity spin-1/2 channel. In other channels we do not resolve overlap of our interpolators with lower energy multi-hadron states. But we expect that with a higher statistics calculation we will resolve signal in the correlation function at larger Euclidean times, and that we will therefore access multi-hadron states in other channels. Therefore an extension to our operator basis similar to [33] will be required to accurately determine the spectrum of nucleon and Δ at our lightest quark masses.

Finally we calculate the mass of the Δ^{++} at our smallest quark masses with great precision. Towards a pion mass of 300 MeV we are beginning to see chiral curvature in the mass of the Δ^{++} as we approach the chiral limit. We find that the ordering of the odd-parity excited states of the Δ^{++} is consistent with the physical spectrum. We find a mass of the even-parity spin-1/2 state that is similar to the masses of the odd-parity states, which is an improvement upon our earlier study.

3

Search for the Θ^+ pentaquark

3.1 Introduction

The reported observations of a baryon state with strangeness $S = +1$ some 100 MeV above the NK threshold has sparked considerable interest in excited hadron spectroscopy. Because this state has minimal quark content $uudd\bar{s}$, its discovery would be the first direct evidence for baryons with an exotic quark structure — namely, baryons whose quantum numbers cannot be described in terms of a three-quark configuration alone.

3.1.1 Phenomenology

Experimental evidence for a pentaquark was reported in real [1, 41–43] and quasi-real photoproduction experiments [44], and further positive sightings were reported in K-nucleus collisions [45], pp [46] and pA [47, 48] reactions, and in neutrino [49, 50] and deep inelastic electron scattering [51], for a total of around a dozen positive results. Currently only the charge and strangeness of this state, which has been labeled Θ^+, are known; its spin, parity and isospin are as yet undetermined, although there are hints [52] that it may be isospin zero. The mass of the Θ^+ is found to be around $M_{\Theta^+} = 1540$ MeV. However, its most striking feature is its exceptionally narrow width. In most cases the width has been smaller than the experimental resolution, while analysis of NK scattering data suggests that the width cannot be greater than ~ 1 MeV [53–57]. Such a narrow state, 100 MeV above threshold, presents a challenge to most theoretical models [58–61].

Subsequently, a number of null results have been reported from e^+e^- [62–67] and $p\bar{p}$ [68] colliders, as well as from pp [69], γp [70], hadron-p [71, 72], hadron-nucleus [73], pA [74, 75], μA [76], and nucleus-nucleus [77] fixed target experiments. The production mechanism for the Θ^+ in these reactions would be via fragmentation, and although the fragmentation functions are not known, these results suggest that if the Θ^+ exists, its production mechanism, along with its quantum numbers, is exotic. In a more recent high statistics experiment [78] the CLAS collaboration reported a non-observation of the Θ^+ in contradiction to their earlier analysis [42]. We note that the more recent non-observation of the Θ^+ by the CLAS collaboration has cast some doubt about the existence of pentaquark states. For more detailed accounts of the current experimental status of pentaquark searches see Refs. [79–81].

While the experimental verification of the existence of the Θ^+, and the determination of its quantum numbers await definitive confirmation, it is timely to examine the theoretical predictions for the masses of $S = +1$ pentaquark states. Numerous model studies have been carried out recently aimed at revealing the dynamical nature of the Θ^+, ranging from chiral soliton models [82–84], QCD sum rules [85, 86], hadronic models [87, 88] and quark models [61, 89–92], to name just a few.

3.1.2 Lattice pentaquark studies

While models can often be helpful in obtaining a qualitative understanding of data, we would like to see what QCD predicts for the masses of the pentaquark states. Currently lattice QCD is the only quantitative method of obtaining hadronic properties directly from QCD, and several, mainly exploratory, studies of pentaquark masses have been performed [93–102].

A crucial issue in lattice QCD analysis of excited hadrons is exactly what constitutes a signal for a resonance. As evidence of a resonance, most lattice studies to date have sought to find the empirical mass splitting between the Θ^+ and the NK threshold at the unphysically large quark masses used in lattice simulations. This leads to the assumption that in the negative parity channel the Θ^+ will be about 100 MeV above the S-wave NK threshold at these masses. However, as we will argue below, a signal for a Θ^+ resonance on the lattice, which holds for all other (non-exotic) excited states studied on the lattice [18, 27, 103], would be the presence of binding at quark masses near the physical regime, where the resonance mass would be below the NK threshold. The evidence of binding at quark masses near the physical regime, which survives in the infinite volume limit, is a sufficient condition to indicate a resonance, but the absence of such binding cannot rigorously exclude the possibility of a resonance at the physical quark masses.

In the positive parity channel, where the N and K must be in a relative P-wave, in a finite lattice volume the energy of the NK state will typically be above the mass of the experimental Θ^+ candidate. Observation of a pentaquark mass below the P-wave NK threshold would then be a clear signal for a Θ^+ resonance. In all of the lattice studies, with the exception of Chiu & Hsieh [99], the mass of the positive parity state has been found to be too large to be interpreted as a candidate for the Θ^+.

One should note that in obtaining a relatively low mass positive parity state, Chiu & Hsieh [99] perform a linear chiral extrapolation of the pentaquark mass in m_π^2 using only the lightest few quark masses, for which the errors are relatively large. Although linear extrapolations of hadron properties are common in the literature, these invariably neglect the non-analyticities in m_π^2 arising from the long-range structure of hadrons associated with the pion cloud [104, 105]. Csikor *et al.* [93] and Sasaki [94] use a slightly modified extrapolation, in which the squared pentaquark mass is fitted and extrapolated as a function of m_π^2. As a cautionary note, since the chiral behaviour of pentaquark masses is at present unknown, extrapolation of the lattice results to physical quark masses can lead to large systematic uncertainties, which are generally underestimated in the literature.

The ordering of the NK and Θ^+ states in the negative parity channel presents some challenges for lattice analyses. Sasaki [102] and Csikor *et al.* [101] argue that if the Θ^+ is more massive than the NK threshold, then one needs to extract from the correlators more than the lightest state with which the operators have overlap. It has been suggested [102] that if one can find an operator that has negligible coupling to the NK state, then one can fit the correlation function at intermediate Euclidean times to extract the mass of the heavier state. The idea of simply choosing an operator that does not couple to the NK threshold is problematic, however, because there is no way to determine *a priori* the extent to which an operator couples to a particular state. Our approach instead will be to use a number of different interpolating fields, which will enhance the ability to couple to different states. This approach has also been adopted by Fleming [106], and by the MIT group [107].

Extracting multiple states in lattice QCD is usually achieved by performing a correlation matrix analysis, which we adopt in this work, or via Bayesian techniques. The analysis of Sasaki [94] uses a single interpolating field and employs a standard analysis with an exponential fit to the correlation function. Csikor *et al.* [93], Takahashi *et al.* [100] and Chiu & Hsieh [99] have, on the other hand, performed correlation matrix analyses using several different interpolating fields. In the negative parity sector, these authors extract from their correlation matrices both a ground state and an excited state. In all of these studies the positive parity state is found to lie significantly higher than the negative parity ground state.

Since the S-wave NK scattering state lies very near the lowest energy state observed on the lattice, the issue of extracting a genuine Θ^+ resonance from lattice simulations presents an important challenge, and a number of ideas have been proposed to distinguish between a true resonance state and the scattering of the free N and K states in a finite volume [95–98]. Using the Bayesian fitting techniques, Mathur *et al.* [95] have examined the volume dependence of the residue of the ground state, noting that each state — the pentaquark, N, and K — is volume normalised such that the residue of the NK state is proportional to the inverse spatial lattice volume. The analysis suggests that the lowest-lying state is the NK scattering state, but leaves open the question of the existence of a higher-lying pentaquark resonance state.

Using a single interpolating field, Ishii *et al.* [96,97] have introduced different boundary conditions in the quark propagators in an attempt to separate a genuine pentaquark resonance state from the NK scattering state. Here the quark propagators mix such that the effective mass of the NK scattering state changes, while the mass of a genuine resonance is unchanged. Again, the lowest-lying state displays the properties of an NK scattering state, but leaves open the issue of whether a higher-lying pentaquark resonance exists.

In identifying the nature of excited states, one should also explore the possibility that the excited state could be a two-particle state. Since we expect that our interpolating fields may couple to all possible two-particle states to some degree, we compare the results of our correlation matrix analysis to all the possible two-particle states. In the negative parity sector this includes the S-wave NK, NK^*, and ΔK^* (isospin-1 only) channels, as well as the $N'K$, where N' is the lowest positive parity excitation of the nucleon. In the positive parity channel we consider the S-wave N^*K two-particle state, where N^* is the lowest-lying negative parity excitation of the nucleon, in addition to the P-wave NK and NK^* states.

3.1.3 Lattice resonance signatures

Our approach to assessing the existence of a genuine pentaquark resonance is complementary to the aforementioned approaches. In the following we search for evidence of attraction between the constituents of the pentaquark state, which is vital to the formation of a resonance. Note that if a particle is a resonance in nature then we label it as such in our discussion.

Doing so requires careful measurement of the effective mass splitting between the pentaquark state and the sum of the free N and K masses measured on the *same lattice*. As discussed in detail below, attraction between the constituents of every baryon resonance ever calculated on the lattice [18,27,103] has been sufficient to render the resonance mass *lower* than the sum of the free decay channel masses at quark masses

near the physical regime. If the behaviour of the pentaquark is similar to that of every other resonance on the lattice, then searching for a signal of a pentaquark resonance above the NK threshold at the large quark masses typically considered in lattice QCD will mean that one is simply looking in the wrong place.

One might have some concern as to whether this lattice resonance signature should appear for exotic pentaquark states where quark-antiquark annihilation cannot reduce the quark content to a "three-quark state". Clearly the approach to the infinite quark mass limit will be different. However, the heavy quark limit is far from the quark masses explored in this investigation, which approach the physical regime. Evidence of nontrival Fock-space components (such as those including $q\bar{q}$ loops) in the hadronic wave functions is abundant. For example, the quenched and unquenched Δ masses differ by more than 100 MeV at the quark masses considered here, with the mass lying *lower* in the presence of dynamical fermions [104, 108]. We consider quark masses as light as 0.05 GeV, which is much less than the hadronic scale, 1.5 GeV, associated with pentaquark quantum numbers. In short, the traditional resonances explored in lattice QCD cannot be considered simply as "three-quark states", so that there is little reason to expect the lattice resonance signature to be qualitatively different for "ordinary" and pentaquark baryons.

In the process of searching for attraction it is essential to explore a large number of interpolating fields having the quantum numbers of the putative pentaquark state. In Sec. 3.2 we consider a comparatively large collection of pentaquark interpolating fields and create new interpolators designed to maximise the opportunity to observe attraction in the pentaquark state. We study two types of interpolating fields: those based on a nucleon plus kaon configuration, and those constructed from two diquarks coupled to an $\bar{s}$ quark.

The technical details of the lattice simulations are discussed in length in Chapter 1 and outlined briefly in Sec. 3.3. It is essential to use a form of improved action, as large scaling violations in the standard Wilson action could lead to a false signature of attraction. Recall from Chapter 1, our simulations are therefore performed with the nonperturbatively $\mathcal{O}(a)$-improved FLIC fermion action [15, 19, 34], which displays nearly perfect scaling, providing continuum limit results at finite lattice spacing [34]. The simulations are carried out on a large, $20^3 \times 40$ lattice, with the $\mathcal{O}(a^2)$–tadpole-improved Luscher-Weisz plaquette plus rectangle gauge action [13]. The lattice spacing is 0.128 fm, as determined via the Sommer scale, $r_0 = 0.49$ fm.

In Sec. 3.4 we present our results for the even and odd parity spin-$\frac{1}{2}$ pentaquark states, in both the isoscalar and isovector channels. As we will see, there is no evidence of attraction in any of the pentaquark channels considered. On the contrary, we find evidence of repulsion at finite volume, with the energy of each five-quark state lying higher than the sum of the free decay channel energies. Thus, the standard lattice resonance signature of the resonance mass lying lower than the sum of the free decay channel masses at quark masses near the physical regime is absent. As we conclude in Sec. 3.5, we find no evidence supporting the existence of a spin-$\frac{1}{2}$ pentaquark resonance in quenched QCD.

3.2 Interpolating Fields

In this section we review the interpolating fields which have been used in recent pentaquark studies, in both the QCD sum rule approach and in lattice QCD calculations. We then propose new interpolators designed to maximise the opportunity to observe attraction between the pentaquark constituents at large quark masses. Two general types of interpolating fields are considered: those based on an "NK" configuration (either nK^+ or pK^0), and those based on a "diquark-diquark-$\bar{s}$" configuration. We examine both of these types, and discuss the relations between them.

3.2.1 NK-type interpolating fields

The simplest "NK"-type interpolating field is referred herein as the "colour-singlet" form,

$$\chi_{NK} = \frac{1}{\sqrt{2}}\epsilon^{abc}(u^{Ta}C\gamma_5 d^b)\left\{u^c(\bar{s}^e i\gamma_5 d^e) \mp (u \leftrightarrow d)\right\} , \tag{3.1}$$

where the $\mp$ corresponds to the isospin $I = 0$ and 1 channels, respectively. One can easily verify that the field χ_{NK} transforms negatively under the parity transformation $q \rightarrow \gamma_0 q$, and therefore the negative parity state will propagate in the upper-left Dirac quadrant of the correlation function, contrary to the more standard "positive-parity" interpolators [103]. Note that the colour-index sum here corresponds to a "molecular" (or "fall-apart") state with both the "N" and "K" components of Eq. (3.1) colour singlets. For negative parity the field χ_{NK} couples the (*large* $\times$ *large*) $\times$ *large* $\times$ (*large* $\times$ *large*) components of Dirac spinors, and should therefore produce a strong signal. For the positive parity projection (see Sec. 3.3.1 below), it involves one lower (or small) component, coupling
(*large* $\times$ *large*) $\times$ *small* $\times$ (*large* $\times$ *large*), which is known to lead to a weaker signal in this channel [103].

Some authors [93,100] have argued that χ_{NK} is a poor choice of interpolator for accessing the pentaquark resonance, and that an interpolator that suppresses the colour-singlet NK channel may provide better overlap with a pentaquark resonance, should it exist. Csikor *et al.* [93], Mathur *et al.* [95], Takahashi *et al.* [100] and Chiu *et al.* [99] (in lattice calculations), and Zhu [86] (in a QCD sum rule calculation), have considered a slightly modified form in which the colour indices between the N and K components of the interpolating field are mixed,

$$\chi_{\widetilde{NK}} = \frac{1}{\sqrt{2}}\epsilon^{abc}(u^{Ta}C\gamma_5 d^b)\left\{u^e(\bar{s}^e i\gamma_5 d^c) \mp (u \leftrightarrow d)\right\} , \tag{3.2}$$

for $I = 0$ and 1, respectively. We refer to this alternative colour assignment as a "colour-fused" interpolator, whereby the coloured three-quark and $q\bar{q}$ pair are fused to form a colour-singlet hadron. Of course, for 1/3 of the combinations the colours e and c will coincide, so that the "colour-singlet"–"colour-singlet" state will also arise from the field $\chi_{\widetilde{NK}}$. Upon constructing the correlation functions associated with each of these interpolators, one encounters a sum of $(3! \times 3)^2 = 324$ colour combinations with a non-trivial contribution to the correlation function. However, only 1/9 of these terms will be common to the colour-singlet and colour-fused correlators.

In Zhu's QCD sum rule (QCDSR) calculation [86] interpolating fields based on the Ioffe current were also considered, such as

$$\gamma_5 \chi^{\rm QCDSR}_{\widetilde{NK}} = \frac{1}{\sqrt{2}}\epsilon^{abc}(u^{Ta}C\gamma_\mu u^b)\gamma_5\,\gamma_\mu d^e(\bar{s}^e i\gamma_5 d^c) + (u \leftrightarrow d)\ . \tag{3.3}$$

It is well known that the Ioffe current,

$$\epsilon^{abc}(u^{Ta}C\gamma_\mu\, u^b)\gamma_5\,\gamma_\mu d^c\,, \tag{3.4}$$

can be written as a linear combination of the standard lattice interpolator,

$$\epsilon^{abc}(u^{Ta}C\gamma_5\, d^b)u^c\,, \tag{3.5}$$

and an alternate interpolator whose overlap with the ground state is suppressed by a factor of ~ 100 [40]

$$\epsilon^{abc}(u^{Ta}C d^b)\gamma_5\, u^c\,. \tag{3.6}$$

In the QCD sum rule approach, the interpolator of Eq. (3.6) can be used to subtract excited state contributions, while the nucleon is accessed via the interpolator of Eq. (3.5) [40, 109]. However, in the lattice approach, the interpolator of Eq. (3.6) plays little to no role in accessing the lowest-lying state properties for either positive or negative parities [18].

3.2.2 Diquark-type interpolating fields

The other type of interpolating field which has been discussed is one in which the non-strange quarks are coupled into two sets of diquarks, together with the antistrange quark. Jaffe and Wilczek [89] suggested that the lowest energy diquark state would have two scalar diquarks in a relative P-wave coupled to the $\bar{s}$. The lowest mass pentaquark would then be one containing two scalar diquarks. The configuration of two isospin $I = 0$ diquarks gives a purely $I = 0$ interpolating field,

$$\chi_{JW} = \epsilon^{abc}\epsilon^{aef}\epsilon^{bgh}(u^{Te}C\gamma_5 d^f)(u^{Tg}C\gamma_5 d^h)C\bar{s}^{Tc}\ . \tag{3.7}$$

If the interpolating field is local, the two diquarks in χ_{JW} are identical, but because their colour indices are antisymmetrised, this field vanishes identically. The field χ_{JW} would be non-zero if the diquark fields were non-local. On the other hand, the use of non-local fields significantly increases the computational cost of lattice calculations. While this remains an important avenue to explore in future studies, in this work we focus on the construction of pentaquark operators from local fields.

A variant of the scalar field χ_{JW} can be utilised by observing that the antisymmetric tensors in Eq. (3.7) can be expanded in terms of Kronecker-δ symbols,

$$\epsilon^{abc}\epsilon^{dec} = \delta^{ad}\delta^{be} - \delta^{ae}\delta^{bd}\,, \tag{3.8}$$

which enables the interpolating field χ_{JW} to be rewritten as

$$\chi_{JW} = \epsilon^{abc}(u^{Ta}C\gamma_5 d^b)\left\{(u^{Tc}C\gamma_5 d^e) - (u^{Te}C\gamma_5 d^c)\right\}C\bar{s}^{Te}\ . \tag{3.9}$$

One can then define two interpolating fields,

$$\chi_{SS} = \frac{1}{\sqrt{2}}\epsilon^{abc}(u^{Ta}C\gamma_5 d^b)(u^{Tc}C\gamma_5 d^e)C\bar{s}^{Te} , \tag{3.10}$$

$$\chi_{\widetilde{SS}} = \frac{1}{\sqrt{2}}\epsilon^{abc}(u^{Ta}C\gamma_5 d^b)(u^{Te}C\gamma_5 d^c)C\bar{s}^{Te} , \tag{3.11}$$

which are equal but do not individually vanish. Clearly these fields transform negatively under parity, and, as with χ_{NK} and $\chi_{\widetilde{NK}}$, couple (*large* $\times$ *large*) $\times$ (*large* $\times$ *large*) $\times$ *large* components for negative parity states, making them ideal for lattice simulations [103].

To determine the isospin of χ_{SS}, one can express the second diquark as a sum of colour symmetric and antisymmetric components,

$$\chi_{SS} = \frac{1}{\sqrt{2}}\,\epsilon^{abc}(u^{Ta}C\gamma_5 d^b)\left\{\frac{1}{2}(u^{Tc}C\gamma_5 d^e - u^{Te}C\gamma_5 d^c) + \frac{1}{2}(u^{Tc}C\gamma_5 d^e + u^{Te}C\gamma_5 d^c)\right\} C\bar{s}^{Te} . \tag{3.12}$$

The first term in the braces in Eq. (3.12), which is isoscalar, is equivalent to the field χ_{JW}, and vanishes for the reasons discussed above. The second term, which does not vanish, is isovector, so that the field χ_{SS} is pure isospin $I = 1$.

An interesting question is how much, if any, overlap exists between the diquark-type field χ_{SS} and the NK-type fields in Sec. 3.2.1. This can be addressed by performing a Fierz transformation on the fields. For the field χ_{SS}, one finds:

$$\chi_{SS} = \frac{1}{4}\epsilon^{abc}(u^{Ta}C\gamma_5 d^b)\{ -(\bar{s}^e u^e)\gamma_5 d^c + (\bar{s}^e\gamma_\mu u^e)\gamma^\mu\gamma_5 d^c + \frac{1}{2}(\bar{s}^e\sigma_{\mu\nu}u^e)\sigma^{\mu\nu}\gamma_5 d^c + (\bar{s}^e\gamma_\mu\gamma_5 u^e)\gamma^\mu d^c - (\bar{s}^e\gamma_5 u^e)d^c\} . \tag{3.13}$$

The last two terms in Eq. (3.13) resemble NK-type interpolating fields, similar to those introduced in Sec. 3.2.1, while the second term corresponds to an NK^*-type configuration.

Note that for the NK-like terms in Eq. (3.13) the colour structure corresponds to the colour-singlet operator χ_{NK}. It has been suggested that the colour-singlet NK interpolating field would have significant overlap with the NK scattering state and hence not couple strongly to a pentaquark resonance. On the other hand, Fierz transforming the field $\chi_{\widetilde{SS}}$, in analogy with Eq. (3.13), would give rise to an NK-like term corresponding to the colour-fused $\chi_{\widetilde{NK}}$ operator. Since the fields χ_{SS} and $\chi_{\widetilde{SS}}$ are equivalent, however, this demonstrates that selection of the operator $\chi_{\widetilde{SS}}$ (with the colour-fused NK configuration) over the operator χ_{SS} (with the colour-singlet NK configuration) would be spurious.

Several authors [94, 96, 97, 99] have also used a variant of the field χ_{JW} in lattice simulations, in which a scalar diquark is coupled to a pseudoscalar diquark [85, 94],

$$\chi_{PS} = \epsilon^{abc}\epsilon^{aef}\epsilon^{bgh}(u^{Te}Cd^f)(u^{Tg}C\gamma_5 d^h)C\bar{s}^{Tc} . \tag{3.14}$$

In this case the two diquarks are not identical and so the field does not vanish. Since both diquarks in χ_{PS} are isoscalar, this field has isospin zero and transforms positively under parity. For positive parity it couples (*large* $\times$ *small*) $\times$ (*large* $\times$ *large*)

$\times$ *large* components of Dirac spinors and is therefore suitable for lattice simulations. For the negative parity projection, it couples (*large* $\times$ *small*) $\times$ (*large* $\times$ *large*) $\times$ *small*, so that the signal will be doubly suppressed relative to the other negative parity state interpolators. Since it has been used in the literature, for completeness we also include χ_{PS} in our analysis. To be consistent with the parity assignments of the other interpolating fields discussed above, one can use a modified form,

$$\chi_{PS} \;\rightarrow\; \gamma_5\, \chi_{PS}\ , \tag{3.15}$$

which then transforms negatively under parity. The effect of this is merely to switch the positive and negative parity components propagating in the $\{(1,1),(2,2)\}$ and $\{(3,3),(4,4)\}$ elements of the correlation function (see Chapter 1).

3.3 Lattice Techniques

In this section we discuss the techniques used to extract bound state masses in lattice calculations. We first outline the computation of two-point correlation functions, both at the baryon level, and at the quark level in terms of the interpolating fields introduced in Sec. 3.2. To study more than one interpolating field, we perform a correlation matrix analysis to isolate the individual states, and describe the basic steps in this analysis. Finally, we present some details of the lattice simulations, including the gauge and fermion actions used.

3.3.1 Two-point correlation functions

Here we reiterate the key features of our analysis of the two-point functions that we discussed at length in Chapter 1. This time our interpolators transform as pseudo-scalars under parity exchanging the locations of positive and negative parity contributions. Let us define a function, $\mathcal{G}$, of the interpolating field χ at Euclidean time t and momentum $\vec{p}$ as

$$\mathcal{G}(t,\vec{p}) \;=\; \sum_{\vec{x}} \exp(-i\vec{p}\cdot\vec{x})\, \langle 0\,|T\, \chi(x)\, \bar{\chi}(0)\,|\,0\rangle\ , \tag{3.16}$$

where we have suppressed the Dirac indices. Inserting a complete set of intermediate momentum, energy and spin states $|B,p',s\rangle$,

$$\mathcal{G}(t,\vec{p}) = \sum_{s,p',B}\sum_{\vec{x}} \exp(-i\vec{p}\cdot\vec{x})\, \langle 0|\, \chi(x)\, |B,p',s\rangle\langle B,p',s|\, \bar{\chi}(0)\, |0\rangle\ , \tag{3.17}$$

and using translational invariance, one can write the function $\mathcal{G}$ as

$$\mathcal{G}(t,\vec{p}) \;=\; \sum_{s,B} \exp(-E_B t)\, \langle 0|\, \chi(0)\, |B,p,s\rangle\langle B,p,s|\, \bar{\chi}(0)\, |0\rangle\ , \tag{3.18}$$

where $E_B = \sqrt{M_B^2 + \vec{p}^2}$ is the energy of the state $|B\rangle$ and M_B is its mass.

Despite transforming as pseudo-scalars by construction, the interpolating field χ has overlap with both positive and negative parity states. The overlap of χ with the

intermediate state $|B^{\mp}\rangle$, where the superscript denotes parity -1 or $+1$, at the source can be parameterised by a coupling strength $\lambda_{B^{\mp}}$,

$$\langle 0|\chi(0)|B^{-},p,s\rangle = \lambda_{B^-}\sqrt{\frac{M_{B^-}}{E_{B^-}}}\,u(p_{B^-},s)\;, \tag{3.19}$$

$$\langle 0|\chi(0)|B^{+},p,s\rangle = \lambda_{B^+}\sqrt{\frac{M_{B^+}}{E_{B^+}}}\,\gamma_5\,u(p_{B^+},s)\;, \tag{3.20}$$

where $E_{B^{\mp}}$ and $M_{B^{\mp}}$ correspond to the energies and masses of the negative and positive parity states, respectively. Note that in Eq. (3.20) the matrix γ_5 premultiplies the spinor $u(p_{B^+},s)$, since the interpolating fields that we use in this analysis all transform negatively under parity. This is in contrast to the more standard case where the fields have positive parity [103], in which case the definitions of $\lambda_{B^{\mp}}$ in Eqs. (3.19) and (3.20) are interchanged.

At large Euclidean times the function $\mathcal{G}$ can be written

$$\begin{aligned}\mathcal{G}(t,\vec{p}) \;\rightarrow\; & \lambda_{B^-}\bar{\lambda}_{B^-}\frac{(\gamma\cdot p_{B^-}+M_{B^-})}{2M_{B^-}}\exp(-E_{B^-}t)\\ & +\lambda_{B^+}\bar{\lambda}_{B^+}\frac{(\gamma\cdot p_{B^+}-M_{B^+})}{2M_{B^+}}\exp(-E_{B^+}t)\;,\end{aligned} \tag{3.21}$$

where p is the on-shell four-momentum vector, and $\bar{\lambda}_{B^{\mp}}$ is the coupling strength of the field $\bar{\chi}$ at the source to the state $|B^{\mp}\rangle$. In our lattice simulations the source is smeared, so that $\lambda_{B^{\mp}}$ and $\bar{\lambda}_{B^{\mp}}$ are not necessarily equal. With fixed boundary conditions in the time direction, one can project out states with definite parity using the matrix [18,110]

$$\Gamma^{\mp} = \frac{1}{2}\left(1 \pm \frac{M_{B^{\pm}}}{E_{B^{\pm}}}\gamma_4\right)\;. \tag{3.22}$$

The parity-projected two-point correlation function can then be expressed as the spinor trace of the function $\mathcal{G}(t,\vec{p})$,

$$G^{\mp}(t,\vec{p}) = \mathrm{tr}[\Gamma^{\mp}\mathcal{G}(t,\vec{p})] \tag{3.23}$$

$$= \sum_B \lambda_{B^{\mp}}\bar{\lambda}_{B^{\mp}}\exp\left(-E_{B^{\mp}}t\right)\;. \tag{3.24}$$

Because of the exponential suppression (at large Euclidean times) of states with energies greater than the ground state energy, in the large-t limit the correlation function for $\vec{p}=0$ (which we use in practice in this analysis) will be dominated by the ground state with mass $m_0^{\mp}$,

$$G^{\mp}(t,\vec{0}) \stackrel{t\rightarrow\infty}{=} \lambda_{0^{\mp}}\bar{\lambda}_{0^{\mp}}\exp\left(-M_{0^{\mp}}\right)\;, \tag{3.25}$$

where $\bar{\lambda}_{0^{\mp}}$ and $\lambda_{0^{\mp}}$ are the ground state couplings for the negative and positive parity states at the source and sink, respectively. The effective mass of the baryon $B^{\mp}$ is then defined in terms of ratios of the correlation function at successive time slices,

$$M_{\mathrm{eff}}^{\mp}(t) = \ln\left(\frac{G^{\mp}(t,\vec{0})}{G^{\mp}(t+1,\vec{0})}\right)\;. \tag{3.26}$$

In the large-t limit one therefore picks out the state with the lowest mass,

$$M_{\mathrm{eff}}^{\mp}(t) \stackrel{t\rightarrow\infty}{=} M_{0^{\mp}}\;. \tag{3.27}$$

In order to study masses of excited states, one can in principle attempt to fit the correlation function at finite t with a sum of exponentials corresponding to the ground state plus one or more excited states. In practice this is difficult. An alternative approach is to use several interpolating fields, and extract masses of an orthogonal set of operators using a correlation matrix analysis, as we discussed in Sec. 2.2.4 above.

The two-point correlation functions discussed above are all derived at the hadronic level. They can be expressed in a form suitable for actual lattice simulations by substituting the interpolating fields in Sec. 3.2 and performing the appropriate Wick contractions of the time-ordered products of fields. The general formulae for the correlation functions expressed in terms of the quark propagators can be found in Appendix D.

Six quark masses are used in the calculations, and the strange quark mass is taken to be the third largest ($\kappa = 0.12885$) quark mass in each case. At this κ the $s\bar{s}$ pseudoscalar mass is 697 MeV, which compares well with the experimental value of $\sqrt{2M_K^2 - M_\pi^2} = 693$ MeV motivated by leading order chiral perturbation theory. The smallest pion mass considered is $m_\pi = 464$ MeV. We have also considered two smaller masses, but find that the signal for these becomes quite noisy, and do not include them in the analysis. The analysis for the NK-type interpolators is based on a sample of 200 configurations and the analysis for the PS and SS-type interpolators is based on an ensemble of 340 configurations. The error analysis is performed by a second-order, single-elimination jackknife, see Sec. 4.2.1, with the χ^2 per degree of freedom obtained via covariance matrix fits, see Appendix C.

3.4 Results and Discussion

In this section we present the results of our lattice simulations of pentaquark masses, in both the $J^P = \frac{1}{2}^-$ and $\frac{1}{2}^+$ channels, and for isospin $I = 0$ and 1. In addition to extracting the masses, we also study the mass differences between the candidate pentaquark states and the free two-particle states. This analysis is actually crucial in determining the nature of the states observed on the lattice, and the identification of true resonances.

3.4.1 Signatures of a resonance

At sufficiently small quark masses, the standard lattice technology will find, at large Euclidean times, the NK decay channel as the ground state of all the five-quark interpolating fields discussed in Sec. 3.2. In previous analyses of pentaquark masses, the observation of a signal at a mass slightly above the NK threshold has been interpreted [93, 94] as a candidate for a pentaquark resonance. A test that has proven useful in studies of excited baryons is a search for binding as a function of the quark mass. The presence of binding at quark masses near the physical regime has been observed in every lattice study of the N^* spectrum in every channel. This feature is central to the study of the electromagnetic properties of decuplet baryons [111] and their transitions [112–114] in lattice QCD.

As an example, consider the $J^P = \frac{1}{2}^-$ odd parity partner of the nucleon, namely the $N^*(1535)$ baryon, in lattice QCD. In the continuum, the $N^*(1535)$ is a resonance which decays to a nucleon and a pion. On the lattice, however, the $N^*(\frac{1}{2}^-)$ is stable at the (unphysically) large quark masses where its mass is smaller than the sum of

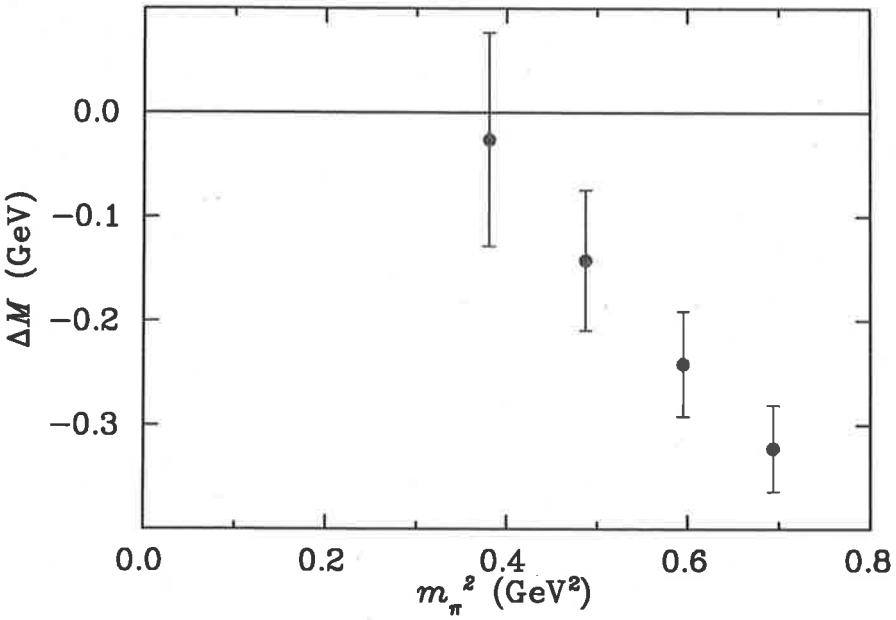

Fig. 3.1: Mass difference between the lowest-lying negative parity excited nucleon bound state, the $I(J^P) = \frac{1}{2}(\frac{1}{2}^-)$ $N^*(1535)$, and the S-wave $N+\pi$ two-particle scattering state.

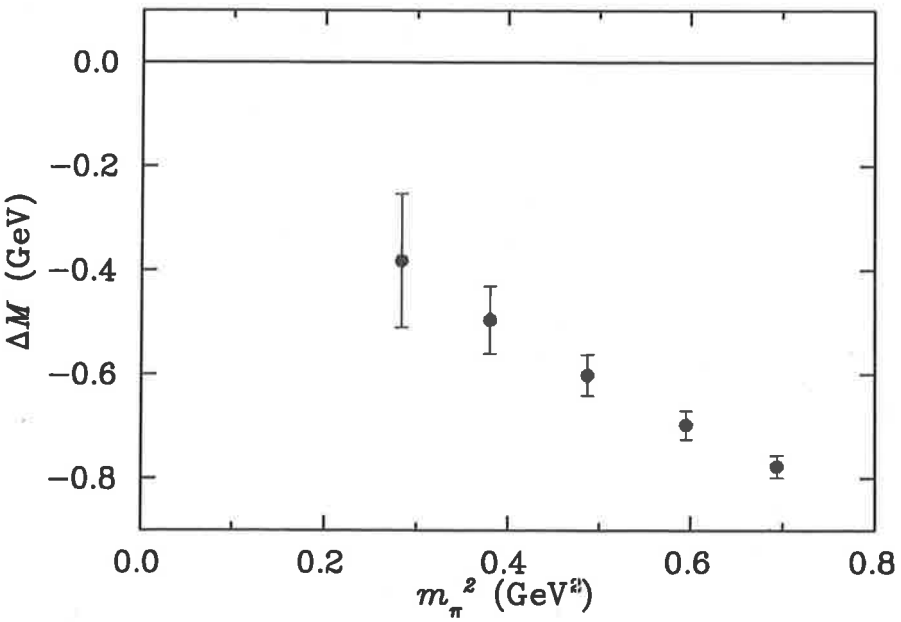

Fig. 3.2: Mass difference between the $I(J^P) = \frac{3}{2}(\frac{3}{2}^+)$ $\Delta(1232)$ and the P-wave $N + \pi$ two-particle scattering state.

the nucleon and pion masses [18]. To illustrate this we show in Fig. 3.1 the mass splitting between the $N^*(\frac{1}{2}^-)$ and the non-interacting S-wave $N+\pi$ two-particle state, calculated on the same lattice. For all values of m_π illustrated the mass of the $N^*(\frac{1}{2}^-)$ is below that of the $N+\pi$. The mass difference clearly increases in magnitude with increasing m_π.

In other words, the binding becomes stronger at larger quark masses. This trend is expected to continue into the heavy quark mass regime, where quark counting rules can be considered. As the $N^*(1535)$ has a three-quark Fock space component, and the $N+\pi$ must contain at least five quarks, the mass ratio $M(3q)/M(5q)$ will approach $3/5$ in the infinite quark mass regime.

A similar behaviour is also observed in the case of the $\Delta(1232)$ isobar. The mass difference between the $J^P = \frac{3}{2}^+$ resonance and the lowest available P-wave $N+\pi$ two-particle energy, shown in Fig. 3.2, is negative, and, as in Fig. 3.1, increases with m_π^2. In fact, this pattern is repeated in every other baryon channel probed in lattice QCD, such as the $J^P = \frac{1}{2}^+$ and $\frac{3}{2}^-$ channels (see, e.g., Refs. [18,27,103]). In the case of the Δ and $N^*(\frac{1}{2}^-)$ baryons featured here, the binding is seen to become stronger at larger quark masses. Indeed, from the minimal quark content in the heavy quark limit, one expects to recover a resonance to $N\pi$ mass ratio of $3/5$. In the case of a pentaquark resonance, the analogous mass ratio will be 1 in the heavy quark limit and the mass splitting will vanish relative to the hadronic mass scale in the heavy quark limit. Hence a lattice resonance signature which might be observed for a pentaquark resonance is binding (a negative mass splitting) at quark masses near the physical regime, with a general trend of binding as a fraction of hadron mass towards zero as the heavy quark limit is approached.

3.4.2 Negative parity isoscalar states

We begin our discussion of the results with the isospin-0, negative parity states. The lowest energy of a system with a nucleon and a kaon would have the N and K in a relative S-wave, in which case the overall parity is negative. Isoscalar states can be constructed with the NK-type interpolating fields, χ_{NK} and $\chi_{\widetilde{NK}}$, as well as with the PS-type field χ_{PS}.

The effective mass for the colour singlet χ_{NK} field is shown in Fig. 3.3 for several representative pion masses. The results for the colour fused operator $\chi_{\widetilde{NK}}$ of Fig. 3.4 are very similar to those for χ_{NK}. (Note that to avoid clutter in the figures we do not show the points at the larger t values which have larger error bars, and have little influence on the fits.) To determine whether these operators have significant overlap with more than one state, a correlation matrix analysis is performed. However, we find that it is not possible to improve the ground state mass as described in Sec. 2.2.4. Consequently the results using the standard (*i.e.*, non-correlation matrix) analysis techniques are reported in this channel. For comparison, in Fig. 3.5 we also show the effective mass of the negative parity χ_{PS} diquark-type field. As expected, because of the presence of two smaller components of Dirac spinors in χ_{PS} compared with χ_{NK} and $\chi_{\widetilde{NK}}$, the signal here is much noisier than for either of the NK-type fields. This is despite the fact that almost twice as many configurations are used for the χ_{PS} than for the NK-type fields.

The pentaquark masses are extracted by fitting the effective masses in Figs. 3.3–3.5 over appropriate t intervals, chosen according to the criterion that the χ^2 per degree of freedom is less than 1.5, and preferably close to 1.0. For the χ_{NK} and $\chi_{\widetilde{NK}}$ fields,

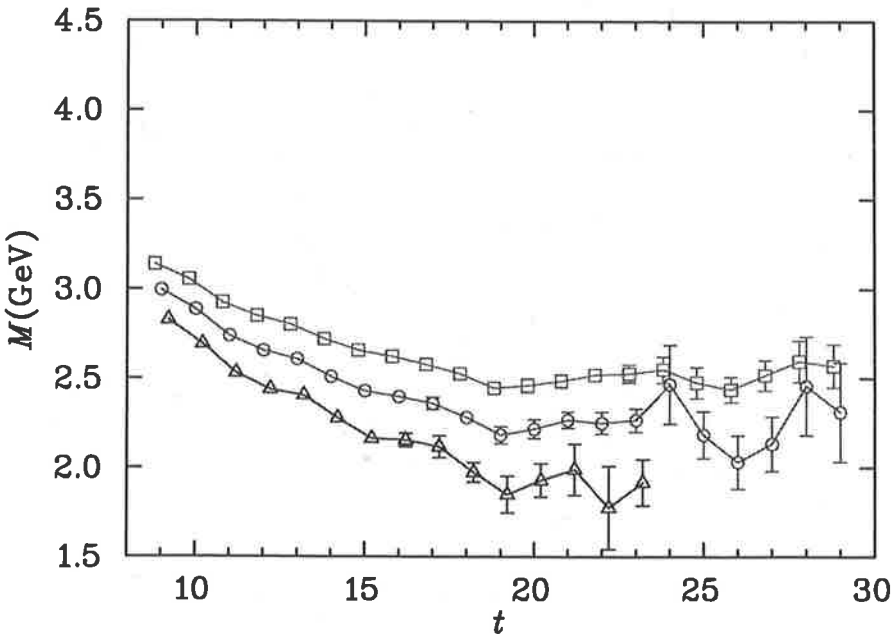

Fig. 3.3: Effective mass of the $I(J^P) = 0(\frac{1}{2}^-)$ colour singlet NK-type pentaquark interpolator, χ_{NK}. The data correspond to $m_\pi \simeq 830$ MeV (squares), 700 MeV (circles), and 530 MeV (triangles).

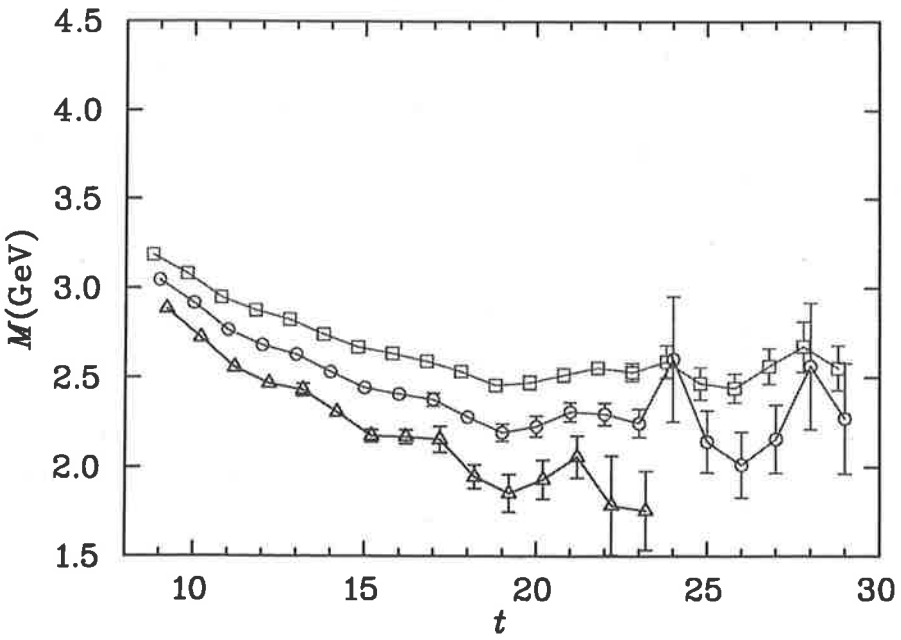

Fig. 3.4: As in Fig. 3.3, but for the $I(J^P) = 0(\frac{1}{2}^-)$ colour fused NK-type pentaquark interpolator, $\chi_{\widetilde{NK}}$.

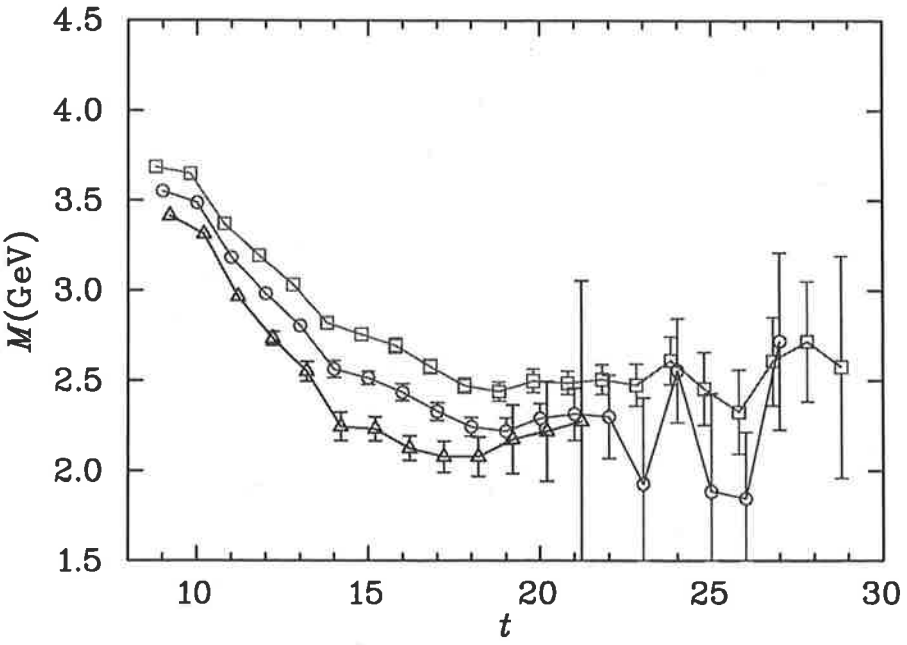

Fig. 3.5: As in Fig. 3.3, but for the $I(J^P) = 0(\frac{1}{2}^-)$ PS-type pentaquark interpolator, χ_{PS}.

fitting the effective mass in the window $t = 19 - 23$ is found to optimise the χ^2/dof. For the χ_{PS} field, the signal is lost at slightly earlier times, and consequently we fit in the time interval $t = 18 - 20$. The results for the masses corresponding to the χ_{NK}, $\chi_{\widetilde{NK}}$ and χ_{PS} fields are tabulated in Table 3.1.

The pentaquark masses are compared with masses of several two-particle states, which are reported in Table 3.2. The lowest-energy two-particle states in the $I(J^P) = 0(\frac{1}{2}^-)$ channel are the S-wave $N + K$, the S-wave $N + K^*$, the P-wave $N^* + K$, where N^* is the lowest negative parity excitation of the nucleon, and the S-wave $N' + K$, where N' is the first positive-parity excited state of the nucleon. The contributions to the correlation function from the P-wave states are likely to be suppressed, however, because there is a contribution to the P-wave signal from two *small* components of the spinors. We therefore focus on the S-wave states in Table 3.2.

The positive parity N' state, which is calculated from the interpolating field χ_2, is known to have poor overlap with the nucleon ground state, as well as with the low-lying $\frac{1}{2}^+$ excitations, such as the Roper $N^*(1440)$. In fact, it gives a mass greater than ~ 2 GeV, significantly above the low-lying $\frac{1}{2}^+$ excitations [18]. We expect, therefore, that our pentaquark fields will not have strong overlap with the $N' + K$ state either.

The results for the extracted masses from Table 3.1 are displayed in Fig. 3.6 as a function of m_π^2. The masses of the pentaquark states extracted from the χ_{NK}, $\chi_{\widetilde{NK}}$ and χ_{PS} fields agree within the errors (the χ_{NK} and $\chi_{\widetilde{NK}}$ masses in particular are very close), although the errors on the χ_{PS} become large at the smaller quark masses. The pentaquark masses are either consistent with or lie above the mass of the lowest two-particle state, namely the S-wave $N + K$, for all of the quark masses considered.

The mass differences ΔM between the low-lying pentaquark states and the two-particle scattering states can be better resolved by fitting the effective mass for the mass difference directly. This allows for cancellation of systematic errors since the pentaquark and two-particle states are generated from the same gauge field configura-

Table 3.1: The pion mass and the masses of the $I(J^P) = 0(\frac{1}{2}^-)$ states extracted with the colour singlet NK, colour fused $\widetilde{NK}$ and PS-type pentaquark interpolating fields for various values of κ.

aM_π	aM_{NK}	$aM_{\widetilde{NK}}$	aM_{PS}
0.540(1)	1.612(17)	1.625(16)	1.601(21)
0.500(1)	1.539(17)	1.553(16)	1.532(23)
0.453(1)	1.449(20)	1.461(20)	1.458(27)
0.400(1)	1.349(28)	1.361(29)	1.396(37)
0.345(2)	1.236(50)	1.245(48)	1.372(72)
0.300(2)	1.145(67)	1.138(80)	1.442(171)

Table 3.2: Masses of the S-wave $N + K$, $N + K^*$, $\Delta + K^*$ and $N' + K$ two-particle states.

aM_π	$aM^{\text{S-wave}}_{N+K}$	$aM^{\text{S-wave}}_{N+K^*}$	$aM^{\text{S-wave}}_{\Delta+K^*}$	$aM^{\text{S-wave}}_{N'+K}$
0.540(1)	1.553(10)	1.762(14)	1.893(13)	2.180(27)
0.500(1)	1.485(11)	1.704(16)	1.848(14)	2.136(32)
0.453(1)	1.404(13)	1.635(19)	1.799(16)	2.092(39)
0.400(1)	1.314(18)	1.561(26)	1.751(19)	2.061(54)
0.345(2)	1.216(32)	1.485(41)	1.709(24)	2.056(87)
0.300(2)	1.130(52)	1.421(68)	1.682(29)	2.093(144)

Table 3.3: Mass differences between the $I(J^P) = 0(\frac{1}{2}^-)$ states extracted with the NK and PS-type pentaquark interpolating fields and the S-wave $N + K$ two-particle state.

aM_π	$aM_{NK} - aM^{\text{S-wave}}_{N+K}$	$aM_{PS} - aM^{\text{S-wave}}_{N+K}$
0.540(1)	0.056(9)	0.051(19)
0.500(1)	0.052(11)	0.052(21)
0.453(1)	0.048(13)	0.060(25)
0.400(1)	0.043(17)	0.086(37)
0.345(2)	0.025(30)	0.148(75)
0.300(2)	-0.011(67)	0.286(177)

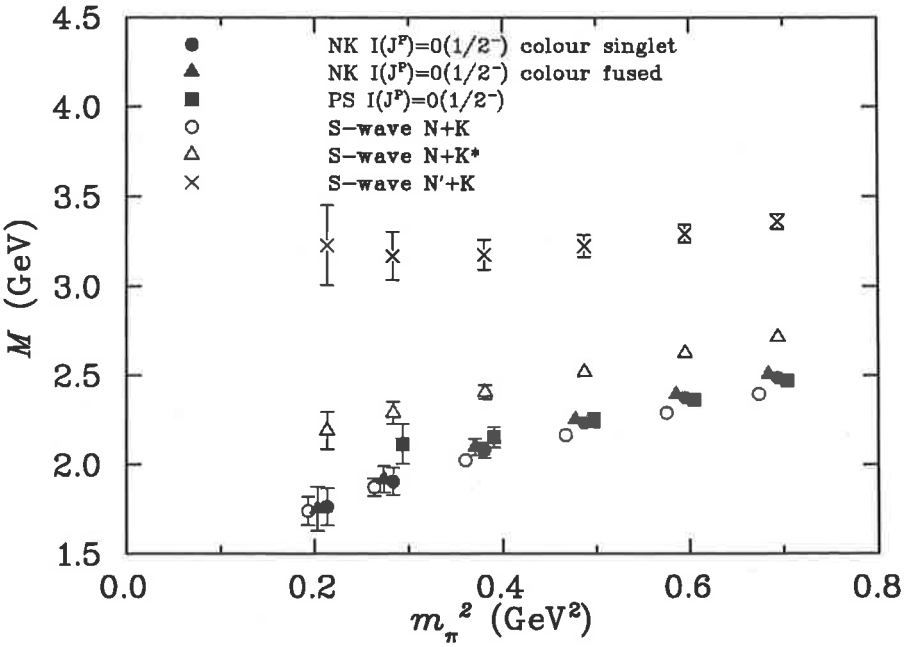

Fig. 3.6: Masses of the $I(J^P) = 0(\frac{1}{2}^-)$ states extracted with the colour singlet NK, colour fused $\widetilde{NK}$ and PS-type pentaquark interpolating fields as a function of m_π^2. For comparison, the masses of the S-wave $N + K$, $N + K^*$ and $N' + K$ two-particle states are also shown. Some of the points have been offset horizontally for clarity.

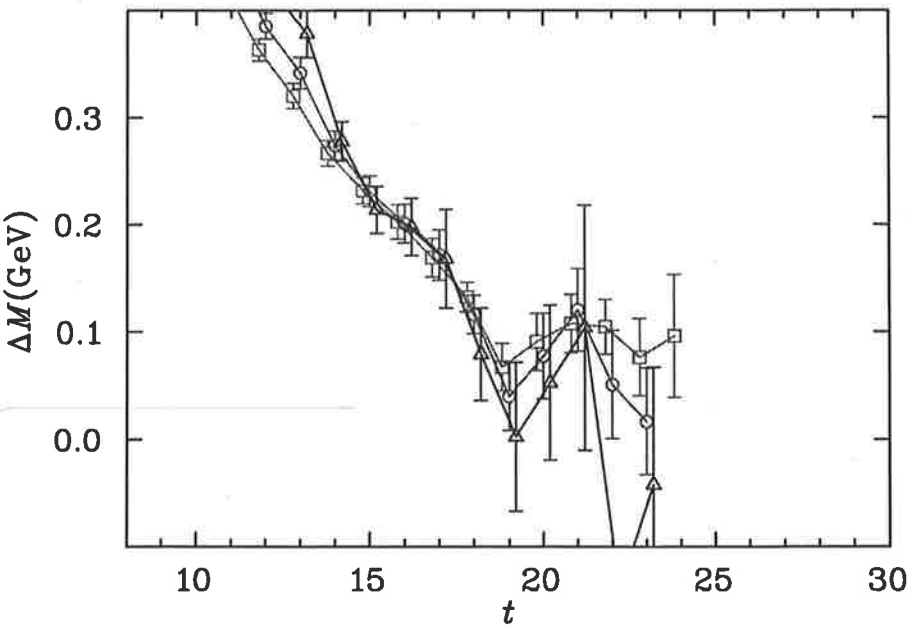

Fig. 3.7: Effective mass difference between the $I(J^P) = 0(\frac{1}{2}^-)$ state extracted with the colour singlet NK-type pentaquark interpolator, χ_{NK}, and the S-wave $N + K$ two-particle state. The data correspond to $m_\pi \simeq 830\,\text{MeV}$ (squares), 700 MeV (circles), and 530 MeV (triangles).

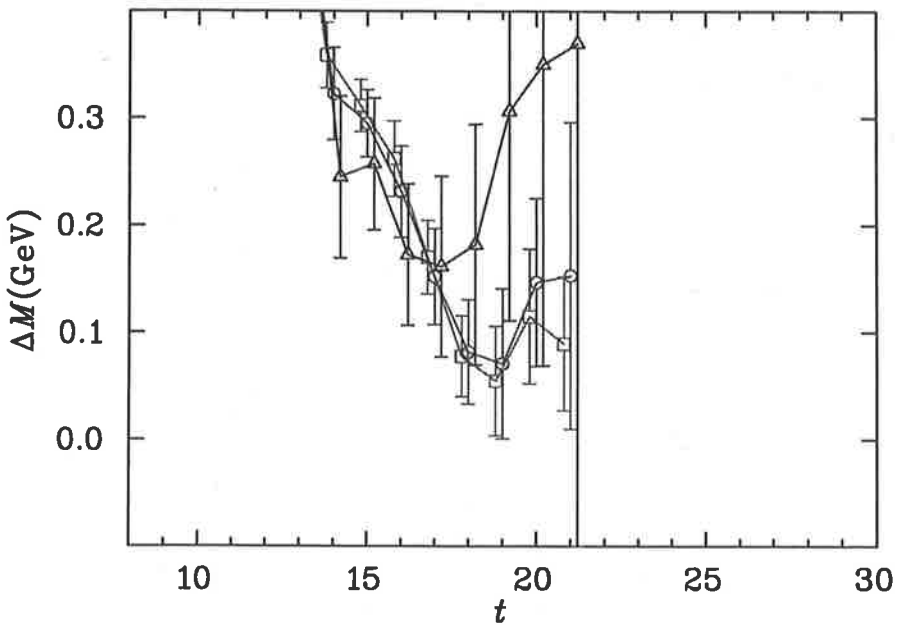

Fig. 3.8: As in Fig. 3.7, but for the $I(J^P) = 0(\frac{1}{2}^-)$ PS-type interpolating field, χ_{PS}.

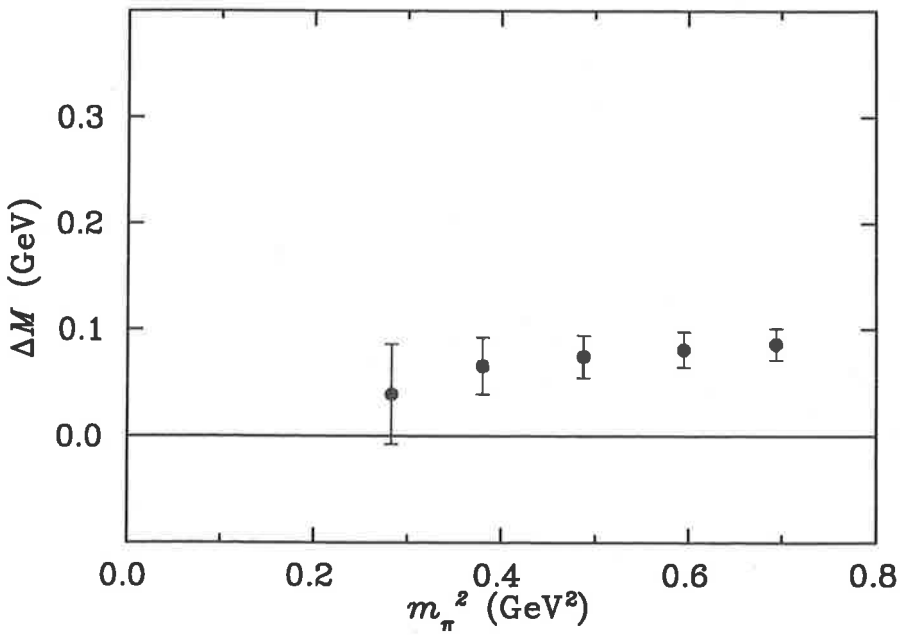

Fig. 3.9: Mass difference between the $I(J^P) = 0(\frac{1}{2}^-)$ state extracted with the NK-type pentaquark interpolating field and the S-wave $N + K$ two-particle state.

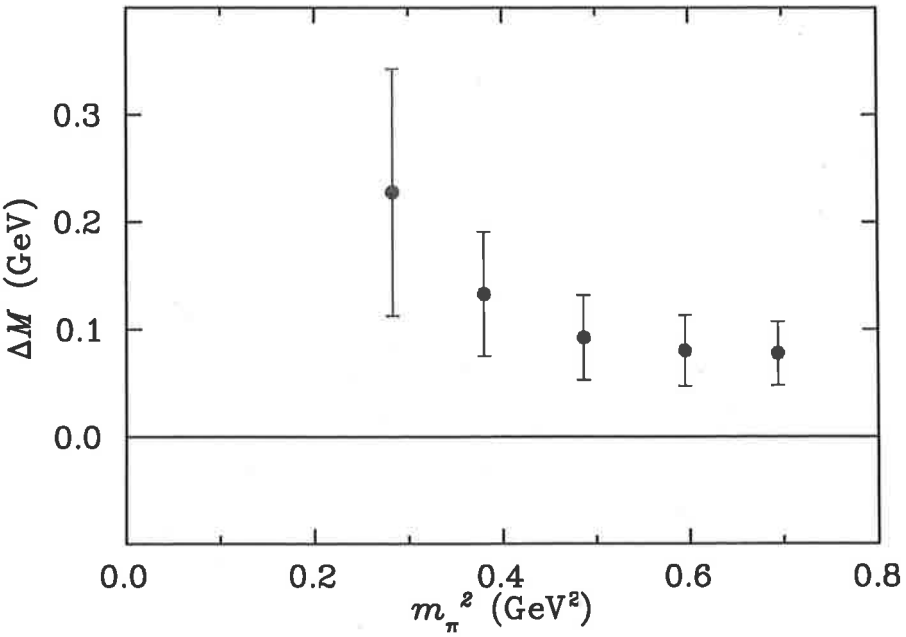

Fig. 3.10: Mass difference between the $I(J^P) = 0(\frac{1}{2}^-)$ state extracted with the PS-type pentaquark interpolating field and the S-wave $N + K$ two-particle state.

tions, and hence their systematic errors are strongly correlated. Figures 3.7 and 3.8 illustrate the effective mass plots for the mass differences. Note that the scale of these figures is enlarged by a factor of six compared with Figs. 3.3–3.5. The mass difference between the state extracted from the colour singlet NK interpolator and the S-wave $N + K$ two-particle state is fitted at time slices $t = 19 - 21$, while that between the PS extracted state and the $N + K$ state is fitted at $t = 18 - 20$.

The results of the mass difference analysis are presented in Table 3.3, and in Figs. 3.9 and 3.10 for the χ_{NK} and χ_{PS} fields, respectively. We see clearly that the masses derived from the NK pentaquark operator are consistently higher than the lowest-mass two-particle state. The mass difference ΔM is ~ 100 MeV at the larger quark masses, and weakly dependent on m_π^2. Note the size of the error bars for the mass difference is reduced compared with the error bars on the masses in Fig. 3.6.

Since the difference between the reported experimental Θ^+ mass and the physical $N + K$ continuum is ~ 100 MeV, naively one may be tempted to interpret the results in Figs. 3.8 and 3.9 as a signature of the Θ^+ on the lattice. On the other hand, the positive mass difference observed in this range of pion mass differs from what is seen for all the N^* states studied on the lattice. This suggests that the observed signal is unlikely to be a pentaquark. Indeed, the volume dependent analysis in Ref. [95] concluded that their signal, which is consistent with our results, corresponds to an NK scattering state.

3.4.3 Negative parity isovector states

For the isospin-1, negative parity sector, we consider three operators which can create $I(J^P) = 1(\frac{1}{2}^-)$ states: the isovector combinations of the colour singlet χ_{NK} and colour fused $\chi_{\widetilde{NK}}$, and the SS-type operator, χ_{SS}. As for the isoscalar case, we perform a 2×2 correlation matrix analysis for the NK-type fields, and here we do find improved

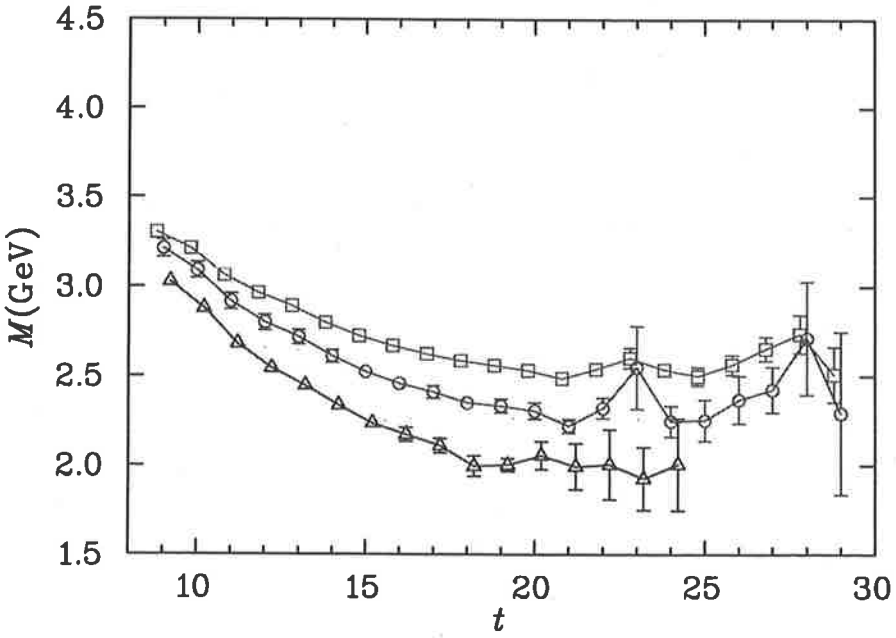

Fig. 3.11: Effective mass of the $I(J^P) = 1(\frac{1}{2}^-)$ state corresponding to the NK-type pentaquark "state 1" for several values of m_π, $m_\pi \simeq 830\,\text{MeV}$ (squares), 700 MeV (circles), and 530 MeV (triangles).

access to the lowest lying state.

Using the paradigm for optimising the results described in Sec. 2.2.4, we perform the correlation matrix analysis for the largest 4 quark masses starting at $t = 20$ with $\Delta t = 3$. Here the ground state mass is found to be lower with the correlation matrix than with the standard analysis, indicating that the contamination of the ground state from excited states is reduced. For the second lightest quark mass we fit at $t = 18$, and for the lightest quark mass at $t = 17$, with $\Delta t = 3$ in both cases. For these two lightest quark masses, the ground state mass is not lowered, so here the standard analysis techniques are used. For the excited state, the masses from the correlation matrix are all higher than with the naive analysis for all quark masses, thus improving the analysis.

The effective masses for the two projected NK-type correlation matrix states, which we refer to as "state 1" (for the ground state) and "state 2" (for the excited state), are shown in Figs. 3.11 and 3.12, respectively. For comparison, we also show the effective mass plot for the SS-type field χ_{SS} in Fig. 3.13. The ground state mass extracted with the NK-type interpolator is fitted at time slices $t = 22 - 26$, while the mass extracted with the SS-type interpolator is fitted at time slices $t = 19 - 28$.

The resulting extracted masses are tabulated in Table 3.4 and shown in Fig. 3.14. A clear mass splitting of ~ 400 MeV is seen between the ground state and the excited state for the NK-type operators. The ground state mass is consistent with that obtained from the χ_{SS} operator for the four smallest quark masses, but is slightly smaller for the two largest quark masses. As for the isoscalar channel, the ground state masses are either consistent with or slightly above the masses of the lowest two-particle state, the S-wave $N + K$. The excited state lies slightly above the S-wave two-particle $N + K^*$ threshold, which suggests that it may be an admixture of $N+K^*$ and $\Delta+K^*$ scattering states.

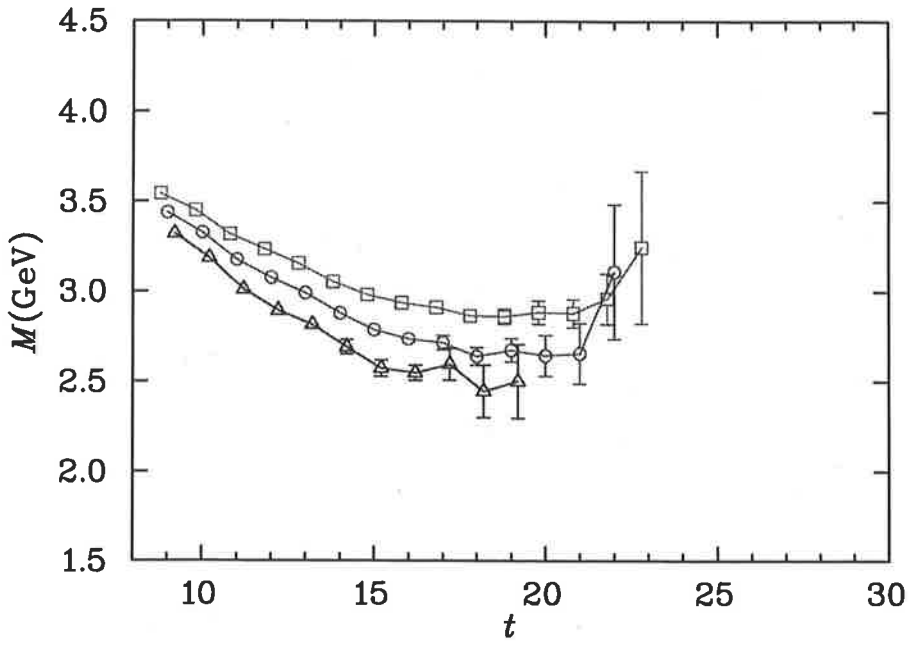

Fig. 3.12: As in Fig. 3.11, but for the $I(J^P) = 1(\frac{1}{2}^-)$ NK-type pentaquark "state 2".

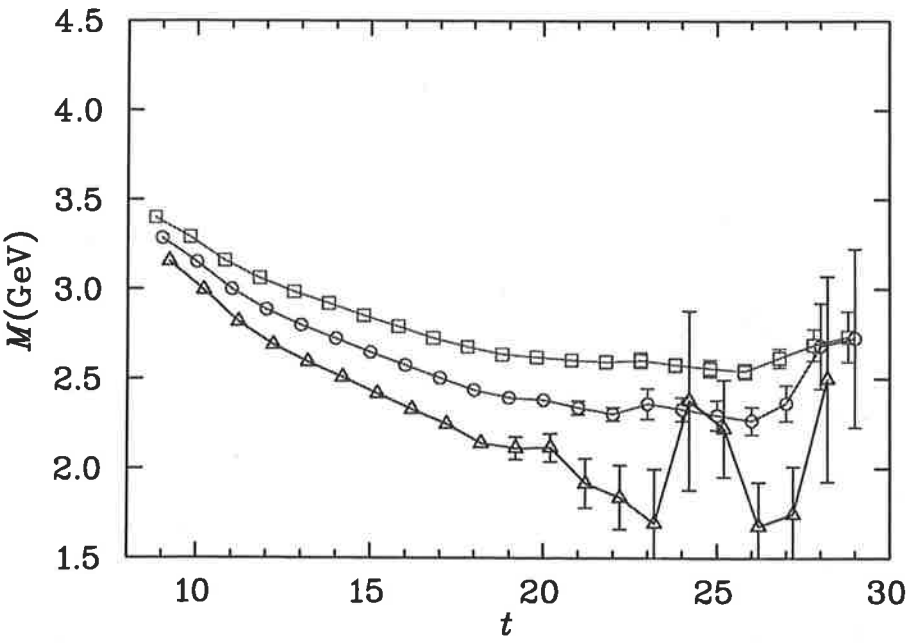

Fig. 3.13: As in Fig. 3.11, but for the $I(J^P) = 1(\frac{1}{2}^-)$ SS-type interpolator, χ_{SS}.

Table 3.4: Masses of the $I(J^P) = 1(\frac{1}{2}^-)$ states extracted with the NK and SS-type pentaquark interpolating fields for various values of κ.

aM_π	$aM_{NK(1)}$	$aM_{NK(2)}$	aM_{SS}
0.540(1)	1.649(15)	1.859(22)	1.692(8)
0.500(1)	1.578(18)	1.797(25)	1.619(9)
0.453(1)	1.497(27)	1.720(31)	1.530(11)
0.400(1)	1.408(48)	1.629(47)	1.434(16)
0.345(2)	1.313(66)	1.577(77)	1.334(26)
0.300(2)	1.251(144)	1.554(175)	1.245(51)

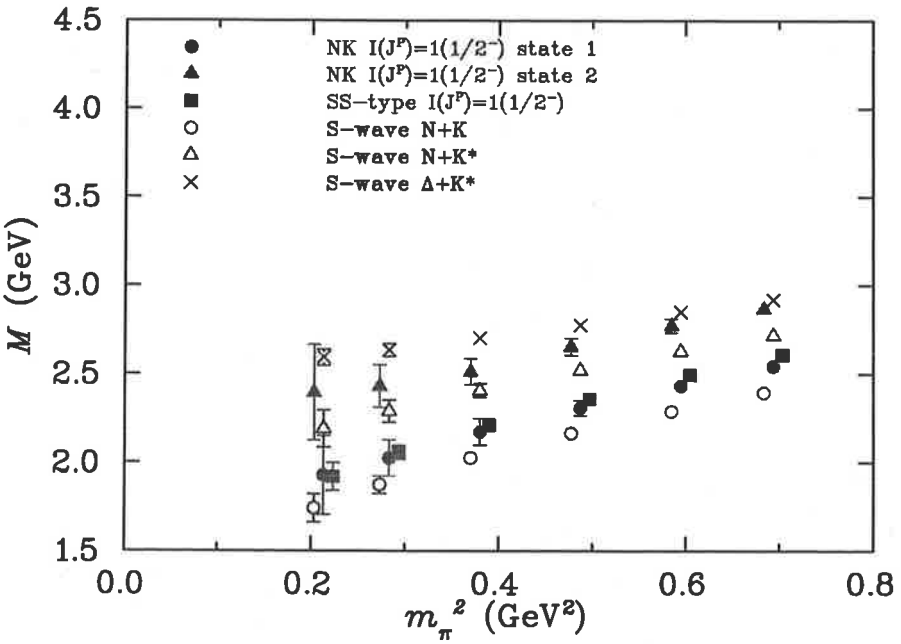

Fig. 3.14: Masses of the $I(J^P) = 1(\frac{1}{2}^-)$ states extracted with the NK and SS-type pentaquark interpolating fields as a function of m_π^2, compared with the masses of the S-wave $N + K$, $N + K^*$ and $\Delta + K^*$ two-particle states. Some of the points have been offset horizontally for clarity.

Table 3.5: Mass differences between the $I(J^P) = 1(\frac{1}{2}^-)$ states extracted with the NK and SS-type pentaquark interpolating fields and the S-wave $N+K$, $N+K^*$ and $N+K$ two-particle states, respectively.

aM_π	$aM_{NK(1)} - aM_{N+K}^{\text{S-wave}}$	$aM_{NK(2)} - aM_{N+K^*}^{\text{S-wave}}$	$aM_{SS} - aM_{N+K}^{\text{S-wave}}$
0.540(1)	0.067(9)	0.109(16)	0.100(11)
0.500(1)	0.063(13)	0.106(18)	0.090(15)
0.453(1)	0.059(21)	0.099(24)	0.071(20)
0.400(1)	0.056(35)	0.082(39)	0.048(26)
0.345(2)	-0.006(53)	0.102(76)	-0.030(78)
0.300(2)	-0.161(223)	0.146(176)	-0.021(75)

The fitted mass differences between the pentaquark and two-particle state effective masses are summarised in Table 3.5, where we quote the differences between the NK-type "state 1" and the S-wave $N+K$, between the NK-type "state 2" and the S-wave $N+K^*$, and between the SS-type and the S-wave $N+K$. These mass differences are illustrated in Figs. 3.15, 3.16 and 3.17, for the three cases, respectively. As for the isoscalar channel, the mass differences for the ground state are clearly positive, and weakly dependent on m_π^2. For both the NK-type and SS-type ground states, the pentaquark masses are $\sim$ 100 MeV larger than the S-wave $N+K$ two-particle state. Similarly, the difference between the excited NK-type pentaquark and the S-wave $N+K^*$ is $\sim$ 150 MeV and approximately constant with m_π^2. Again, the small positive ΔM, observed on our finite volume lattice, could be a signature of repulsion in this channel. There is thus no evidence of attraction and hence no indication of a resonance in the $I(J^P) = 1(\frac{1}{2}^-)$ channel which could be interpreted as the Θ^+.

3.4.4 Positive parity isoscalar states

While each of the pentaquark operators considered above transforms negatively under parity, they nevertheless couple to both negative and positive parity states, as discussed in Sec. 3.3.1. Here we consider whether any of the operators χ_{NK}, $\chi_{\widetilde{NK}}$ or χ_{PS} couple to a bound state in the isospin-0, positive parity channel. We compare the pentaquark states with the masses of the lowest energy two-particle states, which correspond to the P-wave $N+K$ and $N+K^*$, and the S-wave N^*+K states.

A two-particle state in a relative P-wave can be constructed on the lattice by adding one unit of lattice momentum ($p = 2\pi/L$) to the effective mass, $E_{\text{eff}} = \sqrt{M_{\text{eff}}^2 + p^2}$, of each particle. This effectively raises the mass of the two-particle state relative to a positive parity pentaquark. This finite volume effect will clearly aid in the search for a bound pentaquark state below the lowest P-wave scattering state.

As in the negative parity channel, we perform a correlation matrix analysis using the two NK-type fields in order to isolate possible excited states. While the analysis suggests the presence of an excited state, the signal in the positive parity channel is

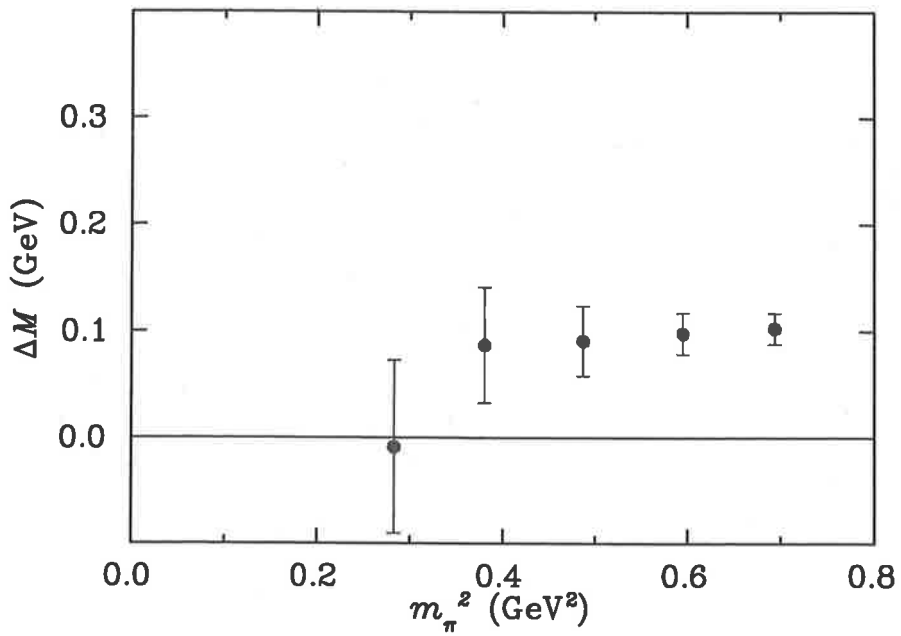

Fig. 3.15: Mass difference between the $I(J^P) = 1(\frac{1}{2}^-)$ state corresponding to the NK-type pentaquark "state 1" and the S-wave $N + K$ two-particle state.

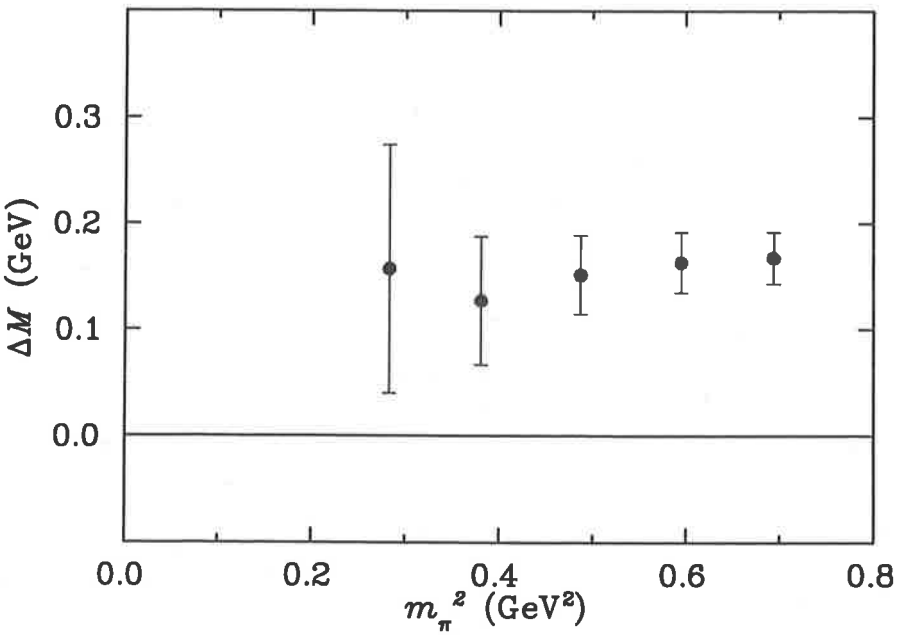

Fig. 3.16: Mass difference between the $I(J^P) = 1(\frac{1}{2}^-)$ state corresponding to the NK-type pentaquark "state 2" and the S-wave $N + K^*$ two-particle state.

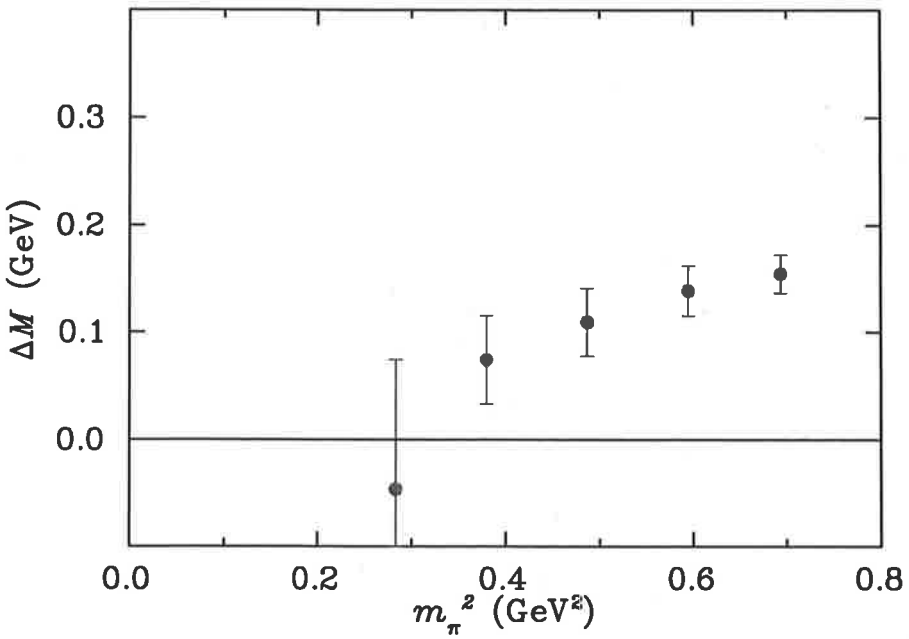

Fig. 3.17: Mass difference between the $I(J^P) = 1(\frac{1}{2}^-)$ state extracted with the SS-type pentaquark interpolating field and the S-wave $N + K$ two-particle state.

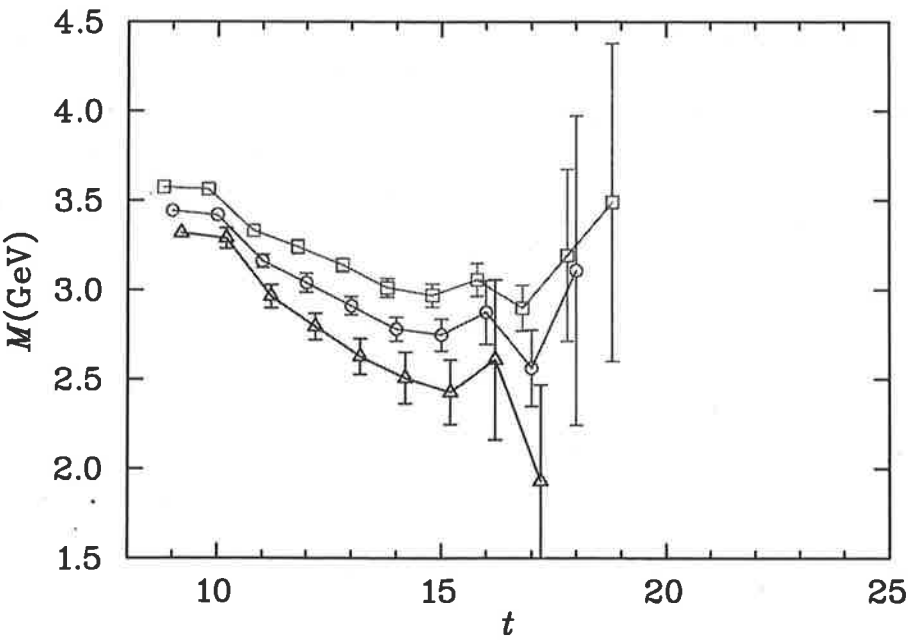

Fig. 3.18: Effective mass of the $I(J^P) = 0(\frac{1}{2}^+)$ colour singlet NK-type pentaquark interpolator, χ_{NK}, for $m_\pi \simeq 830\,\text{MeV}$ (squares), 700 MeV (circles) and 530 MeV (triangles).

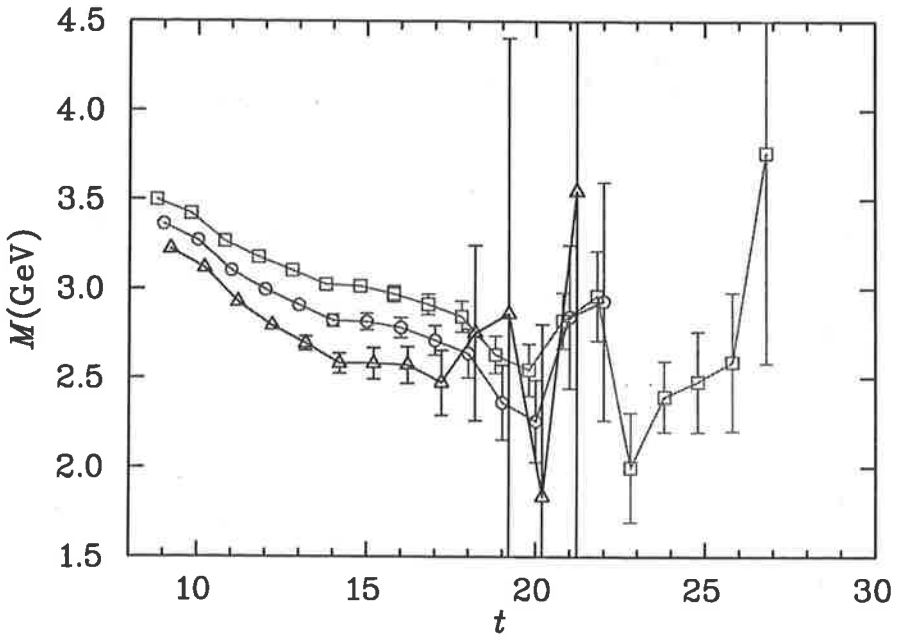

Fig. 3.19: As in Fig. 3.18, but for the $I(J^P) = 0(\frac{1}{2}^+)$ PS-type pentaquark interpolator, χ_{PS}.

considerably more noisy than for negative parity. Consequently, in practice for this channel we revert to the standard analysis method and extract only the ground state. Since the colour singlet and colour fused operators return the same ground state mass, we present the results for the colour singlet operator since the signal here is less noisy.

The effective masses for the NK and PS-type interpolators are shown in Figs. 3.18 and 3.19, respectively. The signal clearly becomes noisier at earlier times, and we fit the effective masses for the NK-type field at $t = 15 - 17$, while those for the PS-type interpolator are fit at $t = 19 - 21$.

The results are tabulated in Table 3.6 and shown in Fig. 3.20. The masses of the positive parity states extracted with the NK and PS-type interpolating fields are very different. The mass extracted with the NK-type interpolator is similar to both the S-wave $N^* + K$ mass and P-wave $N + K^*$ energy, whereas the mass extracted with the PS-type interpolator is consistent with the P-wave $N + K$ energy, which are given in Table 3.8. The signal obtained with the PS-type interpolator is rather noisy where we fit the effective masses, and we therefore only present results for the four largest quark masses for this operator. As mentioned in Sec. 3.4.2, the reason the signal is so poor is that our operators do not couple strongly to the P-wave states due to the additional *small* component of the interpolating field spinors contributing to this state.

For the differences between the pentaquark and two-particle state masses, we also fit the effective masses at $t = 15 - 17$ for the NK-type field, and $t = 19 - 21$ for the PS-type field. The results are shown in Table 3.8, and in Figs. 3.21 and 3.22 for the differences between the masses extracted with the (NK and PS-type) pentaquark interpolating fields and the P-wave $N + K$ two-particle state. The mass obtained with the NK-type field is $\sim$ 300 MeV heavier than the lowest energy two-particle state (P-wave $N + K$) for all quark masses considered. The mass obtained with the PS-type field is consistent with the the lowest energy two-particle state (P-wave $N + K$) for all quark masses considered. Once again this suggests that there is no binding in the

Table 3.6: Masses of the $I(J^P) = 0(\frac{1}{2}^+)$ states extracted with the colour singlet NK, and PS-type pentaquark interpolating fields for various values of κ.

aM_π	aM_{NK}	aM_{PS}
0.540(1)	1.935(40)	1.721(57)
0.500(1)	1.867(50)	1.642(76)
0.453(1)	1.782(66)	1.547(119)
0.400(1)	1.681(90)	1.458(207)
0.345(2)	1.561(126)	...
0.300(2)	1.421(170)	...

Table 3.7: The masses of the P-wave $N+K$, $N+K^*$ and the S-wave N^*+K two-particle states.

aM_π	$aM_{N+K}^{\text{P-wave}}$	$aM_{N+K^*}^{\text{S-wave}}$	$aM_{N^*+K}^{\text{S-wave}}$
0.540(1)	1.692(7)	1.891(27)	1.873(9)
0.500(1)	1.629(8)	1.830(32)	1.818(9)
0.453(1)	1.558(8)	1.760(39)	1.755(10)
0.400(1)	1.483(10)	1.684(53)	1.690(11)
0.345(2)	1.414(13)	1.594(85)	1.631(14)
0.300(2)	1.363(17)	1.433(134)	1.588(17)

Table 3.8: Mass differences between the $I(J^P) = 0(\frac{1}{2}^+)$ states extracted with the colour singlet NK and PS-type pentaquark interpolating fields and the P-wave $N+K$ two-particle state.

aM_π	$aM_{NK} - aM_{N+K}^{\text{P-wave}}$	$aM_{PS} - aM_{N+K}^{\text{P-wave}}$
0.540(1)	0.228(38)	0.035(57)
0.500(1)	0.223(48)	0.021(78)
0.453(1)	0.209(65)	0.003(122)
0.400(1)	0.183(90)	-0.003(210)
0.345(2)	0.132(128)	...
0.300(2)	0.040(174)	...

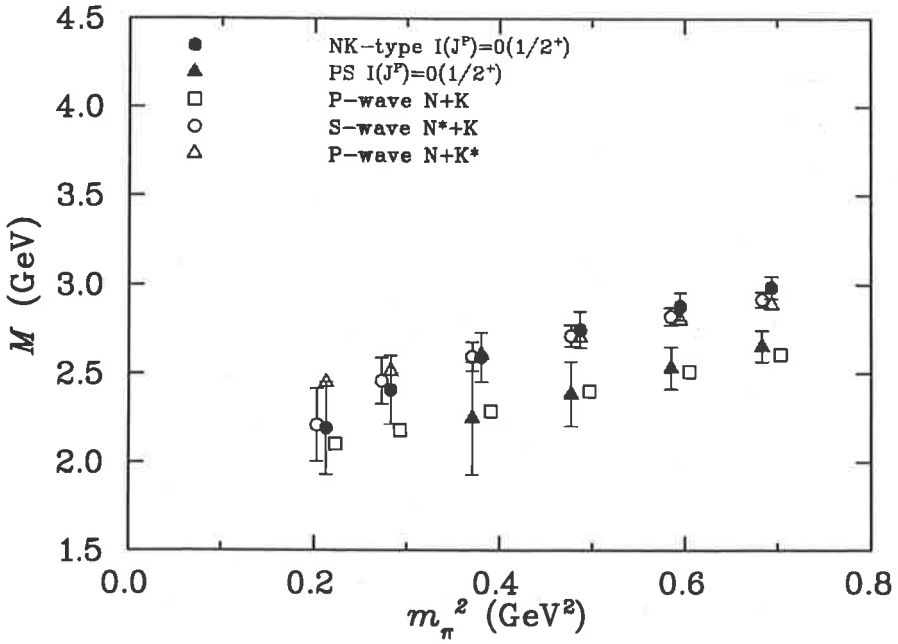

Fig. 3.20: Masses of the $I(J^P) = 0(\frac{1}{2}^+)$ states extracted with the colour singlet NK and PS-type pentaquark interpolating fields as a function of m_π^2. For comparison, the masses of the P-wave $N + K$ and $N + K^*$ and S-wave $N^* + K$ two-particle states are also shown. Some of the points have been offset horizontally for clarity.

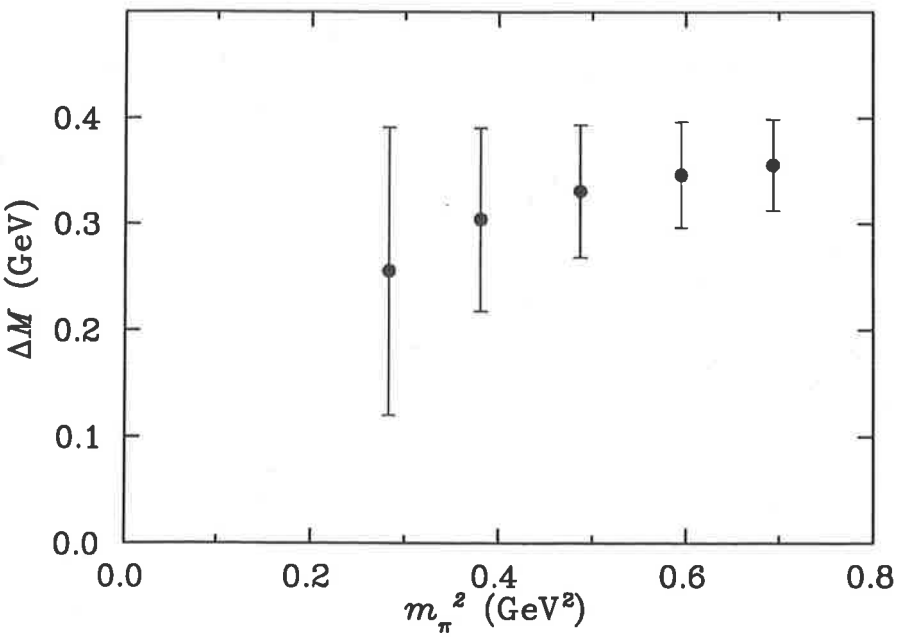

Fig. 3.21: Mass difference between the $I(J^P) = 0(\frac{1}{2}^+)$ state extracted with the NK-type pentaquark interpolating field and the P-wave $N + K$ two-particle state.

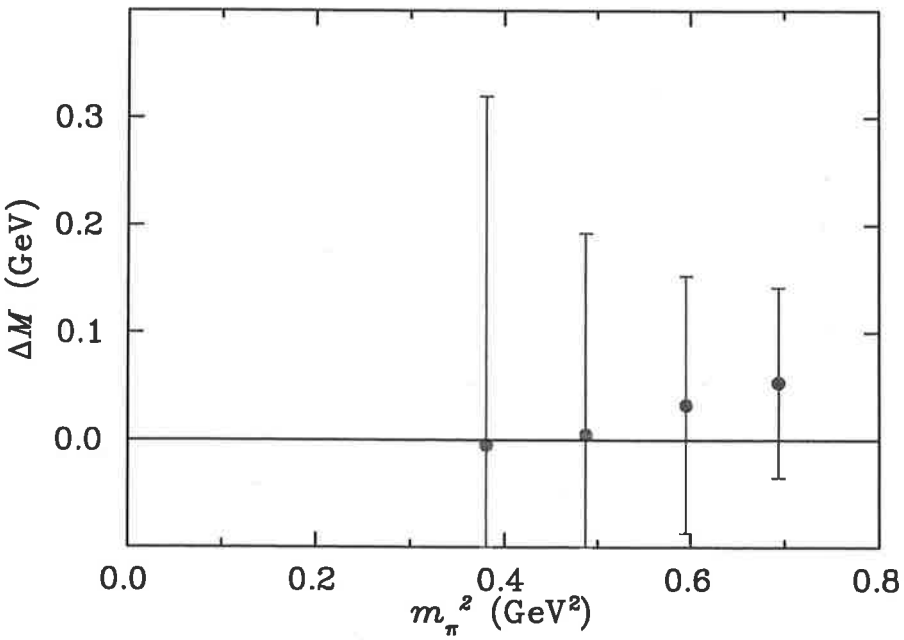

Fig. 3.22: Mass difference between the $I(J^P) = 0(\frac{1}{2}^+)$ state extracted with the PS-type pentaquark interpolating field and the P-wave $N + K$ two-particle state.

Table 3.9: Masses of the $I(J^P) = 1(\frac{1}{2}^+)$ states extracted with the colour singlet NK and SS-type pentaquark interpolating fields for various values of κ.

aM_π	aM_{NK}	aM_{SS}
0.540(1)	1.732(48)	1.956(133)
0.500(1)	1.651(57)	1.939(158)
0.453(1)	1.536(71)	1.954(214)

$I(J^P) = 0(\frac{1}{2}^+)$ channel, and hence no indication of a Θ^+ resonance.

3.4.5 Positive parity isovector states

For the isovector, positive parity channel analysis, we find that the correlation matrix does not produce improved results for the ground state masses compared with the standard analysis. In the case of the largest three κ values the algorithm requires that we step back three or more time slices before the correlation matrix analysis works. The use of a correlation matrix analysis on these data is inappropriate due to large errors in the data.

The effective masses for the NK-type and SS-type interpolating fields are illustrated in Figs. 3.23 and 3.24, respectively. Because the signal for the positive parity is rather more noisy than in the corresponding negative parity channel, we only show the effective mass for the smallest and third-smallest values of κ. For the NK-type pentaquarks, the colour-singlet χ_{NK} and colour-fused $\chi_{\widetilde{NK}}$ fields are found to access the same ground state, and in Fig. 3.23 we show only the results of the former.

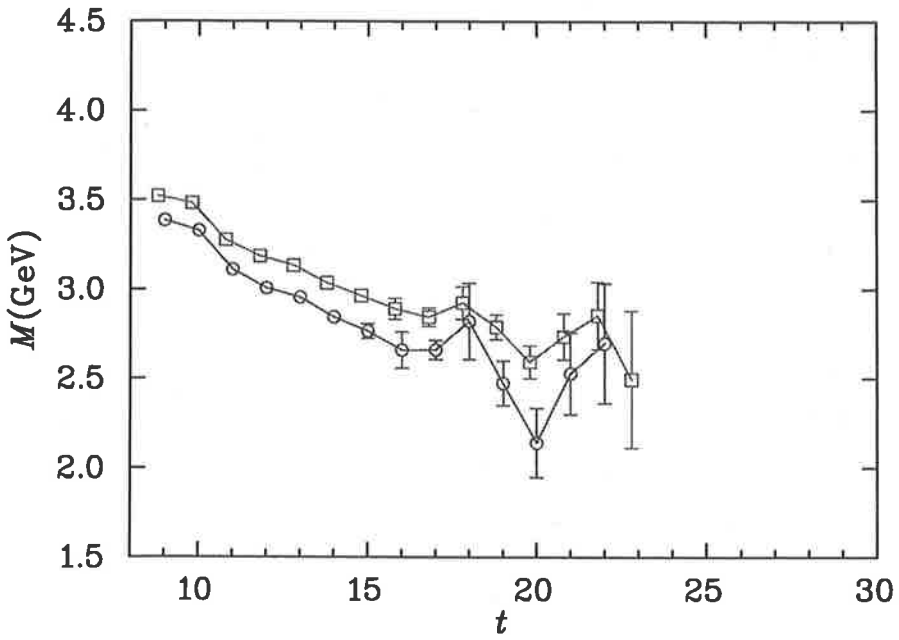

Fig. 3.23: Effective mass of the $I(J^P) = 1(\frac{1}{2}^+)$ colour singlet NK-type pentaquark interpolator, χ_{NK}. The data correspond to $m_\pi \simeq 830\,\mathrm{MeV}$ (squares) and $700\,\mathrm{MeV}$ (circles).

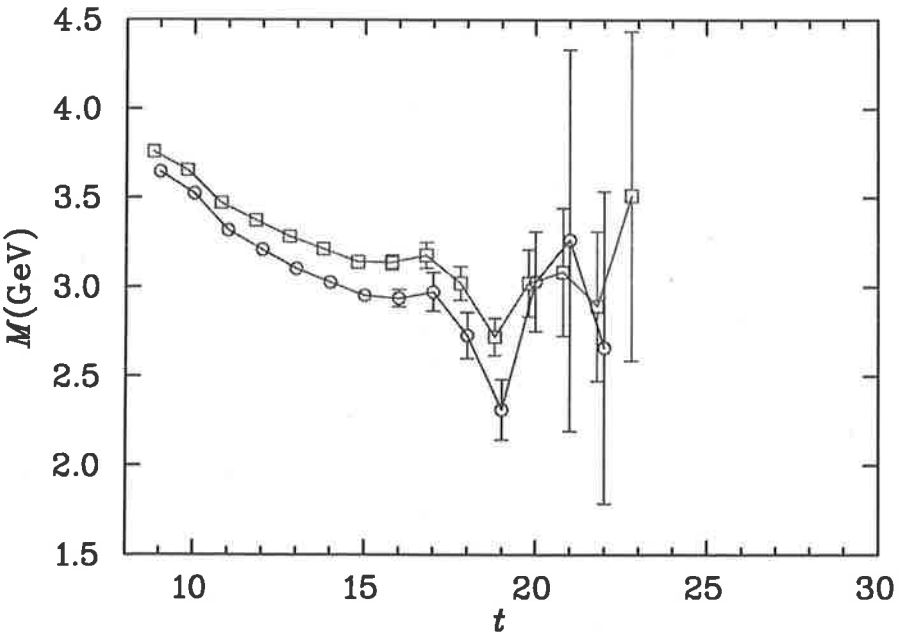

Fig. 3.24: As in Fig. 3.23, but for the $I(J^P) = 1(\frac{1}{2}^+)$ SS-type pentaquark interpolator, χ_{SS}.

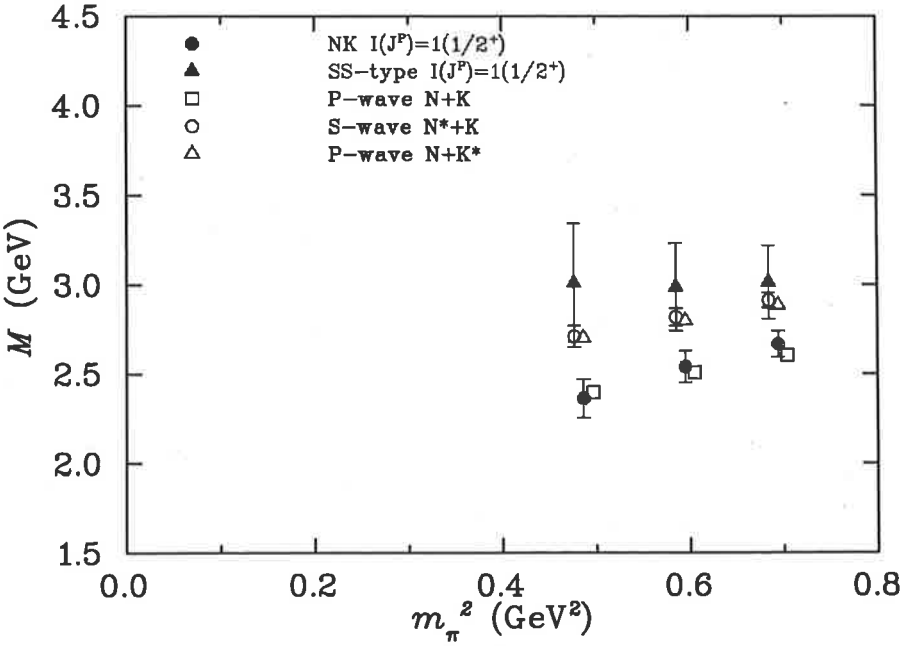

Fig. 3.25: Masses of the $I(J^P) = 1(\frac{1}{2}^+)$ states extracted with the colour singlet NK and SS-type pentaquark interpolating fields as a function of m_π^2. For comparison, the masses of the P-wave $N + K$, S-wave $N^* + K$ and P-wave $N + K^*$ two-particle states are also shown. Some of the points have been offset horizontally for clarity.

The effective masses for the NK and SS-type interpolators are fitted at time slices $t = 20 - 22$ for the three largest quark masses. The results for the extracted masses and the corresponding two-particle states are shown in Table 3.9 and in Fig. 3.25. The ground state masses for the NK and SS-type fields are again very different. The mass extracted with the NK-type interpolator is consistent with the P-wave $N + K$ energy, whereas the mass extracted with the SS-type interpolator is consistent with both the S-wave $N^* + K$ mass and P-wave $N + K^*$ energy.

The results of the mass splitting analysis are shown in Table 3.10, and illustrated in Figs. 3.26 and 3.27. The mass difference between the NK and SS-type pentaquarks and the P-wave $N + K$ two-particle state is positive for the largest quark masses suggesting possible repulsion associtated with finite volume effects. In all cases, the masses exhibit the opposite behaviour to that which would be expected in the presence of binding. We therefore do not see any indication of a resonance that could be interpreted as the Θ^+ in this channel.

3.4.6 Comparison with previous results

To place our results in context, we summarise here the results of earlier lattice calculations of pentaquark masses, and compare those with the findings of this analysis. Table 3.11 presents a concise summary of published lattice simulations, together with the results of this analysis, including the actions and interpolating fields used, analysis methods employed, and some remarks on the results. In every case, the general features of the simulation results are consistent with our findings.

The isoscalar negative parity channel was originally presented by Csikor *et al.* [93] and Sasaki [94] as a candidate for the Θ^+. We therefore summarise in Fig. 3.28 the

Table 3.10: Mass differences between the $I(J^P) = 1(\frac{1}{2}^+)$ states extracted with the colour singlet NK and SS-type pentaquark interpolating fields and P-wave $N + K$ two-particle state.

aM_π	$aM_{NK} - aM_{N+K}^{\text{P-wave}}$	$aM_{SS} - aM_{N+K}^{\text{P-wave}}$
0.540(1)	0.093(43)	0.135(58)
0.500(1)	0.079(53)	0.117(61)
0.453(1)	0.034(70)	0.084(69)

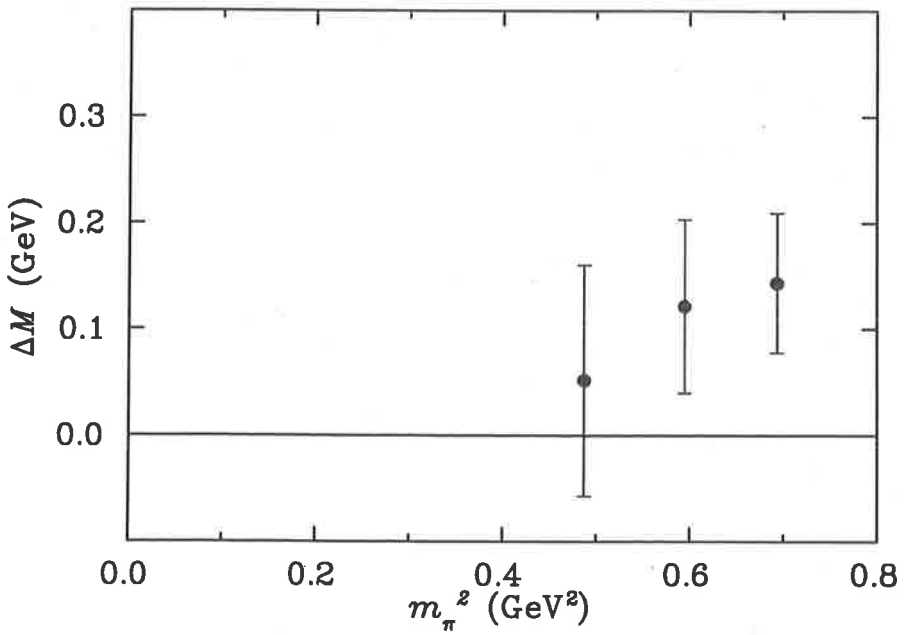

Fig. 3.26: Mass difference between the $I(J^P) = 1(\frac{1}{2}^+)$ state extracted with the NK-type pentaquark interpolating field and the P-wave $N + K$ two-particle state.

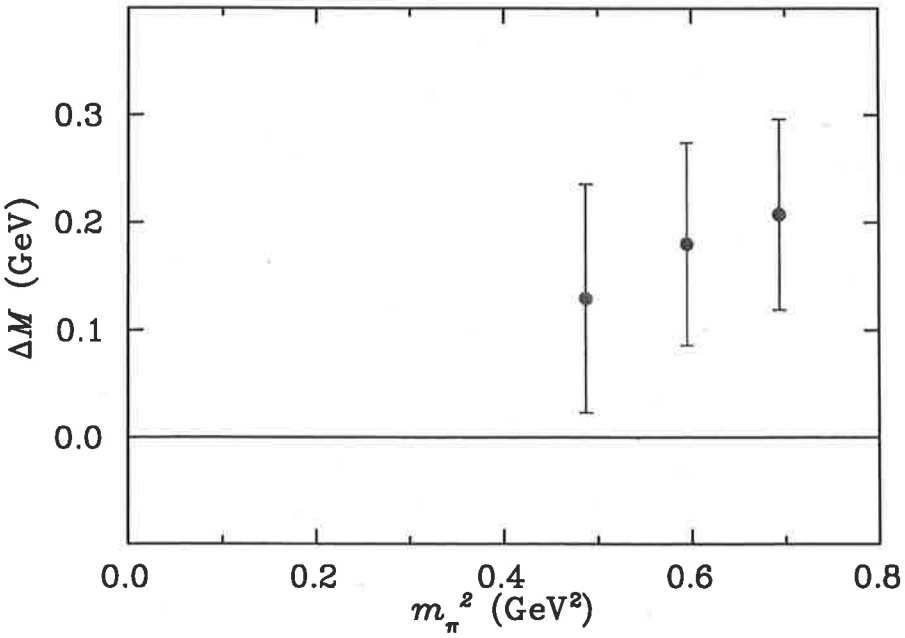

Fig. 3.27: Mass difference between the $I(J^P) = 1(\frac{1}{2}^+)$ state extracted with the SS-type pentaquark interpolating field and the P-wave $N + K$ two-particle state.

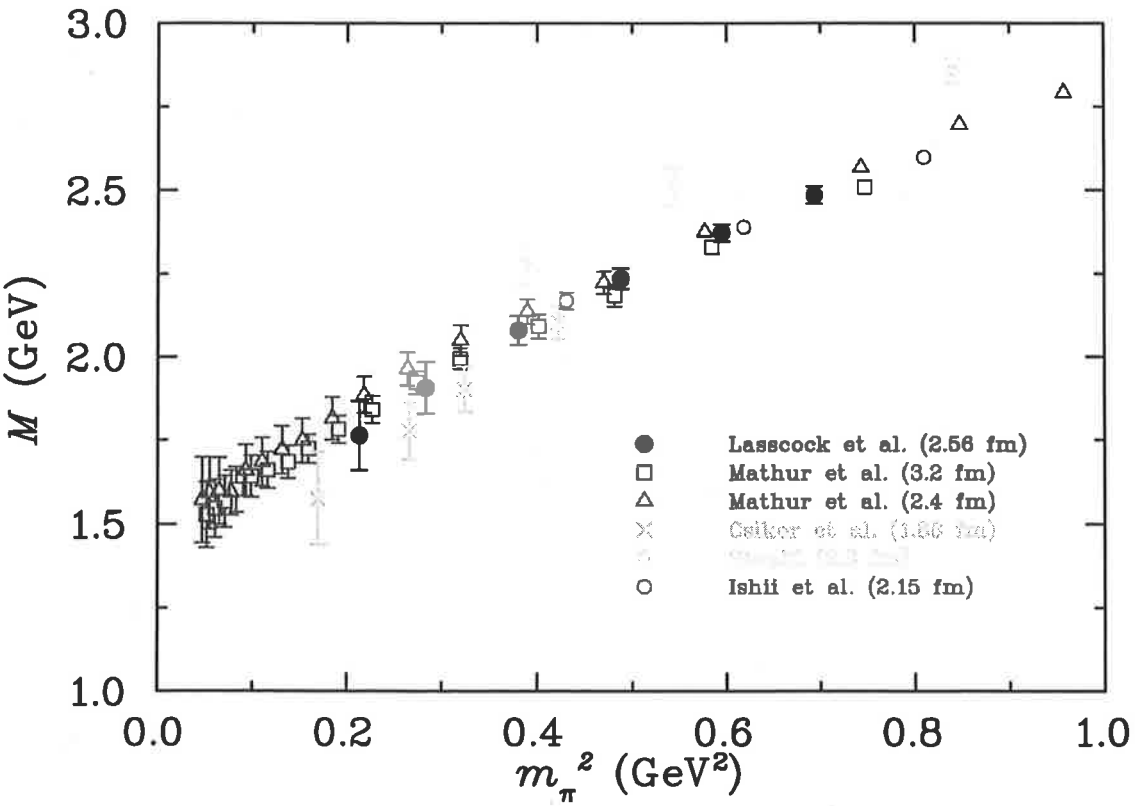

Fig. 3.28: Compilation of results for the lowest-lying $I(J^P) = 0(\frac{1}{2}^-)$ state from lattice QCD pentaquark studies.

results in this channel from the previous lattice simulations. At the larger quark masses the results of our analysis are in excellent agreement with those of Mathur *et al.* [95], Csikor *et al.* [93] and Ishii *et al.* [96,97]. In our analysis, and also in that of Mathur *et al.* [95], improved fermion actions were used, and the results are in agreement at the smaller quark masses. The results from Csikor *et al.* [93] lie slightly lower than the others at small quark masses, which may be due to scaling violations of the Wilson fermion action.

The central issue in all of these analyses is the interpretation of the data. The earlier work of Csikor *et al.* [93] and Sasaki [94] identified the $0(\frac{1}{2}^-)$ channel as a possible candidate for the Θ^+ based on naive linear extrapolations and comparison of quenched QCD with experiment. Later work by Mathur *et al.* [95] analysed the volume dependence of the couplings of the operators to this state and determined that the lowest energy state in this channel was an $N + K$ scattering state. Using hybrid boundary conditions Ishii *et al.* [96,97] also found that this was an $N + K$ scattering state. Our work is consistent with the findings of both of these studies.

3.5 Summary

We have performed a comprehensive analysis of interpolating fields holding the promise to provide good overlap between the QCD vacuum and low-lying pentaquark states. In the region of pion mass which we are able to access, we see no evidence of the attraction that would be associated with the existence of a resonance. This is in contrast with what has been seen for all baryon resonances studied in lattice QCD. Rather, evidence of repulsion may be inferred from the correlation functions giving rise to the lowest-lying five-quark states. It will be essential to explore the volume dependence of this repulsion, as described by Luscher [115, 116], to unambiguously establish the absence or existence of a pentaquark resonance in lattice QCD.

The observation of repulsion is particularly evident in the $I(J^P) = 1(\frac{1}{2}^-)$ state and in the more precise results for the $0(\frac{1}{2}^-)$ state. Similarly, both positive parity states show a positive mass splitting between five-quark and two-particle states, again suggesting repulsion as opposed to attraction. Moreover, in every case where an interpolating field was constructed to favor $J^P = \frac{1}{2}^+$ states, which are more exotic than the colour-singlet pairing of K and N, the approach to the lowest-lying state was compromised. In most cases, the same ground state mass was recovered in the correlation function analysis, but with increased error bars. This provides further evidence that the lowest-lying state is simply an NK scattering state.

An interesting extension of this work would be to consider non-local interpolating fields. In particular the correlator of the P-wave scalar-scalar diquark interpolating field inspired by Jaffe and Wilczek [89] could be explored (see also Ref. [117]).

In the case of the $I(J^P) = 1(\frac{1}{2}^-)$ state, the colour-fused NK interpolator of Eq. (3.2) had sufficient overlap with an exited state to allow a successful correlation matrix analysis. Similarly, the exotic colour-fused NK interpolating failed to produce evidence of the attraction one might expect if a pentaquark existed. The scalar diquark-type interpolating field of Eq. (3.10) also produced effective masses that lie higher than those recovered from the colour-singlet NK-type interpolating field of Eq. (3.1). Again, a low-lying pentaquark state was not observed. In short, evidence supporting the existence of a spin-$\frac{1}{2}$ pentaquark resonance was not found in quenched QCD over the quark mass range and interpolating fields considered.

This result makes it clear that a similar analysis in full dynamical-fermion QCD is essential to resolving the fate of the putative pentaquark resonance. We have resolved mass splittings of the order of 100 MeV, and one might wonder what effect the dynamics of full QCD could have on this state. As differences between baryon masses in full and quenched QCD of order 100 MeV or more have been observed [104], one cannot yet rule out the possible existence of a pentaquark in full QCD.

Table 3.11: Summary of published lattice QCD pentaquark studies, including the fields used, a brief description of the analysis techniques, and some observations from the work.

Group	Action	Operators	Analysis methods	Observations
Lasscock *et al.*	FLIC	χ_{NK}, $\chi_{\widetilde{NK}}$, χ_{SS}, χ_{PS}	2×2 correlation matrix; mass splittings analysis with NK, NK^*	$I(J^P) = 1(\frac{1}{2}^{\pm})$ NK scattering states; $I(J^P) = 0(\frac{1}{2}^{-})$ NK scattering state; $0(\frac{1}{2}^{+})$ N^*K scattering state
Csikor *et al.* [93]	Wilson	χ_{NK}, $\chi_{\widetilde{NK}}$	2×2 correlation matrix; mass ratio with NK	$0(\frac{1}{2}^{-})$ NK degenerate state; $0(\frac{1}{2}^{-})$ excited state, $0(\frac{1}{2}^{+})$ deemed too massive
Sasaki [94]	Wilson	χ_{PS}	standard analysis	$0(\frac{1}{2}^{-})$ above S-wave NK; $0(\frac{1}{2}^{+})$ above P-wave NK
Mathur *et al.* [95]	overlap	χ_{NK}, $\chi_{\widetilde{NK}}$	volume dependence	$0, 1(\frac{1}{2}^{-})$ NK scattering state; $0, 1(\frac{1}{2}^{+})$ P-wave NK degenerate
Ishii *et al.* [96,97]	Wilson	χ_{PS}	hybrid boundary conditions; Bayesian analysis	$0(\frac{1}{2}^{-})$ NK scattering state; $0(\frac{1}{2}^{+})$ deemed too massive
Alexandrou *et al.* [98]	Wilson	χ_{PS}	volume dependence	$0(\frac{1}{2}^{-})$ more consistent with single particle state; NK scattering state not seen
Chiu *et al.* [99]	domain wall	χ_{NK}, $\chi_{\widetilde{NK}}$, [a] χ_{PS}	3×3 correlation matrix	$0(\frac{1}{2}^{-})$ NK scattering state; ground state $0(\frac{1}{2}^{-})$ less massive than $0(\frac{1}{2}^{+})$
Takahashi *et al.* [100]	Wilson	χ_{NK}, $\chi_{\widetilde{NK}}$	2×2 correlation matrix; volume dependence	$\frac{1}{2}^{-}$ NK scattering state; $\frac{1}{2}^{-}$ excited state; $\frac{1}{2}^{+}$ N^*K scattering state

[a] The NK-type fields used by Chiu *et al.* [99] differ by a γ_5 in the nucleon part of the operator from the other groups listed, which effectively reverses the intrinsic parity of the operator.

The Spin-$\frac{3}{2}$ Pentaquark, Lattice Resonance Signature

In our first exploratory study of spin-3/2 pentaquarks [29] we find evidence of the binding, i.e. the mass of the pentquark state becomes less than its lowest energy decay channel, in the spin-3/2, isoscalar even-parity channel.

Here we refine our analysis to include additional terms in the NK^* pentaquark interpolator, we include a new vector-diquark scalar-diquark pentaquark interpolator to study spin-3/2 pentaquark states and we extend the size of our ensemble from 290 configurations, to 396 configurations. These results further support our discovery of attraction in the even-parity, isoscalar, spin-3/2 pentaquark channel, vital to the formation of a pentaquark resonance.

Fundamental to this work is the discrimination of a resonance state from possible scattering states. Several groups have sought to distinguish the resonance and scattering states by comparing the masses at different volumes [95,100,117–119]. The volume dependence of the residue of the lowest lying state has also been proposed as a way to identify the nature of the state [95,118]. Alternatively, hybrid boundary conditions have been used in Refs. [96, 97, 120] to differentiate the resonance in the odd-parity channel from the S-wave NK scattering state. In the even-parity channels, as we discuss in Sec. 4.2, the energy of the P-wave two-particle scattering states are explicitly volume dependent. By comparison, we might assume that the volume dependence of a resonance mass on a lattice with a large physical volume should have only small volume dependence. Therefore measuring the volume dependence of the mass of an even-parity state is also an alternative resonance signature.

In Ref. [28,29] we employed a computationally inexpensive approach to investigate pentaquark resonances by searching for evidence of sufficient attraction between the constituents of the pentaquark state such that the resonance mass becomes lower than the sum of the free decay channel masses. We labeled this pattern as "the standard lattice resonance signature" because this signature is observed for conventional baryon resonances studied on the lattice [18, 27, 103, 121, 122]. By comparing the masses of the five-quark states to the mass of the decay channel we found evidence of binding in the spin-3/2, isoscalar even-parity channel, but otherwise not. The limitation of this resonance signature is that absence of binding cannot be used to exclude the possibility of a resonance as the attractive forces simply may not be strong enough to provide binding. On the other hand, the presence of binding would provide a compelling resonance signature.

Further, we commonly find evidence of a repulsive interaction in the five-quark baryon-meson states. That is the mass or energy of the two-particle state created with our five-quark interpolators is larger than the non-interactive two-particle state because of a repulsive interaction, which is a finite volume effect [115]. It is possible that the same maybe true but with an attractive interaction, making the mass or energy of the two-particle state less than in the non-interacting state, but perhaps insufficient attraction to produce a resonance. An analysis of the volume dependence of the standard resonance signature is therefore vital in determining the fate of the Θ^+. However an important advantage of this resonance signature is that it is effective in

the study of even-parity states, where the data typically contains a larger component of noise than in the odd-parity channel. A precise determination of the residue of the pole is difficult in the best of circumstances.

We discover in [29] the existence of a double plateau structure in the even-parity, isoscalar, spin-3/2 channel. Careful determination that we are not excluding, in our analysis, true signal at large Euclidean times is vital in the determination of the ground state mass of the correlator. In this study we review our techniques for testing that we are not discarding true signal at large Euclidean times and find the application of these techniques crucial in extracting the ground state mass in the analysis of the $I(J^P) = 1(3/2^-)$, $1(1/2^+)$ and $1(3/2^+)$ states extracted with our vector-diquark scalar-diquark interpolator and in the analysis of the $0(3/2^+)$ state extracted with the NK^* interpolator. We argue that the reason for the discrepancy in the $I(J^P) = 0(3/2^+)$ mass extracted with the NK^* interpolator between our work [29] and Doi et al. [120], is because we fit our effective mass data at larger Euclidean times to recover the true ground state mass.

In Sec. 4.1 we review our spin-3/2 pentaquark interpolating fields. In Sec. 4.2 we describe our analysis techniques. An addition to this work is a review in Sec. 4.2.1 of our jackknife estimate of our confidence intervals. We make a comparison between two alternative algorithms for calculating the confidence intervals. Our results are presented in Sec. 4.3, where we discuss in detail the mass splittings between the pentaquark and two-particle scattering states. As in [29] we find evidence of binding in the spin-3/2, isoscalar, even-parity channel. In Sec. 4.3.2 we discuss the discrepancy between our calculation of the mass of the spin-3/2, isoscalar, even-parity state and the corresponding calculation by Doi et al. [120]. Finally, conclusions and suggestions for future work are summarised in Sec. 4.4.

4.1 Interpolating Fields

The simplest NK-type interpolating field used in lattice simulations, referred to in Ref. [28] as the "colour-singlet" NK field, has the form,

$$\chi_{NK} = \frac{1}{\sqrt{2}}\epsilon^{abc}(u^{Ta}C\gamma_5 d^b)\left\{u^c(\bar{s}^e i\gamma_5 d^e) \mp (u \leftrightarrow d)\right\} , \tag{4.1}$$

where the $-$ and $+$ corresponds to the isospin $I = 0$ and 1 channels, respectively. This field has spin $\frac{1}{2}$, and transforms a pseudo-scalar under the parity transformation $q \rightarrow \gamma_0 q$.

One can access spin-$\frac{3}{2}$ states by replacing the spin-0 K-meson part of χ_{NK} with a spin-1 K^* vector meson operator,

$$\chi^\mu_{NK^*} = \frac{1}{\sqrt{2}}\epsilon^{abc}(u^{Ta}C\gamma_5 d^b)\left\{u^c(\bar{s}^e i\gamma^\mu d^e) \mp (u \leftrightarrow d)\right\} , \tag{4.2}$$

where again the $-$ and $+$ corresponds to the isospin $I = 0$ and 1 channels, respectively. The field $\chi^\mu_{NK^*}$ transforms as a vector under the parity transformation, and has overlap with both spin-$\frac{1}{2}$ and spin-$\frac{3}{2}$ pentaquark states. States of definite spin can be projected from $\chi^\mu_{NK^*}$ by applying appropriate projectors, as discussed in Chapter 1.

Following our previous work with spin-1/2 SS and PS interpolators, Eqs. (3.10) and (3.14), we propose a vector diquark-diquark type interpolator that accesses spin-$\frac{3}{2}$

states,

$$\chi^{\mu}_{\widetilde{LY}} = \frac{1}{\sqrt{2}}\epsilon^{abc}(u^{Ta}C\gamma_5\gamma^{\mu}d^b)(u^{Tc}C\gamma_5 d^e)C\bar{s}^{eT} \ . \tag{4.3}$$

It can be easily shown that this field does not have definite isospin by rewriting the second diquark in this field in terms of colour symmetric and colour antisymmetric components,

$$\begin{aligned}\chi^{\mu}_{\widetilde{LY}} \ = \ & \frac{1}{\sqrt{2}}\epsilon^{abc}(u^{Ta}C\gamma_5\gamma^{\mu}d^b) \times \Big\{ \frac{1}{2}\{(u^{Tc}C\gamma_5 d^e) - (u^{Te}C\gamma_5 d^c)\} + \\ & \frac{1}{2}\{(u^{Tc}C\gamma_5 d^e) + (u^{Te}C\gamma_5 d^c)\}\Big\}C\bar{s}^{eT} \ .\end{aligned} \tag{4.4}$$

The colour antisymmetric components in the previous equation is pure isoscalar, as can be shown using isospin raising and lowering operators,

$$\begin{aligned} I_-\{(u^c_\alpha(C\gamma_5)_{\alpha\beta}d^e_\beta) \ - (u^e_\alpha(C\gamma_5)_{\alpha\beta}d^c_\beta)\} \ &= \ \{(d^c_\alpha(C\gamma_5)_{\alpha\beta}d^e_\beta) \ - (d^e_\alpha(C\gamma_5)_{\alpha\beta}d^c_\beta)\} \\ &= \ \{(d^c_\alpha(C\gamma_5)_{\alpha\beta}d^e_\beta) \ + (d^c_\beta(C\gamma_5)_{\alpha\beta}d^e_\alpha)\} \\ &= \ \{(d^c_\alpha(C\gamma_5)_{\alpha\beta}d^e_\beta) \ - (d^c_\beta(C\gamma_5)_{\beta\alpha}d^e_\alpha)\} \\ &= \ 0. \end{aligned} \tag{4.5}$$

Similarly this term vanishes under the isospin raising operator. Therefore since this term vanishes under both raising and lowering operations it is isoscalar. The colour symmetric term can be shown to be isovector by once more using the isospin raising and lowering operators,

$$\begin{aligned} I_-\{(u^c_\alpha(C\gamma_5)_{\alpha\beta}d^e_\beta) \ + (u^e_\alpha(C\gamma_5)_{\alpha\beta}d^c_\beta)\} \ &= \ \{(d^c_\alpha(C\gamma_5)_{\alpha\beta}d^e_\beta) \ + (d^e_\alpha(C\gamma_5)_{\alpha\beta}d^c_\beta)\} \\ &= \ \{(d^c_\alpha(C\gamma_5)_{\alpha\beta}d^e_\beta) \ - (d^c_\beta(C\gamma_5)_{\alpha\beta}d^e_\alpha)\} \\ &= \ \{(d^c_\alpha(C\gamma_5)_{\alpha\beta}d^e_\beta) \ + (d^c_\beta(C\gamma_5)_{\beta\alpha}d^e_\alpha)\} \\ &= \ 2(d^c_\alpha(C\gamma_5)_{\alpha\beta}d^e_\beta) \ . \end{aligned} \tag{4.6}$$

With the isospin raising operator the result is the same, but with $(u \leftrightarrow d)$. Furthermore, this term will vanish under successive raising or lowering operations, which implies that it is purely isovector.

Based on this information we formulate a vector diquark-diquark style interpolator based on Eq.(4.3), which has definite isospin with the following,

$$\begin{aligned}\chi^{\mu}_{LY} \ &= \ \frac{1}{\sqrt{2}}\epsilon^{abc}(u^{Ta}C\gamma_5\gamma^{\mu}d^b)\left\{ \ (u^{Tc}C\gamma_5 d^e) \mp (d^{Tc}C\gamma_5 u^e)\right\}C\bar{s}^{eT} \\ &= \ \frac{1}{\sqrt{2}}\epsilon^{abc}(u^{Ta}C\gamma_5\gamma^{\mu}d^b)\left\{ \ (u^{Tc}C\gamma_5 d^e) \mp (u^{Te}C\gamma_5 d^c)\right\}C\bar{s}^{eT} \ ,\end{aligned} \tag{4.7}$$

where $-$ and $+$ corresponds to isoscalar and isovector channels. To show that this interpolator is pure isoscalar/isovector we act on it with an isospin lowering operator,

$$\begin{aligned} I_-\chi^{\mu}_{LY} \ = \ & \frac{1}{\sqrt{2}}\epsilon^{abc}(\ (d^{Ta}C\gamma_5\gamma^{\mu}d^b)\left\{ \ (u^{Tc}C\gamma_5 d^e) \mp (u^{Te}C\gamma_5 d^c) \ \right\} + \\ & (u^{Ta}C\gamma_5\gamma^{\mu}d^b)\left\{ \ (d^{Tc}C\gamma_5 d^e) \mp (d^{Te}C\gamma_5 d^c) \ \right\} \ )C\bar{s}^{eT} \ . \end{aligned} \tag{4.8}$$

Since $\epsilon^{abc}(d^{Ta}C\gamma_5\gamma^{\mu}d^b) = 0$, and the colour anti-symmetric/symmetric term is zero/non-zero under the isospin lowering operation, and similarly under an isospin raising operation, χ_{LY} has definite isospin. Note that the isoscalar component of χ_{LY} does not

vanish as in the case of the SS interpolator because, as in the case of the PS interpolator, the diquarks are not identical.

The vector diquark in the LY interpolator mixes an additional small component of the spinors. This makes the LY interpolator less suited to the analysis of pentaquark states compared to the NK^* interpolator. We find in our analysis of nucleon interpolators that the χ_2 interpolator, with its pseudo-scalar diquark, does not provide access to the ground state. The NK^* interpolator still holds the most promise for isolating a low-lying pentaquark state.

4.2 Lattice Techniques

Here we highlight the relevant formalism we introduced in Chapter 1. The masses of the spin-$\frac{1}{2}$ and spin-$\frac{3}{2}$ pentaquark states are obtained from the two-point correlation function,

$$\mathcal{G}^{\mu\nu}(t,\vec{p}) = \sum_{\vec{x}} \exp(-i\vec{p}\cdot\vec{x}) \langle 0 | T\, \chi^{\mu}(x)\, \bar{\chi}^{\nu}(0) | 0 \rangle \ . \tag{4.9}$$

To project states of definite spin from the correlation function $\mathcal{G}^{\mu\nu}(t,\vec{p})$ we apply the spin projection operators [27],

$$\begin{aligned} P^{\frac{3}{2}}_{\mu\nu}(p) &= g_{\mu\nu} - \frac{1}{3}\gamma_\mu\gamma_\nu - \frac{1}{3p^2}(\gamma\cdot p\gamma_\mu p_\nu + p_\mu\gamma_\nu\gamma\cdot p) \ , \\ P^{\frac{1}{2}}_{\mu\nu}(p) &= g_{\mu\nu} - P^{\frac{3}{2}}_{\mu\nu}(p) \ , \end{aligned} \tag{4.10}$$

for spin-$\frac{3}{2}$ and $\frac{1}{2}$, respectively. Note here we are again using the Bjorken and Drell representation of the γ-matrices.

The spin-projected correlation function receives contributions from both even and odd-parity states. The use of fixed boundary conditions in the time direction enables states of definite parity to be projected using the matrix [18, 110],

$$\Gamma^{\mp} = \frac{1}{2}\left(1 \pm \frac{M_{B^\pm}}{E_{B^\pm}}\gamma_0\right) \ , \tag{4.11}$$

for odd and even parities, respectively. Masses of states with definite spin and parity can then be obtained from the spinor trace of the spin and parity projected correlation functions,

$$\begin{aligned} G(t,\vec{p}) &= \mathrm{tr}_{\mathrm{sp}}\left[\Gamma\,\mathcal{G}^{\mu\nu}(t,\vec{p})\,P_{\nu\mu}(p)\right] \\ &= \sum_B \lambda^B\bar{\lambda}^B \exp\left(-E_B t\right) \\ &\overset{t\to\infty}{=} \lambda^0\bar{\lambda}^0 \exp\left(-m_0 t\right) \ . \end{aligned} \tag{4.12}$$

This function is a sum over all states, B, with energy E_B, and $\bar{\lambda}^B$ and λ^B are the couplings of the state B to the interpolating fields at the source and sink, respectively.

Since the contributions to the two-point function are exponentially suppressed at a rate proportional to the energy of the state, at zero momentum the mass of the lightest state, m_0, is obtained by fitting a constant in time to the effective mass,

$$M^{\mathrm{eff}}(t) = \ln\left(\frac{G(t,\vec{0})}{G(t+1,\vec{0})}\right)$$

Table 4.1: Lowest energy decay channels for each pentaquark state on the lattice, where the Δ baryon is bound.

$I(J^P)$	Decay channel
$0,1(\frac{1}{2}^-)$	S-wave $N+K$
$0,1(\frac{1}{2}^+)$	P-wave $N+K$
$0(\frac{3}{2}^-)$	S-wave $N+K^*$
$1(\frac{3}{2}^-)$	S-wave $\Delta+K$
$1,0(\frac{3}{2}^+)$	P-wave $N+K$

$$\stackrel{t\to\infty}{=} m_0 \ . \tag{4.13}$$

Following our previous work [28, 29], we search for evidence that the resonance mass has become smaller than the sum of the free decay channel mass for pentaquark states created by our interpolating fields. For this purpose it is useful to define an effective mass splitting. For example, in an S-wave decay channel,

$$\begin{aligned} \Delta M^{\text{eff}}(t) &\equiv M^{\text{eff}}_{5q}(t) - \left(M^{\text{eff}}_{B}(t) + M^{\text{eff}}_{M}(t)\right) \\ &\stackrel{t\to\infty}{=} m_{5q} - (m_B + m_M) \ , \end{aligned} \tag{4.14}$$

where $M^{\text{eff}}_B(t)$ and $M^{\text{eff}}_M(t)$ are the appropriate baryon and meson effective masses for a specific channel. For a P-wave decay channel, the effective masses are combined with the minimum nontrivial momentum on the lattice, $2\pi/L$, to create the effective energy, $E^{\text{eff}}(t) = \sqrt{(M^{\text{eff}}(t))^2 + (2\pi/L)^2}$, for each decay particle, where L is the lattice spatial extent. The advantage of this technique is that it measures a correlated mass difference, thereby suppressing the sensitivity to systematic uncertainties (such as using different fitting ranges).

For a pentaquark resonance we shall consider the mass splittings between the pentaquark state and the corresponding baryon and meson free two-particle scattering states. The signal we are searching for is evidence of a pentaquark bound state at quark masses near the physical regime. In Table 4.1 we summarise the lowest energy decay channels for the various isospin, spin and parity quantum numbers considered in this analysis. In Table 4.2 we summarise the masses and energies of the two-particle state that are relevant to our present study.

4.2.1 Error analysis

We use the Jackknife technique [123] for estimating the confidence intervals, variance and the covariance matrix in our calculation of the χ^2 of our fit. The mean extracted for a Jackknife subensemble is calculated with one of the configurations excluded,

$$\bar{x}_i = \frac{1}{n-1}\sum_{j\neq i}^{n} x_j \ . \tag{4.15}$$

Table 4.2: The masses and energies of the non-interacting two-particle states.

aM_π	$aM^{\text{S-wave}}_{N+K}$	$aM^{\text{S-wave}}_{N+K^*}$	$aM^{\text{S-wave}}_{N^*+K}$	$aM^{\text{S-wave}}_{\Delta+K}$	$aM^{\text{P-wave}}_{N+K}$	$aM^{\text{P-wave}}_{N+K^*}$
0.540(1)	1.560(4)	1.769(6)	1.891(27)	1.696(9)	1.696(4)	1.873(8)
0.500(1)	1.490(5)	1.707(7)	1.830(31)	1.640(10)	1.631(5)	1.817(9)
0.453(1)	1.408(6)	1.637(8)	1.760(39)	1.578(11)	1.557(5)	1.754(10)
0.400(1)	1.321(7)	1.562(10)	1.683(53)	1.514(14)	1.478(7)	1.690(11)
0.345(2)	1.236(11)	1.489(14)	1.594(84)	1.454(18)	1.401(10)	1.630(13)
0.300(2)	1.169(16)	1.431(20)	1.433(133)	1.412(23)	1.342(15)	1.588(16)

For a set of n data points, n Jackknife subensembles are generated with each element deleted in only one of the subensembles. The Jackknife estimate of variance [123] is,

$$\sigma^2 = \frac{n-1}{n}\sum_i^n(\bar{x}_i - \frac{1}{n}\sum_j^n \bar{x}_j)^2 \ . \tag{4.16}$$

If we are sampling from a Gaussian distribution then the 68.3% confidence interval resides within one standard deviation either side of the mean.

Alternatively we can calculate our own confidence intervals by sorting the Jackknife subensembles, $\bar{x}_i$, [123]. For this procedure however we must be careful to include the inflation factor $\sqrt{n-1}$, for the averaged subensembles. The inflated Jackknife subensemble [123] centered around the average of the Jackknife subensembles is,

$$X_i = \sqrt{n-1}\cdot(\bar{x}_i - \frac{1}{n}\sum_j^n \bar{x}_j) + \frac{1}{n}\sum_j^n \bar{x}_j \ . \tag{4.17}$$

Following Efron [123] the confidence intervals are,

$$[X_{lo}, X_{up}] = [X^{(\alpha)}, X^{(1-\alpha)}] \tag{4.18}$$

where $\alpha \cdot 100\%$ of the Jackknife subensembles are less than X^α, $\alpha \cdot 100\%$ are greater than $X^{(1-\alpha)}$ and thus $(1-2\alpha)\cdot 100\%$ of the subensembles are contained in this interval. For the 68.3% confidence $\alpha = 0.1585$. Of course this method does not rely on the assumption of a Gaussian distribution and is therefore more robust.

4.3 Results

In this section we examine a class of pentaquark interpolators that access spin-3/2 states. The correlation functions extracted with the NK^* and LY interpolating fields contain contributions from even and odd-parity states with both spin 1/2 and spin 3/2. We project out correlation functions of states with definite spin and parity using the appropriate projection operators, as highlighted in Sec. 4.2 and discussed extensively

in Chapter 1. The mass of the lowest energy state is extracted with a linear least squares fit of a constant in time to the effective mass Eq. (2.16). We estimate the χ^2 per degree of freedom ($\chi^2_{\rm dof}$) of this fit using a covariance matrix analysis and ideally we demand that the $\chi^2_{\rm dof} \sim 1$ and < 1.5. We must be cautious when applying this criteria though because if we include data points in our fit where the signal has become hidden by noise we can add degrees of freedom to the fit without adding additional constraints. This suppresses the $\chi^2_{\rm dof}$ and may provide a false positive in the selection of a fit regime.

Another concern in blindly applying the above criteria to our selection of data to fit was identified in our previous work [29] where we identify a double plateau structure in the effective mass of the $I(J^P) = 0(3/2^+)$ channel. We find a $\chi^2_{\rm dof} \simeq 1$ for a fit to a limited selection of our data, but that the $\chi^2_{\rm dof}$ becomes large when we include data from larger Euclidean times. This indicates that the interpolator couples relatively weakly to the lower energy state. Indeed, Doi et al. [120] failed to consider this issue in their analysis. The asymptotic limit in Eq. (2.16) demands that we fit the data at the larger Euclidean times, even though the data has a larger component of noise.

With these issues in mind, we will plot the effective mass data up to one data point after we judge that the signal has been lost, or up to time slice 30. We will fix the upper bound of the fit at this point. In some cases the loss of signal means that the next effective mass data point would not appear within a sensible scale in our figures. In this case the extra data point is not shown. The restriction on the $\chi^2_{\rm dof}$ will determine the lower bound of the fit. In this way we can be confident that we satisfy Eq. (2.16) in our extraction of the ground state mass.

In this study we compare the 68% confidence interval given by the two alternative Jackknife estimates Eq. (4.16) and Eq. (4.18). In Fig. 4.1 we compare two estimates of the 68% confidence interval in the effective mass of the $3/2^+$ state extracted with the NK^* interpolator (top) and the pion (bottom), one based on Eq. (4.16) and the other obtained by sorting the inflated Jackknife subensembles Eq. (4.18). In each case the data corresponds to $m_\pi \simeq 700$ MeV. We see that the former Jackknife estimate of the 68% confidence interval in the effective mass of the $3/2^+$ state is typically larger than the 68% confidence obtained by sorting the subensembles. This is because outliers at large distances from the mean. As we evolve to large Euclidean times the component of noise becomes larger and the standard Jackknife estimate of the error becomes more and more dominated by the outliers. The signal has clearly become hidden by the noise where $t \geq 24$, and this data is not included in our analysis. For comparison, in Fig. 4.1 the two Jackknife estimates of the 68% confidence interval in the effective mass of the pion are calculated on the same ensemble. The box contains 68% of the inflated subensembles and the outliers connected by a solid line contains 95% of the inflated subensembles. Here we find the two methods are in excellent agreement. Note in Fig. 4.1 that the fixed boundary effects appear to become important where $t > 30$. To be cautious we do not include these data points in our analysis of pentaquark states.

In Fig. 4.2 we show a histogram of the inflated jacknife subensembles of the masses of the $3/2^+$ state extracted with the NK^* interpolator and the pion used in our estimates of the error. The difference in the two scales of the horizontal axes is 100:1. The distribution of subensembles for the pion is a good approximation to a Gaussian. The distribution of the subemsembles of the $3/2^+$ state is much broader than the pion and there are more outliers. Clearly far more samples of the functional integral of the $3/2^+$ state are needed to reproduce the precision of our calculation of the pion mass where

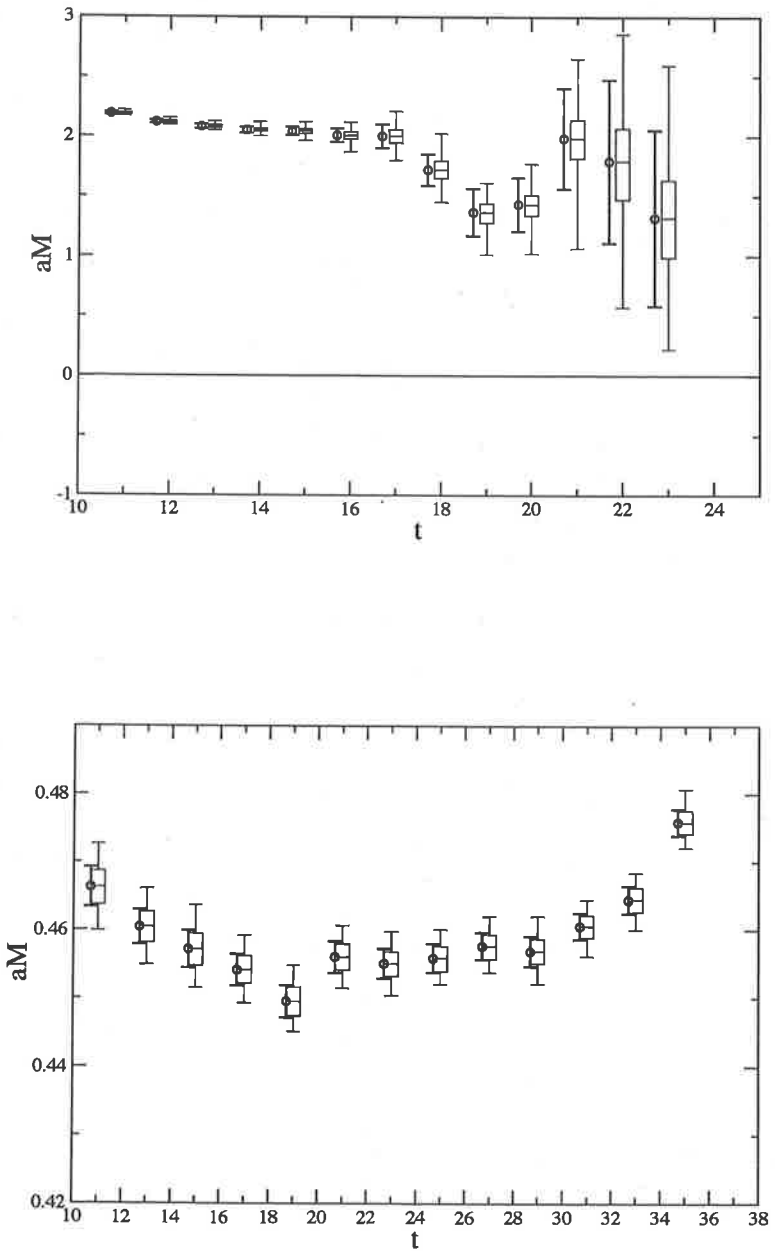

Fig. 4.1: The Jackknife estimates of the 68% confidence interval in the effective mass based on Eq. (4.16) (upper) is compared with the 68% confidence intervals based on Eq. (4.18) (lower). For clarity, we omit every second data point of the pion effective mass.

the sort and cut and the standard Jackknife estimate of the error agree. We will use the more robust sort and cut Eq. (4.18) method to estimate the confidence intervals in the extracted masses.

4.3.1 Isoscalar, negative parity channel

We begin the discussion of our results with the isoscalar, odd-parity channel. Isoscalar states can be constructed with the NK^* and LY interpolating fields, Eqs. (4.2) and Eq. (4.8) respectively. We extract the mass of the $I(J^P) = 0(1/2^-)$ state with the NK^* interpolator with a fit to the effective mass data shown in Fig. 4.3 where $t \geq 18$ at all quark masses. At the three largest quark masses, the $\chi^2_{\rm dof} \simeq 1$ at the fourth largest quark mass the $\chi^2_{\rm dof} = 0.53$, which is acceptable. At the two smallest quark masses the $\chi^2_{\rm dof}$ is 0.33 and 0.22 respectively.

Continuing our analysis of the isoscalar, spin-1/2 state we fit the effective mass extracted with the LY interpolator, Fig. 4.4. If we fit the data at the where $t \geq 19$ at the three largest quark masses we find a $\chi^2 \simeq 1$. At the next two largest quark masses we find a plateau at $t \geq 18$ and a small $\chi^2_{\rm dof}$ for each fit. We find that this analysis and an analysis of the data where $t \geq 19$ are consistent, so fitting the data at the earlier euclidean time is appropriate. At the smallest quark mass our best estimate of the ground state mass is extracted with a fit the the data where $t \geq 17$, where the χ^2 is 0.43.

Next we calculate the mass of the $3/2^-$ state extracted with the NK^* interpolator with a fit to the effective mass data of Fig. 4.5, where $t \geq 18$ is selected at each quark mass. In each case we cut the data where we the signal has become hidden by noise. In particular at the three smallest quark masses the next data point after the last one shown is not contained in the scale of the vertical axes, and so is clearly dominated by noise. At the five largest quark masses the $\chi^2_{\rm dof} \simeq 1$. At the sixth smallest quark masses the $\chi^2_{\rm dof}$ of the fit is 0.20, which is not an ideal. Alternatively if we fit the data where $t \geq 14$ at this quark mass we find an acceptable $\chi^2_{\rm dof}$, but the mass extracted is much larger than in our initial analysis. So we use our former analysis as our best estimate of the ground state mass at this quark mass, because it is more consistent with the asymptotic limit required in Eq. (2.16).

In the $3/2^-$ channel the LY interpolator mixes (small $\times$ large)(large $\times$ large)(small) components of the spinors. The extra small components suppress the signal relative to the NK^* interpolator, which mixes all large components in this channel. Consequently the effective mass data extracted with the LY interpolator, Fig. 4.6, has a larger component of noise compared with the effective mass extracted with the NK^* interpolator, Fig. 4.5.

We see in Fig. 4.6 for the $0(3/2^-)$ state extracted with the LY interpolator, that the effective mass has an apparent plateau at times $14-16$ and then another apparent plateau for $t \geq 18$. If we limit the analysis to the data points at $t = 14 - 16$ then we find a $\chi^2_{\rm dof} = 1.14$ for our fit to the data at the largest quark mass. When the data points at $t = 18-20$ are included in this fit, the $\chi^2_{\rm dof}$ becomes large, as shown in Fig. 4.7 (left). This suggests that there is still a component of signal at $t \geq 18$, reflecting the true ground state of the correlator which must be included in the fit. To determine the appropriate range of data to fit we have to choose an upper bound of our fit. We find that the size of the error bar in the effective mass data shown in Fig. 4.6 (top left) becomes large after time slice 21. Since the contribution of each data point to the fit

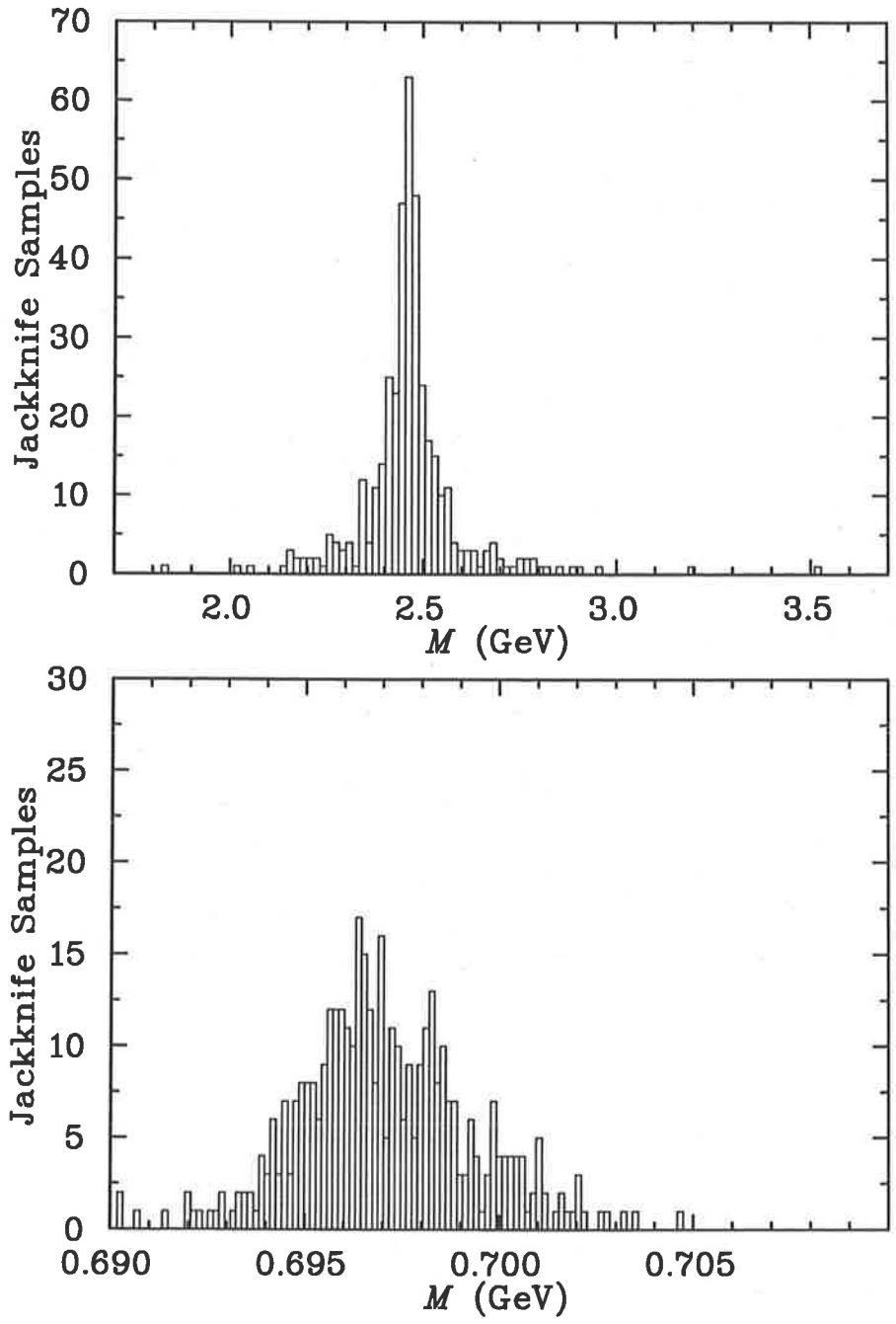

Fig. 4.2: The distribution of Jackknife samples of the masses of the $0(3/2^+)$ state extracted with the NK^* interpolator with a fit the the effective mass data at times $18-22$ (top), and the pion with a fit to the effective mass data $16-20$ (bottom), the data corresponds to $m_\pi \simeq 700$ MeV. Note that the difference in scale on the horizontal axis is 100:1 between the two figures, and the presence of outliers in the upper plot.

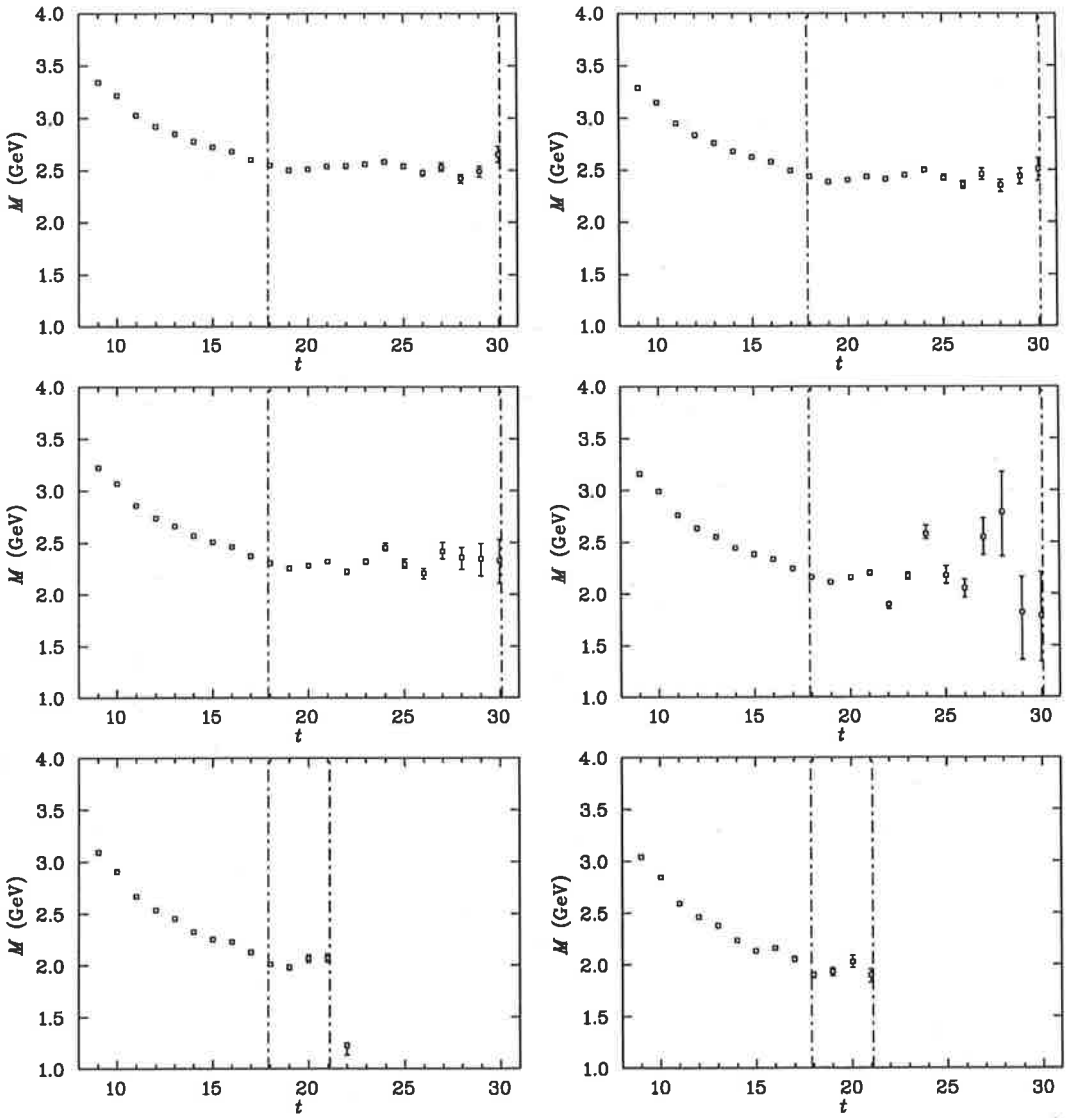

Fig. 4.3: The effective mass of the $I(J^P) = 0(1/2^-)$ state extracted with the NK^* interpolator, the data correspond to $m_\pi \simeq 830\,\text{MeV}$ (top left), 770 MeV (top right), 700 MeV (middle left), 616 MeV (middle right), 530 MeV (bottom left), and 460 MeV (bottom right). The data are illustrated only to the point at which the error bars diverge.

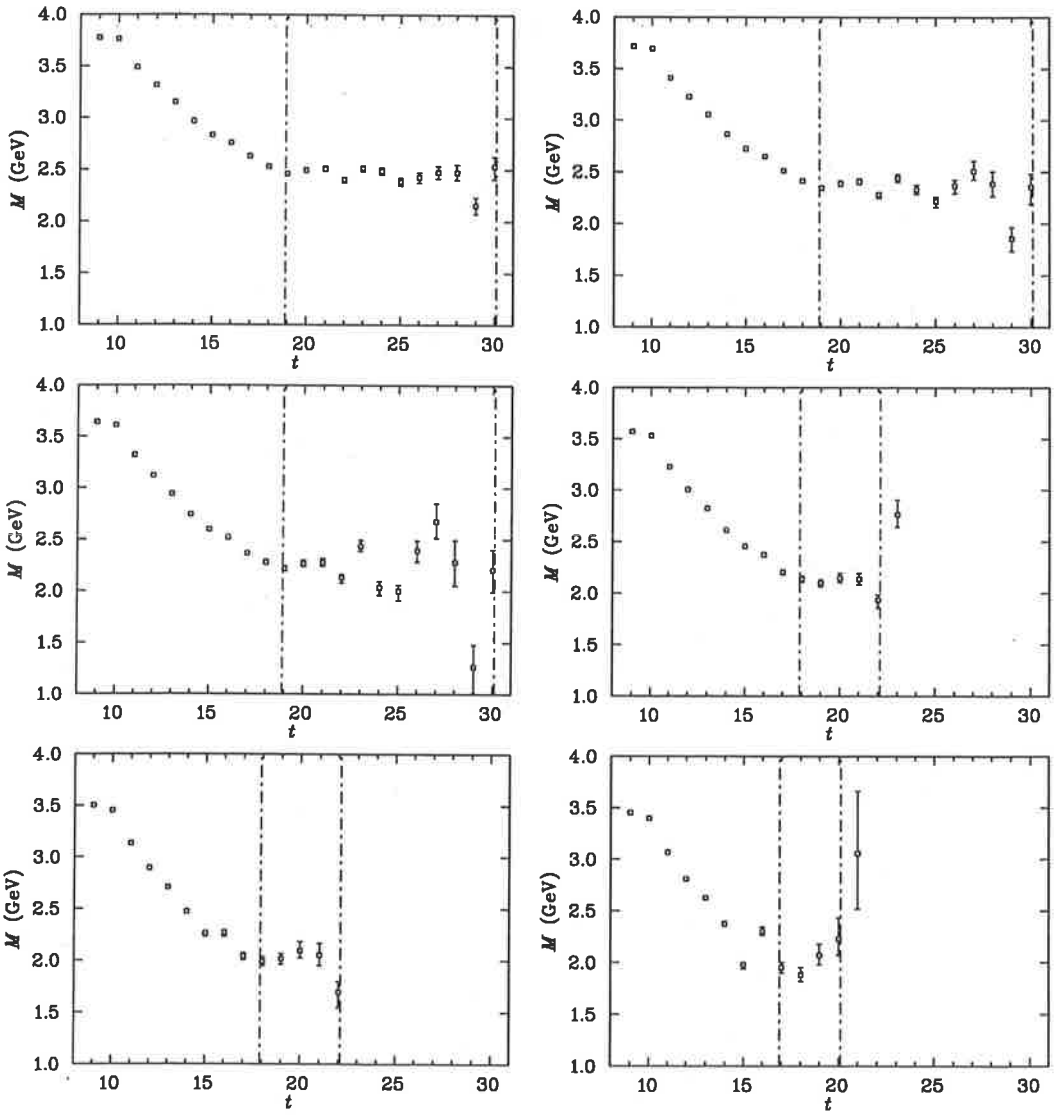

Fig. 4.4: As in Fig. 4.3, but for the $0(1/2^-)$ state extracted with the LY interpolator.

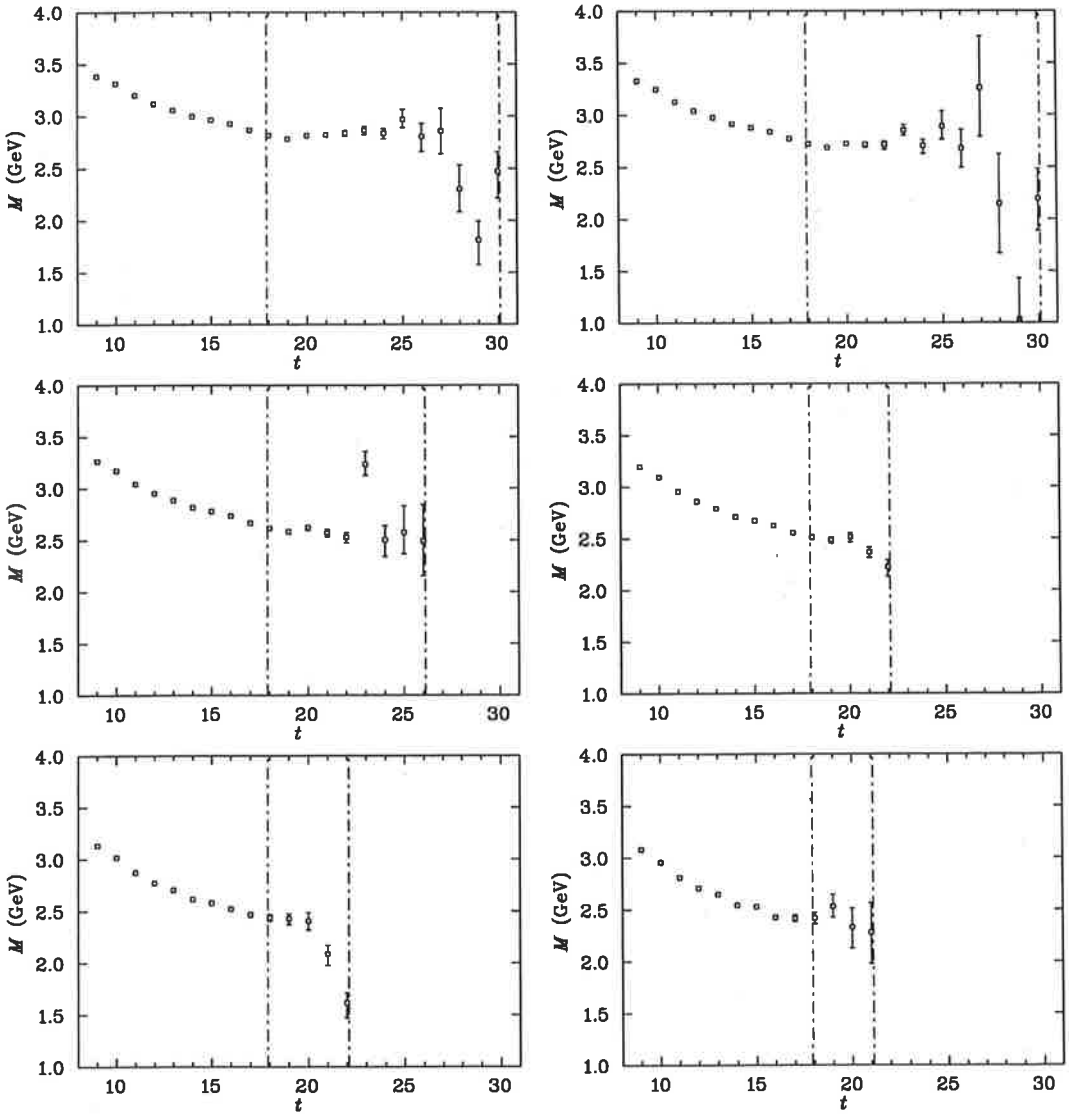

Fig. 4.5: As in Fig. 4.3, but for the $0(3/2^-)$ state extracted with the NK^* interpolator.

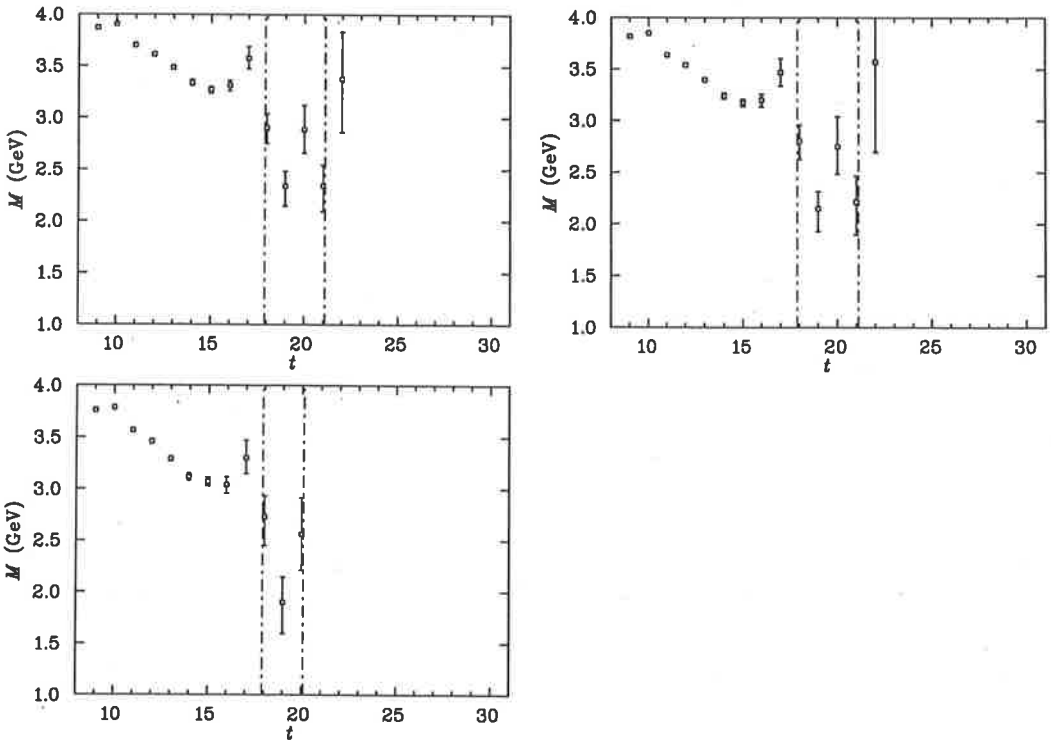

Fig. 4.6: As in Fig. 4.3 but for the $0(3/2^-)$ state extracted with the LY interpolator. The data correspond to $m_\pi \simeq 830\,\mathrm{MeV}$ (top left), 770 MeV (top right), and 700 MeV (bottom left).

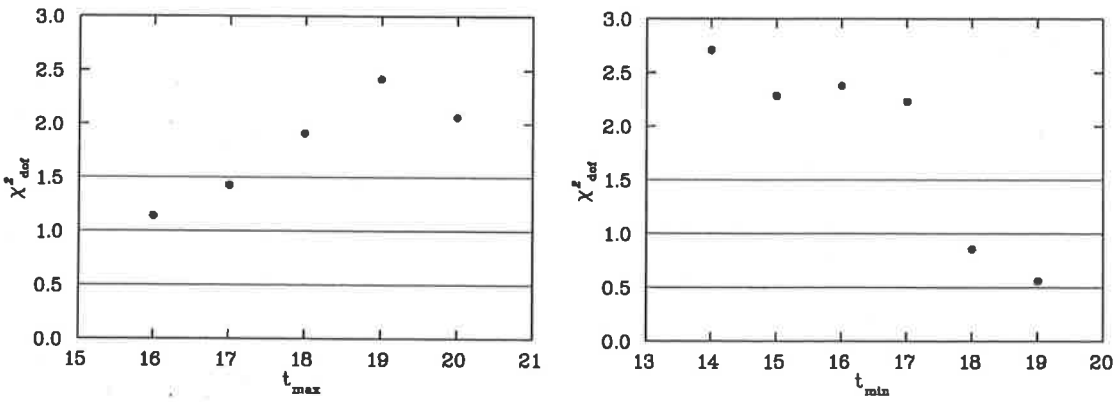

Fig. 4.7: (left) χ^2_{dof} for a series of possible fits with a lower bound fixed at time slice 14, the upper bound shown on the horizontal axis. The data correspond to $m_\pi \simeq 700$ MeV. The horizontal lines correspond to $\chi^2_{\mathrm{dof}} = 0.5, 1.0$ (ideal) and 1.5. Similarly (right), the χ^2_{dof} for a a selection of fits with an upper bound fixed at time slice 21 and a lower bound shown on the horizontal axes.

is weighted by a factor of $1/\sigma^2$, excluding the data a $t \geq 21$ will have a negligible effect on the extracted mass. Therefore we find a suitable upper limit to our fit at time slice 21. In Fig. 4.7 (right), for the largest quark mass we fix the upper bound of the fit to the data at time slice 21 and show the χ^2_{dof} for a selection fits with the lower bound of the fit shown on the horizontal axes. Here we find an acceptable χ^2_{dof} with the lower bound of the fit set to time slice 18. We find the same qualitative behaviour at the next largest quark mass. At the third largest quark mass the $\chi^2_{\text{dof}} = 0.57$.

In Fig. 4.8 we show the mass extracted with both a fit to the data at the earlier plateau time slices $14-16$ (crosses), and another at the larger Euclidean times $18-21$ (closed triangles). Both fits have an acceptable χ^2_{dof}. The fit at the larger Euclidean times is similar to the lowest energy two-particle state that we know the interpolator must couple to and is also consistent with the mass extracted with the NK^* interpolator. In other words, it is the latter fit that correctly accesses the the ground state of the correlator.

The mass extracted with the fit to the data at time slices $14-16$ is much larger than both its lowest energy decay channel and the mass extracted with the NK^* interpolator. This fit does not satisfy the asymptotic limit in Eq. (2.16) and so is not the correct answer. Fortunately there is a clear signal at the two largest quark masses indicating that a naive fit to the first plateau is wrong. Inclusion of the data at larger Euclidean times caused a divergence in the χ^2_{dof}. Thus we must fit the data shown where $t \geq 18$ to extract the mass of the $I(J^P) = 0(3/2^-)$ state. Our analysis of the $3/2^-$ state with the LY interpolator is limited to the three largest quark masses because the signal has become hidden by noise at the smaller quark masses.

This careful examination of the $3/2^-$ state obtained from the LY interpolator serves as a proof of principle in the correlation function analysis. In this case, the correct answer is known from the NK^* interpolator and it is now clear that one cannot simply ignore visually unpleasing data when the χ^2_{dof} is inflated through the inclusion of such data.

Table 4.3 summarises masses of the odd-parity states extracted with the NK^* and LY interpolators. In Fig. 4.8 we also show the masses of the spin-1/2 state extracted with the NK^* interpolator (open circles), the spin-1/2 state extracted with the LY interpolator (open triangles), and the mass of the spin-3/2 state extracted with the NK^* interpolator (close circles). For comparison we include the masses of the non-interacting S-wave $N + K$ (solid line) and $N + K^*$ (dashed line) two-particle states. We find that the mass of the $I(J^P) = 0(1/2^-)$ state extracted the LY interpolator is slightly less than the mass extracted with the NK^* interpolator at the three largest quark masses. The discrepancy in the calculation of the mass is about 3% at three largest quark masses. The $I(J^P) = 0(3/2^-)$ state extracted with the LY interpolator is also slightly smaller than the mass extracted with the NK^* interpolator. We attribute these small differences to excited state contamination in the NK^* case.

To search for evidence of binding we must accurately measure the splitting between the mass of the pentaquark state and its lowest energy decay channel, summarised in Table 4.1. To accomplish this we fit a constant in time to the effective mass splitting Eq. (4.14), in each case we find a good χ^2_{dof} where we use the same fit regimes discussed above. The results are presented in Table 4.4. The masses of the $1/2^-$ states are consistently more massive than the non-interacting S-wave $N + K$ mass, which is consistent with our findings in [28, 29]. The mass of the $3/2^-$ state extracted with the NK^* interpolator is consistently more massive than the non-interacting S-wave $N+K^*$

mass, which is consistent with our findings in [29]. We find that the mass of the $3/2^-$ state extracted with the LY interpolator is consistent within error bars to the mass of the non-interacting S-wave $N + K^*$ mass. Therefore we find no evidence of binding in the isoscalar odd-parity channel.

Table 4.3: The masses of the $I(J^P) = 0(1/2^-)$ and $I(J^P) = 0(3/2^-)$ states extracted with the NK^* and LY interpolators.

aM_π	$aM_{NK^*}^{1/2^-}$	$aM_{LY}^{1/2^-}$	$aM_{NK^*}^{3/2^-}$	$aM_{LY}^{3/2^-}$
0.540(1)	$1.643^{+0.004}_{-0.005}$	$1.599^{+0.006}_{-0.006}$	$1.822^{+0.005}_{-0.008}$	$1.747^{+0.057}_{-0.062}$
0.500(1)	$1.572^{+0.005}_{-0.005}$	$1.528^{+0.007}_{-0.008}$	$1.759^{+0.006}_{-0.009}$	$1.660^{+0.062}_{-0.080}$
0.453(1)	$1.489^{+0.006}_{-0.006}$	$1.445^{+0.010}_{-0.011}$	$1.687^{+0.009}_{-0.011}$	$1.593^{+0.098}_{-0.102}$
0.400(1)	$1.398^{+0.007}_{-0.008}$	$1.375^{+0.015}_{-0.015}$	$1.617^{+0.011}_{-0.014}$	...
0.345(2)	$1.305^{+0.011}_{-0.011}$	$1.301^{+0.023}_{-0.022}$	$1.569^{+0.018}_{-0.020}$	...
0.300(2)	$1.244^{+0.018}_{-0.017}$	$1.267^{+0.031}_{-0.028}$	$1.583^{+0.039}_{-0.035}$	...

Table 4.4: The splitting between the mass of the $I(J^P) = 0(1/2^-)$ and $I(J^P) = 0(3/2^-)$ states extracted with the NK^* and LY interpolators and the relevant two-particle states.

aM_π	$a\Delta M_{NK^*}^{1/2^-}$	$a\Delta M_{LY}^{1/2^-}$	$a\Delta M_{NK^*}^{3/2^-}$	$a\Delta M_{LY}^{3/2^-}$
0.540(1)	$0.088^{+0.003}_{-0.003}$	$0.039^{+0.005}_{-0.006}$	$0.065^{+0.005}_{-0.006}$	$-0.006^{+0.058}_{-0.068}$
0.500(1)	$0.088^{+0.003}_{-0.003}$	$0.039^{+0.006}_{-0.007}$	$0.065^{+0.006}_{-0.007}$	$-0.032^{+0.063}_{-0.084}$
0.453(1)	$0.086^{+0.004}_{-0.004}$	$0.040^{+0.009}_{-0.010}$	$0.065^{+0.009}_{-0.009}$	$-0.029^{+0.099}_{-0.107}$
0.400(1)	$0.081^{+0.006}_{-0.006}$	$0.060^{+0.013}_{-0.013}$	$0.070^{+0.012}_{-0.011}$	...
0.345(2)	$0.075^{+0.009}_{-0.009}$	$0.071^{+0.022}_{-0.020}$	$0.093^{+0.019}_{-0.020}$	...
0.300(2)	$0.090^{+0.015}_{-0.014}$	$0.090^{+0.027}_{-0.022}$	$0.167^{+0.039}_{-0.033}$	...

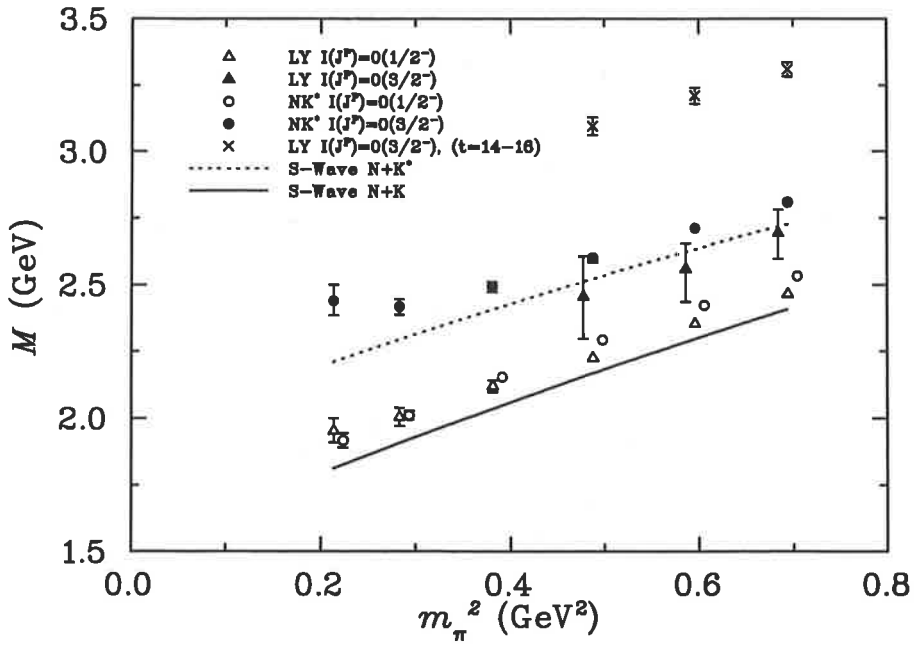

Fig. 4.8: The masses of the isoscalar, spin-1/2 state (open symbols) and spin-3/2 state (closed symbols) extracted with the LY and NK^* interpolators. The data correspond to $m_\pi \simeq 830$, 770, 700, 616, 530, and 460 MeV. The data points corresponding to the spin-1/2 states and the spin-3/2 state extracted with the LY interpolator have been offset horizontally for clarity.

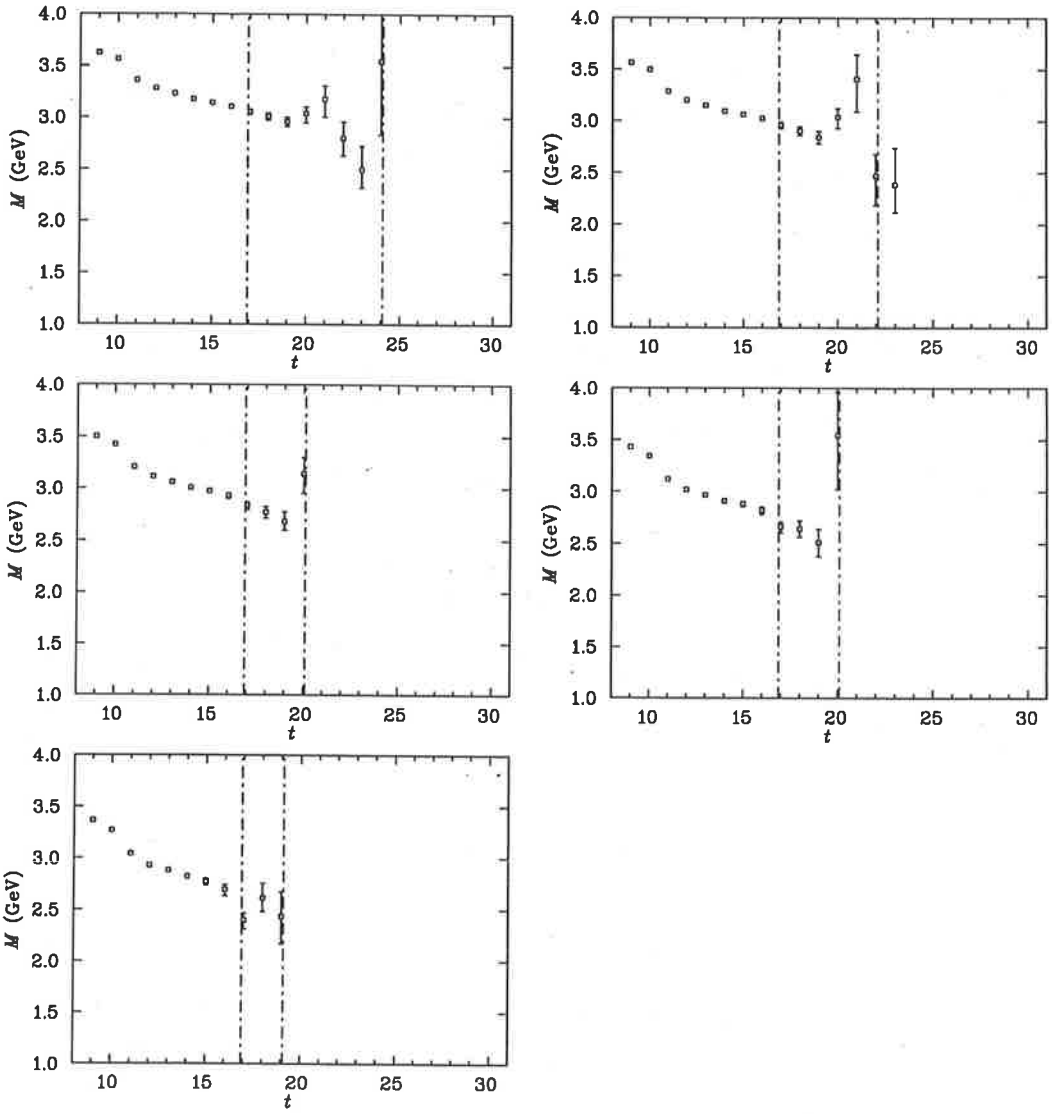

Fig. 4.9: The effective mass of the $I(J^P) = 0(1/2^+)$ state extracted with the NK^* interpolator, the data correspond to $m_\pi \simeq 830\,\text{MeV}$ (top left), 770 MeV (top right), 700 MeV (middle left) and 616 MeV (middle right) 530 MeV (bottom left).

4.3.2 Isoscalar, positive parity channel

We continue our analysis with the isoscalar, even-parity channel. The mass of the spin-1/2 state is extracted with the NK^* interpolator with a fit to the effective mass data shown in Fig. 4.9 for $t \geq 17$ at each quark mass. At the four largest quark masses we find a $\chi^2_{\text{dof}} \simeq 1$. At the smallest quark mass shown we find a $\chi^2_{\text{dof}} = 0.27$.

Continuing our analysis of this state with the LY interpolator in Fig. 4.10 we find an apparent plateau starting at time slice 14. A fit to the data shown where $t \geq 14$ returns an ideal $\chi^2_{\text{dof}} \simeq 1$ at the four largest quark masses, and a $\chi^2_{\text{dof}} = 1.31$ and 0.58 for the two smaller quark masses. The mass extracted for this fit is consistently larger than the mass of the same state extracted with the NK^* interpolator. Repeating the calculation with a fit to the data where $t \geq 17$ we find $\chi^2_{\text{dof}} = 0.53, 0.28, 0.17, 0.70$ and 1.45 at each quark mass respectively. The χ^2_{dof} in this analysis is generally less ideal than our initial analysis, however there is some systematic drift in the effective mass

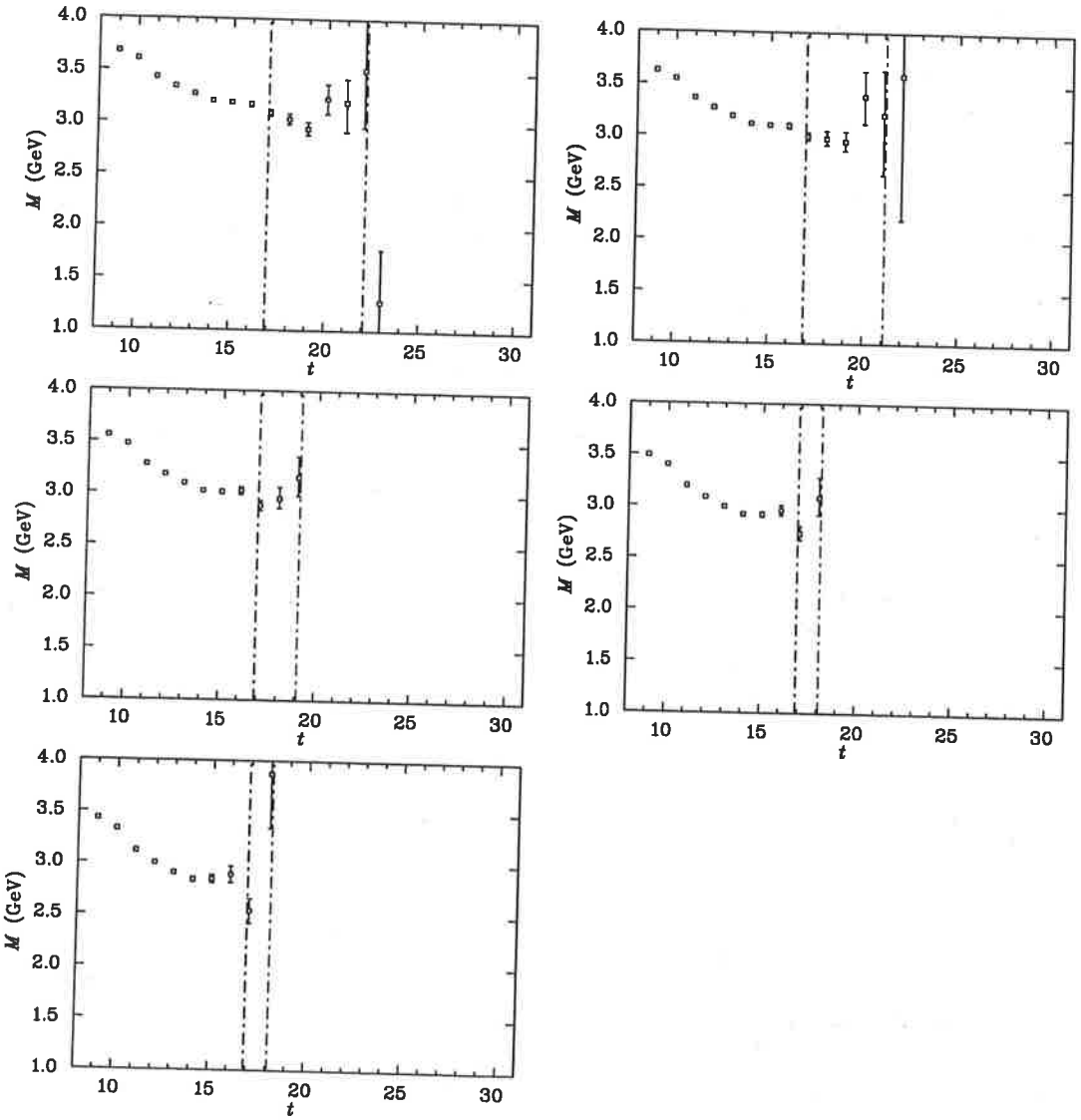

Fig. 4.10: As in Fig. 4.9, but for the $0(1/2^+)$ state extracted with the LY interpolator.

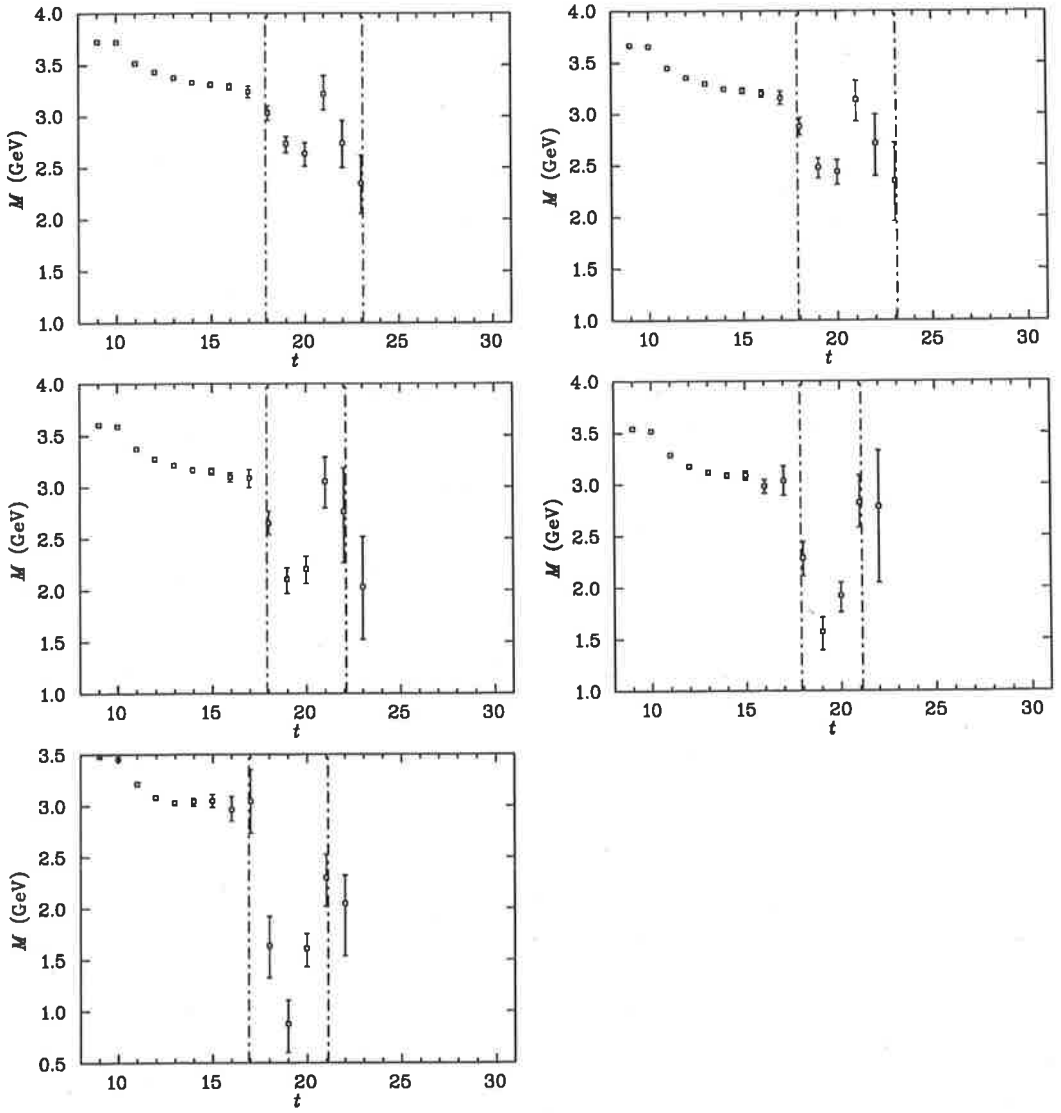

Fig. 4.11: As in Fig. 4.9 but for the $0(3/2^+)$ state extracted with the NK^* interpolator.

to time slice 17. The mass extracted for $t \geq 17$ is consistent with the mass extracted with the NK^* interpolator. So we present this analysis as our best estimate of the lowest energy state that this interpolator couples to in this channel.

Next we consider the spin-3/2 state extracted with the NK^* interpolator. Similar to our analysis of the $I(J^P) = 0(3/2^-)$ state extracted with the LY interpolator, we find the same double plateau structure in the effective mass data, Fig. 4.11 at time slices $13 - 17$. To determine the correct fit regime here we focus on our analysis of data at the third largest quark mass. At a glance at Fig. 4.11 (middle left), it may be tempting to fit the apparent plateau in the effective mass at $t = 13 - 17$. However we will demonstrate that such a fit does not describe the lowest lying state.

Figure 4.12 (left) displays the χ^2 per degree of freedom for a selection of fits to the effective mass data Fig. 4.11 (middle left), where the lower bound of the fit is fixed at time slices 13 or 14, 4 or 5 time slices from the source respectively. The upper bound of the fit is displayed on the horizontal axis. We see that when the data at $t \geq 18$ is included in the fit, the χ^2 per degree of freedom becomes large. We must therefore conclude that the data at time slices 18 onwards is true signal, reflecting

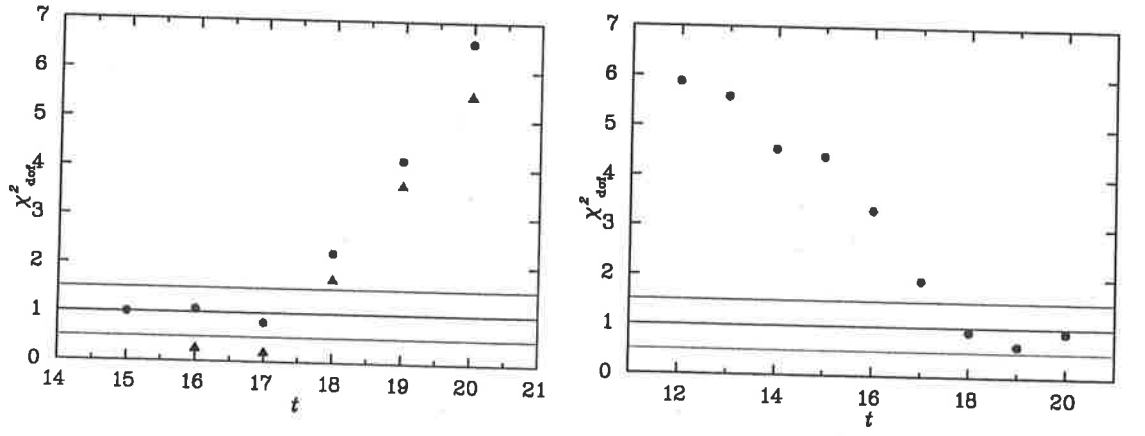

Fig. 4.12: (left) The $\chi^2_{\rm dof}$ for a series of possible fits with a lower bound fixed at time slice 13 (circles) and time slice 14 (triangles) and an upper bound shown on the horizontal axis. (right) The $\chi^2_{\rm dof}$ for a series of possible fits with the upper bound fixed at time slice 22 and the lower bound shown on the horizontal axis. The data correspond to $m_\pi \simeq 700\,\text{MeV}$. The horizontal lines correspond to $\chi^2_{\rm dof}$ of 0.5,1.0(ideal) and 1.5.

the ground state of the correlation function and therefore must be included in the fit. This "double plateau" structure can occur when the interpolator couples strongly to a more massive state and relatively weakly to the lower energy state, the former dominates at earlier times, then due to exponential suppression the latter dominates at later times. In this study we also find this behaviour in the effective mass of the $0(3/2^-)$, $1(1/2^+)$ and $1(3/2^+)$ states extracted with the LY interpolator. In each case the correct consideration of the data at the larger times is vital in extracting the ground state mass. To determine the appropriate upper bound for the fit, we begin by returning to Fig. 4.11 (middle left). The rapid proliferation of the error bar suggests that the signal is becoming hidden by the noise after time slice 22. We note that since we use a linear least squares fit to extract hadron masses from the effective mass, contributions to the extracted mass at each timeslice is weighted by a factor of $1/\sigma^2$. Fitting data with a relatively large component of noise can have the effect of suppressing the $\chi^2_{\rm dof}$ calculated in Eq. (C.3), see [124], but has negligible effect on the magnitude of the extracted mass.

Having fixed the upper bound of the fit at time slice 22, we proceed with determining the lower bound. In Fig. 4.12 (right) we show the $\chi^2_{\rm dof}$ of a series of fits to the data with the upper bound of the fit fixed to time slice 22, and the lower bound of the fit shown on the horizontal axes.

As a general rule a $\chi^2_{\rm dof} \simeq 1$ and < 1.5 indicates that the fit of a constant to the data is appropriate. A $\chi^2_{\rm dof} >> 1$ indicates that the effective mass data has not reached a plateau and therefore a fit of a constant to the data is not well motivated. Alternatively $\chi^2_{\rm dof} << 1$ is unlikely to be a good fit, but can be due to a large component of noise in the effective mass data. A review of the undesirable features of the covariance matrix analysis is discussed in [124]. For further analysis of the goodness of fit we calculate the probability that another sample of random data would have a larger or equal $\chi^2_{\rm dof}$. For a good fit this probability should be $\sim 50\%$ [125].

In Fig. 4.12 (right) we find that a fit with a lower bound of $18-20$ has an acceptable $\chi^2_{\rm dof}$. In Fig. 4.13 we present a summary of the extracted mass corresponding to each of

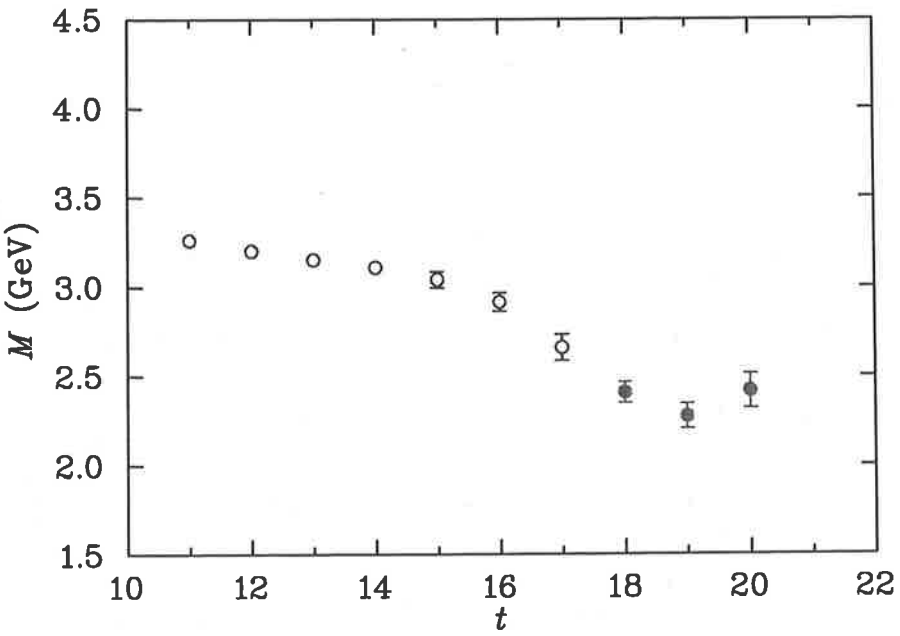

Fig. 4.13: The $0(3/2^+)$ mass extracted with a selection of fits with an upper bound fixed at time slice 22 and a lower bound shown on the horizontal axes. The data corresponds to $m_\pi \simeq 700\,\mathrm{MeV}$.

these fit regimes. The extracted mass corresponding to the selection of a lower bound of time slices $18-20$ agree to within $\sim 68\%$ confidence interval. We choose time slice 18 as the lower bound of the fit, because for this fit the $\chi^2_{\mathrm{dof}} \simeq 1$.

For the same reasons discussed above, we extract the mass of the spin-3/2 state with the NK^* interpolator with a fit to the data shown in Fig. 4.11 where $t \geq 18$ at the four largest quark masses and where $t \geq 17$ at the smallest quark mass. In each case we find $\chi^2_{\mathrm{dof}} \simeq 1$. At the smallest quark mass we also examined an alternative fit to the data where $t \geq 18$, in this case the $\chi^2_{\mathrm{dof}} = 0.55$. The mass extracted with both analyses agree to within errors, so we use the former analysis. Our analysis is restricted to the five largest quark masses after which we judge that the ground state signal has been hidden by the noise.

Next we consider the spin-3/2 state extracted with the LY interpolator. Here we find a systematic drift in the effective mass data extracted with the LY interpolator, shown in Fig. 4.14, towards time slice 21. At this large time the data is beginning to be dominated by the noise. However we have a sufficient signal at the three largest quark masses to fit the data shown where $t \geq 21$. The χ^2_{dof} for a fit to the data where $t \geq 21$ at the three largest quark mass is 0.85, 0.65 and 0.46 respectively. In Fig. 4.15, at the two smallest quark masses we graph the effective mass data point at time slice 21 because we judge that the signal is lost at time slice 22.

Unlike the analysis of the $I(J^P) = 0(3/2^-)$ state extracted with the LY interpolator and the $0(3/2^+)$ state extracted with the NK^* interpolator, the χ^2_{dof} test does not exclude a fit to the data at earlier times. We can repeat this analysis at smaller times and fit the data where $t \geq 19$. In this case we find $\chi^2_{\mathrm{dof}} \simeq 1$ at the three largest quark masses, and $\chi^2_{\mathrm{dof}} = 0.32$ and 0.02 at the two smaller quark masses. In each case we find a mass consistent with the energy of the non-interacting P-wave $N + K$ two-particle state.

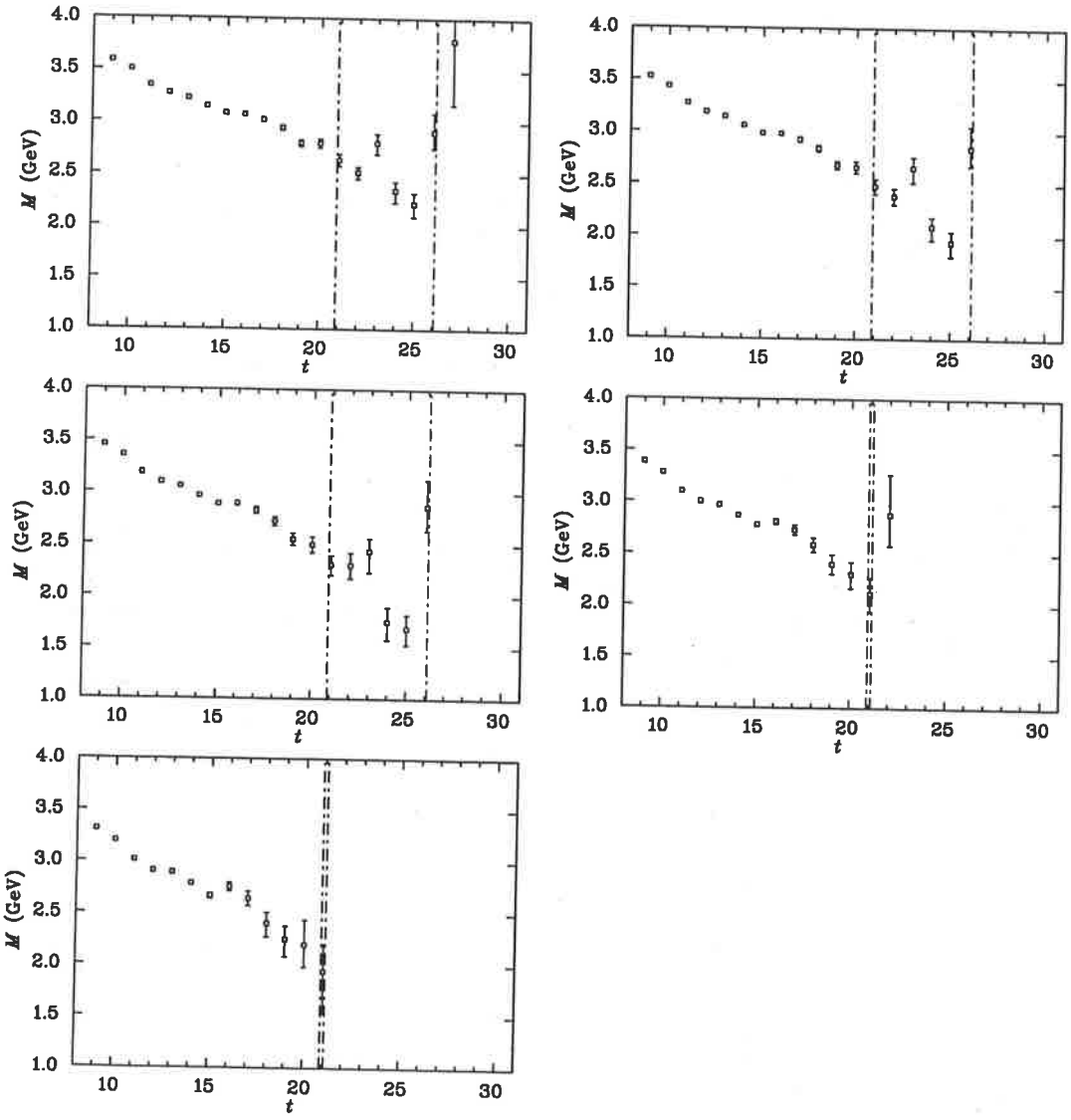

Fig. 4.14: As in Fig. 4.9 but for the $0(3/2^+)$ state extracted with the LY interpolator.

The mass extracted from these two approaches are not consistent and therefore clearly better statistics is required to resolve the ground state mass with greater confidence. Whilst we report the mass extracted with both fit procedures, the systematic drift in the lattice results suggests the more cautious fits for $t \geq 21$ will provide a better estimate of the ground state mass.

A summary of the masses are shown in Fig. 4.15 along with the relevant two particle states. We find that the mass of the spin-1/2 states (open symbols) are consistently larger than the lowest energy two-particle states, the $N + K$ in P-wave (solid line), which is consistent with our findings in [28, 29]. In this case the interpolators appear to couple more strongly to either the S-wave $N^* + K$ (dashed line) or P-wave $N + K^*$ (dotted line), which unfortunately have similar energies on our lattice.

The mass of the spin-3/2 state extracted with the LY interpolator (closed triangles) in our analysis with a lower bound of the fit starting before time slice 21, is consistent with the lowest energy decay channel. But the mass extracted with the LY interpolator with a fit to the data at $t \geq 21$ (crosses), is *smaller* than the non-interacting two-particle energy of the P-wave $N + K$ state at each quark mass. The mass extracted with the latter analysis is likely a better estimate of the ground state mass as the qualitative behaviour of the effective mass suggests excited state contamination before time slice 21.

Similarly the mass extracted with the NK^* interpolator (open circles) becomes *smaller* than the non-interacting two-particle energy of the P-wave $N + K$ state at the two smallest quark masses shown. This is consistent with our findings in [29]. At large quark masses, the mass extracted with the LY interpolator is consistently smaller than the mass extracted with the NK^* interpolator, indicating that the NK^* interpolator has a stronger coupling to one or more excited states.

We make a more accurate determination of the binding energy by calculating the mass splittings defined in Eq. (4.14). The mass splittings are shown in Fig. 4.16 and summarised in Table 4.6 In this case the $N + K$ in relative P-wave is the lowest energy state of both the spin-1/2 and spin-3/2 five quark states. The discrepancy between the mass splittings between the spin-3/2 state extracted with the two interpolators and the two-particle energy of the P-wave $N + K$ state is likely due to excited state contamination. With vastly improved statistics a correlation matrix analysis would be beneficial.

As discussed in the previous section and in Ref. [28], the transition of a resonance at light quark masses to a state which lies below the free particle decay channel at quark masses larger but near the physical quark masses is the standard resonance signature in lattice QCD. Moreover the approach to the heavy quark limit is in accord with expectations. Recall that in the case of the Θ^+, which has a "fall-apart" decay mechanism, quark counting indicates that the Θ^+ to $N + K$ mass ratio will approach 1 as the heavy quark limit is approached. At intermediate quark masses, however, one expects the resonance signature analogous to the Δ baryon [28, 29]. The pentaquark mass extracted with the NK^* interpolator at the two smallest quark masses lies below the scattering state, indicating attraction, vital to the formation of a resonance.

Table 4.5: The masses of the $I(J^P) = 0(\frac{3}{2}^+)$ and $0(\frac{1}{2}^+)$ states extracted with the NK^* and LY interpolators.

aM_π	$aM_{NK^*}^{1/2^+}$	$aM_{LY}^{1/2^+}$	$aM_{NK^*}^{3/2^+}$	$aM_{LY}^{3/2^+}$
0.540(1)	$1.968^{+0.016}_{-0.016}$	$1.992^{+0.021}_{-0.021}$	$1.886^{+0.028}_{-0.038}$	$1.659^{+0.022}_{-0.029}$
0.500(1)	$1.906^{+0.018}_{-0.018}$	$1.943^{+0.027}_{-0.024}$	$1.771^{+0.037}_{-0.040}$	$1.557^{+0.028}_{-0.037}$
0.453(1)	$1.824^{+0.021}_{-0.024}$	$1.881^{+0.032}_{-0.031}$	$1.599^{+0.042}_{-0.050}$	$1.460^{+0.043}_{-0.053}$
0.400(1)	$1.720^{+0.029}_{-0.039}$	$1.799^{+0.046}_{-0.043}$	$1.334^{+0.053}_{-0.059}$	$1.374^{+0.989}_{-0.117}$
0.345(2)	$1.580^{+0.042}_{-0.056}$	$1.673^{+0.061}_{-0.075}$	$1.168^{+0.077}_{-0.084}$	$1.257^{+0.171}_{-0.268}$

Table 4.6: The splitting between the mass of the $I(J^P) = 0(3/2^+)$ states extracted with the NK^* and LY interpolators and the energy of the non-interacting P-Wave $N + K$ two-particle state.

aM_π	$a\Delta M_{NK^*}^{1/2^+}$	$a\Delta M_{LY}^{1/2^+}$	$a\Delta M_{NK^*}^{3/2^+}$	$a\Delta M_{LY}^{3/2^+}$
0.540(1)	$0.411^{+0.015}_{-0.015}$	$0.298^{+0.023}_{-0.021}$	$0.197^{+0.030}_{-0.038}$	$-0.044^{+0.022}_{-0.027}$
0.500(1)	$0.417^{+0.017}_{-0.017}$	$0.311^{+0.026}_{-0.023}$	$0.146^{+0.037}_{-0.042}$	$-0.083^{+0.029}_{-0.037}$
0.453(1)	$0.415^{+0.020}_{-0.022}$	$0.321^{+0.030}_{-0.029}$	$0.049^{+0.046}_{-0.048}$	$-0.108^{+0.042}_{-0.053}$
0.400(1)	$0.394^{+0.028}_{-0.034}$	$0.314^{+0.044}_{-0.045}$	$-0.136^{+0.053}_{-0.061}$	$-0.103^{+0.095}_{-0.117}$
0.345(2)	$0.333^{+0.038}_{-0.053}$	$0.258^{+0.058}_{-0.074}$	$-0.227^{+0.070}_{-0.080}$	$-0.145^{+0.174}_{-0.262}$

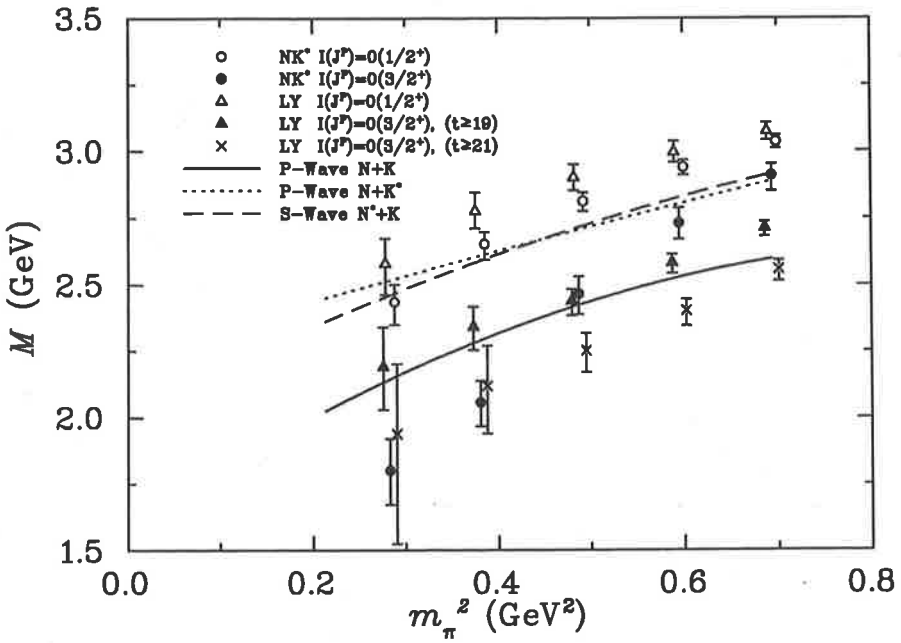

Fig. 4.15: As in Fig. 4.8, but for the isoscalar, even-parity states.

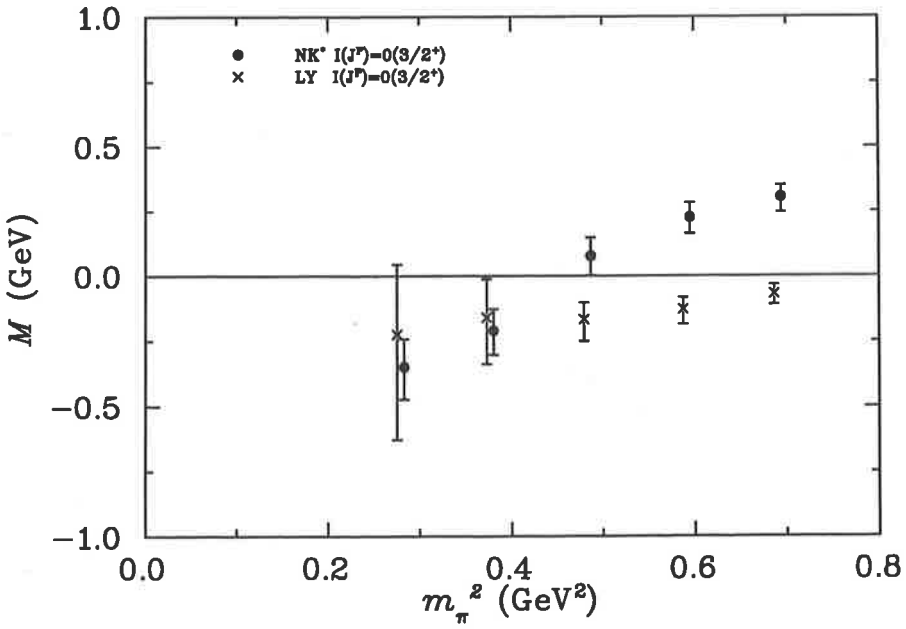

Fig. 4.16: The mass splitting between the $I(J^P) = 0(3/2+)$ state extracted with the NK^* (closed circles) and LY (crosses) interpolators and the P-wave N+K energy.

Response to criticism made by Doi et.al

We feel that it is necessary to respond in this thesis, to criticism made in Ref. [120] of our analysis in this channel [28]. Quoting Ref. [120]:

> Now, several comments are in order. (1) Reference [67] reported the existence of a low-lying 5Q state in the $J^P = 3/2^+$ channel using the NK^*-type interpolating field. However, we have not observed such a low-lying 5Q state in our calculation. There are a number of differences in the lattice QCD setup between the current studies and Ref. [67], such as the gauge and the quark actions, and the implementation of the smeared source. However, we consider that, rather than being a consequence of these differences, the discrepancy mainly comes from the low statistics adopted in Ref. [67]. We emphasize again that spin-3/2 pentaquark correlators are quite noisy, and therefore require better statistics. (2) Recall that, except for a single calculation [59], lattice QCD calculations indicate that the $J^P = 1/2^+$ state is heavy [57,58,60-66], for instance $m_{5Q} \simeq 2.25$ GeV in Ref. [61]. From the viewpoint of the diquark picture, it could be natural to obtain such massive 5Q states in the $J^P = 3/2^+$ channel. If there were a low-lying 5Q state in the $J^P = 3/2^+$ channel, then the diquark picture could suggest also a low-lying 5Q state in the $J^P = 1/2^+$ channel nearby. [1]

In response to comment (1), it is well known in the field that in calculating the two-point correlation function in momentum space one takes a Fourier transform which includes a sum over all spatial lattice sites. Therefore where the hadron fills the lattice, the size of the error bar depends on the volume of the lattice times the number of configurations. Currently the only other study on of spin-3/2 pentaquarks, Ref. [120], is on a 12^3 by 96 anisotropic lattice with an ensemble of 1000 configurations. This is to be compared to our original calculation Ref. [29] on a 20^3 by 40 lattice with an ensemble of 290 configurations, which in fact which corresponds to 25% higher statistics. Therefore Ref. [29] is the most precise publication of spin-3/2 pentaquarks at the time of writing. The data presented in this study correspond to an ensemble of 396 configurations, that is $\simeq 35\%$ greater statistics than Ref. [120] and we still find the resonance signature.

The reason that the size of the error bar in the mass of the $0(3/2^+)$ state in our previous study [29] is larger than in the study [120] is because the latter chose to analyse the data at the smaller Euclidean times. In Fig. 4.17 we compare the analysis of [120] with an analysis of the effective mass data in [29] where we fit at time slices $14 - 17$. We find both calculations are in excellent agreement and that the size of our error bar is smaller as argued above. But we stress that, the quality of the fit is not determined by the size of the error bars, but in this case it is determined by the χ^2 goodness of fit and the extent to which we satisfy the asymptotic limit in Eq. (2.16).

Comment (2) brings up the absence of evidence of a $J^P = 1/2^+$ partner to the candidate $J^P = 3/2^+$ pentaquark state. Firstly, the evidence of binding in this channel does not necessarily imply the existence of a $J^P = 3/2^+$ pentaquark. An alternative

[1] To find the relevant reference in this study, translate Ref. [67] to our paper Ref. [29], Ref. [57] corresponds to Ref. [93], Ref. [58] corresponds to Ref. [94], Ref. [59] corresponds to Ref. [99], Ref. [60] corresponds to Ref. [95], Ref. [61] corresponds to Ref. [96], Ref. [62] corresponds to Ref. [119], Ref. [63] corresponds to Ref. [28], Ref. [64] corresponds to Ref. [118], Ref. [65] corresponds to Ref. [117], and Ref. [66] corresponds to Ref. [126].

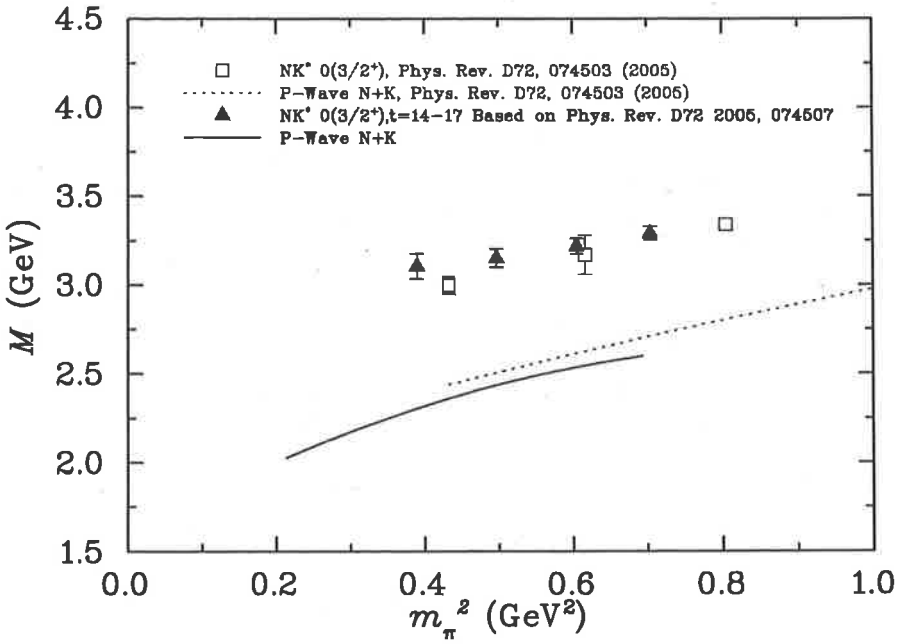

Fig. 4.17: A comparison between the mass of the $0(3/2^+$ state extracted with the NK^* interpolator from [120] and for comparison a fit to the effective mass data in [29] at time slices $14 - 17$.

explanation for the evidence of binding in this channel is that this is also a $N + K$ scattering state where the interaction is attractive, but not sufficiently attractive to give rise to a resonance. If this were true then the non-observation of the $J^P = 1/2^+$ state is of no consequence.

Secondly there has been no lattice calculation that has proved that a $J^P = 1/2^+$ state does not exist in quenched lattice QCD. In our study in Ref. [28] does not have sufficient precision to rule out such a state. Further we have stressed that the lack of evidence of the standard lattice resonance signature cannot disprove the existence of a pentaquark state. What we have done is identify the $0(3/2^+)$ channel as a promising channel for further study of pentaquark existence. As such, the $0(1/2^+)$ channel is also worthy of a high precision analysis.

Finally we explain the discrepancy between the two calculations. An examination of Fig. 6b in Ref. [120] reveals evidence of the double plateau structure we observe in the effective mass in our study. In their analysis however the authors choose to fit the earlier Euclidean times $23 - 28$, which corresponds a time evolution of $1.04 - 1.26$ fm from the source, compared to our analysis where we fit at $2.4 - 2.9$ fm from the source. Further, the authors make no comment about the validity of a fit including data from time slice 29 onwards. Nor do they make any comment about why the mass they extract is not consistent, up to finite volume effects, with the lowest energy two-particle state in this channel, the P-wave $N + K$.

Therefore a correct explanation for the discrepancy between the results of Ref. [120] and Ref. [29] is that Doi et al. simply did not evolve to sufficiently large Euclidean time to extract the lowest lying state. To support this hypothesis, in Fig. 4.18 (top) we include the current $0(3/2^+)$ mass extracted with the NK^* interpolator, where we fit effective mass at time slices $13 - 17$. Note that the χ^2_{dof} is acceptable for this fit

regime, see Fig. 4.12 (left), provided we exclude data at time slice 18 and beyond. The extracted mass subject to this fit regime and the mass reported by Ref. [120] agree well given that the lattice volume used in each case is different. Note that the analysis of Doi et al. is restricted to relatively large quark masses. However we have shown that this is *not* the lowest energy state. It cannot be the lowest energy state because at the very least we should access, up to finite volume effects, the lowest energy two-particle state in this channel which is the P-wave $N + K$.

By comparison in Fig. 4.18 (bottom) we show the two calculations of the $0(3/2^-)$ mass extracted with the NK^* interpolator. In this channel both calculations are in excellent agreement.

To summarise, the discrepancy in the mass of the $3/2^+$ state between Doi et al. [120] and our studies in this channel is because we fit our data at larger Euclidean times to isolate the ground state. For a fair comparison with our work, the authors of Ref. [120] must increase the precision of their calculation, probe lighter quark masses below the SU(3) flavour limit where evidence of binding is the most significant, and demonstrate that their fit regime does not exclude real signal at larger Euclidean times. The quality of the fit is not a function of the size of the error bars. Nor should visually displeasing data be cast aside without serious consideration.

4.3.3 Isovector, negative parity states

We continue our analysis with the isovector odd-parity states. The effective mass of the $1/2^-$ state extracted with the NK^* interpolator is shown in Fig. 4.19. At the two smallest quark masses shown the last data point represents the point at which we judge that the signal has become hidden by noise. This data point is not included in the fit. We extract the mass of the $1/2^-$ state with the NK^* interpolator with a fit to the data shown for $t \geq 19$. The $\chi^2_{\text{dof}} \simeq 1$ at the five largest quark masses and 0.25 at the lightest quark mass. An alternative analysis finds an acceptable χ^2_{dof} at the lightest quark mass shown where we fit the data for $t \geq 17$. In this case the mass extracted is much larger than in our former analysis. Therefore we use our former analysis as our best estimate of the ground state mass. The effective mass extracted with the LY interpolator is shown Fig. 4.20. As with our analysis of this state with the NK^* interpolator, the last data point at the two smallest quark masses represents the point where the signal is lost and so is not included in the fit. We extract the mass of this state with a fit to the effective mass data shown for $t \geq 19$, and in each case $\chi^2_{\text{dof}} \simeq 1$.

Next we consider the $3/2^-$ state. The effective mass extracted with the NK^* interpolator is shown in Fig. 4.21. There is a clear systematic drift in the effective mass data towards time slice 19. So we extract the mass with a fit to the data shown for $t \geq 19$. As with our analysis of the spin-1/2 state, at the three smallest quark masses we judge that the last data point shown is noise and is not included in the analysis. For these fits we find a $\chi^2_{\text{dof}} \simeq 1$ at the five largest quark masses and $\chi^2_{\text{dof}} = 0.33$ for the fit to the data at the smallest quark mass shown. The χ^2_{dof} at the smallest quark mass is not ideal, but is our best estimate of the ground state mass.

The effective mass extracted with LY interpolator is shown in Fig. 4.22. As discussed in Sec. 4.3.1 the LY interpolator mixes two extra small components of the spinors in this channel, compared to the NK^* interpolator. So the component of noise relative to the signal is much larger. Consequently our analysis is limited to the three largest quark masses. For a fit to the data shown we find a $\chi^2_{\text{dof}} \simeq 1$ where we fit

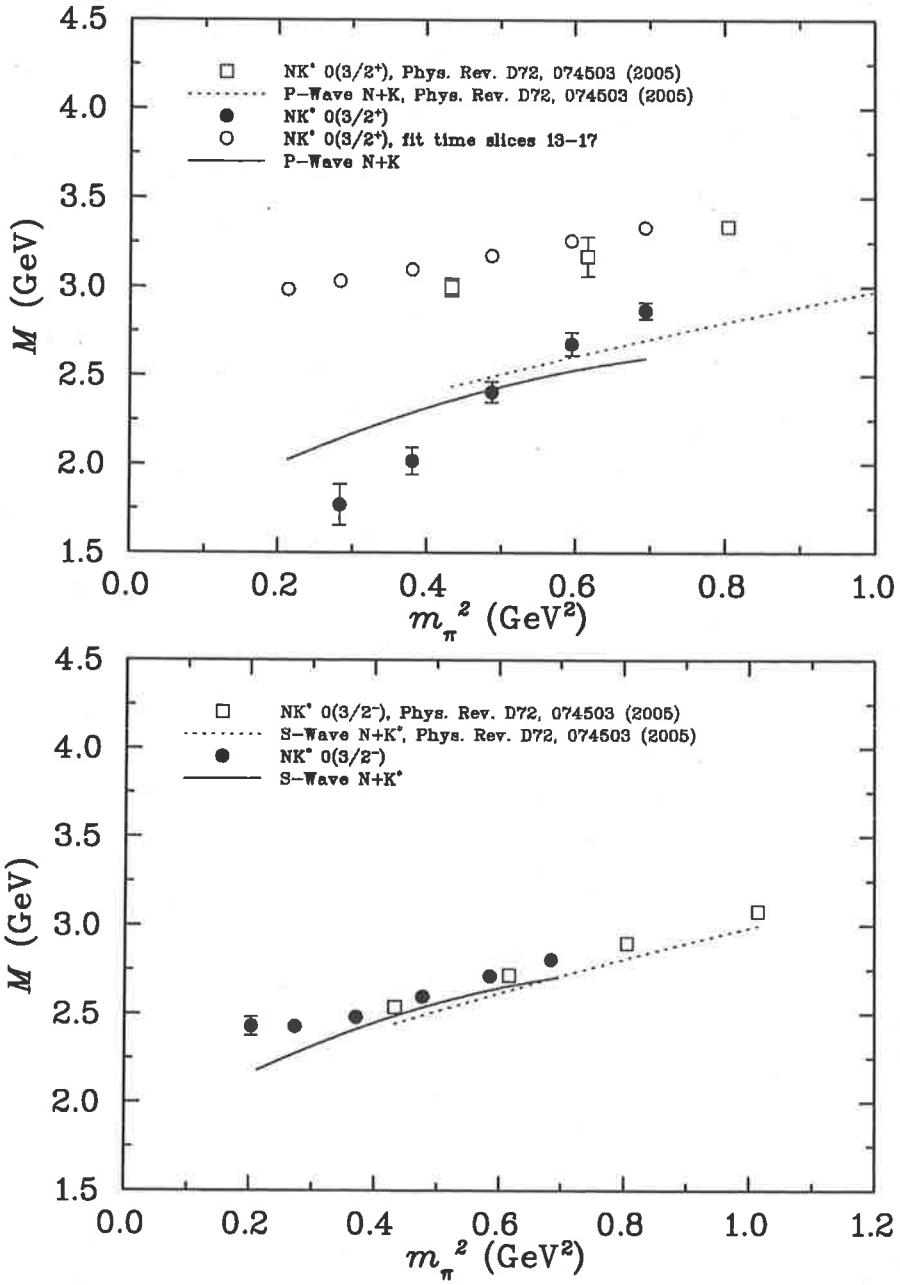

Fig. 4.18: (top) The $I(J^P) = 0(3/2^+)$ mass extracted with the NK^* interpolator and the P-Wave N+K decay channel energy. The data correspond to Ref. [120] (squares), an alternative fit to our data at time slices $13-17$ (open circles) and our calculation of the ground state mass (closed circles). (bottom) For comparison we show the mass of the $I(J^P) = 0(3/2^-)$ state extracted with the NK^* interpolator and the S-Wave N+K decay channel energies from the same two studies.

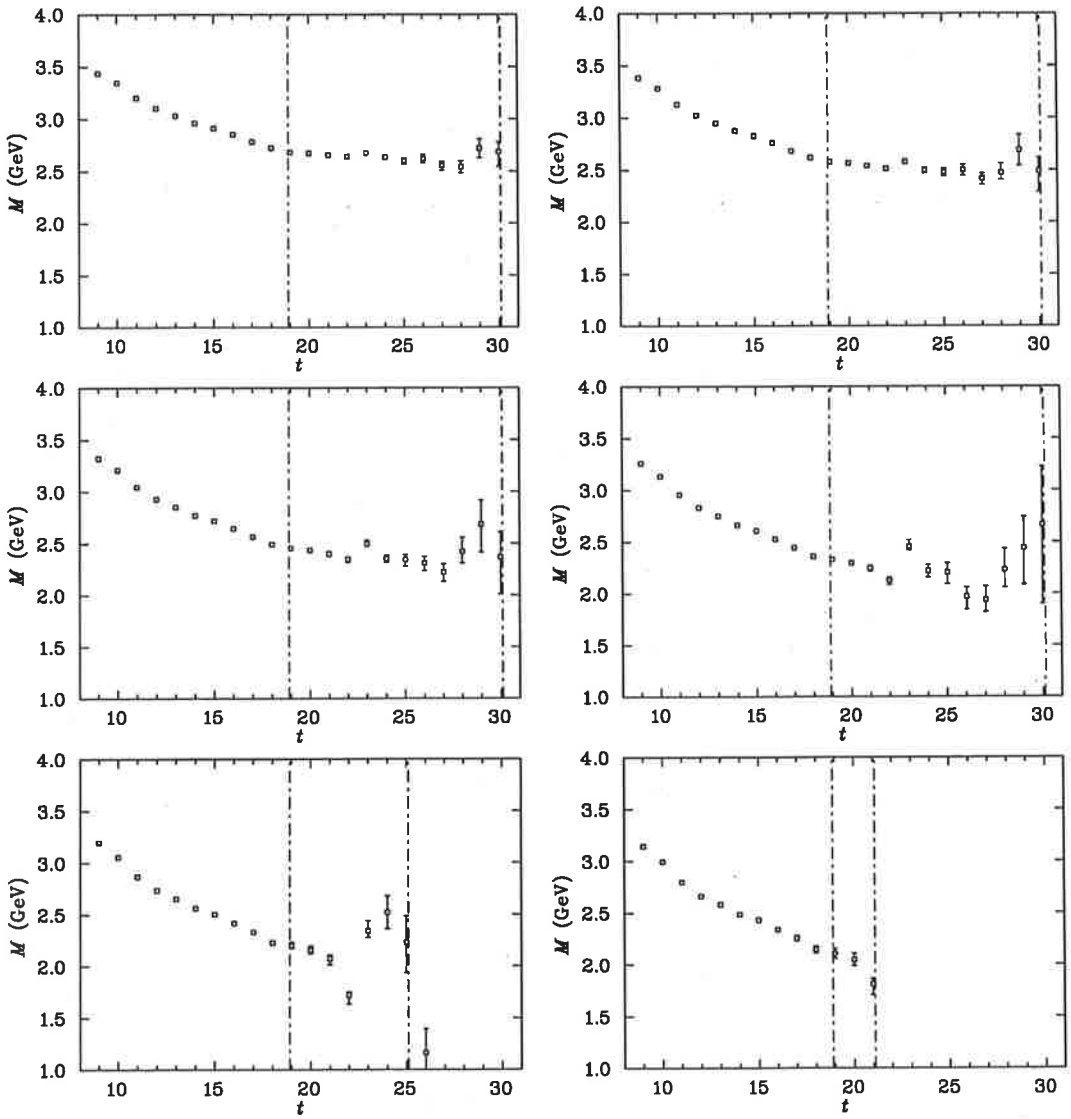

Fig. 4.19: The effective mass of the $I(J^P) = 1(1/2^-)$ state extracted with the NK^* interpolator. The data correspond to $m_\pi \simeq 830\,\text{MeV}$ (top left), 770 MeV (top right), 700 MeV (middle left), 616 MeV (middle right), 530 MeV (bottom left), and 460 MeV (bottom right).

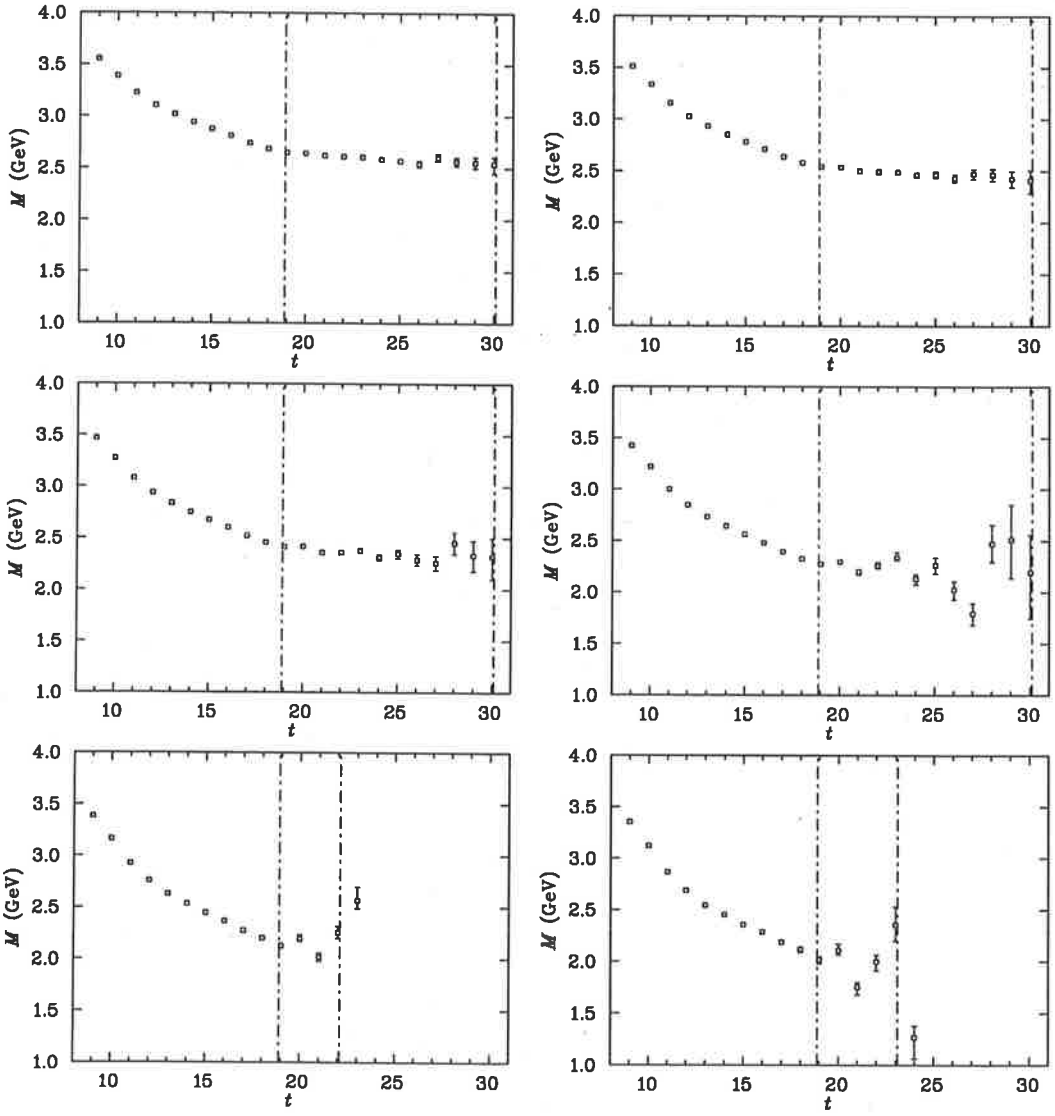

Fig. 4.20: As in Fig. 4.19 but for the $1(1/2^-)$ state extracted with the LY interpolator.

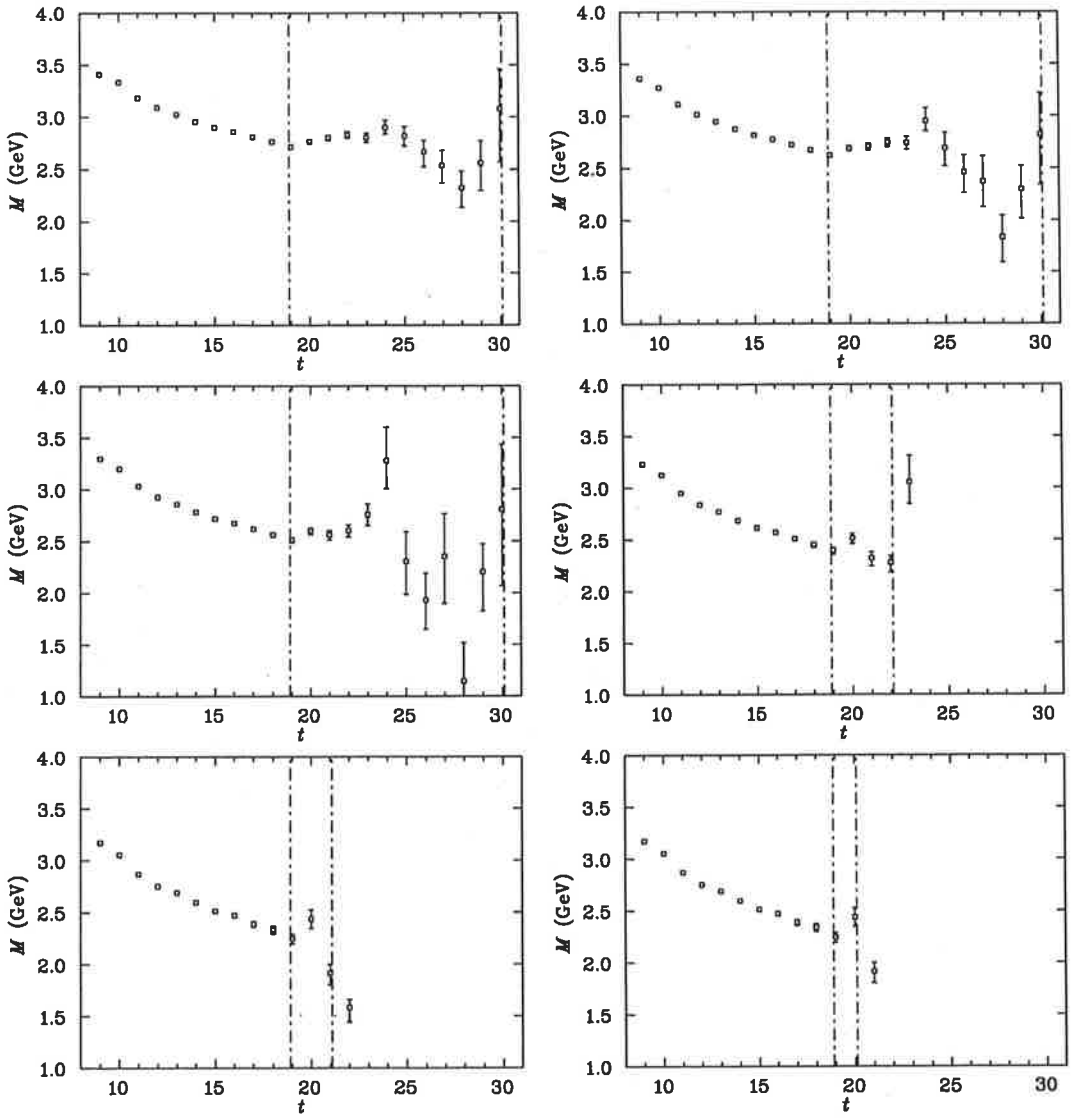

Fig. 4.21: As in Fig. 4.19 but for the $1(3/2^-)$ state extracted with the NK^* interpolator.

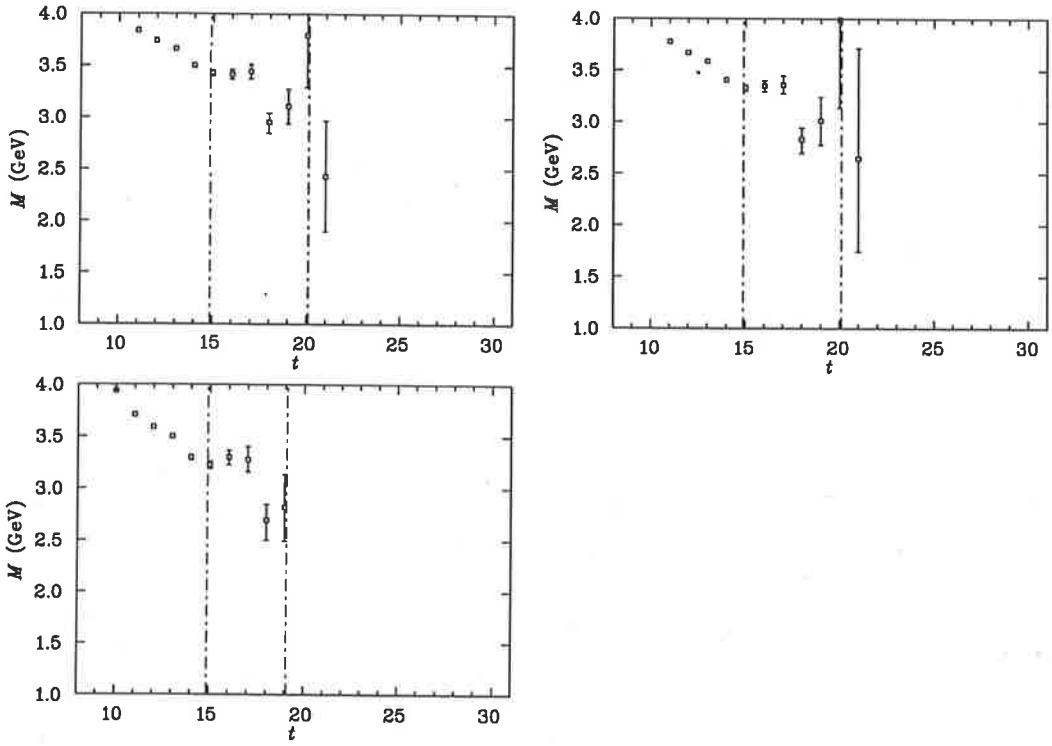

Fig. 4.22: As in Fig. 4.19 but for the $I(J^P) = 1(3/2^-)$ state extracted with the LY interpolator.

the data shown from $t \geq 15$. As in the isoscalar channel we see an apparent double plateau structure in the effective mass, however unlike the isoscalar channel the χ^2_{dof} test favours the fit at the smaller Euclidean times. The mass extracted with the LY interpolator is much greater than the lower energy two-particle states, and we can reasonably conclude that there is significant contribution to the correlation function from excited states. Clearly this interpolator is not suitable for studying this state.

Table 4.7 summarises the mass of each state extracted with our interpolators. These masses along with the relevant two particle states are shown in Fig. 4.15. Here the lowest energy decay channel of the $3/2^-$ state is the S-wave $\Delta + K$. We see that the mass of the $3/2^-$ state extracted with the NK^* interpolator (closed circles) is consistent with the $\Delta + K$ (dashed line) at the two smallest quark masses shown. However the calculation of the mass splitting between the five-quark state and the $\Delta+K$ in Table 4.8 reveals no evidence of binding.

The masses of the $1/2^-$ states extracted with the NK^* and LY interpolators are very similar, but as in the isoscalar channel the mass extracted with the LY interpolator is consistently less than the mass extracted with the NK^* interpolator. Here the discrepancy is $\sim 1.5\%$. We attribute this discrepancy to excited state contamination. The mass of this state extracted with these interpolators is consistently larger than the respective mass of the $1/2^-$ state in the isoscalar channel. In our previous study [28] we used a 2×2 correlation matrix, with the "colour singlet" and "colour fused" variations in the colour assignment of the NK interpolator, to study the isovector $1/2^-$ state. We found that the correlation matrix returned a smaller ground state mass than the "colour singlet" NK interpolator alone, and that the mass of the isoscalar and isovector, $1/2^-$ states, were the similar to $\sim 1\sigma$. So we presume that the isovector $1/2^-$ states reported

here are larger than the isoscalar $1/2^-$ states because of the additional excited state contamination from the two particle states with the Δ, which the isoscalar interpolators do not couple to.

The splitting between the mass of the $1/2^-$ states and the mass of the S-wave $N+K$ particle state and the splitting between the mass of the $3/2^-$ states and the mass of the S-wave $N + K^*$ particle state are summarised in Table. 4.8. In each case we find no evidence of binding.

4.3.4 Isovector, positive parity states

We finish our analysis with the isovector, even-parity states. The effective mass of the $1/2^+$ state extracted with the NK^* interpolator is shown in Fig. 4.24. In each case we omit the last data point in our fit. When we fit the data shown for $t \geq 17$ the χ^2_{dof} is $0.25, 0.29$ and 0.58 at each quark mass respectively. Our analysis of this state is limited to the three largest quark masses after which we judge that the ground state signal has become hidden by noise.

The effective mass of the $1/2^+$ state extracted with the LY interpolator is shown in Fig. 4.25. Again we see an apparent plateau in the effective mass data at time slices $15 - 17$ and another at larger times. In Fig. 4.26 (left) we show the χ^2_{dof} for a series of fits to the data at the largest quark mass, where the lower bound of the fit is fixed at time slice 15 and the upper bound is shown on the horizontal axes. We see that as soon as the data from time slice 18 onwards is included in the analysis the χ^2_{dof} becomes large, indicating that there is true signal corresponding to a lower energy state at $t \geq 18$.

In Fig. 4.25 (top left) the effective mass data point at time slice 25 is not contained within the vertical scale of the figure, because the signal is lost in the noise. Therefore we select time slice 24 as the upper bound of the fit in our analysis. In Fig. 4.26 (right) we show the χ^2_{dof} for a series of fits to the data at the largest quark mass, where the upper bound of the fit is fixed at time slice 24 and the lower bound is shown on the horizontal axes. We find that the $\chi^2_{\text{dof}} \simeq 1$ where for a lower bound is fixed at time slice 19. Based on this argument we fit the data shown in Fig. 4.25 for $t \geq 19$ at the three largest quark masses and $t \geq 18$ at the three smallest quark masses. For this analysis at the four largest quark masses the $\chi^2_{\text{dof}} \simeq 1$ for each fit. At the two smallest quark masses the $\chi^2_{\text{dof}} = 0.19$ and 0.01. However despite the small χ^2 at these quark masses this analysis remains our best estimate of the ground state mass.

The effective mass of the $3/2^+$ state extracted with the NK^* interpolator is shown in Figs. 4.27. We extract the mass of this state with the NK^* interpolator with a fit to the data shown where $t \geq 17$ at all quark masses. At each quark mass the $\chi^2_{\text{dof}} = 0.25, 0.14, 0.13, 0.08$ and 0.17 respectively. A fit to the data where $t \geq 16$ returns a mass much larger than in our original analysis, which we find is inconsistent with the mass extracted with the LY interpolator in this channel, and much larger than the lowest energy two-particle state. Given the systematic drift in the effective mass, our former analysis provides our best estimate of the ground state mass in this channel.

The effective mass of the $3/2^+$ state extracted with the LY interpolators is shown in Fig. 4.28, at each quark mass the last data point shown is considered to be dominated by noise and is not included in our analysis. Again we find that the effective mass plateaus around time slices $15 - 17$, before transitioning to lower energy plateau at

Table 4.7: The masses of the $I(J^P) = 1(1/2^-)$ and $I(J^P) = 1(3/2^-)$ states extracted with the NK^* and LY interpolators.

aM_π	$aM^{1/2^-}_{NK^*}$	$aM^{1/2^-}_{LY}$	$aM^{3/2^-}_{NK^*}$	$aM^{3/2^-}_{LY}$
0.540(1)	$1.726^{+0.005}_{-0.006}$	$1.698^{+0.005}_{-0.005}$	$1.795^{+0.010}_{-0.012}$	$2.206^{+0.017}_{-0.022}$
0.500(1)	$1.655^{+0.006}_{-0.007}$	$1.627^{+0.005}_{-0.006}$	$1.734^{+0.013}_{-0.016}$	$2.151^{+0.018}_{-0.025}$
0.453(1)	$1.574^{+0.007}_{-0.008}$	$1.546^{+0.006}_{-0.007}$	$1.660^{+0.016}_{-0.017}$	$2.091^{+0.023}_{-0.027}$
0.400(1)	$1.491^{+0.011}_{-0.011}$	$1.459^{+0.008}_{-0.009}$	$1.568^{+0.017}_{-0.025}$	...
0.345(2)	$1.415^{+0.018}_{-0.018}$	$1.383^{+0.012}_{-0.015}$	$1.458^{+0.027}_{-0.039}$	...
0.300(2)	$1.353^{+0.025}_{-0.033}$	$1.324^{+0.019}_{-0.018}$	$1.427^{+0.046}_{-0.059}$	...

Table 4.8: The splitting between the mass of the $I(J^P) = 1(1/2^-)$ and $I(J^P) = 1(3/2^-)$ states extracted with the NK^* and LY interpolators and the relevant two-particle states.

aM_π	$a\Delta M^{1/2^-}_{NK^*}$	$a\Delta M^{1/2^-}_{LY}$	$a\Delta M^{3/2^-}_{NK^*}$	$a\Delta M^{3/2^-}_{LY}$
0.540(1)	$0.144^{+0.005}_{-0.007}$	$0.113^{+0.006}_{-0.005}$	$0.073^{+0.009}_{-0.011}$	$0.507^{+0.017}_{-0.020}$
0.500(1)	$0.135^{+0.007}_{-0.008}$	$0.108^{+0.005}_{-0.006}$	$0.068^{+0.014}_{-0.015}$	$0.509^{+0.019}_{-0.023}$
0.453(1)	$0.117^{+0.009}_{-0.012}$	$0.103^{+0.008}_{-0.008}$	$0.058^{+0.019}_{-0.022}$	$0.511^{+0.022}_{-0.026}$
0.400(1)	$0.085^{+0.014}_{-0.021}$	$0.094^{+0.011}_{-0.015}$	$0.026^{+0.027}_{-0.032}$	...
0.345(2)	$0.073^{+0.025}_{-0.036}$	$0.091^{+0.027}_{-0.029}$	$-0.030^{+0.052}_{-0.057}$	...
0.300(2)	$0.147^{+0.037}_{-0.044}$	$0.186^{+0.036}_{-0.034}$	$-0.062^{+0.104}_{-0.096}$	...

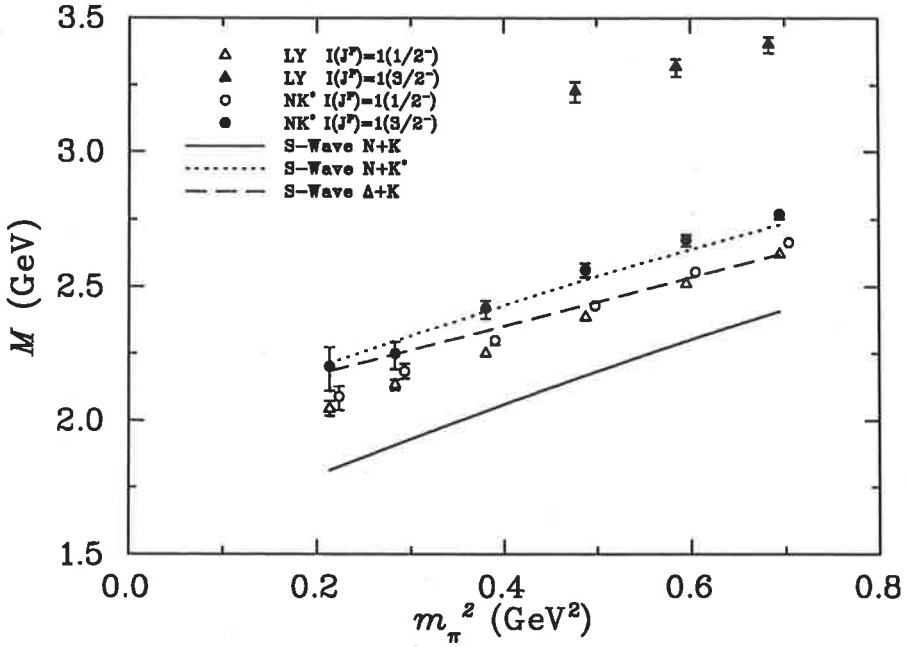

Fig. 4.23: The masses of the odd-parity, isovector spin-1/2 state (open symbols) and spin-3/2 state (closed symbols) extracted with the LY and NK^* interpolators. The data correspond to $m_\pi \simeq 830$, 770, 700, 616, 530, and 460 MeV. The data corresponding to the spin-1/2 state extracted with the NK^* interpolator has been offset horizontally for clarity.

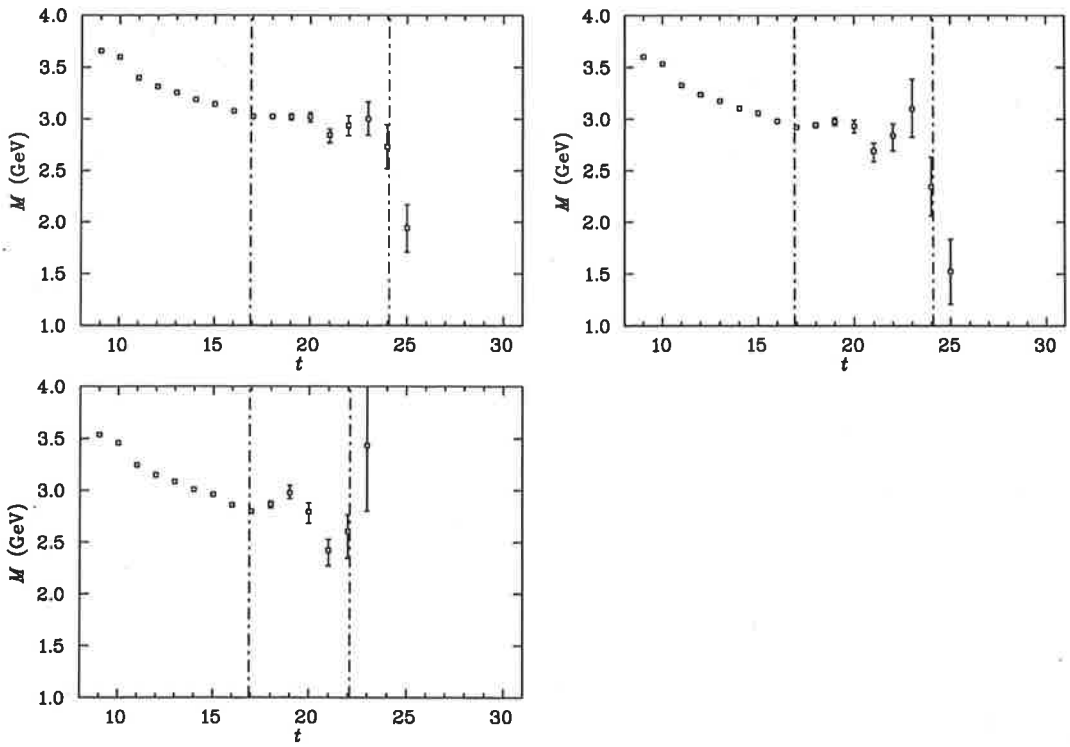

Fig. 4.24: The effective mass of the $I(J^P) = 1(1/2^+)$ state extracted with the NK^* interpolator, the data correspond to $m_\pi \simeq 830\,\text{MeV}$ (top left), 770 MeV (top right), 700 MeV (bottom left), and 616 MeV (bottom right).

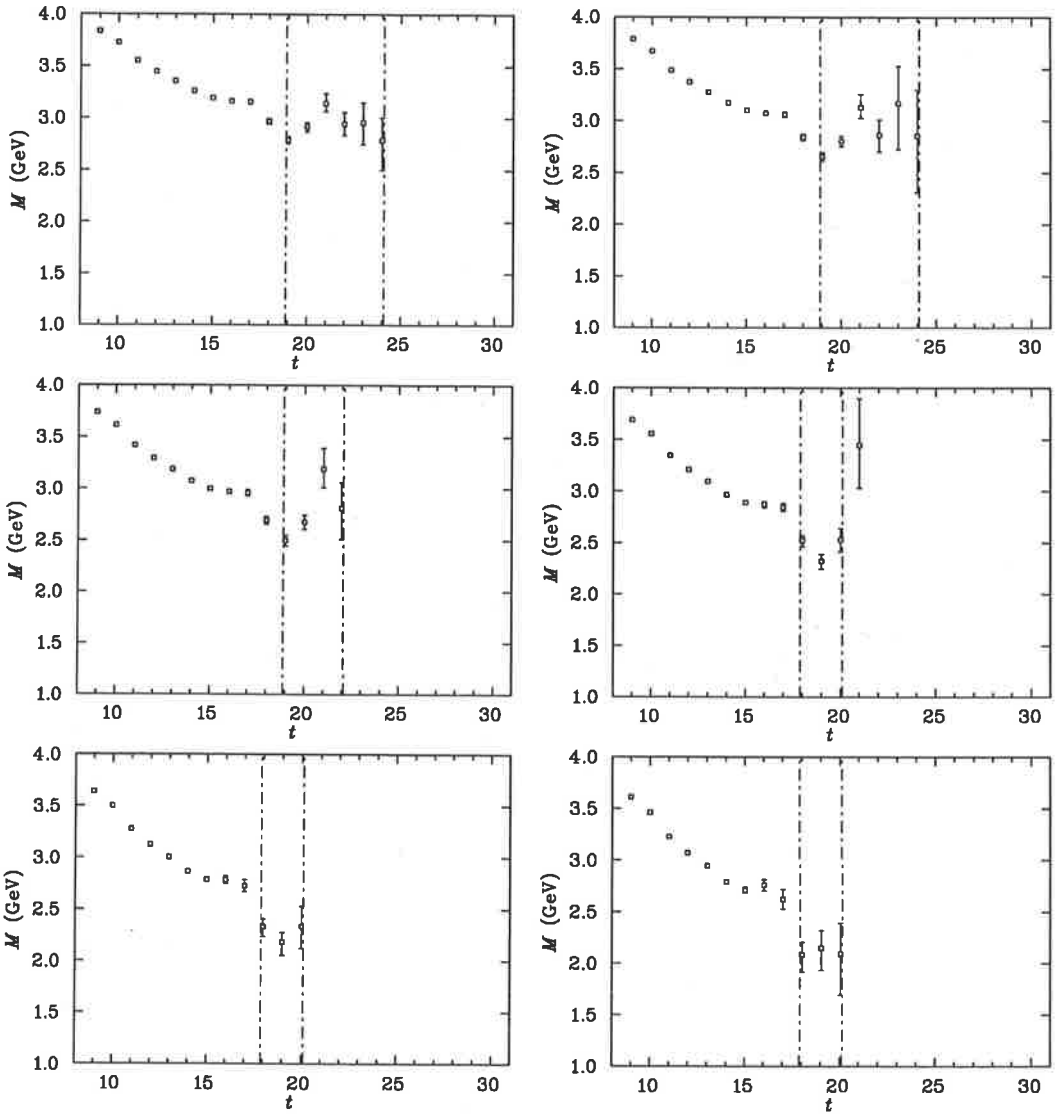

Fig. 4.25: The effective mass of the $I(J^P) = 1(1/2^+)$ state extracted with the LY interpolator, the data correspond to $m_\pi \simeq 830\,\mathrm{MeV}$ (top left), 770 MeV (top right), 700 MeV (middle left), 616 MeV (middle right), 530 MeV (bottom left), and 460 MeV (bottom right).

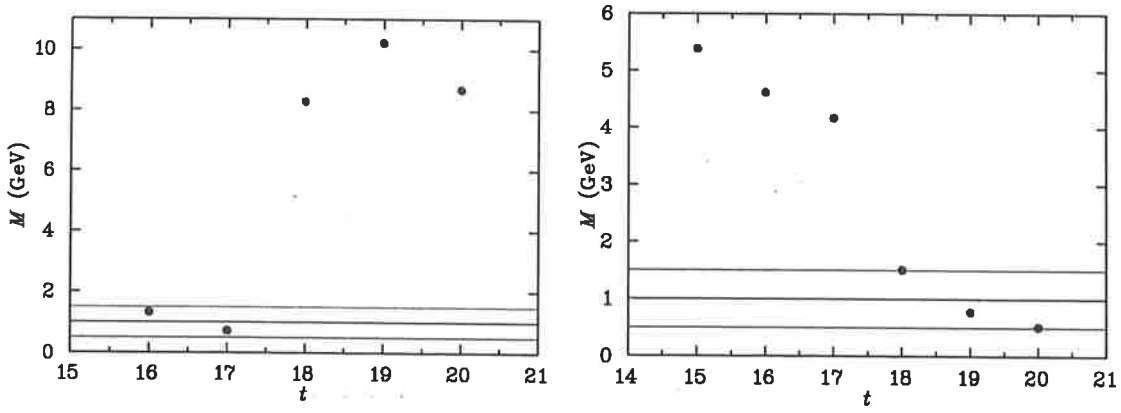

Fig. 4.26: (left) The $\chi^2_{\rm dof}$ for a series of possible fits of the $1(1/2^+)$ state with a lower bound fixed at time slice 15 and an upper bound shown on the horizontal axis. (right) The $\chi^2_{\rm dof}$ for a series of possible fits with the upper bound fixed at time slice 24 and the lower bound is shown on the horizontal axis. The data correspond to $m_\pi \simeq 830\,\text{MeV}$. The horizontal lines correspond to $\chi^2_{\rm dof}$ of 0.5,1.0(ideal) and 1.5

later times. As in the $I(J^P) = 0(3/2^-)$ and $1(1/2^-)$ states extracted with the LY interpolator and the $I(J^P) = 0(3/2^+)$ state extracted with the NK^* interpolator, we must be careful to satisfy the asymptotic limit in Eq. 2.16 to recover the correct ground state mass. In Fig. (4.29) (left) we show the $\chi^2_{\rm dof}$ for a series of fits at the largest quark mass, where the lower bound of the fit is fixed at time slice 15 and the upper bound is shown on the horizontal axis. As soon as the data from time slice 18 is included in the fit, the χ^2 becomes large. This indicates that the data at the larger times is true signal dominated by a lower energy state. In Fig. 4.28 (top left) the next data point after time slice 25 is not contained on the scale and so is lost to noise. Therefore an upper bound of the fit fixed at time slice 25 is reasonable. In Fig. 4.29 (right) we show the $\chi^2_{\rm dof}$ for a series of fits with an upper bound fixed at time slice 25 and a lower bound shown on the horizontal axis. We find a $\chi^2_{\rm dof} = 1.5$ where the lower bound is time slice 18, which is acceptable. Following these arguments we select a fit to the data shown for ≥ 18. The $\chi^2_{\rm dof} = 1.52, 1.39, 0.92, 0.47$ and ~ 0 respectively. Although most of these χ^2 values are not ideal, this analysis returns our best estimate of the asymptotic ground state mass.

Table 4.9 contains the masses of the even-parity, isovector, spin-1/2 and spin-3/2 states extracted with the LY and NK^* interpolators. They are summarised in Fig. 4.15 along with the relevant two particle states. We find that the mass of the $3/2^+$ state extracted with the NK^* interpolator (closed circles) is slightly larger than the mass of this state extracted with the LY interpolator (closed triangles). Possible excited state contamination in the mass extracted with the NK^* interpolator might explain the small discrepancy. In each case the mass extracted is much greater than the lowest energy two-particle state with these quantum numbers, namely the P-wave $N + K$ (solid line). So unlike the isoscalar $3/2^+$ state we clearly find no evidence of binding despite the use of the same analysis techniques to obtain the true ground state.

In the $1(1/2^+)$ channel we find that the masses extracted with the LY (open triangles) and NK^* (open circles) interpolators are in agreement. Given the greater precision in our calculation achieved in this study, we are able to fit the effective mass

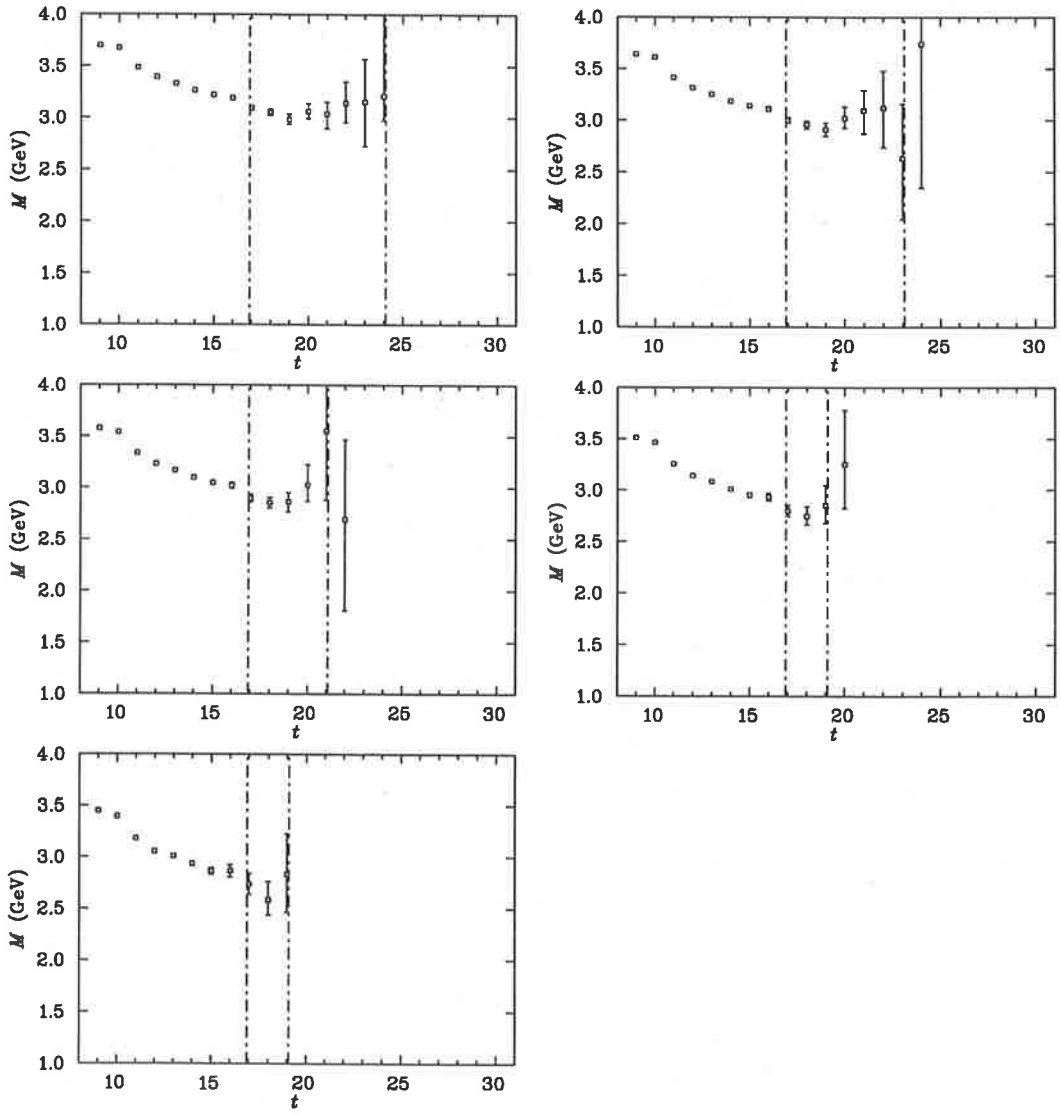

Fig. 4.27: As in Fig. 4.25 but for the $1(3/2^+)$ state extracted with the NK^* interpolator.

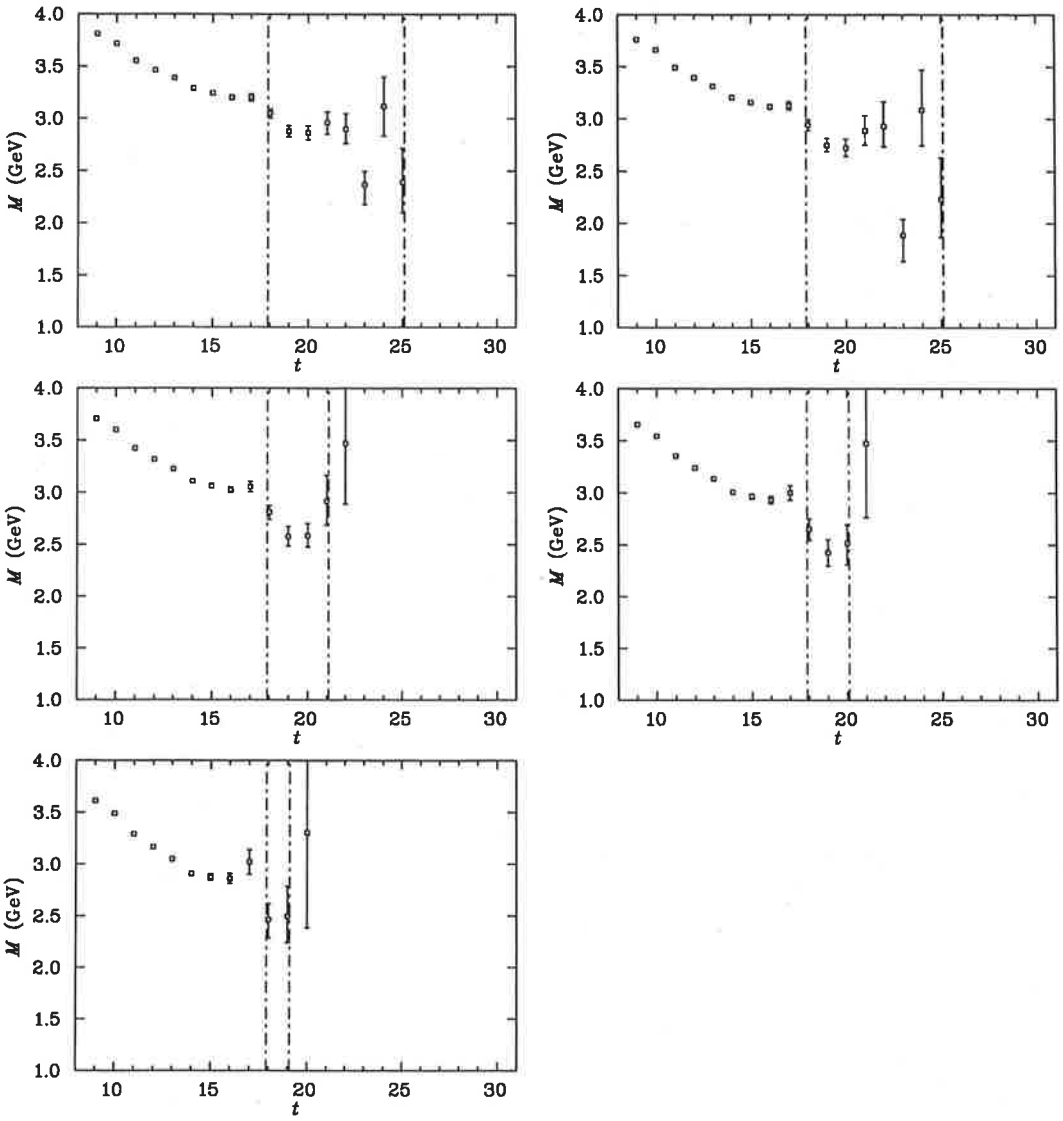

Fig. 4.28: As in Fig. 4.25 but for the $1(3/2^+)$ state extracted with the LY interpolator.

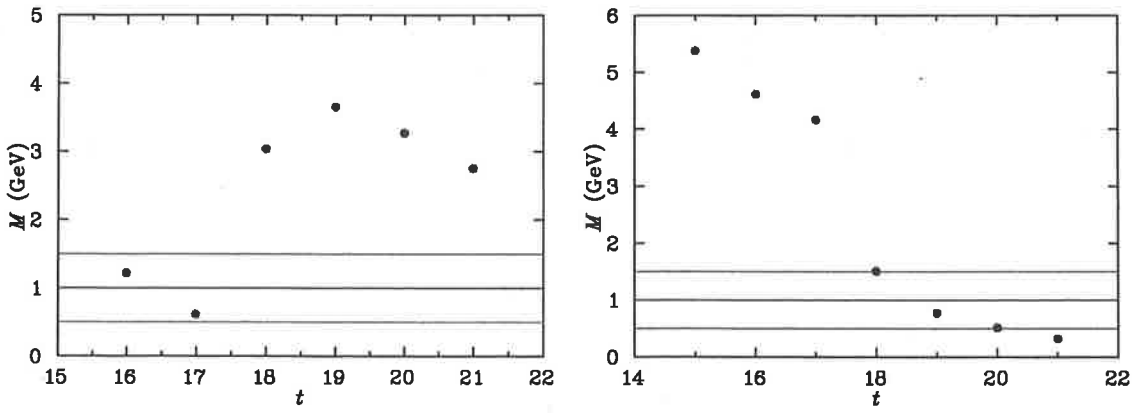

Fig. 4.29: As in Fig. 4.26, but for the spin-3/2 state extracted with the LY interpolator.

data extracted with the NK^* interpolator at larger Euclidean times compared to [29]. This new analysis extracts a ground state mass of the even-parity spin-1/2 isovector which is more consistent with the P-wave $N + K$. It is also consistent with the ground state mass extracted with the spin-1/2 interpolator in Chapter 3.

For comparison we also show the mass of the isovector, even-parity, spin-1/2 (plus signs) and spin-3/2 (crosses) states extracted with the LY interpolator where we incorrectly fit the effective mass data at time slice $15 - 17$. We find that in each case the mass extracted is significantly more massive that both the lowest energy two particle state and mass of the same state extracted with the NK^* interpolator, and so the mass extracted with the LY interpolator, with the alternative naive fit to the data at the earlier time slices is clearly not the ground state mass.

Table 4.10 contains the mass splitting between the non-interacting P-wave $N + K$ two particle state and the mass of the $1/2^+$ state extracted with the LY and NK^* interpolators. As with the $3/2^+$ state in this channel we find no evidence of binding.

4.4 Summary

We have extended our initial study of spin-3/2 pentaquark interpolators [29] to include the additional terms in the correlation function given by Eq. (2.3) with $\mu = 1 - 4, \nu = 1 - 4$ and have expanded the ensemble from 290 to 396 configurations. We also include an analysis with the χ_{LY} interpolator that also accesses spin-3/2 states. We find evidence of the standard lattice resonance signature in the $0(3/2^+)$ state extracted with the NK^* interpolator in quenched lattice QCD. We find that the effective mass of the same state extracted with LY interpolator displays a systematic drift to values consistent with the NK^* results at light quark masses. This evidence of binding is now confirmed.

We have reviewed our Jackknife estimate of the standard error and found that the "sort and cut" method of estimating the error is better than making the standard assumption that the distribution of Jackknife samples is Gaussian.

We demonstrated that the discrepancy between the extraction of the mass of the $0(3/2^+)$ state with the NK^* interpolator in the work of Doi et al. [120] and our earlier work [29] is entirely due to Doi et al. [120] fitting the effective mass data at earlier Euclidean times than our in study. We demonstrate that the criticism [120] that our analysis [29] has poorer statistics is incorrect because the size of the error bar depends on the lattice volume times the number of configurations. We show that a fit to our effective mass data in [29] at time slice $13 - 17$ extracts a mass consistent with the calculation in [120], has smaller error bars and is not consistent with the asymptotic limit in Eq. (2.16). Otherwise in the $0(3/2^-)$ channel the two studies [120] and [29] are in excellent agreement.

We have shown that the double plateau structure found in the effective mass data of the $0(3/2^-)$, $1(1/2^+)$ and $1(3/2^+)$ states extracted with the LY interpolator and the $0(3/2^+)$ NK^* interpolator makes it essential to test for true signal at the large Euclidean times in order to recover the ground state mass. We review our analysis methods that deal with this test and once again stress that we must not judge the quality of the fit based entirely on the size of our error bars or the visual nature of the data.

We explored isoscalar and isovector, spin-1/2 and spin-3/2, even and odd-parity

Table 4.9: The masses of the $I(J^P) = 1(1/2^+)$ and $I(J^P) = 1(3/2^+)$ states extracted with the NK^* and LY interpolators.

aM_π	$aM_{NK^*}^{1/2^+}$	$aM_{LY}^{1/2^+}$	$aM_{NK^*}^{3/2^+}$	$aM_{LY}^{3/2^+}$
0.540	$1.957^{+0.009}_{-0.010}$	$1.856^{+0.021}_{-0.023}$	$1.989^{+0.013}_{-0.014}$	$1.925^{+0.024}_{-0.023}$
0.500	$1.899^{+0.010}_{-0.014}$	$1.779^{+0.023}_{-0.025}$	$1.935^{+0.017}_{-0.017}$	$1.856^{+0.031}_{-0.028}$
0.453	$1.830^{+0.013}_{-0.017}$	$1.686^{+0.026}_{-0.030}$	$1.873^{+0.023}_{-0.023}$	$1.776^{+0.038}_{-0.041}$
0.400	...	$1.610^{+0.030}_{-0.039}$	$1.809^{+0.034}_{-0.035}$	$1.675^{+0.054}_{-0.061}$
0.345	...	$1.498^{+0.047}_{-0.065}$	$1.751^{+0.067}_{-0.058}$	$1.604^{+0.097}_{-0.110}$
0.300	...	$1.362^{+0.074}_{-0.104}$	...	...

Table 4.10: The splittings between the mass of the $I(J^P) = 1(1/2^+)$ and $I(J^P) = 1(3/2^+)$ states extracted with the NK^* and LY interpolators and the relevant two-particle state.

aM_π	$a\Delta M_{NK^*}^{1/2^+}$	$a\Delta M_{LY}^{1/2^+}$	$a\Delta M_{NK^*}^{3/2^+}$	$a\Delta M_{LY}^{3/2^+}$
0.540	$0.400^{+0.009}_{-0.011}$	$0.166^{+0.020}_{-0.022}$	$0.295^{+0.014}_{-0.015}$	$0.064^{+0.026}_{-0.024}$
0.500	$0.410^{+0.012}_{-0.012}$	$0.154^{+0.023}_{-0.022}$	$0.304^{+0.018}_{-0.017}$	$0.052^{+0.032}_{-0.029}$
0.453	$0.419^{+0.014}_{-0.017}$	$0.137^{+0.026}_{-0.029}$	$0.314^{+0.025}_{-0.021}$	$0.034^{+0.037}_{-0.039}$
0.400	...	$0.139^{+0.027}_{-0.040}$	$0.326^{+0.034}_{-0.042}$	$0.002^{+0.053}_{-0.058}$
0.345	...	$0.102^{+0.047}_{-0.064}$	$0.341^{+0.066}_{-0.061}$	$-0.003^{+0.096}_{-0.108}$
0.300	...	$0.031^{+0.072}_{-0.109}$	...	...

five quark states with the NK^* and LY interpolating fields in quenched lattice QCD. In our analysis of the spin-1/2 states we find a small discrepancy at the largest quark masses between the mass extracted with the NK^* and LY interpolators. We also find that the mass of the isoscalar spin-1/2 states extracted with the NK^* and LY interpolators are consistently larger than in our previous study [28], where a correlation matrix was used to access the lowest energy state. We conclude here then that these small discrepancies are due to excited state contamination. In a future study of five quark states with these interpolators it will be important therefore to use a correlation matrix to remove the excited state contamination.

As in [28, 29] we search for evidence of binding to identify favourable quantum numbers for the existence of the Θ^+ resonance on the lattice. We emphasize that lack of evidence of binding does not exclude the possible existence of the Θ^+ in the other channels we explored. We find clear evidence of binding in the $0(3/2^+)$ state extracted with the NK^* interpolator and a confirmation of this via the LY interpolator. An analysis of the volume dependence of this signal remains to determine if this evidence of binding suggests a $0(3/2^+)$ Θ^+ candidate in quenched lattice QCD. Of course, it is important to repeat these calculations in full QCD, so we can determine if the evidence of binding persists in the full theory.

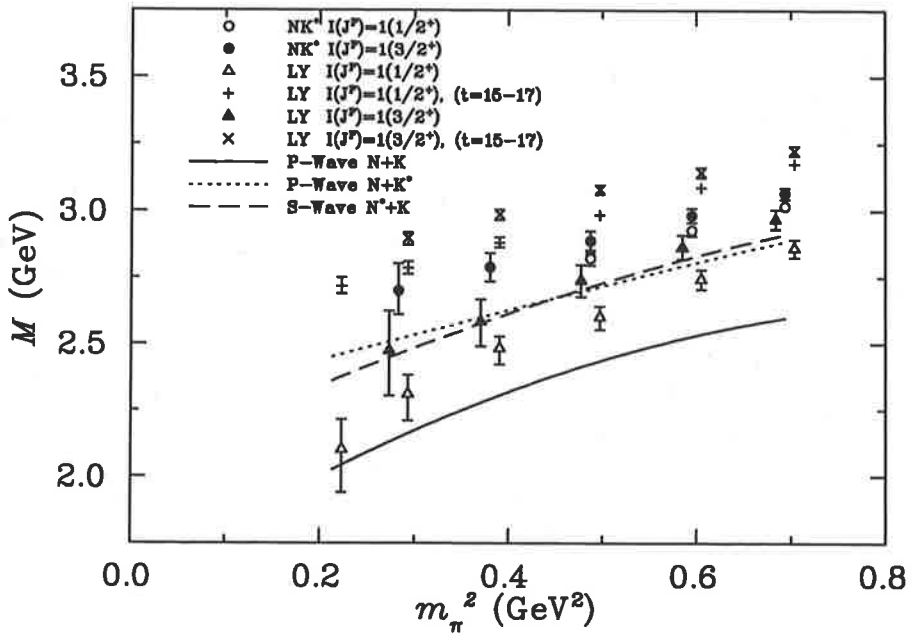

Fig. 4.30: As in Fig. 4.23 but for the isovector even-parity pentaquark states. Here the states extracted with the LY interpolator have been offset horizontally for clarity.

5

Conclusions

In this thesis we have performed a comprehensive analysis of the nucleon and Δ spectrum and of the spectrum of pentaquark states in QQCD. In Chapter 2 of this thesis we have extended the earlier work of [18] and [27] with a high statistics calculation of the spectrum of nucleon and Δ resonances with a large volume lattice. We provide a complete review of how we extract baryon masses in lattice QCD. We extend the earlier work with 2×2 and 3×3 correlation matrix analyses over a basis of our three nucleon interpolators.

With a precise calculation of the nucleon spectrum, see Fig. 2.2, we find that the level ordering of the odd parity spin-1/2 and spin-3/2 states on the lattice is reversed at our larger quark masses compared to the physical spectrum. We noted that it is indeed this reversed ordering that is predicted by quark models. Another interesting feature of this calculation is the observation of a mass consistent with the S-wave $N+\pi$ and S-wave $N+\eta'$ multi-hadron state in the odd parity spin-1/2 channel at our second smallest quark mass. The realisation of a transition to lower energy multi-hadron state at light quark masses must guide future calculations as we move closer to the chiral limit.

With our correlation matrix analyses we find that the χ_3 interpolator has a strong overlap with both the χ_1 and χ_2 interpolators. Pursuing this further with a Fierz transformation, we find that the χ_3 interpolator can be expressed in terms of χ_1 and χ_2, plus other terms. In our analysis of the 3×3 correlation matrix, see Fig. 2.16, we find no evidence of a Roper like excited state of the nucleon. Therefore what overlap the nucleon interpolators have with such a state must be small if non-zero.

In the odd parity channel we do not find evidence of the excited state reported in [18]. Our conclusion is that the large amount of fermion source smearing employed in this study has removed evidence of this excited state. A careful study of the optimal source smearing prescription for extracting the excited hadron spectrum remains as future work. In practice this should be combined with an expansion of our interpolator basis with variations of the source and sink smearing prescriptions, as in Burch et al. [33].

In our analysis of the Δ resonances, see Fig. 2.20, we find that the level ordering of the odd parity states is consistent with the physical spectrum. With improved statistics over earlier calculations, we also find that the mass of the even parity spin-1/2 Δ is more consistent with the masses of the odd parity states, as in the physical spectrum. Finally, as we probe closer to the chiral limit we begin to see the chiral curvature in the mass of the Δ^{++} that has been predicted by chiral effective field theory.

With a strong foundation in the analysis of the spectrum of nucleon and Δ resonances we extend our study to an analysis of the pentaquark spectrum. Central to this work is the formulation of a robust lattice resonance signature. In the study of conventional resonances the standard lattice resonance signature is binding at quark masses near the physical regime. This evidence of attraction is universally observed in our study of nucleon and Δ resonances. We note that the absence of binding cannot rule out the existence of the Θ^+ pentaquark. However, the presence of attraction is vital to the formation of a resonance.

In Chapter 3 we search for evidence of the Θ^+ spin-1/2 state using a comprehensive

basis of local pentaquark interpolating fields. We include a correlation matrix analysis with the NK and $\widetilde{NK}$ pentaquark interpolators Eqs. (3.1) and (3.2) in the odd parity channels. In the isovector channel we extract two states. The ground state has a mass similar to the S-wave $N+K$. The excited state has a mass similar to the S-wave $N+K^*$. In each case the mass of the state extracted is larger than the multi-hadron state, which is evidence of a repulsive interaction due to the finite volume of the lattice. Similarly we find evidence of repulsion in the other odd parity channels with every interpolator used. In the even parity channels we find that the mass extracted is generally much larger than the lowest energy multi-hadron state. The exception is the mass of the $0(1/2^+)$ state extracted with the PS interpolator, which we find is consistent with the P-wave $N+K$ energy, but binding is not ruled out.

In Chapter 4 we expanded our search for the Θ^+ with an analysis of spin-3/2 states. Using the formalism developed in Chapter 2 we extract the masses of spin-1/2 and spin-3/2 states with our NK^* and LY interpolators of Eqs. (4.2) and (4.8). It was with the former interpolator that we originally uncovered evidence of attraction in the $0(3/2^+)$ channel in our first study [29]. In this thesis we reaffirm the evidence of binding with the mass extracted with the NK^* interpolator and confirm it with the LY interpolator, see Fig. 4.15.

In our analysis of the effective mass data extracted with each interpolator we consistently find what we describe as a double plateau structure. An important feature of this double plateau structure is that a limited fit to the effective mass data at small Euclidean times can have an acceptable χ^2_{dof}, but one does not extract the ground state mass. We conclusively demonstrate that we must not ignore the signal at large Euclidean times purely on the basis of aesthetics. A rigorous analysis of the effect on the χ^2_{dof} of including data at larger Euclidean times is mandatory in correctly extracting the ground state of the correlator. Further we show that the discrepancy between our calculation of the mass of the $0(3/2^+)$ state and the analysis of Doi et al. [120] is because Doi et al. fit the data at much smaller Euclidean times and ignore the large Euclidean time points.

We have clearly established that the $0(3/2^+)$ channel is worthy of future study. As a priority we should focus our attention on measuring the volume dependence of the resonance signature. This analysis should include an effort to improve our statistics so that we can probe closer towards the chiral limit. Clearly we must also repeat this simulation in full QCD to see if the resonance signature persists in the full theory.

Bibliography

[1] **LEPS Collaboration** Collaboration, T. Nakano *et. al.*, *Observation of $s = +1$ baryon resonance in photo-production from neutron*, *Phys. Rev. Lett.* **91** (2003) 012002 [hep-ex/0301020].

[2] K. G. Wilson, *Confinement of quarks*, *Phys. Rev.* **D10** (1974) 2445–2459.

[3] M. Creutz, *Monte carlo study of quantized su(2) gauge theory*, *Phys. Rev.* **D21** (1980) 2308–2315.

[4] N. Cabibbo and E. Marinari, *A new method for updating su(n) matrices in computer simulations of gauge theories*, *Phys. Lett.* **B119** (1982) 387–390.

[5] H. J. Rothe, *Lattice Gauge Theories: an Inroduction.* World Scientific, 1994.

[6] F. Bissey *et. al.*, *Gluon flux-tube distribution and linear confinement in baryons*, hep-lat/0606016.

[7] G. S. Bali, K. Schilling and C. Schlichter, *Observing long color flux tubes in su(2) lattice gauge theory*, *Phys. Rev.* **D51** (1995) 5165–5198 [hep-lat/9409005].

[8] E. Eichten, K. Gottfried, T. Kinoshita, K. D. Lane and T.-M. Yan, *Charmonium: Comparison with experiment*, *Phys. Rev.* **D21** (1980) 203.

[9] C. Michael, *The running coupling from lattice gauge theory*, *Phys. Lett.* **B283** (1992) 103–106 [hep-lat/9205010].

[10] T. R. Klassen, *The (lattice) qcd potential and coupling: How to accurately interpolate between multiloop qcd and the string picture*, *Phys. Rev.* **D51** (1995) 5130–5152.

[11] R. G. Edwards, U. M. Heller and T. R. Klassen, *Accurate scale determinations for the wilson gauge action*, *Nucl. Phys.* **B517** (1998) 377–392 [hep-lat/9711003].

[12] F. D. R. Bonnet, P. O. Bowman, D. B. Leinweber, A. G. Williams and J. M. Zanotti, *Infinite volume and continuum limits of the landau-gauge gluon propagator*, *Phys. Rev.* **D64** (2001) 034501 [hep-lat/0101013].

[13] M. Luscher and P. Weisz, *On-shell improved lattice gauge theories*, *Commun. Math. Phys.* **97** (1985) 59.

[14] R. Sommer, *A new way to set the energy scale in lattice gauge theories and its applications to the static force and alpha-s in su(2) yang-mills theory*, *Nucl. Phys.* **B411** (1994) 839–854 [hep-lat/9310022].

[15] **CSSM Lattice Collaboration** Collaboration, J. M. Zanotti *et. al.*, *Hadron masses from novel fat-link fermion actions*, *Phys. Rev.* **D65** (2002) 074507 [hep-lat/0110216].

[16] F. D. R. Bonnet, D. B. Leinweber and A. G. Williams, *General algorithm for improved lattice actions on parallel computing architectures*, *J. Comput. Phys.* **170** (2001) 1–17 [hep-lat/0001017].

[17] D. B. Leinweber *et. al.*, *Flic fermions and hadron phenomenology*, *Eur. Phys. J.* **A18** (2003) 247 [nucl-th/0211014].

[18] W. Melnitchouk *et. al.*, *Excited baryons in lattice qcd*, *Phys. Rev.* **D67** (2003) 114506 [hep-lat/0202022].

[19] S. Boinepalli, W. Kamleh, D. B. Leinweber, A. G. Williams and J. M. Zanotti, *Improved chiral properties of flic fermions*, hep-lat/0405026.

[20] **MILC Collaboration** Collaboration, T. DeGrand, *Simple observables from fat link fermion actions*, *Phys. Rev.* **D60** (1999) 094501 [hep-lat/9903006].

[21] M. Falcioni, M. L. Paciello, G. Parisi and B. Taglienti, *Again on su(3) glueball mass*, *Nucl. Phys.* **B251** (1985) 624–632.

[22] **APE Collaboration** Collaboration, M. Albanese *et. al.*, *Glueball masses and string tension in lattice qcd*, *Phys. Lett.* **B192** (1987) 163.

[23] B. Sheikholeslami and R. Wohlert, *Improved continuum limit lattice action for qcd with wilson fermions*, *Nucl. Phys.* **B259** (1985) 572.

[24] S. Bilson-Thompson, F. D. R. Bonnet, D. B. Leinweber and A. G. Williams, *Cooling for instantons and the wrath of nahm*, *Nucl. Phys. Proc. Suppl.* **109A** (2002) 116–120 [hep-lat/0112034].

[25] S. O. Bilson-Thompson, D. B. Leinweber and A. G. Williams, *Highly-improved lattice field-strength tensor*, *Ann. Phys.* **304** (2003) 1–21 [hep-lat/0203008].

[26] S. Gusken, *A study of smearing techniques for hadron correlation functions*, *Nucl. Phys. Proc. Suppl.* **17** (1990) 361–364.

[27] **CSSM Lattice Collaboration** Collaboration, J. M. Zanotti *et. al.*, *Spin-3/2 nucleon and delta baryons in lattice qcd*, *Phys. Rev.* **D68** (2003) 054506 [hep-lat/0304001].

[28] B. G. Lasscock *et. al.*, *Search for the pentaquark resonance signature in lattice qcd*, *Phys. Rev.* **D72** (2005) 014502 [hep-lat/0503008].

[29] B. G. Lasscock *et. al.*, *Spin 3/2 pentaquark resonance signature in lattice qcd*, *Phys. Rev.* **D72** (2005) 074507 [hep-lat/0504015].

[30] **Bern-Graz-Regensburg** Collaboration, D. Brommel *et. al.*, *Excited nucleons with chirally improved fermions*, *Phys. Rev.* **D69** (2004) 094513 [hep-ph/0307073].

[31] F. X. Lee *et. al.*, *Excited baryons from bayesian priors and overlap fermions*, *Nucl. Phys. Proc. Suppl.* **119** (2003) 296–298 [hep-lat/0208070].

[32] K. Sasaki and S. Sasaki, *Excited baryon spectroscopy from lattice qcd: Finite size effect and hyperfine mass splitting*, *Phys. Rev.* **D72** (2005) 034502 [hep-lat/0503026].

[33] T. Burch *et. al.*, *Excited hadrons on the lattice: Baryons*, *Phys. Rev.* **D74** (2006) 014504 [hep-lat/0604019].

[34] J. M. Zanotti, B. Lasscock, D. B. Leinweber and A. G. Williams, *Scaling of flic fermions*, *Phys. Rev.* **D71** (2005) 034510 [hep-lat/0405015].

[35] S. Boinepalli, D. B. Leinweber, A. G. Williams, J. M. Zanotti and J. B. Zhang, *Precision electromagnetic structure of octet baryons in the chiral regime*, hep-lat/0604022.

[36] **UKQCD Collaboration** Collaboration, C. McNeile and C. Michael, *Mixing of scalar glueballs and flavour-singlet scalar mesons*, *Phys. Rev.* **D63** (2001) 114503 [hep-lat/0010019].

[37] L. Zhou and F. X. Lee, *Spin-3/2 baryons from an anisotropic lattice qcd action*, hep-lat/0604023.

[38] Y. Chung, H. G. Dosch, M. Kremer and D. Schall, *Baryon sum rules and chiral symmetry breaking*, *Nucl. Phys.* **B197** (1982) 55.

[39] **Particle Data Group** Collaboration, S. Eidelman *et. al.*, *Review of particle physics*, *Phys. Lett.* **B592** (2004) 1.

[40] D. B. Leinweber, *Nucleon properties from unconventional interpolating fields*, *Phys. Rev.* **D51** (1995) 6383–6393 [nucl-th/9406001].

[41] **CLAS Collaboration** Collaboration, S. Stepanyan *et. al.*, *Observation of an exotic $s = +1$ baryon in exclusive photoproduction from the deuteron*, *Phys. Rev. Lett.* **91** (2003) 252001 [hep-ex/0307018].

[42] **CLAS Collaboration** Collaboration, V. Kubarovsky *et. al.*, *Observation of an exotic baryon with $s = +1$ in photoproduction from the proton*, *Phys. Rev. Lett.* **92** (2004) 032001 [hep-ex/0311046].

[43] **SAPHIR Collaboration** Collaboration, J. Barth *et. al.*, *Observation of the positive-strangeness pentaquark theta+ in photoproduction with the saphir detector at elsa*, hep-ex/0307083.

[44] **HERMES Collaboration** Collaboration, A. Airapetian *et. al.*, *Evidence for a narrow $-s-$ $= 1$ baryon state at a mass of 1528-mev in quasi-real photoproduction*, *Phys. Lett.* **B585** (2004) 213 [hep-ex/0312044].

[45] **DIANA Collaboration** Collaboration, V. V. Barmin *et. al.*, *Observation of a baryon resonance with positive strangeness in k+ collisions with xe nuclei*, *Phys. Atom. Nucl.* **66** (2003) 1715–1718 [hep-ex/0304040].

[46] **COSY-TOF Collaboration** Collaboration, M. Abdel-Bary *et. al.*, *Evidence for a narrow resonance at 1530-mev/c**2 in the k0 p system of the reaction p p –¿ sigma+ k0 p from the cosy- tof experiment*, *Phys. Lett.* **B595** (2004) 127–134 [hep-ex/0403011].

[47] **SVD Collaboration** Collaboration, A. Aleev *et. al.*, *Observation of narrow baryon resonance decaying into p k0(s) in p a interactions at 70-gev/c with svd-2 setup*, hep-ex/0401024.

[48] P. Z. Aslanyan, V. N. Emelyanenko and G. G. Rikhkvitzkaya, *Observation of s = +1 narrow resonances in the system k0(s) p from* $p + c - 3_h - 8$*collision at 10-gev/c*, hep-ex/0403044.

[49] A. E. Asratyan, A. G. Dolgolenko and M. A. Kubantsev, *Evidence for formation of a narrow k0(s) p resonance with mass near 1533-mev in neutrino interactions*, *Phys. Atom. Nucl.* **67** (2004) 682–687 [hep-ex/0309042].

[50] L. Camilleri, "presented at neutrinos 2004 paris." http://neutrino2004.in2p3.fr/slides/tuesday/camilleri.ps, 2004.

[51] **ZEUS Collaboration** Collaboration, S. Chekanov *et. al.*, *Evidence for a narrow baryonic state decaying to k0(s) p and k0(s) anti-p in deep inelastic scattering at hera*, *Phys. Lett.* **B591** (2004) 7–22 [hep-ex/0403051].

[52] **HERMES Collaboration** Collaboration, W. Lorenzon, *Pentaquark search at hermes*, hep-ex/0411027.

[53] S. Nussinov, *Some comments on the putative theta+ (1543) exotic state*, hep-ph/0307357.

[54] R. A. Arndt, I. I. Strakovsky and R. L. Workman, *K+ nucleon scattering and exotic s = +1 baryons*, *Phys. Rev.* **C68** (2003) 042201 [nucl-th/0308012].

[55] J. Haidenbauer and G. Krein, *Influence of a z(1540)+ resonance on k+ n scattering*, *Phys. Rev.* **C68** (2003) 052201 [hep-ph/0309243].

[56] R. N. Cahn and G. H. Trilling, *Experimental limits on the width of the reported theta(1540)+*, *Phys. Rev.* **D69** (2004) 011501 [hep-ph/0311245].

[57] W. R. Gibbs, *The pentaquark in k+ d total cross section data*, *Phys. Rev.* **C70** (2004) 045208 [nucl-th/0405024].

[58] B. K. Jennings and K. Maltman, *Z* resonances: Phenomenology and models*, *Phys. Rev.* **D69** (2004) 094020 [hep-ph/0308286].

[59] F. E. Close and J. J. Dudek, *Pentaquark symmetries, selection rules and another potentially narrow state*, *Phys. Lett.* **B586** (2004) 75–82 [hep-ph/0401192].

[60] T. Burns, F. E. Close and J. J. Dudek, *Pentaquark implications for exotic mesons*, *Phys. Rev.* **D71** (2005) 014017 [hep-ph/0411160].

[61] K. Maltman, *Constituent quark models and pentaquark baryons*, hep-ph/0412328.

[62] **ALEPH Collaboration** Collaboration, S. Schael *et. al.*, *Search for pentaquark states in z decays*, *Phys. Lett.* **B599** (2004) 1–16.

[63] C. Lin, "presented at ichep2004." http://ichep04.ihep.ac.cn, 2004.

[64] S. R. Armstrong, *Pentaquark searches in electron positron annihilations and two-photon collisions at lep*, *Nucl. Phys. Proc. Suppl.* **142** (2005) 364–369 [hep-ex/0410080].

[65] **BES Collaboration** Collaboration, J. Z. Bai *et. al.*, *Search for the pentaquark state in psi(2s) and j/psi decays to k0(s) p k- anti-n and k0(s) anti-p k+ n*, *Phys. Rev.* **D70** (2004) 012004 [hep-ex/0402012].

[66] **BELLE Collaboration** Collaboration, K. Abe *et. al.*, *Study of the baryon antibaryon low-mass enhancements in charmless three-body baryonic b decays*, hep-ex/0409010.

[67] **BABAR Collaboration** Collaboration, B. Aubert *et. al.*, *Search for strange pentaquark production in e+ e- annihilations at s**(1/2) = 10.58-gev and in upsilon(4s) decays*, hep-ex/0408064.

[68] **CDF** Collaboration, D. O. Litvintsev, *Pentaquark searches at cdf*, *Nucl. Phys. Proc. Suppl.* **142** (2005) 374–377 [hep-ex/0410024].

[69] **E690 Collaboration** Collaboration, D. Christian, "presented at qnp2004." http://www.qnp2004.org, 2004.

[70] **FOCUS Collaboration** Collaboration, K. Stenson, *Pentaquark searches at focus*, hep-ex/0412021.

[71] **SELEX Collaboration** Collaboration, J. Engelfried, "presented at quark confinement 2004." http://www.eurocongress.it/Quark, 2004.

[72] J. Napolitano, J. Cummings and M. Witkowski, *Search for theta(1540)+ in the reaction k+ p –¿ k+ n pi+ at 11-gev/c*, hep-ex/0412031.

[73] **HyperCP Collaboration** Collaboration, M. J. Longo *et. al.*, *High statistics search for the theta+(1.54) pentaquark*, *Phys. Rev.* **D70** (2004) 111101 [hep-ex/0410027].

[74] **HERA-B Collaboration** Collaboration, K. T. Knopfle, M. Zavertyaev and T. Zivko, *Search for theta+ and xi(3/2)– pentaquarks in hera-b*, *J. Phys.* **G30** (2004) S1363–S1366 [hep-ex/0403020].

[75] **SPHINX Collaboration** Collaboration, Y. M. Antipov *et. al.*, *Search for theta(1540)+ in exclusive proton-induced reaction p + c (n) –¿ theta(+) anti-k0 + c (n) at the energy of 70-gev*, *Eur. Phys. J.* **A21** (2004) 455–468 [hep-ex/0407026].

[76] **COMPASS Collaboration** Collaboration, G. Brona and B. Badelek, "Search for pentaquark states in the compass experiment." http://wwwcompass.cern.ch/compass/publications/ , 2004.

[77] **PHENIX Collaboration** Collaboration, C. Pinkenburg, *Search for the anti-theta- –¿ k- anti-n with phenix*, *J. Phys.* **G30** (2004) S1201–S1206 [nucl-ex/0404001].

[78] **the CLAS** Collaboration, R. De Vita *et. al.*, *Search for the theta+ pentaquark in the reactions gamma p - -¿ anti-k0 k+ n and gamma p –¿ anti-k0 k0 p*, *Phys. Rev.* **D74** (2006) 032001 [hep-ex/0606062].

[79] K. Hicks, *An experimental review of the theta+ pentaquark*, hep-ex/0412048.

[80] K. Hicks, *Workshop summary: Experiment (pentaquark 2004)*, hep-ex/0501018.

[81] A. R. Dzierba, C. A. Meyer and A. P. Szczepaniak, *Reviewing the evidence for pentaquarks*, hep-ex/0412077.

[82] D. Diakonov, V. Petrov and M. V. Polyakov, *Exotic anti-decuplet of baryons: Prediction from chiral solitons*, *Z. Phys.* **A359** (1997) 305–314 [hep-ph/9703373].

[83] M. Praszalowicz, *Pentaquark in the skyrme model*, *Phys. Lett.* **B575** (2003) 234–241 [hep-ph/0308114].

[84] J. R. Ellis, M. Karliner and M. Praszalowicz, *Chiral-soliton predictions for exotic baryons*, *JHEP* **05** (2004) 002 [hep-ph/0401127].

[85] J. Sugiyama, T. Doi and M. Oka, *Penta-quark baryon from the qcd sum rule*, *Phys. Lett.* **B581** (2004) 167–174 [hep-ph/0309271].

[86] S.-L. Zhu, *Understanding pentaquark states in qcd*, *Phys. Rev. Lett.* **91** (2003) 232002 [hep-ph/0307345].

[87] A. Sibirtsev, J. Haidenbauer, S. Krewald and U.-G. Meissner, *New results on the limit for the width of the exotic theta+ resonance*, *Phys. Lett.* **B599** (2004) 230–235 [hep-ph/0405099].

[88] Y. Oh, K. Nakayama and T. S. H. Lee, *Pentaquark theta(1540)+ production in gamma n –¿ k anti-k n*, hep-ph/0412363.

[89] R. L. Jaffe and F. Wilczek, *Diquarks and exotic spectroscopy*, *Phys. Rev. Lett.* **91** (2003) 232003 [hep-ph/0307341].

[90] F. Stancu and D. O. Riska, *Stable u u d d anti-s pentaquarks in the constituent quark model*, *Phys. Lett.* **B575** (2003) 242–248 [hep-ph/0307010].

[91] M. Karliner and H. J. Lipkin, *The constituent quark model revisited: Quark masses, new predictions for hadron masses and k n pentaquark*, hep-ph/0307243.

[92] C. E. Carlson, C. D. Carone, H. J. Kwee and V. Nazaryan, *Phenomenology of the pentaquark antidecuplet*, *Phys. Lett.* **B573** (2003) 101–108 [hep-ph/0307396].

[93] F. Csikor, Z. Fodor, S. D. Katz and T. G. Kovacs, *Pentaquark hadrons from lattice qcd*, *JHEP* **11** (2003) 070 [hep-lat/0309090].

[94] S. Sasaki, *Lattice study of exotic $s = +1$ baryon*, *Phys. Rev. Lett.* **93** (2004) 152001 [hep-lat/0310014].

[95] N. Mathur *et. al.*, *A study of pentaquarks on the lattice with overlap fermions*, *Phys. Rev.* **D70** (2004) 074508 [hep-ph/0406196].

[96] N. Ishii *et. al.*, *Penta-quark baryon in anisotropic lattice qcd*, *Phys. Rev.* **D71** (2005) 034001 [hep-lat/0408030].

[97] N. Ishii *et. al.*, *Anisotropic lattice qcd studies of penta-quark anti- decuplet*, hep-lat/0410022.

[98] C. Alexandrou, G. Koutsou and A. Tsapalis, *The pentaquark potential, mass and density-density correlator*, *Nucl. Phys. Proc. Suppl.* **140** (2005) 275–277 [hep-lat/0409065].

[99] T.-W. Chiu and T.-H. Hsieh, *A study of theta+ (u d u d anti-s) in lattice qcd with exact chiral symmetry*, *Phys. Rev.* **D72** (2005) 034505 [hep-ph/0403020].

[100] T. T. Takahashi, T. Umeda, T. Onogi and T. Kunihiro, *Lattice qcd study of the pentaquark baryons*, hep-lat/0410025.

[101] F. Csikor, Z. Fodor, S. D. Katz and T. G. Kovacs, *The status of pentaquark spectroscopy on the lattice*, hep-lat/0407033.

[102] S. Sasaki, *Pentaquarks: Status and perspectives for lattice calculations*, *Nucl. Phys. Proc. Suppl.* **140** (2005) 127–133 [hep-lat/0410016].

[103] D. B. Leinweber, W. Melnitchouk, D. G. Richards, A. G. Williams and J. M. Zanotti, *Baryon spectroscopy in lattice qcd*, *Lect. Notes Phys.* **663** (2005) 71–110.

[104] R. D. Young, D. B. Leinweber, A. W. Thomas and S. V. Wright, *Chiral analysis of quenched baryon masses*, *Phys. Rev.* **D66** (2002) 094507 [hep-lat/0205017].

[105] D. B. Leinweber, A. W. Thomas and R. D. Young, *Physical nucleon properties from lattice qcd*, *Phys. Rev. Lett.* **92** (2004) 242002 [hep-lat/0302020].

[106] G. T. Fleming, *Looking for pentaquarks in lattice qcd*, hep-lat/0501011.

[107] J. W. Negele, "presented at qnp2004." http://www.qnp2004.org, 2004.

[108] C. W. Bernard *et. al.*, *The qcd spectrum with three quark flavors*, *Phys. Rev.* **D64** (2001) 054506 [hep-lat/0104002].

[109] D. B. Leinweber, *Qcd sum rules for skeptics*, *Annals Phys.* **254** (1997) 328–396 [nucl-th/9510051].

[110] F. X. Lee and D. B. Leinweber, *Negative-parity baryon spectroscopy, Nucl. Phys. Proc. Suppl.* **73** (1999) 258–260 [hep-lat/9809095].

[111] D. B. Leinweber, T. Draper and R. M. Woloshyn, *Decuplet baryon structure from lattice qcd, Phys. Rev.* **D46** (1992) 3067–3085 [hep-lat/9208025].

[112] D. B. Leinweber, T. Draper and R. M. Woloshyn, *Baryon octet to decuplet electromagnetic transitions, Phys. Rev.* **D48** (1993) 2230–2249 [hep-lat/9212016].

[113] C. Alexandrou *et. al.*, *N to delta electromagnetic transition form factors from lattice qcd, Phys. Rev.* **D69** (2004) 114506 [hep-lat/0307018].

[114] C. Alexandrou *et. al.*, *The n to delta electromagnetic transition form factors from lattice qcd, Phys. Rev. Lett.* **94** (2005) 021601 [hep-lat/0409122].

[115] M. Luscher, *Volume dependence of the energy spectrum in massive quantum field theories. 2. scattering states, Commun. Math. Phys.* **105** (1986) 153–188.

[116] M. Luscher, *Signatures of unstable particles in finite volume, Nucl. Phys.* **B364** (1991) 237–254.

[117] F. Csikor, Z. Fodor, S. D. Katz, T. G. Kovacs and B. C. Toth, *A comprehensive search for the theta+ pentaquark on the lattice*, hep-lat/0503012.

[118] C. Alexandrou and A. Tsapalis, *A lattice study of the pentaquark state*, hep-lat/0503013.

[119] T. T. Takahashi, T. Umeda, T. Onogi and T. Kunihiro, *Search for the possible s = +1 pentaquark states in quenched lattice qcd, Phys. Rev.* **D71** (2005) 114509 [hep-lat/0503019].

[120] N. Ishii, T. Doi, Y. Nemoto, M. Oka and H. Suganuma, *Spin 3/2 penta-quarks in anisotropic lattice qcd, Phys. Rev.* **D72** (2005) 074503 [hep-lat/0506022].

[121] S. Sasaki, T. Blum and S. Ohta, *A lattice study of the nucleon excited states with domain wall fermions, Phys. Rev.* **D65** (2002) 074503 [hep-lat/0102010].

[122] **QCDSF** Collaboration, M. Gockeler *et. al.*, *Negative-parity baryon masses using an o(a)-improved fermion action, Phys. Lett.* **B532** (2002) 63–70 [hep-lat/0106022].

[123] B. Efron and R. J. Tibshirani, *An Introduction to the Bootstrap.* Chapman & Hall, 1993.

[124] D. Seibert, *Undesirable effects of covariance matrix techniques for error analysis, Phys. Rev.* **D49** (1994) 6240–6243 [hep-lat/9305014].

[125] P. R. Bevington and D. K. Robinson, *Data reduction and error analysis for the physical sciences, 2nd Ed.* McGraw-Hill Inc., 1992.

[126] K. Holland and K. J. Juge, *Absence of evidence for pentaquarks on the lattice*, hep-lat/0504007.

[127] **JLQCD** Collaboration, S. Aoki *et. al.*, *Analysis of hadron propagators with one thousand configurations on a* 24 3×64 *lattice at* $\beta = 6.0$, *Nucl. Phys. Proc. Suppl.* **47** (1996) 354–357 [hep-lat/9510013].

[128] D. B. Leinweber, R. M. Woloshyn and T. Draper, *Electromagnetic structure of octet baryons*, *Phys. Rev.* **D43** (1991) 1659–1678.

A

γ-matrix Representations

In this appendix we review the representations of the γ-matrices we use in this thesis. In each case the γ-matrices obey the Clifford algebra,

$$\{\gamma^\mu, \gamma^\nu\} = 2g^{\mu\nu} \ . \tag{A.1}$$

In our phenomenology we use the Bjorken and Drell representation of the γ-matrices,

$$\gamma_0 = \begin{pmatrix} I & 0 \\ 0 & -I \end{pmatrix} \qquad \gamma^i = \begin{pmatrix} 0 & \sigma_i \\ -\sigma_i & 0 \end{pmatrix} , \qquad \gamma^5 = \begin{pmatrix} 0 & I \\ I & 0 \end{pmatrix} . \tag{A.2}$$

Where σ_i are the Pauli matrices and I is the 2×2 identity. In the Bjorken and Drell representation the charge conjugation matrix $C = i\gamma^0\gamma^2$.

However in our lattice calculations at the quark level, it is convenient to have a Hermitian representation. In the Sakuarai representation,

$$\gamma_i^S = -i\gamma^i \ , \ \gamma_4^S = \gamma_0 \ , \ \gamma_5^S = -\gamma^5. \tag{A.3}$$

The charge conjugation matrix in the Sakurai representation is exactly equal to the charge conjugation matrix in the Bjorken and Drell representation. Of course with the Sakurai representation $C = \gamma_4\gamma_2$.

B

Transformation properties of the interpolating fields

Here we briefly discuss the Lorentz transformation properties of the interpolators continuous with the identity. As an example we show how $\chi_3^\mu(x)$ transforms to illustrate the utility of the charge conjugation matrix C. The quark fields transform as spinors, so

$$u(x) \rightarrow S(\Lambda)\ u(\Lambda x)\ , \tag{B.1}$$

where the $S(\Lambda) = e^{-i\omega^{\mu\nu}\sigma_{\mu\nu}}$. So we transform each of the quark fields in χ_3^μ in Eq. (2.1),

$$\chi_3^\mu(x) \rightarrow \epsilon^{abc}(u^{Ta}(\Lambda x)\ S(\Lambda)^T\ C\gamma_5\gamma^\mu\ S(\Lambda)\ d^b(\Lambda x))\gamma_5\ S(\Lambda)\ u^c(\Lambda x)\ . \tag{B.2}$$

In this expression $S(\Lambda)^T\ C$ is $C\ S^{-1}(\Lambda)$ because

$$\begin{aligned} S(\Lambda)^T\ C &= e^{-i\omega^{\mu\nu}\sigma_{\mu\nu}^T}\ C \\ &= CC^T\ (1 - i\omega^{\mu\nu}\sigma_{\mu\nu}^T - \ (\omega^{\mu\nu}\sigma_{\mu\nu}^T)^2 + ...\ )\ C \\ &= C\ e^{-i\omega^{\mu\nu}C\ \sigma_{\mu\nu}^T\ C^T}\ . \end{aligned} \tag{B.3}$$

We evaluate the expression in the exponent,

$$C\sigma_{\mu\nu}^T C^T \ = \ -\sigma_{\mu\nu} \tag{B.4}$$

So simplifying Eq. (B.3),

$$\begin{aligned} C\ e^{-i\omega^{\mu\nu}C\ \sigma_{\mu\nu}^T\ C^T} &= C\ e^{+i\omega^{\mu\nu}\sigma_{\mu\nu}} \\ &= C\ S^{-1}(\Lambda)\ . \end{aligned} \tag{B.5}$$

So we can write Eq. (B.2),

$$\begin{aligned} \chi_3^\mu(x) \ &\rightarrow \ \epsilon^{abc}(u^{Ta}(\Lambda x)\ C\gamma_5 S^{-1}(\Lambda)\gamma^\mu\ S(\Lambda)\ d^b(\Lambda x))\gamma_5\ S(\Lambda)\ u^c(\Lambda x) \\ &= \ \Lambda_\nu^\mu\ S(\Lambda)\ \epsilon^{abc}\ (u^{Ta}(\Lambda x)\ C\gamma_5\gamma^\nu\ d^b(\Lambda x))\gamma_5\ u^c(\Lambda x) \\ &= \ \Lambda_\nu^\mu\ S(\Lambda)\ \chi_3^\mu(\Lambda x)\ . \end{aligned} \tag{B.6}$$

We use the identity $S^{-1}(\Lambda)\gamma^\mu\ S(\Lambda) = \Lambda_\nu^\mu\gamma^\nu$, where Λ_ν^μ is the lorentz transformation for four-vectors. Therefore χ_3^μ transforms as a vector times a spinor under proper Lorentz transformations. Similarly we can trivially show that the interpolators such as χ_1 and χ_2 transform like spinors.

The Covariance Matrix

As discussed previously, we fit a constant in time to the effective mass data to extract the masses from our correlation functions. The appropriate procedure for the effective mass data is to minmise the function

$$\chi^2 = \sum_i \frac{1}{\sigma_i^2}(M^{\text{eff}}(t_i) - m) \cdot (M^{\text{eff}}(t_i) - m) \ , \tag{C.1}$$

with respect to the parameter m. The standard measure of the fit is the χ^2 per degree of freedom (χ^2_{dof}). The χ^2_{dof} should generally be $\simeq 1$ for an ideal fit. However the effective mass data is correlated in time, and it has been shown by [127] that the probability of finding a plateau over a number of time slices is small. Therefore it is necessary to include a contribution from the correlations in the data in the calculation χ^2. So we minimise,

$$\chi^2 = \sum_{i,j}(M^{\text{eff}}(t_i) - m) \cdot \mathrm{C}_{ij}^{-1} \cdot (M^{\text{eff}}(t_j) - m) \ , \tag{C.2}$$

to find the value of χ^2 which we use as our measure of the fit. In our analysis we use the jackknife estimate of the covariance matrix,

$$\mathrm{C}_{\alpha\beta} = \sum_i^n (\bar{x}_i(t_\alpha) - \frac{1}{n}\sum_j^n x_j(t_\alpha)) \ \cdot (\bar{x}_i(t_\beta) - \frac{1}{n}\sum_j^n x_j(t_\beta)) \ . \tag{C.3}$$

We use a singular value decomposition to invert the covariance matrix in Eq. (C.2). The number of degrees of freedom of the fit is then the number of time slices, less the number of fit parameters, less the number of singularities encountered in inverting the covariance matrix. As discussed in [124], the mass extracted with Eq. (C.2) may not coincide with the effective mass data, which is counter intuitive. So the correct procedure is still to use Eq. (C.1) to calculate the mass, but keep the value of χ^2 in Eq. (C.2) as the measure of the fit.

D

The two-point functions at the quark level

A general nucleon interpolator is,

$$\begin{aligned}
\chi_\gamma &= \epsilon^{abc}(u^a_\alpha A_{\alpha\beta} d^b_\beta) B_{\gamma\delta} u^c_\delta \\
\bar{\chi}_{\gamma'} &= \epsilon^{abc} u^{c'\dagger}_{\delta'} (C^\dagger\gamma_0)_{\delta'\gamma'} \ (d^{b'\dagger}_{\beta'} (D^\dagger)_{\beta'\alpha'} u^{a'\dagger}_{\alpha'}) \\
&= \epsilon^{abc} \bar{u}^{c'}_{\delta'} (\gamma_0 C^\dagger \gamma_0)_{\delta'\gamma'} \ (\bar{d}^{b'}_{\beta'} (\gamma_0 D^\dagger \gamma_0)_{\beta'\alpha'} \bar{u}^{a'}_{\alpha'}) \\
&= \epsilon^{abc} \bar{u}^{c'}_{\delta'} \widetilde{C}_{\delta'\gamma'} \ (\bar{d}^{b'}_{\beta'} \widetilde{D}_{\beta'\alpha'} \bar{u}^{a'}_{\alpha'}) \ , \qquad \text{(D.1)}
\end{aligned}$$

where A,B,C,D are some arbitrary products of γ-matrices, the letters (a,b,c) label the colour indices and the Greek letters label the spinor indices. Above we have made the replacement $\widetilde{D} = (\gamma_0 D^\dagger \gamma_0)$ and $\widetilde{C} = (\gamma_0 C^\dagger \gamma_0)$. Extracting the correlation function with the χ_1, χ_2 and χ_3 interpolators is done by selecting the appropriate combinations of γ-matrices A,B,C and D. The general solution for the nucleon style two-point function is,

$$\begin{aligned}
&G_{\gamma\gamma'}(t,\vec{p}) \ = \\
&\left\langle \sum_{\vec{x}} e^{-i\vec{p}\cdot\vec{x}} \ (BU^{cc'}\widetilde{C})_{\gamma\gamma'} Tr[(AD^{bb'}\widetilde{D})^T U^{aa'}] + (BU^{cc'}(AD^{bb'}\widetilde{D})^T U^{aa'}\widetilde{C})_{\gamma\gamma'} \right\rangle \ , \qquad \text{(D.2)}
\end{aligned}$$

where the capital U and D indicate up and down-quark propagators from the source to the sink.

An arbitrary Δ interpolator is,

$$\begin{aligned}
\chi_\gamma &= \epsilon^{abc}(u^a_\alpha A_{\alpha\beta} u^b_\beta) B_{\gamma\delta} u^c_\delta \\
\bar{\chi}_{\gamma'} &= \epsilon^{a'b'c'} u^{c'\dagger}_{\delta'} (C^\dagger\gamma_0)_{\delta'\gamma'} \ (u^{b'\dagger}_{\beta'} (D^\dagger)_{\beta'\alpha'} u^{a'\dagger}_{\alpha'}) \\
&= \epsilon^{a'b'c'} \bar{u}^{c'}_{\delta'} (\gamma_0 C^\dagger \gamma_0)_{\delta'\gamma'} \ (\bar{u}^{b'}_{\beta'} (\gamma_0 D^\dagger \gamma_0)_{\beta'\alpha'} \bar{u}^{a'}_{\alpha'}) \\
&= \epsilon^{a'b'c'} \bar{u}^{c'}_{\delta'} \widetilde{C}_{\delta'\gamma'} \ (\bar{u}^{b'}_{\beta'} \widetilde{D}_{\beta'\alpha'} \bar{u}^{a'}_{\alpha'}) \ , \qquad \text{(D.3)}
\end{aligned}$$

again A,B,C,D are some arbitrary products of γ-matrices, with the condition that the diquark is isovector. This requires that the matrices A and D be symmetric. If D is symmetric then $\widetilde{D}$ is also symmetric. The general formula for the Δ correlation function is,

$$\begin{aligned}
G_{\gamma\gamma'}(t,\vec{p}) \ = \ &\left\langle \sum_{\vec{x}} e^{-i\vec{p}\cdot\vec{x}} \right. \\
&\left. 2(BU^{cc'}\widetilde{C})_{\gamma\gamma'} Tr[(AU^{bb'}\widetilde{D})^T U^{aa'}] + \ 4(BU^{cc'}\widetilde{D}(U^{bb'})^T A U^{aa'}\widetilde{C})_{\gamma\gamma'} \right\rangle . \qquad \text{(D.4)}
\end{aligned}$$

Next we discuss the general formula for the correlation functions extracted with the $\chi_{NK}, \chi_{\widetilde{NK}}$ or χ_{NK^*}. The NK style of pentaquark interpolator, Eq. (3.1), has two terms with a relative sign which is chosen depending on the isospin of the interpolator. The first part of the NK interpolator is like a proton and K^0 interpolator coupled together, we label this as χ_{PK^0}. The second part of the interpolator is like a neutron and a K^+ interpolator coupled together, we label this as χ_{NK^+}. The correlation function

has four terms, the diagonal terms PK^0/PK^0 and NK^+/NK^+ and the cross term PK^0/NK^+ and NK^+/PK^0. Because we have isospin symmetry in our simulation we need only evaluate one of the diagonal terms and one of the cross terms to construct the correlation functions. We proceed here by evaluating the PK^0/PK^0 contribution to the correlation function at the quark level. The general PK^0 style of interpolator is,

$$\begin{aligned}
\chi_{\gamma}^{PK^0} &= \epsilon^{abc}(u_\alpha^a A_{\alpha\beta} d_\beta^b) B_{\gamma\delta} u_\delta^c \ (\bar{s}_\sigma^e C_{\sigma\rho} d_\rho^a) \\
\bar{\chi}_{\gamma'}^{PK^0} &= \epsilon^{a'b'c'}(\bar{d}_{\rho'}^{e'}(\gamma_0 D^\dagger \gamma_0)_{\rho'\sigma'} s_{\sigma'}^{e'}) \ \bar{u}_{\delta'}^{c'}(\gamma_0 E^\dagger \gamma_0)_{\delta'\gamma'} \ (\bar{d}_{\beta'}^{b'}(\gamma_0 F^\dagger \gamma_0)_{\beta'\alpha'} \bar{u}_{\alpha'}^{a'}) \\
\bar{\chi}_{\gamma'}^{PK^0} &= \epsilon^{a'b'c'}(\bar{d}_{\rho'}^{e'} \widetilde{D}_{\rho'\sigma'} s_{\sigma'}^{e'}) \ \bar{u}_{\delta'}^{c'} \widetilde{E}_{\delta'\gamma'} \ (\bar{d}_{\beta'}^{b'} \widetilde{F}_{\beta'\alpha'} \bar{u}_{\alpha'}^{a'}) \ . \qquad \text{(D.5)}
\end{aligned}$$

The general formula of the correlation function is,

$$\begin{aligned}
G_{\gamma\gamma'}^{PK^0/PK^0}(t,\vec{p}) &= \Big\langle \sum_{\vec{x}} e^{-i\vec{p}\cdot\vec{x}} \Big\{ \ - Tr[(\gamma_5 S^{*ee'} \gamma_5)(CD^{ee'} \widetilde{D})^T] \times \\
&\quad \Big((BU^{cc'} \widetilde{E})_{\gamma\gamma'} Tr[(AD^{bb'} \widetilde{F})^T U^{aa'}] - (BU^{ca'} (AD^{bb'} \widetilde{F})^T U^{ac'} \widetilde{E})_{\gamma\gamma'} \Big) \\
&\quad + (BU^{cc'} \widetilde{E})_{\gamma\gamma'} Tr[(CD^{eb'} \widetilde{F})^T (\gamma_5 S^{*ee'} \gamma_5) \ (AD^{be'} \widetilde{D})^T U^{aa'}] \\
&\quad - ((BU^{ca'})(CD^{eb'} \widetilde{F})^T (\gamma_5 S^{*ee'} \gamma_5) \ (AD^{be'} \widetilde{D})^T (U^{ac'} \widetilde{E}))_{\gamma\gamma'} \Big\} \Big\rangle \ . \qquad \text{(D.6)}
\end{aligned}$$

We have used the relation $(\gamma_5 S^{ee'}(x,0)\gamma_5)^*_{\sigma\sigma'} = S^{e'e}(0,x)_{\sigma'\sigma}$ to evaluate the anti-strange quark propagator, labelled capital S.

Next we evaluate the PK^0/NK^+ cross term.

$$\bar{\chi}_{\gamma'}^{NK^+} = \epsilon^{a'b'c'}(\bar{u}_{\rho'}^{e'} \widetilde{D}_{\rho'\sigma'} s_{\sigma'}^{e'}) \ \bar{d}_{\delta'}^{c'} \widetilde{E}_{\delta'\gamma'} \ (\bar{d}_{\beta'}^{b'} \widetilde{F}_{\beta'\alpha'} \bar{u}_{\alpha'}^{a'}) \ . \qquad \text{(D.7)}$$

The general formula of the correlation function is,

$$\begin{aligned}
G_{\gamma\gamma'}^{PK^0/NK^+}(t,\vec{p}) &= \Big\langle \sum_{\vec{x}} e^{-i\vec{p}\cdot\vec{x}} \Big\{ \\
&\quad - \ ((BU^{ce'} \widetilde{D})(\gamma_5 S^{*ee'} \gamma_5)^T (CD^{eb'} \widetilde{F}) U^{aa'T} (AD^{bc'} \widetilde{E}))_{\gamma\gamma'} \\
&\quad + \ ((BU^{ce'} \widetilde{D})(\gamma_5 S^{*ee'} \gamma_5)^T (CD^{ec'} \widetilde{E}))_{\gamma\gamma'} \ Tr[(AD^{bb'} \widetilde{F})^T U^{aa'}] \\
&\quad + \ ((BU^{ca'})(CD^{eb'} \widetilde{F})^T (\gamma_5 S^{*ee'} \gamma_5)(U^{ae'} \widetilde{D})^T (AD^{bc'} \widetilde{E})_{\gamma\gamma'} \\
&\quad - \ ((BU^{ca'})(AD^{bb'} \widetilde{F})^T (U^{ae'} \widetilde{D})(\gamma_5 S^{*ee'} \gamma_5)^T (CD^{ec'} \widetilde{E}))_{\gamma\gamma'} \Big\} \Big\rangle \ , \\
G_{\gamma\gamma'}(t,\vec{p}) &= 2\Big\{ G^{PK^0/PK^0} + G^{PK^0/NK^+} \Big\} \ . \qquad \text{(D.8)}
\end{aligned}$$

To compute the colour fused style, $\widetilde{NK}$ interpolator we interchange the colour indices in the general formulae.

Finally we discuss the general formula for the diquark-diquark style of interpolating field that we use to extract the correlation functions with the χ_{PS}, χ_{SS} and χ_{LY}. The general diquark-diquark style interpolating field is,

$$\begin{aligned}
\chi_{\gamma}^{DD} &= \epsilon^{abc}(u_\alpha^a A_{\alpha\beta} d_\beta^b)(u_\sigma^c A_{\sigma\rho} d_\rho^e) \ C_{\gamma\delta} \bar{s}_\delta^e \\
\bar{\chi}_{\gamma'}^{DD} &= \epsilon^{a'b'c'} s_{\delta'}^{e'}(\gamma_0 D^\dagger \gamma_0)_{\delta'\gamma'} \ (\bar{d}_{\rho'}^{e'}(\gamma_0 E^\dagger \gamma_0)_{\rho'\sigma'} \bar{u}_{\sigma'}^{c'}) \ (\bar{d}_{\beta'}^{b'}(\gamma_0 F^\dagger \gamma_0)_{\beta'\alpha'} \bar{u}_{\alpha'}^{a'}) \\
&= \epsilon^{a'b'c'} s_{\delta'}^{e'} \widetilde{D}_{\delta'\gamma'} \ (\bar{d}_{\rho'}^{e'} \widetilde{E}_{\rho'\sigma'} \bar{u}_{\sigma'}^{c'}) \ (\bar{d}_{\beta'}^{b'} \widetilde{F}_{\beta'\alpha'} \bar{u}_{\alpha'}^{a'}) \qquad \text{(D.9)}
\end{aligned}$$

The general formula for the correlation function is,

$$
\begin{aligned}
G^{DD}_{\gamma\gamma'}(t,\vec{p}) \;=\; & -\Big\langle \sum_{\vec{x}} e^{-i\vec{p}\cdot\vec{x}}\, (C\gamma_5 S^{*ee'}\gamma_5 \widetilde{D})_{\gamma\gamma'} \times \Big\{ \\
& Tr[(BD^{ee'}\widetilde{E})^T U^{cc'}]\, Tr[(AD^{bb'}\widetilde{F})^T U^{aa'}] \\
- \;& Tr[(BD^{ee'}\widetilde{E})^T U^{ca'} (AD^{bb'}\widetilde{F})^T U^{ac'}] \\
- \;& Tr[(BD^{eb'}\widetilde{F})^T U^{cc'} (AD^{be'}\widetilde{E})^T U^{aa'}] \\
+ \;& Tr[(BD^{eb'}\widetilde{F})^T U^{ca'}]\, Tr[(AD^{be'}\widetilde{E})^T U^{ac'}] \Big\} \Big\rangle \; . \qquad \text{(D.10)}
\end{aligned}
$$

The different colour assignments required to evaluate the correlation function with LY interpolator is accomplished by relabeling the colour indices in the general formula.

Following spin and parity projection, the correlation functions are made real by including both the U and U^* gauge field configurations in the ensemble averaging. This provides an improved unbiased estimator which is strictly real. This is easily implemented at the correlation function level by observing that,

$$
M^{-1}(\{U^*_\mu\}) = \left[C\gamma_5\, M^{-1}(\{U_\mu\})\, (C\gamma_5)^{-1}\right]^* \; , \qquad \text{(D.11)}
$$

holds for quark propagators. For a more detailed discussion of this issue see Refs. [18, 128].